UNIVERSITY OF LIVERPOOL

School of Engineering

PhD Thesis

Dynamic polarization control using spatial light modulators for advanced ultrafast laser surface-structuring

Thesis submitted in accordance with the requirements of The University of Liverpool for the degree of Doctor in Philosophy

By

Yang Jin

October 2016

Laser Group
Department of Engineering
The University of Liverpool
Brownlow Street
Liverpool
L69 3GH
UK

Declaration

I hereby declare that all of the work contained within this dissertation has not been submitted for any other qualification.

Signed: _____

Date: _____

Abstract

Reflective liquid-crystal-based Spatial Light Modulators (SLM), addressed with optimised Computer Generated Holograms (CGH), have been integrated with two picosecond laser systems to control and manipulate the phase front and polarization states of laser beams, both statically and dynamically, for ultrafast laser surface micro-structuring.

Firstly, two SLMs were used in combination to structure the optical fields and wavefront of a 532 nm, 10-picosecond laser beam, producing planar or vortex wavefronts with radial or azimuthal polarization states. Multiple first-order cylindrical vector beams with vortex or planar wavefront have been generated and used to nano-structure a highly polished stainless steel metal surface. Then, synchronization of the two SLMs with the picosecond laser system was achieved for dynamic modulation of the polarization states of the laser beam. Consequently, for the first time, four states of polarization, linear horizontal and vertical, radial and azimuthal, all with a ring intensity distribution, were dynamically switched at a frequency up to ν = 12.5 Hz while synchronized with a motion control system and the 532 nm picosecond laser. Surface patterning with these 4 states resulted in ~0.5 μm pitch plasmonic structures, easily discernible when using white light diffraction.

In separate experiments, CGH's applied to a single SLM were synchronised with a galvo scanner and a 1064 nm, 10 ps laser system for dynamic linear polarisation modulation. This real time polarisation control allowed complex laser surface patterning of polished

metals with linear, periodic, ~1 μm pitch surface plasmonic structures. Hence, iridescent metal surface colouring with various geometric patterns was achieved.

Finally, with an advanced digital scanner fully synchronized with the 532 nm, 10 ps laser system, high speed parallel multi-beam surface patterning of a 30 nm thick Aluminium thin film on a flexible Polyethylene Terephthalate (PET) was achieved. With laser repetition rate of 200 kHz and 8 diffracted first order beams, a film removal rate of $R > 0.5$ cm^2/s was demonstrated with 5W average laser power delivered without damage to the PET substrate. The effective laser repetition rate was $f \sim 1.3$ MHz. During this work, the single pulse front and rear side single pulse ablation thresholds of the Al film on PET were determined to be $F_{th} = 0.20 \pm 0.01$ $J \cdot cm^{-2}$ and 0.15 ± 0.01 $J \cdot cm^{-2}$ respectively, much lower than the PET ablation threshold, $F_{th} = 1.2$ $J \cdot cm^{-2}$, providing a clear processing window.

List of Publications to Date by Author

Peer-Reviewed Journal Publication

1. **Y. Jin**, O. J. Allegre, W. Perrie, K. Abrams, J. Ouyang, E. Fearon, S. P. Edwardson, G. Dearden "*Dynamic modulation of spatially structured polarization fields for real-time control of ultrafast laser-material interactions*" Opt. Express 21(21), 25333-25343 (2013) - **First author**

2. **Y. Jin**, W. Perrie, O. J. Allegre, K. Abrams, P. Harris, G. Dearden "*Multi-beam picosecond laser thin film pattering of Aluminum on Polyethylene Terephthalate*" Optics and Lasers in Engineering 74 (2015) 67-74 - **First author**

3. J. Allegre, **Y. Jin**, W. Perrie, J. Ouyang, E. Fearon, S. P. Edwardson, and G. Dearden, "*Complete wavefront and polarization control for ultrashort-pulse laser microprocessing*" Opt. Express 21(18), 21198–21207 (2013) - **Corresponding author**

4. A. R. Neale, **Y. Jin**, J. Ouyang, S. Hughes, S.P. Edwardson, L. J. Hardwick "*Electrochemical performance of laser micro-structured nickel oxyhydroxide cathodes*" Journal of Power Sources 271 (2014) 42-47

5. L. Ye, W. Perrie, O. J. Allegre, **Y. Jin**, Z. Kuang, P. J. Scully, E. Fearon, D. Eckford, S. P. Edwardson and G. Dearden "*NUV femtosecond laser inscription of volume Bragg gratings in poly(methyl)methacrylate with linear and circular polarizations*" Laser Phys. 23 (2013) 126004 (10pp)

6. J. Ouyang, W. Perrie, O. J. Allegre, T. Heil, **Y. Jin**, E. Fearon, D. Eckford, S. P. Edwardson, and G. Dearden "*Tailored optical vector fields for ultrashort-pulse laser induced complex surface plasmon structuring*" Opt. Express 23(10), 12562–12572 (2015)

Conference Publications

1. **Y. Jin**, W. Perrie, O. J. Allegre, S. P. Edwardson and G. Dearden, (2014) "*Multi-beam picosecond laser thin film patterning of Aluminium on Polyethylene Terephthalate (PET)*", Photon 14, London

2. **Y. Jin**, O. J. Allegre, W. Perrie, J. Ouyang, S. P. Edwardson and G. Dearden, (2014) "*Complete wavefront and polarization control for ultrafast laser microprocessing*", Photon 14, London

3. **Y. Jin**, J. Ouyang, W. Perrie, G. Dearden, and O. J. Allegre, (2015) "*Wavefront and polarization structuring for shaping the focal fields of ultrashort-pulse laser beams*." Lasertagung Mittweida 2015, At University of Applied Sciences, Mittweida, Germany.

4. J. Ouyang, **Y. Jin**, O. J. Allegre, W. Perrie, E. Fearon, S. P. Edwardson and G. Dearden, (2015). "*Tailored optical fields and their application in ultrafast laser materials processing*." Lasertagung Mittweida 2015, At University of Applied Sciences, Mittweida, Germany.

5. A. J. Allegre, **Y. Jin**, W. Perrie, S. P. Edwardson and G. Dearden, (2013) "*Experimental study of radially and azimuthally polarized ultrafast laser beams.*" Proceedings of the 2nd biannual Industrial Laser Applications Symposium (ILAS). Association of Laser Users, Nottingham pp 10

6. A. J. Allegre, **Y. Jin**, W. Perrie, S. P. Edwardson and G. Dearden, (2013) "*Generation and analysis of radial polarization fields in a picosecond-pulse laser beam.*" Proceedings of Advanced Solid State Lasers. Optical Society (OSA), Paris, France pp JTh2A.14

7. W. Perrie, L. Ye, **Y. Jin,** O. J. Allegre, S. P. Edwardson, G. Dearden, (2013) "*Ultrafast laser processing with the aid of Spatial Light Modulators*". Proceedings of the 2nd biannual Industrial Laser Applications Symposium (ILAS). Association of Laser Users, Nottingham pp 10

8. A. J. Allegre, W. Perrie, **Y. Jin**, S. P. Edwardson and G. Dearden, (2014) "*Dynamic polarisation control for improved laser micro- and nano-structuring of surfaces*." Photon 14, London

9. S. P. Edwardson, O. J. Allegre, **Y. Jin,** W. Perrie and G. Dearden, (2014) "*Dynamic wavefront and polarisation control for ultrashort-pulse laser microprocessing*." (Invited Keynote). In: 8th International Conference on Photonic Technologies, City Hall.

10. A. J. Allegre, J. Ouyang, W. Perrie, **Y. Jin**, S. P. Edwardson and G. Dearden (2015) "*Advanced beam shaping for ultrafast laser micro-processing*." 38th International MATADOR conference proceedings, Huwei, Taiwan, pp73-78.

11. G. Zhu, W. Perrie, O. J. Allegre**, Y. Jin**, S. P. Edwardson and G. Dearden, (2014) "*Filamentation in poly(methyl) methacralate with linear, circular, Radial and Azimuthal polarisation with Vortex wavefronts*." Photon 14, London

12. J. Ouyang, O. J. Allegre, W. Perrie**, Y. Jin**, S. P. Edwardson and G. Dearden, (2014) "*Three-dimensional investigation of focal fields produced with ultrashort-pulse cylindrical vector beams*." Photon 14, London

Acknowledgements

I would like to thank everyone who has supported and encouraged me during my PhD.

First of all, I would like to thank my supervisors, Prof. Geoff Dearden and Dr. Stuart Edwardson for their unwavering support, guidance and encouragement throughout this research. Thanks must go to Dr. Walter Perrie and Dr. Olivier Allegre for their invaluable advice, constant help and endless support. Their inexhaustible supply of scientific enthusiasm made my PhD both interesting and enjoyable.

I would like to thank Dr. Eamonn Fearon and Mr Doug Eckford for their invaluable suggestions and assistance throughout my PhD research. I would also like to acknowledge everyone from the Laser group of University of Liverpool who was involved in my research, in particular, Dr. Dun Liu, Dr. Zheng Kuang, and Dr. Spencer Shang.

Additionally, I would like to thank my fellow students, Jinglei Ouyang, Linyi Ye, Liwei Fu, Guangyu Zhu, Ghazal Sheikholeslami, Jiangling Li and Hui Gao, for their help and advice.

Finally, I would like to sincerely acknowledge my family members, especially my parents for their constant support and unwavering faith throughout my PhD and all past studies. Special thanks to my beloved wife, Shu Yu, for her constant support, understanding, and company.

Table of Contents

List of Symbols

Symbol	Unit	Description
$\|E\|$	$V \cdot cm^{-1}$	*Amplitude of electric field*
$\vec{i}$	*n/a*	*Unit vector along one axis of a coordinate system*
$\vec{j}$	*n/a*	*Unit vector along one axis of a coordinate system*
$\vec{k}$	cm^{-1}	*Wave vector of a laser beam*
C	$J \cdot cm^{-3} \cdot K^{-1}$	*Volume specific heat*
d	*nm*	*Thickness*
D	$cm^2 \cdot s^{-1}$	*Diffusivity*
E	$V \cdot cm^{-1}$	*Electric field*
E_p	μJ	*Pulse energy*
F	$J \cdot cm^{-2}$	*Laser Fluence*
f	*Hz*	*Laser repetition rate*
G	*n/a*	*Gain factor*
H_m	$J \cdot cm^{-3}$	*Melting enthalpy*
H_v	$J \cdot cm^{-3}$	*Evaporation enthalpy*
I	$W \cdot cm^{-2}$	*Laser beam Intensity*
i	*n/a*	*Imaginary unit*
J	*n/a*	*Jones vector represent of electric vector*
l_h	μm	*Heat diffusion depth*
l_s	μm	*Optical penetration depth or optical skin depth*
l_{th}	*nm*	*Penetration depth of phonons*
m	*n/a*	*Topological charge*

M^2	n/a	Beam quality factor
m_o	n/a	Diffraction order
n	n/a	Refractive index of a material
N	n/a	Pulse overlap
P	W	Power
P_C	MW	Critical power for self-focusing
P_{SLM}	n/a	Jones matrix of a phase delay caused by a SLM
Q	n/a	Jones matrix of a quarter-wave plate
R	n/a	Reflectivity
R_a	nm	Surface roughness
R_c	n/a	Jones matrix rotating a reference coordinate system
R_r	$cm^2 \cdot s^{-1}$	Thin film patterning rate
S	n/a	Degree of incubation
s	$mm \cdot s^{-1}$ or $m \cdot s^{-1}$	Speed
T_0	$^\circ C$	Room temperature
Tm	$^\circ C$	Melting point
T_v	$^\circ C$	Boiling point
α	cm^{-1}	Absorption coefficient
β	Rad	Phase modulation
δ	Rad	Phase delay (or phase difference) between two waves
Δt	ms	Time
Δv	nm	Spectrum bandwidth
η_{+1}	n/a	First order diffraction efficiency
θ	$^\circ$	Angle

κ	$cm^2 \cdot s^{-1}$	*Thermal diffusivity*
λ	*nm*	*Central wavelength of a radiation*
Λ	μm	*Grating period or pitch period of LIPSS*
ν	*Hz*	*Frequency of changing CGHs on SLM*
τ	*seconds*	*Time*
$\tau_{e\text{-}ph}$	*ps or fs*	*Electron-phonon coupling time*
τ_p	*ns, ps, fs*	*Pulse duration, pulse length, pulsewidth*
φ	*Rad*	*Phase of complex field*
ϕ	*Rad*	*Phase delay*
$\tilde{\omega}$	m^{-1}	*Magnitude of a wave vector*

List of Abbreviations

ACEL	Alternating Current Electroluminescent Lamps
Al	Aluminium
AOM	Acousto-Optic Modulator
CCD	Charge-Coupled Device
CGH	Computer Generated Holograms
CPA	Chirped Pulse Amplification
CW	Continuous Wave
DMD	Digital Micro-mirror Device
DOE	Diffractive Optical Elements
DVI	Digital Visual Interface
EDX	Energy-dispersive X-ray spectroscopy
FLC-SLM	Ferroelectric Liquid Crystal SLMs
GS algorithm	Gerchberg-Saxton algorithm
GVD	Group Velocity Dispersion
HAZ	Heat Affect Zone
HSD	High-Speed Driver
HSFL	High Spatial Frequency LIPSS
ITO	Indium Tin Oxide
KLM	Kerr Lens Modelocking
LBO	Lithium Triborate
LCD	Liquid Crystal Display
LCOS	Liquid Crystal On Silicon

LCSLM	Liquid Crystal Spatial Light Modulator
LIPSS	Laser Induced Periodic Surface Structures
LSFL	Low Spatial Frequency LIPSS
MPI	Multi-Photon Ionization
NI	National Instruments
NA	Numerical Aperture
OAM	Orbital Angular Momentum
PAL-SLM	Parallel-Aligned nematic Liquid crystal SLM
PEN	Polyethylene Naphthalate
PET	Polyethylene Terephthalate
PMMA	Poly(methyl)methacrylate
PSO	Position Synchronized Output
RFID	Radial Frequency Identification
RTC	Real Time Control
SEM	Scanning Electron Microscope
SESAM	Semiconductor Saturable Absorber Mirror
SLM	Spatial Light Modulator
SS	Stainless Steel
TCO	Transparent Conducting Oxide
TNLC-SLM	Twisted Nematic Liquid Crystal SLM

Chapter 1 – Introduction

1.1 Background and motivation

The unique properties of ultrafast lasers having temporal pulse lengths less than a few tens of picoseconds have opened up a new era for materials processing. The extremely high peak intensity and extremely short timescale enable both linear and non-linear interactions of laser radiation with matter. For example, micro-nano drilling and cutting materials with minimised heat affect zone (HAZ) [1,2], functional surface production [3-8] and micro-welding of similar and dissimilar materials [9]. Also, high intensity non-linear light interaction with matter such as self-focusing [10], filamentation [11-13], and multi-photon ionization (MPI) in atoms [14,15], molecules [16], and solids [17,18], are contributing to making photonic device, microfluidics, and microelectronics [19].

Remarkable development of ultrafast laser technology in the last decade enables current commercial ultrafast laser systems to reach hundreds of watts average output power with mJ to Joule level pulse energy and with less than 40 femtosecond pulse [20]. For example, recent development in diode pumped thin disc laser technology can generate 150 GW peak power pulses from a Regenerative amplifier (TRUMPF Scientific – DIRA 200-1, 200 mJ/1.5 ps/1 kHz, DIRA 150-5, 30 mJ/1.5 ps 5 kHz) [21].

Maximizing the speed of production is a key aspect to industrialize the ultrafast laser processing. However, with single beam processing, often significant pulse energy has to be thrown away to achieve thermal free ablation [22]. By altering the wavefront of the incident energetic laser beam with SLM, multiple diffractive first order laser beams can be generated to achieve high throughput, high quality, thermal free ultrafast laser processing [23,24].

Some commercialized ultrafast laser systems have the capabilities to adjust pulse repetition rate, pulse energy and wavelength output via harmonic conversion. However, the output polarisation of most laser systems is generally linear.

Polarization is a critical parameter in ultrafast laser material processing. For example, surface nano-structuring of metals, semi-conductors and dielectrics using structured optical field [25-31], high aspect ratio micro-drilling of metal sheet using cylindrical vector beams [32,33], and polarization dependent surface ablation of polymer poly(methyl)methacrylate (PMMA) [34]. Hence the ability to control and manipulate the polarization state of the incident laser beam is desirable. Static methods include for example the generation of spatially structured polarization fields such as radial or azimuthal with a birefringent plate [35-37] or a Spatial Light Modulator (SLM) [38-47]. Dynamic methods include continuously rotating waveplates [48-50] or using a low bandwidth orthogonal linear polarization states switching liquid crystal polarization rotator [51].

Accordingly, tailoring the optical field and the wavefront statically or dynamically has the potential to maximise the throughput and optimise the quality of ultrafast laser processing, or even open up a new era for ultrafast laser-material interactions. However, limited research has been carried out in this field. While static generation of arbitrary, complex polarisation fields has been achieved previously [38-47,52-57]. Simultaneous modulation of both wavefront and polarization state to generate first order cylindrical vector beams has not been reported previously, and applied to high power laser surface micro-structuring. Hence, this thesis focuses on the research using SLMs for arbitrary

simultaneous manipulation of polarization state and the wavefront of high power picosecond laser beams both statically and dynamically for laser-materials ablation.

The main objectives of this thesis are:

1) To use two SLMs in combination to arbitrarily modulate the wavefront and optical field of picosecond lasers to generate multiple diffractive first order cylindrical vector beams with vortex or planar wavefront for surface ablation.

2) To demonstrate high speed, dynamic modulation of spatially structured polarization fields of a picosecond-pulse laser for real-time control of ultrafast laser-material interactions.

3) To demonstrate dynamic modulation of the direction of a linear polarization with synchronised SLM for high speed metal surface colourizing.

4) To utilize an advanced picosecond laser system to demonstrate multi-beam high speed thin film patterning of 30 nm Aluminium on Polyethylene Terephthalate (PET).

1.2 Contribution of this thesis

This thesis is the first to explore high speed dynamical modulation of spatially structured polarization states in a picosecond laser system with synchronized SLM to control laser-material interaction. This approach offers great potential for industrial applications in both surface and volume micro- and nano-structuring in the areas of, for example, solar cell micro-structuring [31], surface security marking [58], and permanent 5D data writing in fused silica with high data rates [30].

The thesis started with the generation of static, multiple diffractive cylindrical vector beams with vortex or planar wavefront using two SLMs in combination. This was followed by real time synchronisation of the application of CGHs to two SLMs and integrated with an advanced micro-positioning system and picosecond laser - the first demonstration of this technique at a bandwidth of 12.5 Hz with 4 states of polarisation, including linear horizontal and vertical, radial and azimuthal, all ring intensity modes.

In order to demonstrate the power of the SLM-synchronized picosecond laser system, high speed metal surface colourizing and high speed multi-beam thin film selective patterning were carried out. Polychrome metal surface patterns were generated at high speed with dynamic modulation of the direction of a linearly polarized beam. Thin Aluminium films with 30 nm thickness were selectively patterned at a rate of ~0.5 cm^2/s with 5 W average power impinging on the sample with no significant damage to the sensitive polymer substrate. A clear process window for this thin film was determined from ablation thresholds of thin film and substrate. Both examples demonstrated the significant increase in processing speed and improved quality of ultrafast laser processing.

1.3 Overview of the thesis

The thesis consists of eight chapters. The current chapter is the main introduction of the work.

Chapter 2 reviews the general background and research related to this thesis, ranging from the introduction of the background on ultrafast laser systems and ultrafast laser-material interaction mechanisms including a review of methods for phase and polarization modulation.

Chapter 3 is the experimental basis of the thesis, where the main equipment deployed for the research is introduced in detail and experimental setups are discussed and demonstrated.

Chapter 4 presents the results of static modulation of the wavefront and the polarization of a 532 nm picosecond laser beam for obtaining desired single or multi-diffractive first order cylindrical vector beams with planar or vortex wavefront.

Chapter 5 focus on dynamic modulation of the optical field of the 532 nm picosecond laser system for real-time control of the laser-material interaction, where the results demonstrate four states of polarization, linear horizontal and vertical, radial and azimuthal, dynamically switched at a frequency ν=12.5 Hz while synchronized with a motion control system, showing that the technique enables a remarkable level of real-time control of the optical light field for real-time surface patterning.

In chapter 6, the linear polarization direction of a 1064 nm picosecond laser was dynamically modulated for colourizing metal surfaces. Up to 36 different directional linear polarization states have been dynamically utilized for colourizing a highly polished brass sample, resulting in a polychrome surface patterning on the sample surface. An example of adopting this method for security patterning of high value goods was demonstrated in the chapter.

Chapter 7 describes a study of high speed multi-beam thin film selective patterning of Aluminium on PET with an advanced scanning Galvanometer system. Basic studies of picosecond laser interaction with thin Al on PET film and high speed thin film patterning

at a film remove rate of $R > 0.5$ cm^2/s have been demonstrated in this chapter along with ablation thresholds.

Chapter 8 summarises the results and conclusions of the thesis followed by recommendation for future works.

Chapter 2 - Literature Review

2.1 Introduction

This chapter reviews the background literature of current research. Ultrafast laser systems and ultrafast laser-material interaction mechanisms will be presented first, followed by an introduction section of phase and polarization and their effects on ultrafast laser-material interaction. Microprocessing with Spatial Light Modulators by controlling the phase and polarization will be reviewed in this chapter and also polarization dependent Laser Induced Periodic Surface Structures (LIPSS) will be introduced in this chapter. Finally, thin film processing with ultrafast laser and applications will be described.

2.2 Ultrafast laser systems and ultrafast laser material interaction

Ultrafast laser refers to a laser that generates light pulses with temporal duration shorter than a few tens of picoseconds (1 ps =10^{-12}) [1]. Producing these ultrashort pulses with adequate pulse energy for material processing requires special technologies such as modelocking and chirped pulse amplification (CPA) [2].

2.2.1 Mode locking and chirped pulse amplification

- **Mode locking**

Only six years after the invention of laser by Theodore Maiman [59], De Maria *et al.* produced the first ultrashort pulse, estimated to be picoseconds long, using a passively modelocked Nd:glass laser [60]. In a laser, each of the longitudinal modes will oscillate randomly in the laser's resonant cavity. Modelocking is a technique used for generating

ultrashort laser pulses by inducing a fix phase relationship between the longitudinal modes. The laser active medium requires a wide spectrum bandwidth to generate ultrashort pulses as there is a fixed relation between the spectrum bandwidth $\Delta\nu$ and the generated output pulse of duration τ_p by the expression, $\tau_p \cdot \Delta\nu = constant$ [61,62]. By modelocking broadband laser modes in the laser cavity, ultrashort pulses can be created by constructive and destructive interference, as shown in figure 2.1.

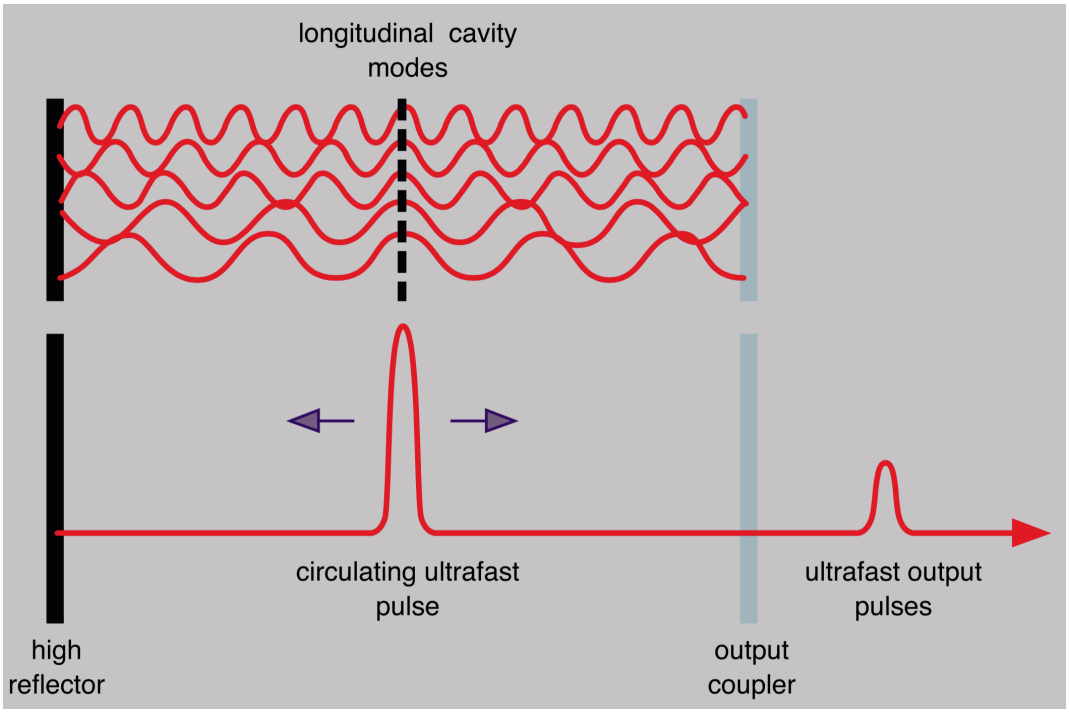

Figure 2.1 *Mechanism of laser pulse modelocking* [63].

Modelocking methods are classified as active and passive modelocking [64]. Active modelocking uses an intracavity dynamic optical modulator, typically an acousto-optic modulator, which is driven externally with a synchronized signal. On the other hand, passive modelocking uses nonlinear materials, such as a saturable absorber or artificial saturable absorber (Kerr lens) inside the cavity. Compared with active modelocking,

passive modelocking produce much shorter pulse durations and hence have been more widely used in ultrafast laser systems [64].

A saturable absorber used in passive modelocking is a nonlinear material that selectively transmits high intensity light while absorbing low intensity light. Saturable absorbers can be organic dyes, solid state, and semi-conductors [64]. Compared to dye saturable absorbers and solid-state saturable absorbers, semiconductors can absorb over a wide range of wavelengths and provide controllable absorption recovery time and saturation fluence [64]. After integrating a semiconductor absorber into a laser cavity mirror structure, one of the most widely used passive modelocking method can be obtained, termed a Semiconductor Saturable Absorber Mirror (SESAM) [65]. Thanks to these unique properties of SESAM, most diode-pumped picosecond lasers adopt this method.

Kerr lens modelocking (KLM) is another important passive modelocking method, which is the most widely used modelocking method in femtosecond lasers where temporal pulse lengths are < 100 fs [66-68]. The Kerr effect causes a change of refractive index of the medium in response to the applied optical electric field. As the refractive index increases with the intensity, self-focusing results, hence the high intensity part of the incident beam onto Kerr lens can be focused through an aperture placed after the Kerr lens, discriminating against CW operation, resulting in an ultra-short intense pulse [64]. Kerr lens modelocking is able to produce remarkably short pulses when combined with a large bandwidth gain medium, such as Ti-Sapphire. For example, less than 6 femtosecond pulse duration has been generated in Ti:sapphire laser when compensating Group Velocity Dispersion (GVD) [67,68].

Ultrashort, femtosecond lasers are often based on Ti-sapphire. This material has a large gain bandwidth of ~ 200 THz hence can support fs pulses with pulse length τ_p ~ 1/200 THz, which is ~5 fs or two optical cycles. Kerr lens mode locking of Ti-sapphire results in equal gain on all the many longitudinal modes within this massive gain bandwidth, ~300 nm wide. When added coherently, these interfere to generate ultrashort pulses <10 fs when GVD is corrected. Also, the Fourier transform of a fs pulse to frequency space yields a large bandwidth (and vice versa), hence the inverse relationship showing that the shorter the pulse, the wider is its Fourier spectrum.

- **Chirped pulse amplification (CPA)**

With modelocking techniques, ultrashort pulses are generated with high repetition rate (typically >30 MHz) and low pulse energy typically in the nanojoule (nJ) level, which is insufficient for laser micromachining and many other applications. Picosecond (ps) pulses emitted from oscillator can be regeneratively amplified in a gain medium directly to the microjoule (~100 μJ) level for many applications including micromachining.

Direct amplification of femtosecond pulses on the other hand would create nonlinear effects at ultrahigh peak intensities well above the self-focusing threshold, so that damage to amplifying medium and optical surfaces would result. Thus, CPA is required for amplification (Fig.2.2) [70]. In CPA, the large bandwidth pulses from the oscillator are temporally stretched in a dispersive delay line, eg, using a pair of gratings [71], which introduce positive GVD where the red end of the spectrum travels a shorter path than the blue end. Pulses from this pulse train are selected and injected into a regenerative amplifier with gain G ~10^6 bringing pulse energy to the mJ level. After amplification, the stretched

pulse is then compressed to the original pulse duration by a grating pair with the opposite, negative GVD. A schematic of chirped pulse amplification is shown in figure. 2.2.

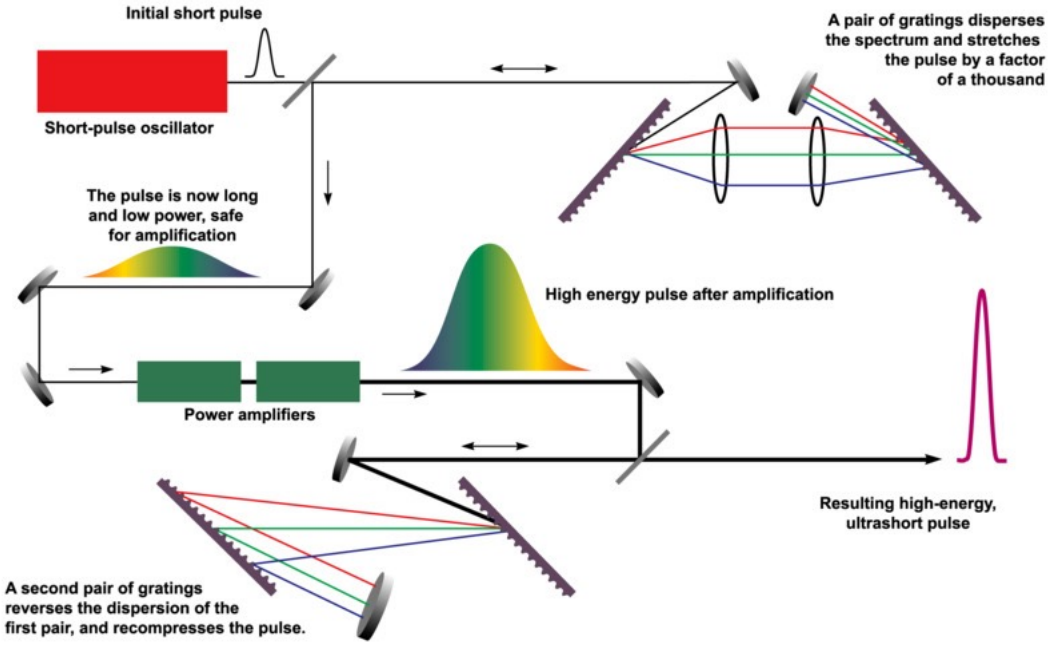

Figure 2.2 *Diagrammatic scheme of chirped pulse amplification* [69].

2.2.2 Ultrafast laser material interaction

This section gives a brief review of laser material interaction mechanisms of ultrashort pulse regime ($\tau_p \leq 10$ ps). As a comparison, mechanisms of material processing with long pulse duration will also be introduced here.

- **Overall**

When a laser pulse impinges on an opaque target material, depending on the reflectivity of the surface material, a portion of light penetrates a very thin layer of the substrate. The electrons are heated to high temperature by absorbing the laser energy, followed by the energy transfer to the ion lattice due to electron-phonon coupling within a picosecond time

scale, for most materials. Pulses that is longer than picosecond induce more energy transfer to the ion lattice, resulting in heating, melting and vaporization of the material.

- **Optical penetration**

The intensity of transmitted light into a material decreases exponentially with distance when the light absorption is linear, described using Beer-Lamberts' law [72]:

$$I(z) = I_0 \exp(-\alpha z) \tag{2-1}$$

where I_0 (W·cm^{-2}) and $I(z)$ (W·cm^{-2}) are the incident intensity on the material surface and transmitted intensity reaching depth z from the surface respectively. $\alpha(\lambda)$ (cm^{-1}) is the absorption coefficient of the target material which determines how far a particular wavelength can penetrate the material before it is absorbed. The optical penetration depth or optical skin depth l_s is a useful term that describes how much energy is absorbed by the material within a depth of

$$l_s = 1/\alpha \tag{2-2}$$

One can see that 86% of the incident light is absorbed within $2l_s$ from the surface.

- **Heat diffusion**

After the incident light penetrated to a thin layer of the material, electrons inside the layer absorb the laser energy first and then the absorbed energy is transferred to the lattice by electron-phonon interaction. The depth of heat penetration in the material during the pulse is defined as the heat diffusion depth l_h, given by:

$$l_h = 2\sqrt{\kappa \tau_p} \tag{2-3}$$

where κ is the thermal diffusivity ($cm^2 \cdot s^{-1}$) and τ_p is the pulse duration. From equation 2-3, it is obvious that shorter pulse duration τ_p limits heat diffusion to a small volume in the material, increasing absorbed energy density.

With a particular target material, the optical skin depth l_s is determined by the light wavelength whereas the heat diffusion depth l_h is determined by the laser pulse duration. If $l_s > l_h$, the volume of material heated is determined by the optical penetration depth and vice versa with a long pulse [73]. The volume of material heated directly affects the ablation threshold of the material.

- **Long pulse and ultrashort pulse**

Not only does the ablation threshold increase with pulse duration, long pulses (ns) also cause many other problems for material processing, such as large heat affected zone, recast layer and shockwaves. With long pulse laser-material interaction, the material close to the surface of the target is heated, melts, and vaporized within the pulse duration. The result is significant melting with a loss of micro-structuring precision. Also, heat diffusion causes heat flow to regions outside of processing area, resulting in collateral damage along with unwanted heat affected zone. As material evaporates during the pulse, plasma absorption may also be induced resulting in Shockwaves which may cause surface ripples or even damage the nearby device structures.

With ultrashort pulse laser-material processing, the pulse duration is considerably shorter than the thermalization time of the material. Hence most of the pulse energy heats a small

localized volume of material, raising its temperature rapidly past the melt temperature to vaporization point [74]. Although there will be some residual thermal effects due to the thermal diffusion after the ultrashort pulse, most of the heated material is directly vaporized, ending up with minimum heat effect on the material. A brief schematic compares long pulse and ultra-short pulse laser interaction is given in figure 2.3. With extremely high intensity, ultrafast laser pulses also interact with high transmissivity dielectrics and semiconductors. In this case, nonlinear effects such as multiphoton absorption and Coulomb explosion need to be considered [75,76]. Note that even with ultrashort pulses, thermal damage can happen with high fluence input due to residual thermal diffusion [74].

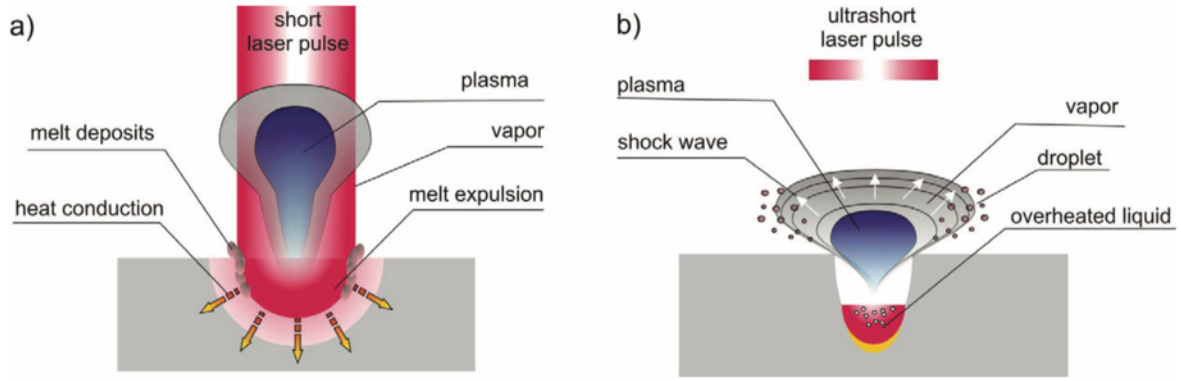

Figure 2.3 *(a) Long pulse laser material ablation and (b) ultrashort pulse laser material ablation* [77].

2.3 Introduction of phase and polarization

Phase and polarization are important factors that influence the efficiency and quality of ultrafast laser micromachining. In this thesis, novel methods are developed to control the laser phase and polarization. This section presents a brief introduction of phase and polarization and their effects on ultrafast laser interaction.

2.3.1 Definition of phase and polarization

- **Phase**

The beam emitted from a laser cavity is a form of self-propagating coherent transverse oscillating electromagnetic wave. In the electromagnetic wave, the phase can be defined as the position of a point in time on the wave, or the position of a point on the wave where it has a specified amplitude value. For example, phase a and phase b in figure 2.4 (a) can be defined as the point on the wave when the wave travels to $t_{1,}$and t_2 respectively, or the point on the wave when the amplitude equals to A_1 and A_2 respectively. Another important concept is phase front or wavefront, defined as a surface of constant phase of a coherent propagating electromagnetic wave disturbance. When there is no phase difference among a group of coherent waves propagating in the same direction, the waves are called in-phase with a planer wavefront, see figure 2.4 (b). Contrarily, as shown in figure 2.4 (c), the waves are out-of-phase.

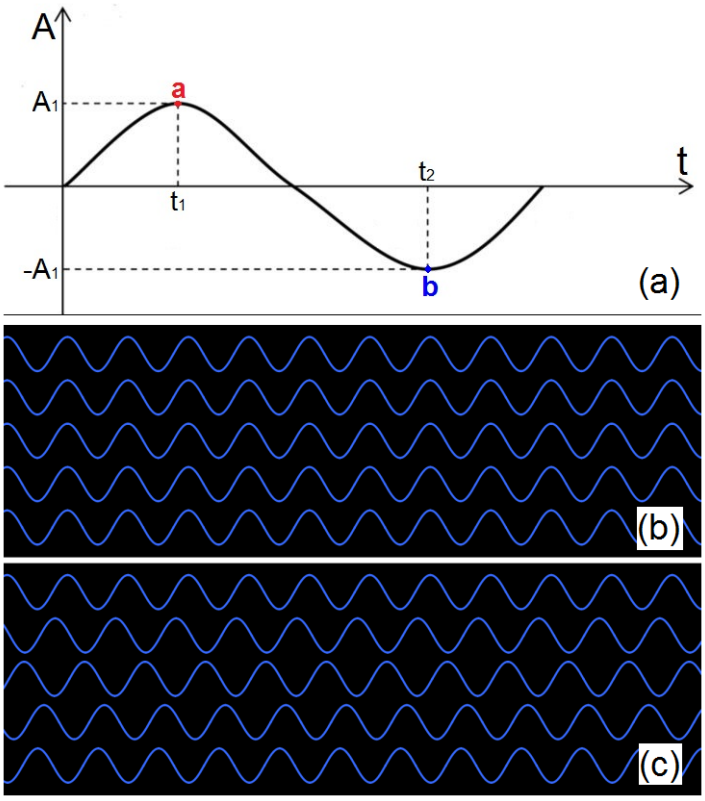

Figure 2.4 (a) diagram for phase definition. Diagram of waves that are propagating in-phase (b) and out-of-phase (c).

- **Polarization**

The polarization is a term refers to the oscillating direction of the electric field of the electromagnetic wave [78]. In the case of a linear polarization or plane polarization, the electric field of the electromagnetic wave is oscillating alternately up and down in a plane perpendicular to the direction of propagation. The tip of electric field vector describes a line in any fixed transverse section. With elliptical polarization, the strength and the direction of the electric field of a wave are both varying during the propagation, and the tip of the electric field vector at a given time in space describes an ellipse as time progresses. Circular polarization is a particular case of elliptical polarization, in which the

strength of the electric field stays the same but the direction of the electric field changes in a rotary manner during the propagation.

The electric field of a polarized wave can be resolved into two orthogonal parts, forming a coordinate system. A linearly polarized wave can be resolved into two orthogonal in-phase linear components and a circularly polarized wave contains two orthogonal linear parts but with $\pi/2$ phase difference.

- **Jones vector and Jones matrix representing of polarization and linear optical components**

The electric field of a transverse wave *E* can be resolved into two orthogonal components E_x and E_y in a coordinate system, described in the following equation:

$$E = \vec{i}E_x + \vec{j}E_y \tag{2-4}$$

$\vec{i}$ and $\vec{j}$ are unit vectors along the *x* and *y* axis of the coordinate system, E_x and E_y are the components of the electric vectors corresponding to *x* and *y* axis, which can be written in exponential form as: a

$$E_x = |E_x|\exp(i\varphi_x) \tag{2-5}$$

$$E_y = |E_y|\exp(i\varphi_y) \tag{2-6}$$

where $|E_x|$ and φ_x are the amplitude and phase of E_x respectively, and similarly for E_y. Equations 2-5 and 2-6 can be written in a matrix form known as the Jones vector:

$$\begin{bmatrix} E_x \\ E_y \end{bmatrix} = \begin{bmatrix} |E_x|\exp(i\varphi_x) \\ |E_y|\exp(i\varphi_y) \end{bmatrix} \tag{2-7}$$

- **Linear polarization**

In the case of linear polarization, by it's definition, there is no phase difference between the *x* and *y* axis, which means $\varphi_x = \varphi_y \pm n\pi = \varphi$ (*n* can be any integer), in which case the angle of the polarization depends on the ratio of $|E_x|/|E_y|$.

Assuming a wave *E* linearly polarized and impinged on a coordinate system with θ degrees to the *x* axis, accordingly, we get $|E_x| = |E|\cos\theta$ and $|E_y| = |E|\sin\theta$, the equation 2-7 in this case can be written as:

$$\begin{bmatrix} E_x \\ E_y \end{bmatrix} = \begin{bmatrix} |E|\cos\theta\exp(i\varphi) \\ |E|\sin\theta\exp(i\varphi) \end{bmatrix} = |E|\exp(i\varphi)\begin{bmatrix} \cos\theta \\ \sin\theta \end{bmatrix} \tag{2-8}$$

Jones vector $\begin{bmatrix} \cos\theta \\ \sin\theta \end{bmatrix}$ can be used to represent a linearly polarized wave at θ degrees relative to the *x* axis. For example, if the wave is linearly polarized in the *x* axis, where $\theta = 0$, the Jones vector is $\begin{bmatrix} 1 \\ 0 \end{bmatrix}$. Similarly, if $\theta = 90$ or $\theta = 45$, then the normalized Jones vector for the corresponding wave is $\begin{bmatrix} 0 \\ 1 \end{bmatrix}$ or $\frac{1}{\sqrt{2}}\begin{bmatrix} 1 \\ 1 \end{bmatrix}$. Normalized vectors have $|E_x|^2 + |E_y|^2 = 1$

- **Circular polarization**

With circular polarization, the phase delay between the orthogonal components is $\delta = \pm \pi/2$, and the amplitude of the two components is equal $|E_x| = |E_y| = |E|$, equation 2-7 can be written as:

$$\begin{bmatrix} E_x \\ E_y \end{bmatrix} = \begin{bmatrix} |E|\exp(i\varphi_x) \\ |E|\exp[i(\varphi_x \pm \pi/2)] \end{bmatrix} = |E|\exp(i\varphi_x)\begin{bmatrix} 1 \\ \exp(\pm i\pi/2) \end{bmatrix} = |E|\exp(i\varphi_x)\begin{bmatrix} 1 \\ \pm i \end{bmatrix} \quad (2\text{-}9)$$

the last part of the equation can be used to represent the polarization of the wave $\begin{bmatrix} 1 \\ \pm i \end{bmatrix}$.

$\begin{bmatrix} 1 \\ i \end{bmatrix}$ represents left hand circular polarization, and $\begin{bmatrix} 1 \\ -i \end{bmatrix}$ represents right hand circular polarization.

- **Jones matrix represents linear optical components**

A number of optical elements influence the orientation of the polarization, and they can be generally classified into two catalogs: polarizers and phase retarders. A linear polarizer transmits light polarized along the transmission axis and cuts off waves of the orthogonal linear polarization. On the other hand, a phase retarder induces a phase retardation between the waves that pass along the fast axis and the slow axis of the phase retarder. The effect of such elements on a light wave can be described in a similar notation as the polarization states, known as Jones matrix. Multiply a Jones matrix which represents a linear optical component with a Jones vector which represents an incident wave to the optical component results in a Jones vector that represents the polarization state of the

output wave. Hence, if the influence on the incident polarization is known, the corresponding Jones matrix can be found. The Jones matrix for several optical elements are represented in Table 2.1.

Table 2.1 *Jones Matrix for some linear optical elements*

Optical element	Jones matrix
Quarter-wave plate with fast axis horizontal	$\begin{bmatrix} 1 & 0 \\ 0 & i \end{bmatrix}$
Quarter-wave plate with fast axis vertical	$\begin{bmatrix} 1 & 0 \\ 0 & -i \end{bmatrix}$
Relative phase retarder	$\begin{bmatrix} e^{i\phi_x} & 0 \\ 0 & e^{i\phi_y} \end{bmatrix}$
Half-wave plate with fast axis either horizontal or vertical	$\begin{bmatrix} 1 & 0 \\ 0 & -1 \end{bmatrix}$

In this thesis, some of the above optical elements are applied to change the polarization of a laser beam.

2.3.2 Cylindrical vector beams

Laser beams with the polarization states presented above, such as linear, circular and elliptical polarization, are all spatially homogeneous states of polarization. Cylindrical

vector beams, with a spatially inhomogeneous state of polarization, are now attracting more attention due to their interesting properties and potential applications [79]. Cylindrical vector beams are beams with cylindrical symmetry in polarization. Two particular cases of cylindrical vector beams are radial and azimuthal polarization, in which the electric vectors have a radial and azimuthal distribution respectively when viewing along the beam propagation direction (Figure 2.5).

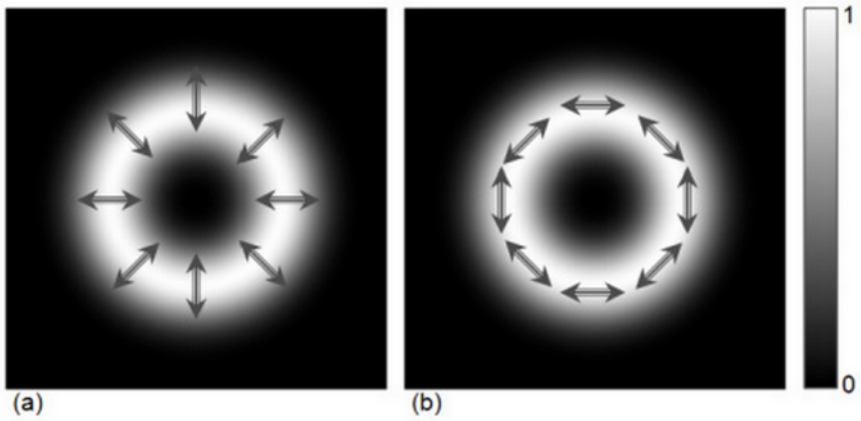

Figure 2.5 *(a) the cross section and polarization vectors of a radially polarized beam and (b) azimuthally polarized beam, the arrows indicate the direction of local electric vectors* [80].

To represent radial and azimuthal polarization in Jones vector, a Cartesian coordinate system is used (see Figure 2.6), θ in the coordinate system represents the polar angle and the polar angle θ varies with localized electric vectors in the beam. The Jones vector represent a radial polarized beam can be written as: $\begin{bmatrix} \cos\theta \\ \sin\theta \end{bmatrix}$, whereas an azimuthal polarized beam can be represented by $\begin{bmatrix} \sin\theta \\ \cos\theta \end{bmatrix}$. As θ is varying with localized electric vectors in the beam, the localized electric vectors are spatially varying with the polar

angle. Note that the Jones vector representing an azimuthally polarized beam should not be confused with the Jones vector that represents a linearly polarized beam oriented at an angle θ, where the electric vectors of the latter are not spatially varying with the polar angle θ.

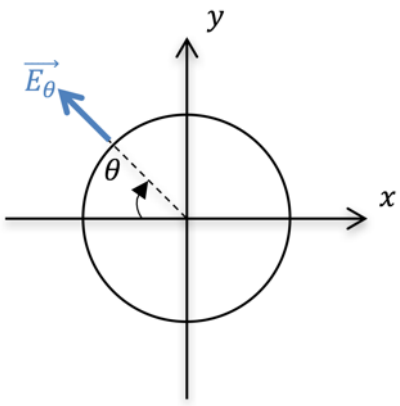

Figure 2.6 *Schematic of the cross section of a radially polarized beam with a vector represented in a Cartesian coordinate system, the polar angle θ is varying with localized electric vectors in the beam.*

Laser beams can have both a polarization and a phase structure [35]. Regarding the phase structure of a laser beam, two particular cases of interest are laser beams with a planar wavefront and with a vortex wavefront (see Figure 2.7). A laser beam with a vortex wavefront carries orbital angular momentum due to the spiral wavefront [81]. This differs from spin angular momentum, which depends on the polarization state. Topological charge *m* is a term used to describe the strength and the angle of orbital angular momentum, see Figure 2.7 which shows the schematic of orbital angular momentum with different topological charges.

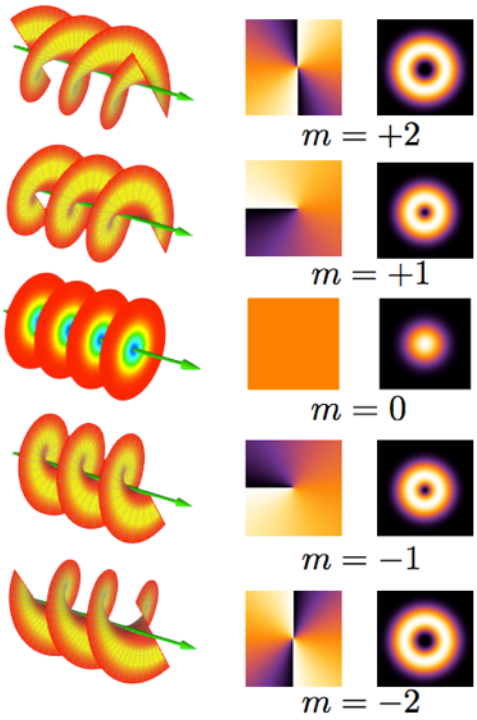

Figure 2.7 *Schematic of laser beams different phase structures. "m" refers to the topological charge of the beam* [82].

The Jones vector representing a radially polarized beam with planar wavefront or with vortex wavefront is slightly different. A radially polarized beam with planar wavefront can be represented by $J_{RP}(\theta) = \begin{bmatrix} \cos\theta \\ \sin\theta \end{bmatrix}$ and a radially polarized beam with vortex wavefront can be represented by $J_{RV}(\theta) = e^{i\theta}\begin{bmatrix} \cos\theta \\ \sin\theta \end{bmatrix}$. Consider a radially polarized beam with vortex wavefront in a coordinate system as shown in Figure 2.6. When $\theta = 0$, the Jones vector of the localized electric vectors is $J_{RV}(0) = e^{i\times 0}\begin{bmatrix} \cos 0 \\ \sin 0 \end{bmatrix} = \begin{bmatrix} 1 \\ 0 \end{bmatrix}$, whereas when $\theta = \pi$, the Jones vector represents the localized electric vectors becomes $J_{RV}(\pi) = e^{i\pi}\begin{bmatrix} \cos\pi \\ \sin\pi \end{bmatrix} = e^{i\pi}\begin{bmatrix} -1 \\ 0 \end{bmatrix}$. One can see that there is a π phase difference between

$J_{RV}(0)$ and $J_{RV}(\pi)$, and that the electric vectors of $J_{RV}(0)$ and $J_{RV}(\pi)$ are pointing in opposite directions.

2.3.3 Phase modulation for laser material interaction

By tailoring the phase of a laser beam, laser intensity distribution and wavefront structure can be precisely controlled, leading to a great improvement of efficiency and quality of laser material processing. For example, by inserting an axicon lens in the beam path, one can generate a zero order non-diffractive Bessel beam [83]. Bessel beams have been successfully used in ultrafast laser micromachining [83-87]. M. K. Bhuyan [88] demonstrated fabrication of nanovoids in fused silica with a diameter in the range of 200-400 nm and aspect ratios exceeding 1000 using 4.7 picosecond Bessel beams, which has great potential for fabricating micro nano fluidics. Thanks to the non-diffractive property of Bessel beams, surface ablation with structure feature sizes less than 200 nm has been achieved on Au thin films with a much tighter focused spot than conventional Gaussian beams [85]. As well as zero order non-diffractive Bessel beams, the first order diffractive annular beams generated from an axicon lens have also been used for percussion drilling of large diameter holes, which is more efficient than the complex and time consuming optical trepanning with a Gaussian beam [89,90].

Laser beams with vortex wavefront and spatially homogeneous state of polarization is another efficient way to generate annular shaped beam intensity for laser micromachining. Microneedle fabrication on metal surfaces has been demonstrated with nanosecond vortex laser beams, which eliminated bottom-up technique requiring several chemical processes [91]. With vortex annular beam, the ring intensity distribution of the beam as well as the

induced orbital angular momentum helps to obtain clearer and smoother nanosecond laser processed surfaces [92]. In [92], experiments show that vortex annular beams could be used to drill a deeper hole on Ta plates than with beams having no vortex wavefront. Also, vortex annular beams provide longer depth of focus than Gaussian beam, so that laser ablation is less susceptible to the sample misalignment and translation stage errors [93]. Driven by the theory that beams with optical vortices are more resistant to self-focusing and therefore can be applied with high power beam propagation over long distances, optical properties of femtosecond vortex beam inside material have been studied recently as well [94].

Another approach to modifying the phase of the laser beam is using diffractive optical elements (DOE) in the beam path to generate multiple diffractive beams to achieve high throughput thermal free ultrafast laser micromachining [23,24]. Even with femtosecond laser, material processing with focused millijoule level energy could cause thermal effects due to residual thermal diffusion and intense plasma-surface coupling [74]. Precision micro-structuring with ultrafast lasers requires fluencies ideally a few times above threshold fluence. Hence a single beam focused to a surface requires significant attenuation to the μJ level to avoid major thermal effects. This is highly inefficient, throwing away most of the laser output. Hence, diffraction of the laser beam emitted from an amplifier with millijoule level into multiple beams with microjoule level energy is a solution to efficiently utilize much more of the laser output energy and increase processing efficiency. By adopting this method, M. Silvennoinen [95] arranged to generate 400 diffractive spots (from energetic incident beam) with sufficient pulse energy for ultrafast ablation of metal, a tremendous increase in processing efficiency. Splitting one beam into

multiple diffractive beams is a general method that can be applied to increase the processing speed of almost all the ultrafast laser microprocessing applications, including surface processing [23,24,95,96], micro drilling [97], and internal structuring [11,98].

2.3.4 Polarization effects on laser material interaction

Polarization is a critical parameter in linear and non-linear laser material interaction. For example, simple Fresnel reflection from a dielectric interface near Brewster's angle [99], high intensity non-linear phenomena, such as self-focusing [10], filamentation [11-13], and multi-photon ionization [14-18], and ultrafast laser surface ablation [34] all show significant effects of incident polarization state.

- **Non-linear interaction**

The critical power for generating filamentation in doped phosphate glass is polarization dependent: $P_C^{Lin} = 1.03MW$ for linear polarization and $P_C^{Circ} = 1.53MW$ for circular polarization, a factor of 1.5 [100]. A series of polarization effects on refractive index change in fused silica have been investigated by K. Yamada *et al.* [101-103], showing that the cross section of the filaments produced with linear polarization are elliptical (ellipticity = 0.85) with its long axis parallel to the polarization direction, whereas the cross section of filaments produced with circular polarization are more round (ellipticity = 0.93).

Another example is polarization effects on multi-photon ionization, which have been studied in the past 4 decades since the first observation in 1971 [14], indicating that multi-photon ionization in atoms [15], molecules [16], and solids [17,18] are all polarization

sensitive. Theoretical and experimental results are agreed that circular polarization couples stronger than linear polarization with multi-photon ionization at low nonlinear order ≤ 4 [14,15,17]. However, a significant reversal was expected for higher nonlinear order > 4 [104], and confirmed in 6-photon multi-photon ionization of fused silica and sapphire [18].

- **Linear interaction**

Laser cutting of metals is one of the most widespread application of laser processing. Since the observation of linear polarization effects on laser cutting in the early days [105,106], circular polarization is the most commonly used polarization state for laser cutting and drilling [72]. Recent theoretical studies indicate that radially polarized beam could potentially increase the cutting speed up to 1.5-2 times faster compared to circularly polarized beam [107]. Polarization effects on laser cutting and drilling can be briefly explained by the polarization dependent selective energy absorption on the sidewall of the hole drilled by the first few laser pulses [32,33].

M Karus [108] demonstrated that the polarization effects on laser drilling is also material dependent, for example, laser drilling of steel with azimuthal polarization can be twice as faster than radial polarization, whereas radial polarization is more suitable for drilling brass and copper [109], but overall, the drilling speed and quality with radial and azimuthal are better than traditionally spatially homogeneous polarization states [109]. Not only can faster drilling speed be achieved with radial and azimuthal polarization, significantly smaller microvias can be produced on silicon wafers with radial polarization than with linear polarization [110].

Regarding laser cutting, radial polarization gives a faster cutting rate than both azimuthal and circular polarization, but circular polarization gives a better cutting quality [32]. Although radial and azimuthal polarization states have promising cutting and drilling efficiency, linear polarization has still found its position in ultrafast drilling. C. Hnatovsky [25] demonstrated 20 nm wide grooves could be achieved in fused silica with linear polarization and tight focusing, smaller than grooves produced by any other polarization states.

Ultrafast laser induced nanostructure-covered conical microstructures have been considered as a unique method to prepare hydrophobic surfaces for self–cleaning applications [111]. The shape of the conical microstructures has a significant dependence on the polarization of the incident beam [112]. With circularly polarized laser irradiation, the shape of the conical structures is conical. However, with linearly polarized laser irradiation, the conical microstructures tend to have an elliptic conical shape with its long axis perpendicular to the polarization direction [112,113].

LIPSS is another type of surface structure obtained by laser irradiation. The direction of the LIPSS is strongly dependent on the irradiation polarization direction [4]. By modifying the irradiation polarization state, geometry and direction of LIPSS can be precisely tailored for various applications, which will be reviewed in detail in section 2.4.

2.4 Laser Induced Periodic Surface Structure

This section presents a brief introduction of LIPSS formation, classification, theory and applications.

2.4.1 Classification of LIPSS

Since the first observation of LIPSS on silicon surface in 1965 [114], various types of LIPSS have been produced on metal [58], dielectric [115-118], and semiconductor surfaces [26,27,119]. LIPSS can be created on the surface of a material when the fluence of the irradiation approaches the damage threshold of the material [58]. The two most commonly observed types of LIPSS are so called Low Spatial Frequency LIPSS (LSFL) and High Spatial Frequency LIPSS (HSFL) produced with linearly polarized beams, as can be seen in Figure 2.8.

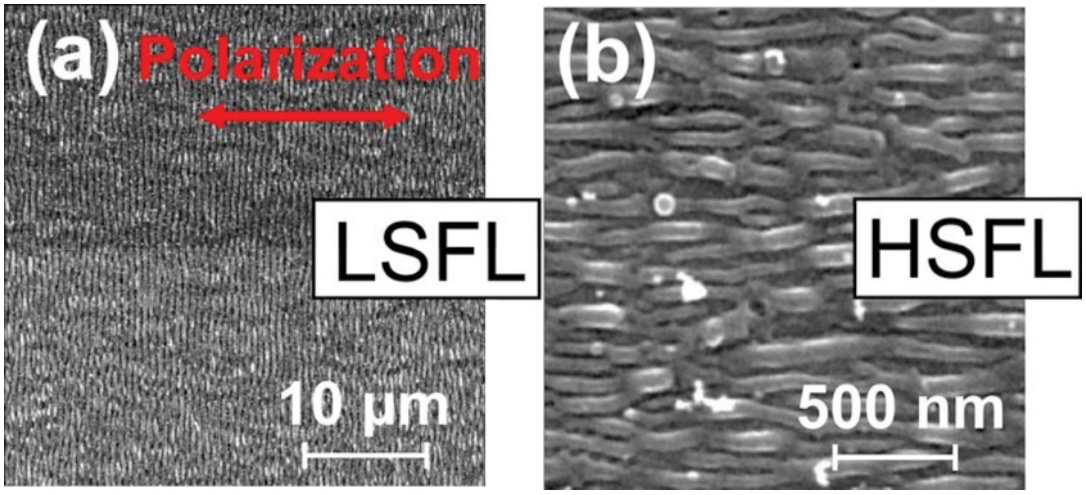

Figure 2.8 *(a) LSFL and (b) HSFL produced on titanium surface. The red arrow indicates the polarization state of the incident beam* [4].

- **HSFL**

HSFL refers to LIPSS with a period which is significantly smaller than the wavelength of the incident laser, generally smaller than $\lambda/2$ [4] with their orientation either parallel [26,27] or perpendicular [115,119] to the incident linear polarization state. Note that HSFL have only been produced with ultrafast laser in picosecond and femtosecond

regime. The fundamental mechanism of HSFL formation is not yet fully understood and still under debate. Several theories have been proposed to explain HSFL, including self-organization [119], second-harmonic generation [26,27], excitation of surface plasmon polaritons [28], and Coulomb explosion [120]. As this thesis does not involve HSFL, further details will not be discussed here.

- **LSFL**

LSFL refers to LIPSS with their periodicity similar or slightly smaller than the incident irradiation wavelength. LSFL can be produced with Continuous Wave (CW) laser, long pulse laser and ultrashort pulse laser [121].

2.4.2 Theory of LSFL formation

D. C. Emmony *et al*. proposed the first explanation of LSFL in 1973 that LSFLs were a consequence of the interference between the incident laser beam and surface-scattered waves which were created by laser impinging on dust or scratches on the sample surface [122]. An equation was given in the paper to predict the period of the LIPSS with laser beam incident at θ:

$$\Lambda = \frac{\lambda}{1 \pm \sin\theta} \tag{2-10}$$

The theory gives a heuristic picture of the formation of LSFL and has a good agreement with experimental results.

However, J. E. Sipe *et al*. doubted that the above theory is not physically consistent: the scattered wave should propagate with a wavelength of λ/n (n is the refractive index of

the material) instead of λ since the damaged pattern is produced by absorption of the energy within the material. At normal-incidence, the scattered wave has to be longitudinally polarized which does not satisfy the Maxwell equations [123].

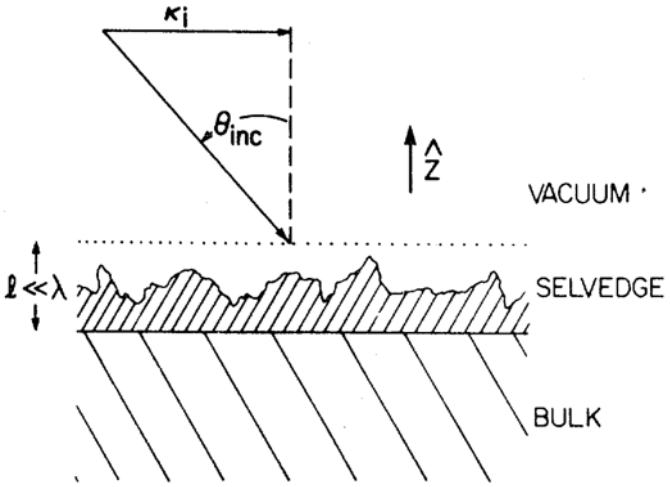

Figure 2.9 *The geometry of light incident on a rough surface* [123].

A more comprehensive theory was developed by J. E. Sipe *et al*. based on a formal solution of Maxwell equations, indicating LSFL was formed by inhomogeneous deposition of energy into a material via interference between the incident laser beam and fields scattered from a microscopic rough surface [123]. The theory has been considered as the most commonly accepted theory for LSFL formation [121].

J. E. Sipe proposed a 'selvedge region' just beneath the sample surface with microscopic roughness, of height much less than the incident wavelength λ, as shown in Figure 2.9. An incident laser beam defined by a wave vector $\vec{k}$ with a magnitude $\tilde{\omega} = 2\pi/\lambda$, the angle of incidence θ, and the polarization, impinging on the sample surface. Part of the incident beam is refracted into the bulk material and also, owing to the microscopic rough surface, a scattered field is produced in the bulk at $\vec{k}_{\pm} = \vec{k}_i \pm \vec{k}$, where $\vec{k}_i$ is the component

of the wave vector parallel to the surface. The interference between the refracted beam and the scattered field leads to inhomogeneous intensity distribution below the selvedge region. The spatial Fourier transform of the field intensity just below the surface indicating it contains strong peaks and the strong peaks occur at values of $\vec{k}$ that satisfy:

$$\left|\vec{k}_i \pm \vec{k}\right| = \tilde{\omega} \tag{2-11}$$

or

$$\left|\vec{k}_i \pm \vec{k}\right| = \tilde{\omega} n \tag{2-12}$$

where n is the refractive index of the material. It needs to be pointed out that the position of these peaks is in good agreement with equation 2-10.

The importance of feedback mechanism in formation of LSFL was also highlighted in the publication by Z. Guosheng [124]. In line with the theory of surface scattered wave interference, Z. Guosheng proposed an initial sinusoidal temperature distribution caused by the interference. The temperature variation will be equal to the interference period. Due to the temperature dependent property, the refractive index on the sample surface would vary in the same way as the temperature, which then acts like a grating. If the modulated power absorption is in-phase with the initial temperature variation, regions that are already warmer will experience a faster rate of temperature rise, ending up with a reinforced temperature gradient and a stronger index variation, which in turn strengthens the diffraction causing the intensity fringes more pronounced. Positive feedback is established. However, if the power absorption is anti-phase with the initial temperature

variation, initially colder regions would absorb more power and any perturbation would be soon erased, ending up with no feedback and no growth situation.

2.4.3 LIPSS modification

Various laser parameters can be used to modify the LIPSS formed on sample surface. With CW and long pulse laser, only LSFL can be produced, whereas ultrafast laser can generate both LSFL and HSFL by careful choosing the laser fluence and exposure [121]. For example, both LSFL and HSFL can co-exist on one spot produced with ultrashort pulse Gaussian laser irradiation. LSFL can be observed in the centre of the spot, where the fluence is higher than the wings of the Gaussian beam, whereas HSFL can be formed around the edge of the spot where laser fluence is relative low [26]. Similarly, whole spot area covered with HSFL or LSFL can be achieved by careful choosing of the incident laser fluence with uniform distribution, such as a flattop beam [4]. Alternatively, using a low fluence Gaussian beam, one can generate HSFL on the sample surface by carefully increasing the number of pulse overlap on one spot area [4]. Another modification of LIPSS is the period of the LIPSS, which can be tailored by changing the laser wavelength, the incident angle, or the effective refractive index [29].

Of particular interest in this thesis is the modification of the LIPSS direction by control the incident irradiation polarization. Both HSFL and LSFL are significantly dependent on the direction of linear polarization of the incident beam [121]. With HSFL, the direction of the LIPSS can be either parallel or perpendicular to the incident linear polarization with normal incidence [121]. Orientations of LSFL formed on strong absorbing materials such as metals or semiconductors are always observed perpendicular to the incident linear

polarization direction [4]. However, LSFL produced on dielectrics surface can be either perpendicular or parallel to the beam polarization [4].

With static spots produced with laser beams, LIPSS directions are dominated by the incident polarization. However, when covering large surface area with LIPSS by scanning the beam, scan direction also affects the LIPSS direction [125-128]. If scan direction is parallel to the LIPSS direction, the LIPSS can be laterally extended coherently along the scan direction [125,128], which generates highly uniformed LIPSS over lage areas. However, if the scan direction is perpendicular to the LIPSS direction, the LIPSS are not connected along the LIPSS direction, which means the quality (fringe finesse) is degraded [125,128], as can be seen in figure 2.10. Recently, P. J. Liu reported that with a fixed polarization irradiation, the LIPSS direction on a silicon surface could be rotated by about $40°$ through changing laser scanning direction [126].

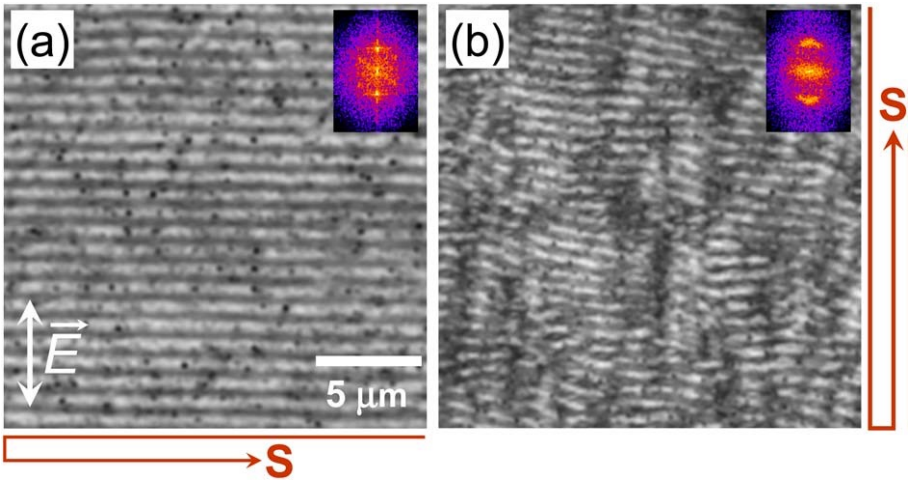

Figure. 2.10 *Optical micrographs of LIPSS gratings written with the scan direction S (a) parallel and (b) perpendicular to the ripples* [125].

Not only the relative angle between the LIPSS orientation and the beam scanning direction affects the uniformity of the LIPSSs [125,128]. The beam intensity distribution also affects the uniformity of the LIPSS. LIPSSs produced with a Gaussian beam has a

degradation of LIPSS in the center due to over-exposure and lack of LIPSS in the outer region because of the under-exposure. Whereas, the LIPSSs produced with a top-hat intensity profile significantly reduced this effects [129]. Laser fluence has the influence on the LIPSS uniformity as well. LIPSSs produced with high fluence has a worse uniformity than those produced with proper chosen laser fluence. If the fluence is further reduced, the LIPSSs become discontinuous, see figure 2.11 [130].

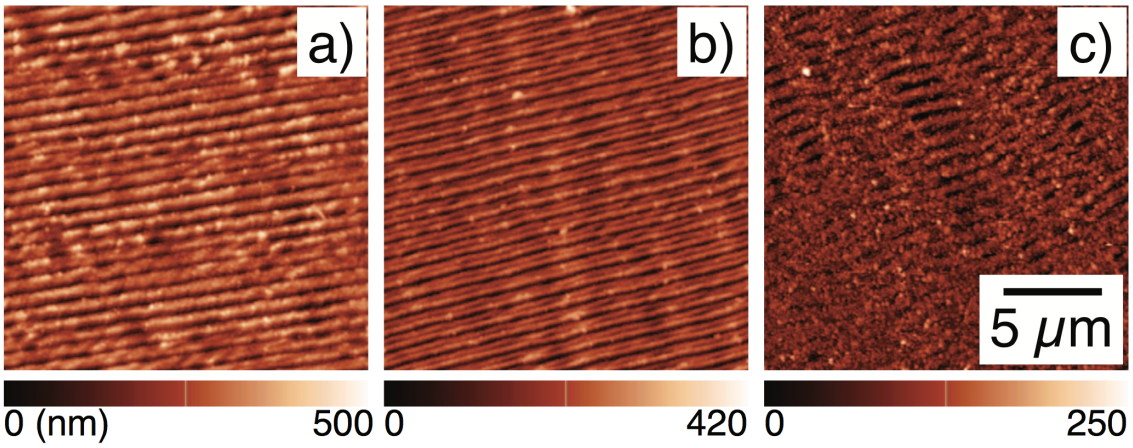

Figure. 2.11 *AFM image of LIPSS generated on the surface of a Cr film for three different pulse energies. The common parameters are: pulse duration τp ≈ 400 fs, scan speed v = 1500 mm/s and repetition rate f = 500 kHz. The energies are a) 2,1 μJ, b) 1,5 μJ and c) 1,2 μJ* [130].

The pulse overlap applied on the sample was reported to be an influential factor to the uniformity and period of the LIPSS [131,132]. It was found that lack of pulse overlaps would result in the LIPSS only covers various isolated location, result in the LIPSSs are not connected and uniform. With the increase of the pulse overlap, the LIPSSs become clearly recognisable and uniform. However, too many pulse overlap makes the LIPSSs become discontinue and start to disappear, leading to a less uniform LIPSS structure [131,

132]. It was also reported that the period of the LIPSS reduces with the increase of the pulse overlap [131-133].

The polishing orientation of the sample has been reported has a significant effect on LIPSS uniformity. As shown in figure 2.12, the LIPSS direction follows the surface defect when the orientation of the LIPSS has a relatively small angle to the defect [134]. However, the effect can be used to improve the LIPSS uniformity by having generated the LIPSS orientation perpendicular to the direction of the surface polishing direction. The requirements on this technique is that the sample has to be unidirectional polished. Figure 2.13 shows an example that was produced with this method [134].

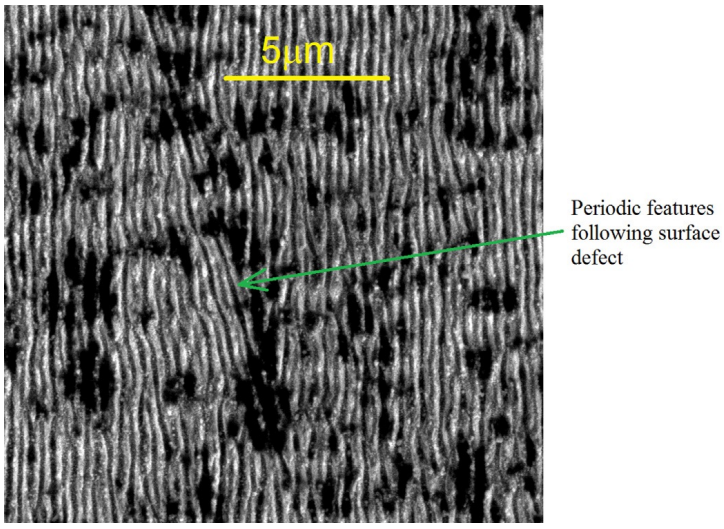

Figure 2.12 *LIPSS features on stainless steel (Sandvik Chromflex) demonstrating the impact of pre-existing surface imperfections. A diagonal scratch causes some of the features to follow the disruption rather than the adjacent features* [134].

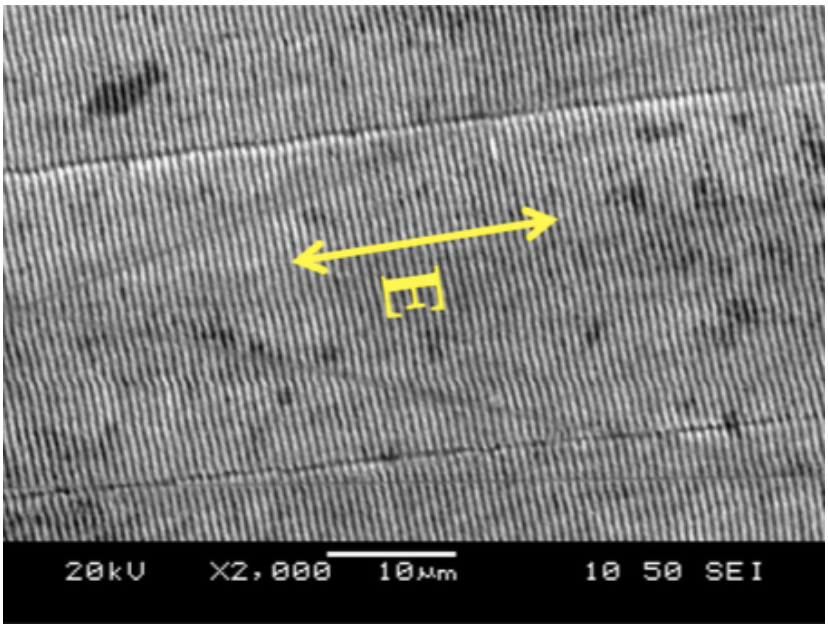

Figure 2.13 *SEM images showing the development of LIPSS features on Sankvik Chromflex 7C27Mo2. Arrow shows alignment of the incident E-field* [134].

2.4.5 Application of LIPSS

Since LIPSS with uniform micro/nano structure can be rapidly produced on large surface areas by single step direct laser irradiation with near damage threshold fluence, this technique has found a number of applications. For example, metallic surface wettability modification, either hydrophobic or hydrophilic [3], chemical etching rate control for microfluidic applications [135], reduction of friction coefficient of metal surfaces for tribological applications [136], and large surface area biosensors applications [137,138].

Recently, there is a considerable interest in colourizing metal surfaces with micro/nano structures for various applications [5]. Compared with other traditional methods, such as lithography, interference of two coherent beams, and chemical etching, LIPSS are easier to fabricate, eco-friendly and display superior production efficiency. Colour appearance on LIPSS covered aluminum and platinum surfaces was reported by A. Y. Vorobyev [6].

Various colours can be observed on the same sample by changing the viewing angle, see Figure 2.14. As the period of the LIPSS produced is 500 nm, which is in order of visible wavelength, such periodic surfaces thus act like a reflecting diffraction grating, diffracting various wavelengths of white light to different angles, which explained the colour change dependent on observation angle, shown in Figure 2.15.

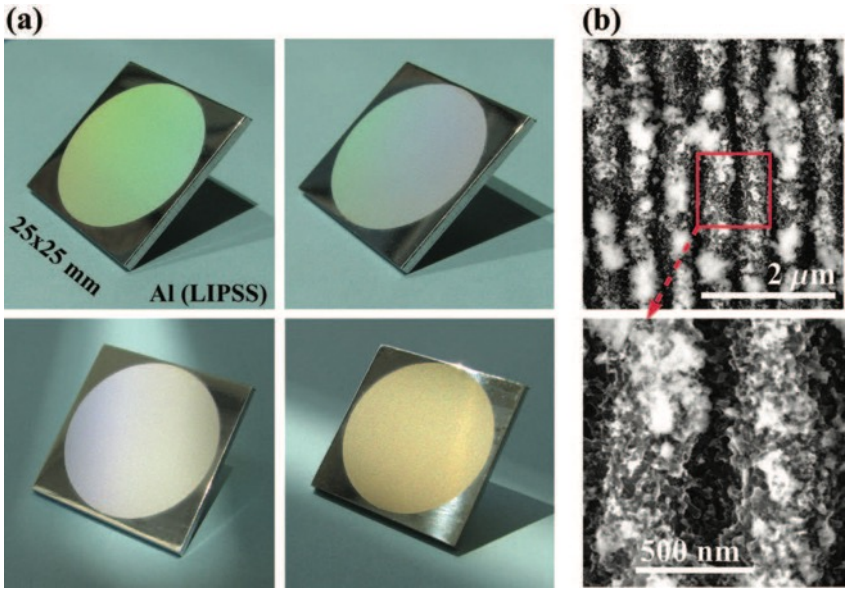

Figure 2.14 *LIPSS covered aluminium sample. (a) Various colours can be observed on the same sample by varying the viewing angle. (b) LIPSS structure produced on the sample surface with a period of 500 nm* [6].

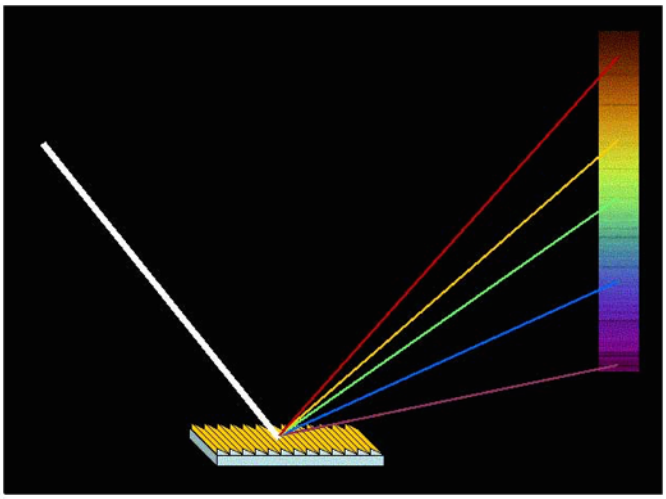

Figure 2.15 *Schematic illustration of white light diffraction on LIPSS covered metal surface, end up with different colour dependent on viewing angle.*

The same effect has been observed on LIPSS covered copper surface by Z. Ou [7]. He reported that the colour is not only changing with the inspecting angle, but also related to the LIPSS's period and the morphology of the LIPSS. According to the grating equation:

$$\Lambda \cdot sin\theta = m_o \cdot \lambda \tag{2-13}$$

where Λ is the period of the surface grating, θ is the inspecting angle with light incident normal to the grating surface, m_o is the diffraction order, and λ is the central wavelength being observed by the viewer. LIPSS covered metal surfaces are certainly not perfect surface gratings. They show flaws, such as discontinuities of the LIPSS along the LIPSS direction and other nanostructures co-exist within the LIPSS. These morphologies including the depth of the LIPSS can all influence the diffraction behaviour, leading to inhomogeneous colour appearance on the metal surface.

Selective colour patterns appearance on metal surface has been investigated by J. Yao [58] by applying two perpendicular LIPSS direction to different areas. Illuminating the sample

at selective angles, the area covered with LIPSS with their direction perpendicular to the illumination source direction will appear coloured, whereas the area covered with LIPSS with their direction parallel to the illuminate source direction will remain dark, as demonstrated in Figure 2.16 (a). With two light sources that illuminate the sample horizontally and vertically, both areas covered with horizontal and vertical direction LIPSS present a colour appearance, either the same or different depending on the illumination angle, as demonstrated in Figure 2.16 (b).

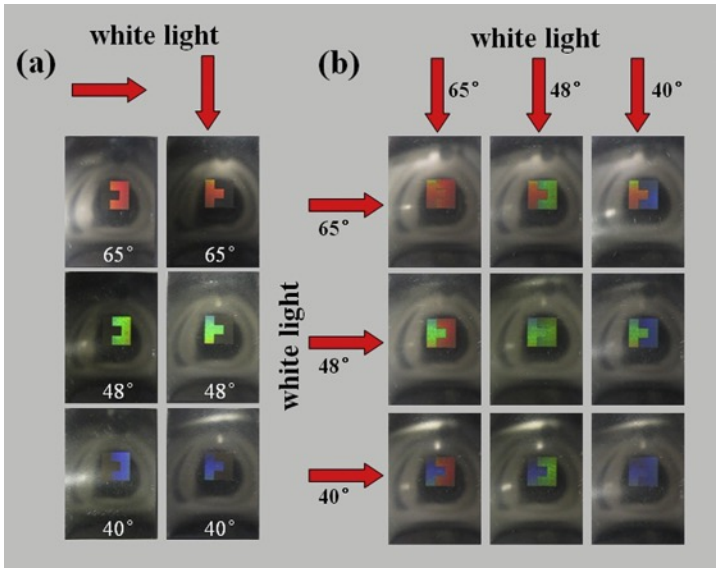

Figure 2.16. *Selective colour appearance on LIPSS covered areas with two orthogonal LIPSS direction. The red arrows indicate the illumination source direction. (a) Selective colour appearance of one LIPSS covered area with the LIPSS's direction perpendicular to the illumination source direction. (b) Colour appearance on both areas covered with orthogonal LIPSS direction and illuminated with orthogonal light sources* [5].

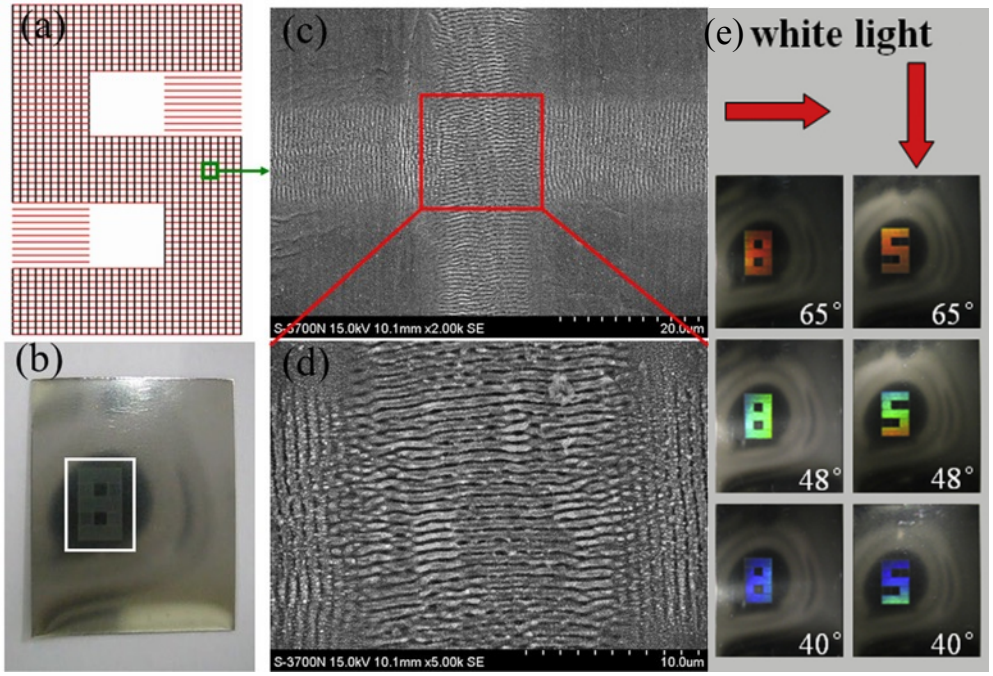

Figure 2.17 *Selective display of two symbols (5 and 8) with spatial overlapping two orthogonal direction LIPSSs, (a) horizontal LIPSS represented by red lines, forming symbol 8, and black lines stands for vertical LIPSS, forming symbol "5", (b) two spatial overlapping symbols produced on stainless steel surface, (c) SEM image of two orthogonal direction LIPSS produced on sample surface and (d) magnified SEM image of overlapping area, (e) light illumination with different direction for selective appearance of two symbols, red arrows represent the white illumination direction [5].*

By spatial overlapping two symbols with orthogonal LIPSS directions simultaneously on the same area, selective colour appearance can still be achieved. As can be seen in Figure 2.17, LIPSS with horizontal direction forms a "8" symbol, represented by red lines in Figure 2.17 (a), and dark lines represent LIPSS with vertical direction forms a "5" symbol, which is spatially overlapped with the symbol "8". Although the LIPSS direction on the spatially overlapped area shows one direction (Horizontal), Figure 2.17 (d), it still diffracts light source incident horizontally and vertically, as demonstrated in Figure 2.17 (e).

Substantial progress on colourizing metal surface with LIPSS was reported by B. Dusser [8]. Since the colour diffracted from the LIPSS covered area is viewing angle dependent, it is hard to define the central spectrum with different LIPSS morphologies unless a fixed angle of viewing is proposed. By using a standard reading scanner, in which the light source and a charge-coupled device (CCD) sensor is always at a fixed angle, colours appearing on the metal surface covered with different LIPSS morphologies thus can be defined. The digital image on the right of Figure 2.18 was obtained by scanning a stainless steel sample covered with different LIPSS morphologies with a normal scanner. The left side SEM images of Figure 2.18 indicate the LIPSS directions on different areas, which leads to a colour difference after scanning.

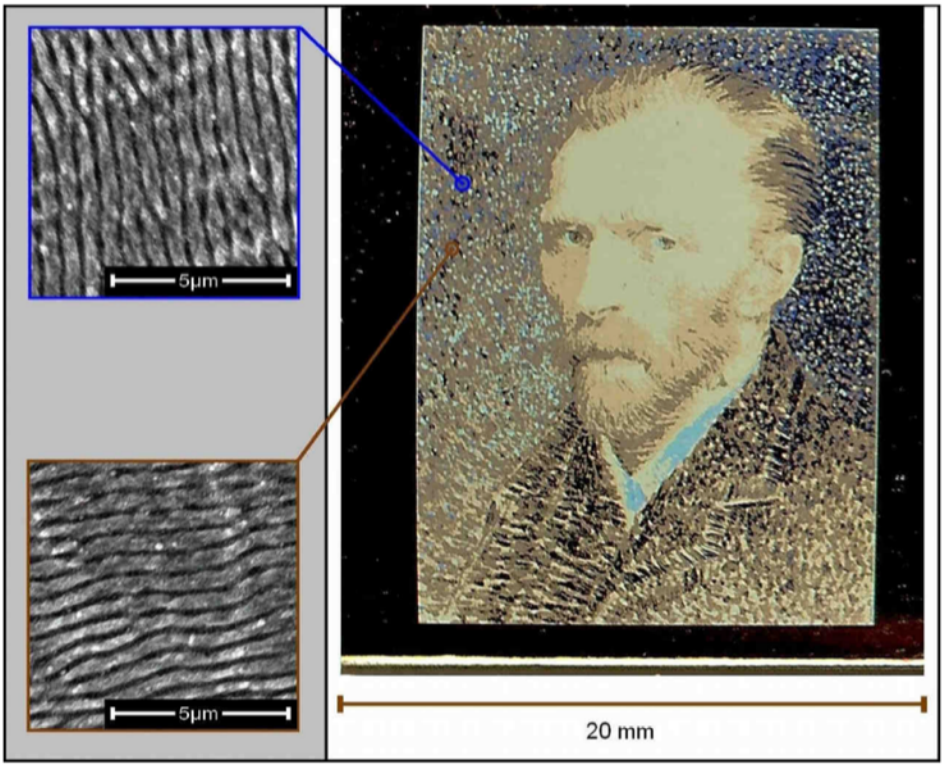

Figure 2.18 *On the right, digital image obtained by scanning a LIPSS covered metal surface with a normal scanner, the direction of the LIPSSs are varying depending on area (left side SEM images), leading to different colour appearances after scanning* [8].

As the scanner provides a fixed angle of viewing and illumination, LIPSS with fixed period would only give one colour. By changing the LIPSS direction on the sample surface, the effective period of the LIPSS in the direction the light source changes, thus various colours can be obtained. In the image above, the direction of the LIPSS was modified by changing the incident linear polarization direction, controlled by manually rotating a half-wave plate, which has a very low efficiency and throughput. Another scanned image of stainless steel sample marked by thirty-six disc sections with LIPSS direction in each section orientated at an angle to horizontal direction is given in Figure 2.19.

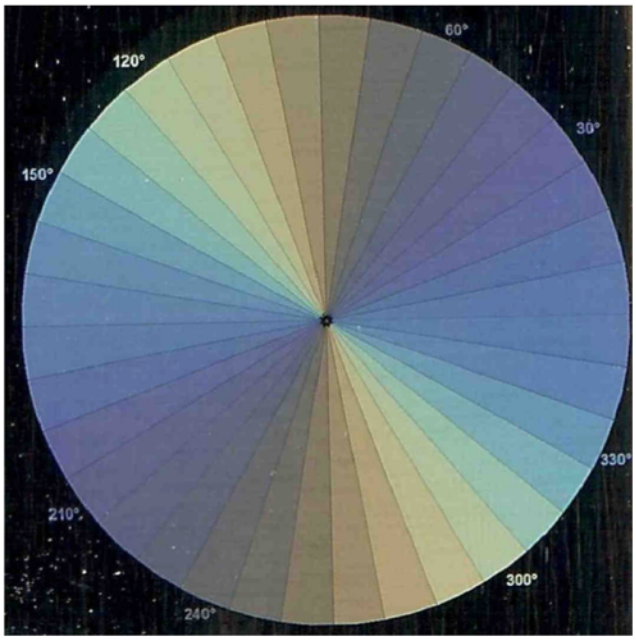

Figure 2.19 *Scanned image of stainless steel sample marked by thirty-six disc sections with LIPSS direction in each section orientated at an angle to horizontal direction (0°)* [8].

2.5 Control the phase and polarization with Spatial Light Modulator

In all the examples of phase and polarization modulation for laser material processing given above, the ability to control and manipulate the wavefront and polarization state of the incident beam is desirable as it allows better control of laser-material interactions. A number of methods have been developed for phase and polarization control. Among these methods, nematic liquid crystal SLM provides remarkable ability to control the phase and polarization of an incident ultrafast laser beam.

2.5.1 Introduction of Spatial Light Modulator

- **Classification of Spatial Light Modulators**

Spatial Light Modulator is a general term describing devices that are able to modulate amplitude, phase, or polarization of light wave in space and time [139]. Current available SLMs can be cataloged to either optical microelectromechanical system or Liquid Crystal Display (LCD) technology. The most commonly used SLMs for ultrafast laser machining are Digital Micro-mirror Device (DMD), ferroelectric liquid crystal SLM (FLC-SLM), and nematic liquid crystal SLM.

The DMD is a reflective device consisting of arrays of micro-mirrors. Each of the micro-mirrors can be seen as a pixel, which can be addressed individually to binary states, on or off. Due to the binary ability of the DMD, they are mainly used for beam shaping and rarely used for aberration correction in ultrafast laser micromachining [140]. DMDs are

cheap and easily available from a DLP home projector [141]. Also, the high refresh rate, kHz ability [141], makes them popular in ultrafast laser processing area.

FLC-SLMs have a thin layer of ferroelectric liquid crystal sandwiched by two protective glass plates, each coated with a transparent electrode layer. Similar to DMD, FLC-SLMs are addressed with binary CGHs, which have a very low diffraction efficiency [142]. However, due to kHz refreshing frame rate, the FLC-SLMs have been adopted in applications that require less diffraction efficiency but high refreshing rate [143]. Additionally, FLC-SLMs can be configured for fast rotation of the direction of incident linear polarization by up to 90 degrees [144]. Another application of this device is amplitude modulation by combining this device with a polarizer placed afterwards [144].

Currently used nematic liquid crystal SLMs are based on Liquid Crystal On Silicon (LCOS) technology, designated LCOS-SLM. Two types of LCOS-SLMs have been widely used for high efficient modulation of laser light: twisted nematic liquid crystal SLM (TNLC-SLM) and parallel-aligned nematic liquid crystal SLM (PAL-SLM). With TNLC-SLM, not only the phase of the incident beam will be modified, but also undesired polarization modification will be induced [145]. PAL-SLM provides the ability of phase only modulation with certain optical configuration [145].

- **Parallel-aligned nematic liquid crystal SLM**

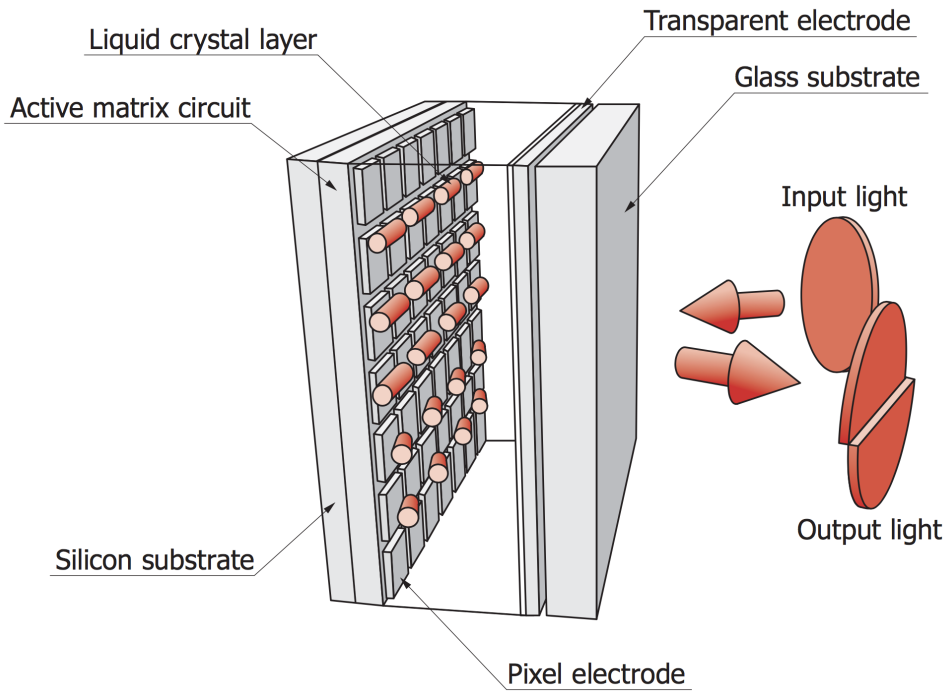

Figure 2.20 *Typical structure of PAL-SLM* [146].

The structure of a PAL-SLM is demonstrated in Figure 2.20. While twisted nematic liquid crystals are aligned with an angle to each other, liquid crystals in the PAL-SLM are aligned parallel to each other, shown in Figure 2.20. Thanks to the pixelated structure, each pixel in the PAL-SLM can be individually addressed by applying a corresponding voltage on the pixel electrode, causing a change of refractive index within each pixel. Localized refractive index changes lead to a relative phase delay after a laser beam transmitted through or reflected from the PAL-SLM device. A PAL-SLM controller transfers a grey level to a corresponding voltage, enabling users to address SLM with Computer Generated Holograms (CGH) through a normal PC. By applying different optical configurations, a PAL-SLM can be used for phase-only modulation, polarization modulation and amplitude modulation. For example, if the incident beam is polarized

parallel to the optic axis (director) of the liquid crystal, only the phase will be modified after reflection from the PAL-SLM. However, if the incident beam is polarized at 45 degrees to the optic axis of the liquid crystal, the polarization will be altered due to the resulting phase shift induced between the two orthogonal electric field components. Compared to other SLMs, the PAL-SLM enables high efficiency phase modulation of laser beams by a range of values of 0 to 2π while eliminating undesired polarization modulation with TNLC-SLM.

Since this thesis only uses PAL-SLMs, for clarity, in the following content, the term SLM or phase-only SLM will refer to PAL-SLM.

2.5.2 Phase control methods

Modulation of the phase of an incident beam can be achieved by placing a refractive optic or a DOE in the beam path. For example, by using an axicon lens in the beam path, one can obtain an annular Bessel beam [147]. Another way to obtain an annular beam is by inserting a spiral phase element in the beam path [91,148]. The beam obtained with this method exhibits a ring mode intensity distribution (Laguerre–Gaussian) and a vortex wavefront, which carries an orbital angular momentum (OAM) [91]. Multiple diffractive beams can be achieved by using a diffractive beam splitter [149] or a micro-lens array [150,151].

Compared to the refractive optics or DOEs that can only be used for modifying one state of light. Liquid Crystal Spatial Light Modulator (LCSLM) can be used as a diffractive optic or a refractive optic, provides the flexibility of generating any desired wavefront, including Bessel and vortex beams. Literature review shows that SLMs have been used

for generating Bessel beams [84,86,152], annular beams [153,154], vortex annular beams [155,156], multiple diffractive beams [11,23,24,95-98], and multiple diffractive annular beams [90].

Y. Hayasaki *et al*. [24] first demonstrated adopting a SLM in a femtosecond laser system capable of generating arbitrary diffractive multiple beams for micro processing. However, several issues have been found when using SLM to generate multi-diffractive beams, such as poor intensity uniformity of multi-diffracted beams, beam distortion of large angle diffracted spot, and effects of the zero order beam during micromachining.

Z. Kuang *et al*. reported multiple diffractive spots with asymmetric locations could be used to improve the intensity uniformity of multi-diffracted beams [23,96]. Alternatively, adding a feedback system in the beam path could be used to control the intensity uniformity of the multi-diffractive spots or even to modify the intensity of individual diffracted laser beams [95]. Large angle diffracted beam distortion with SLM in a femtosecond laser system was reported by Z. Kuang *et al*, which was caused by the wide bandwidth of a femtosecond laser [157]. By adopting a SLM in a picosecond laser system, which has a much narrower spectral bandwidth, the distortion was reduced to a negligible level [96]. The zero order beam can be blocked around the focal plane of the first lens of an added 4f system in the beam path after the SLM [157] or by adding a Fresnel lens hologram on the SLM to change the focal plane of the diffractive spots from the focal plane of the zero order beam [96].

The phase control ability of an SLM can do more than generate annular beams, vortex beams, or multiple diffractive beams. By superposition of an axicon lens hologram with a

multi-beam hologram, multiple diffractive annular beams were generated with one SLM and increased the micro-drilling speed significantly [158].

2.5.3 Polarization control methods

The ability to control the polarization state in ultrafast laser processing is highly desirable, from laser cutting [32,107], drilling [108-110], surface processing [4,25,58,114] to material internal processing [100-103]. This section will discuss state of the art polarization modification methods. As well as control method for standard homogeneous polarization states, this section will also introduce various methods of static and dynamic generation of cylindrical vector beams, especially radial and azimuthal polarization states.

- **Spatial homogenous polarization modulation**

It is well known that half-wave plates can be used to change the polarization direction of the incident linear polarization and a quarter-wave plate is able to convert a linearly polarized beam into an elliptically or a circularly polarized beam. In addition, by continuously rotating a half-wave plate during laser micromachining, the polarization-trepanning technique has been developed to improve ultrafast laser drilling qualities [48-50]. However, mechanical rotation of optical components can suffer from vibrations and is prone to mechanical failure. Alternatively, real time switching of two orthogonal linear polarization states with a ferroelectric liquid crystal polarization rotator has been reported for ultrafast laser drilling [51]. Adopting a SLM in the beam path for arbitrary rotation of the direction of incident linear polarization was demonstrated by Chun Ye in 1995 [159], although demonstrating showing the potential application of dynamic control of polarization, has never been deployed for ultrafast processing.

- **Generation of radial and azimuthal polarization**

Driven by the potential applications of radial and azimuthal polarization in imaging, optical trepanning, data storage and laser machining, different methods have been developed for generation of radial and azimuthal polarization [25,32,33,35-47,52-55,57,79,80,109,160-175]. To generate radial or azimuthal polarization, either active generation methods or passive generation methods can be used.

The active generation method usually involves redesign of the laser cavity, by placing additional optical components in the laser cavity, such as a birefringent component [164-166], a conical Brewster prism [167], or using a circular multilayer polarizing grating end mirror in the cavity [168].

Passive generation methods generally involve converting the polarization state from the laser cavity, typically linear or circular polarization, to radial and azimuthal polarization outside laser cavity. Since passive generation methods provide more convenience without involving redesigning laser cavity, a number of methods have been developed to generate radial or azimuthal polarization. For example, segmented spatially variant retardation plates [161,163], birefringent plates [35-37], fiber optic mode couplers [170], and dielectric subwavelength gratings [171] have all been demonstrated to be able to generate radial and azimuthal polarization states.

Another very popular passive method involves liquid crystal technologies. Generation of radial or azimuthal polarization with a liquid crystal polarization converter was reported by M. Stalder in 1996 [172] and commercialized later by ARCoptix Switzerland [176]. Liquid crystal polarization converters are built specially for converting linear polarization

to radial or azimuthal polarization. With a liquid crystal polarization converter in the beam path, one can convert linear polarization to either radial or the orthogonal azimuthal polarization by simply altering a voltage on the device, eliminating any misalignment from manually rotating optical components. For applications that require dynamic switching of polarization state, liquid crystal polarization converter provides the possibility of dynamic switching between radial and azimuthal polarization state.

Besides this liquid crystal converter, other liquid crystal based SLMs have also been used for radial and azimuthal polarization generation. FLC-SLM has been used to generate radial polarization using interferometric approach [46,52]. The interferometric approach is based on the linear combination of two orthogonal polarization modes, which have tailored intensity and phase profiles. Figure 2.21 (a) and (b) are TEM10 and TEM01 modes with two orthogonal polarizations. The interference of the two beam modes generates radial polarization, as shown in Figure 2.21 (c). Various types of interferometers such as Mach-Zehnder interferometer, Sagnac interferometer, and diffractive optical element interferometer have been used to combine the two orthogonal polarization modes into radial polarization [45]. The drawback of the FLC-SLM is the low diffraction efficiency [43,44]. TNLC-SLMs have a much better diffractive efficiency compared to FLC-SLM, hence they have been widely used to generate arbitrary polarization distributions using interferometric approach, including radial and azimuthal polarization [41,45,47,53,162]. However, these studies that adopt interferometric approach, which are often hampered by phase stability [57].

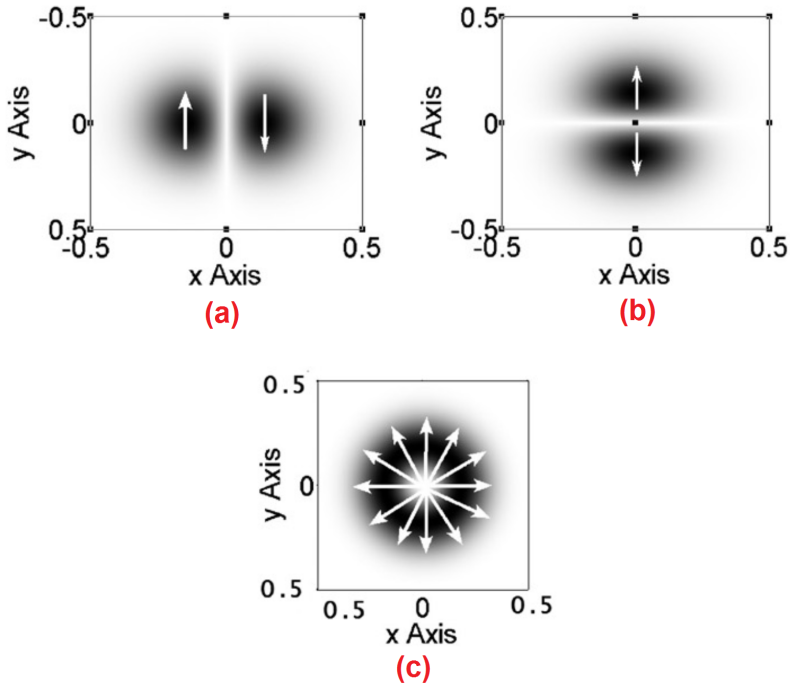

Figure 2.21 *(a) TEM10 and (b) TEM01 modes with orthogonal polarization states, (c) is the generated radial polarization by the interference of (a) and (b)* [47].

Generation of radial or azimuthal polarization with PAL-SLM is more stable and easier. The optical setup is simple, mainly contains a pair of waveplates and the PAL-SLM [32]. Instead of using interferometric approach, birefringent property of parallel aligned liquid crystals in the PAL-SLM is the main mechanism used for modulating the incident polarization. Generation of radial and azimuthal polarization with two PAL-SLMs was reported by M. R. Beversluis in 2006 [38], where the first PAL-SLM generated a compensation vortex phase while the second PAL-SLM modified the polarization, ending up with radial/azimuthal polarized beams with planar wavefront. With one PAL-SLM in the beam path, O. J. Allegre *et al.* [32] reported using one one PAL-SLM to generate a radial or azimuthal polarization with a vortex front. Similar results were also reports by W. Han [40] and J. Qi [39]. Alternatively, a method to generate radial/azimuthal vortex

beam is to passes a radially/azimuthally polarized beam through a spiral phase element to attach a topological charge to the beam [173]. Additional methods of generating radial or azimuthal polarization involving PAL-SLM were reported in [39,40,42,177].

2.5.4 Phase and polarization modulation with Spatial Light Modulator

Although phase control and polarization control with SLMs have been well investigated separately in the past decades, modification of both phase and polarization in optical configuration has been seldom investigated.

Vortex beams with associated OAM are widely used in optical tweezers for trapped particle rotation around trapping beam axis, whereas optical trapping with circularly polarized laser beams that has a spin angular momentum forces the particle to rotate around its own axis [178]. Recent study has shown that tight focused radially polarized beams provide an extreme axial gradient force used to trap metallic particles, which are generally considered difficult to trap [179]. Regarding laser microprocessing, a radially polarized beam with a planar wavefront focused with a low NA lens has a ring intensity shape, which has a high M^2 factor than Gaussian. For applications requiring radial polarization but with low beam-propagation factor M^2, radially polarized vortex beams are well suited since the focused spot has a near Gaussian intensity distribution. In all these cases, both phase and polarization need to be modified in the same optical configuration.

G. Machavariani *et al*. first reported a method of generating radial polarized vortex beam with Near-Gaussian intensity distribution by passing radially polarized planar wavefront beam through a spiral phase element, which induced a spiral wavefront to the radially

polarized beam [173]. The M^2 of the output radially polarized vortex beam was measured to be 1.7 compared to the input radial planar wavefront beam with $M^2 = 2.8$. J. Qi *et al.* [39] proposed using one SLM to generate a radially polarized beam with planar or vortex wavefront. In his optical setup, the SLM was separated into two halves. The laser beam first arrives on one half of the SLM, where the phase of the laser beam can be modified to have a spiral phase or not, then the modified beam was reflected on the other half of the SLM and passed through a quarter wave plate, which in combination alters the incident circular polarization to radial or azimuthal polarization. A similar result was also demonstrated by W. Han but using two SLMs in combination [40].

Multiple diffracted beams with polarization distribution control was reported to reduce the interval of the adjacent diffracted spots after focus [174]. In some applications, the multiple diffracted beams need to be very close to each other. However, distortion of diffractive beams arises due to the mutual interference when the beams get too close [174]. By applying orthogonal linear polarization states on the adjacent diffractive spots, the interval can be reduced to half compared to diffractive beams with no polarization control [174].

2.5.5 Theory of phase and polarization control with spatial light modulator

SLM can be involved in two different optical setups to tailor the phase or the polarization of the incident laser beam. With parallel-aligned nematic liquid crystal SLM, the liquid crystal molecules in the SLM are aligned horizontally or vertically. As the liquid crystal molecules in the Hamamatsu SLM are aligned horizontally, the phase delay caused by the

liquid crystals only applies to laser light horizontally polarized components. Hence, the SLM has a birefringent property and the fast axis (extraordinary axis) of the Hamamatsu SLM is horizontal.

- **Optical configurations for phase and polarization control**

For the applications requiring phase only modulation, the incident beam on the SLM needs to be linearly polarized parallel to the fast axis of the SLM. With appropriate CGH applied, this results in a desired tailored laser wavefront, i.e. vortex beam [155,156] and multiple diffractive beams [11,23,24,95-98]. The polarization state of the laser beam is thus unaffected by the SLM in this situation.

To control the polarization of the incident laser beam with SLM, the incident polarization needs to be either circular polarization [39], or linear polarization at 45 degrees to the fast axis of the SLM [32,174]. A quarter-wave plate needs to be placed after the SLM for both cases. In the current research, polarization control with SLM is achieved with linear polarization incident on the SLM at $+45°$ to the fast axis of the SLM and a quarter-wave plate placed after the SLM with its fast axis orientated at -45°. Due to the birefringent property of the parallel-aligned liquid crystal molecules, the phase delay caused by the SLM only applies to the horizontal component of the incident beam, whereas the vertical component beam reflected from the SLM suffers no phase delay. The relative phase delay between the horizontal component light and the vertical component light leads to a change of polarization, from $+45°$ linear polarization to elliptical polarization. For special cases, i.e. zero phase delay or $\pi/2$ phase delay to the horizontal component light, the output polarization states are $+45°$ linear polarization or circular polarization, respectively. The

quarter-wave plate placed after the SLM with its fast axis set at $-45°$, changing the elliptical polarization after the SLM to linear polarization. In other word, with $+45°$ linearly polarized beam incident, a SLM and a quarter-wave plate with its fast axis at $-45°$ forms a polarization converter.

- **Jones Matrix analysis of polarization converter**

Firstly, a reference coordinate system with horizontal (x) and vertical (y) axis centered on the optical axis of the laser is defined. The incident linearly polarized beam at $+45°$ can be written as $J_{inc} = \frac{1}{\sqrt{2}}\begin{pmatrix} 1 \\ 1 \end{pmatrix}$. Secondly, instead of consider all the pixels in the SLM, one pixel of interest is considered here, which induces a phase delay ϕ to the horizontal component of the incident beam. The Jones matrix represent the horizontal phase delay by the SLM can be written as $P_{SLM} = \begin{bmatrix} 1 & 0 \\ 0 & e^{i\phi} \end{bmatrix}$. The Jones Vector after the beam reflected from the SLM can be calculated that: $J_{SLM} = J_{inc} \times P_{SLM} = \frac{1}{\sqrt{2}}\begin{pmatrix} 1 \\ e^{i\phi} \end{pmatrix}$, indicating the polarization states after the SLM is elliptical polarization. The quarter-wave plate with its fast axis set at $-45°$ placed after the SLM can be expressed with $Q = \begin{bmatrix} 1 & 0 \\ 0 & e^{-i\frac{\pi}{2}} \end{bmatrix}$. However, the Jones matrix of the quarter-wave plate is expressed in a reference coordinate system with one of its axis parallel to the fast axis of the quarter-wave plate, in which case

a rotation matrix is induced to rotate the original reference coordinate $45°$, $R_c = \frac{1}{\sqrt{2}}\begin{bmatrix} 1 & -1 \\ 1 & 1 \end{bmatrix}$.

The polarization state of laser beam pass through the polarization converter can be calculated:

$$J_{out} = J_{inc} \times P_{SLM} \times R \times Q = e^{-i\frac{\pi}{2}} \cdot e^{i\frac{\phi}{2}} \cdot \begin{pmatrix} \sin\frac{\phi}{2} \\ \cos\frac{\phi}{2} \end{pmatrix} \tag{2-14}$$

It is noted that the Jones vector representing incident polarization is expressed in a reference coordinate system with horizontal and vertical axis, but the Jones vector representing the output polarization after the polarization converter is expressed in a coordinate system tilted at $45°$.

The output beam after the polarization converter contains three terms, as can be seen in equation 2-14. The first term $e^{-i\frac{\pi}{2}}$ is a constant, which doesn't vary with SLM induced phase delay. The second term $e^{i\frac{\phi}{2}}$ is a phase delay induced by the pixel of interest. The third term represents the linear polarization state of the output beam after passing through the pixel of interest and a quarter-wave plate. Any phase delay ϕ induced by the pixel of interest changes the angle of the linear polarization.

- **Homogeneous and inhomogeneous polarization modulation with polarization converter**

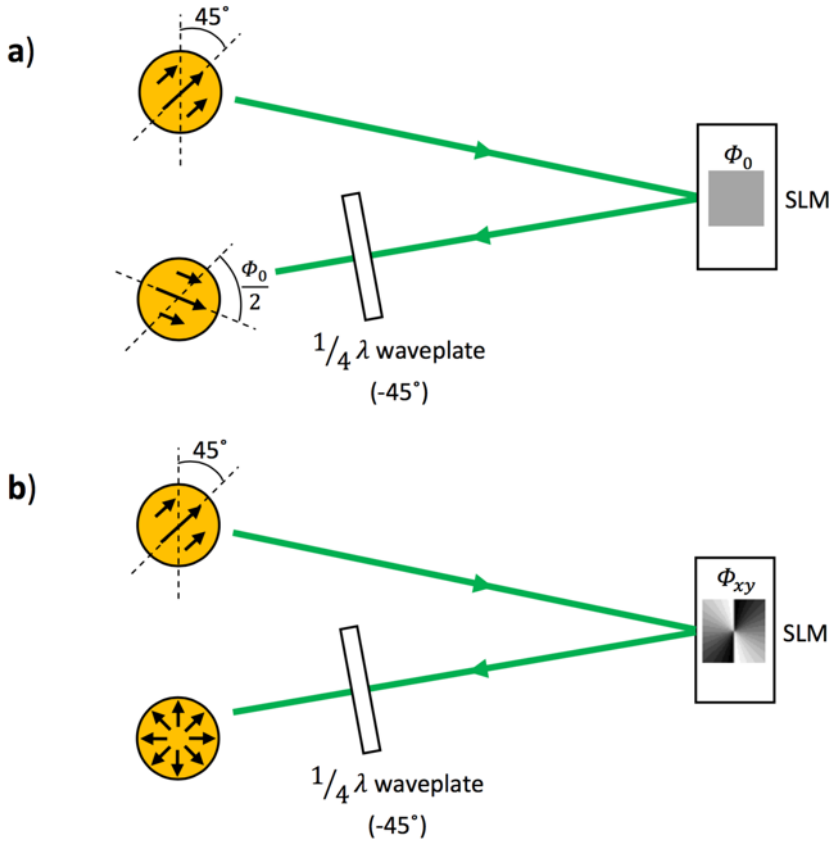

Figure 2.22 *(a) Homogeneous change of the incident linear polarization angle with polarization converter, (b) with a spatial varying grey level CGH applied on the SLM, the incident linear polarization is tailored to spatial inhomogeneous polarization state.*

Figure 2.22 demonstrated two types of polarization modulation with polarization converter. Depending on the CGH applied on the SLM, the incident linear polarization can be modulated to spatial homogeneous linear polarization at desired angles (Figure 2.22 a), or tailored to spatial inhomogeneous cylindrical vector beam (Figure 2.22 (b) shows a radial polarization). With a homogeneous grey level CGH applied on the SLM, the phase delay induced by every pixel is the same, resulting in modification of the incident linear polarization angle with grey level. However, with a CGH whose grey level alters spatially across the pixels, the angle of the linear polarization modified by each pixel are varies spatially corresponding to the grey level on the pixel.

2.5.6 Dynamic control of phase for laser material interaction

Dynamic control of phase for ultrafast laser material processing was first reported by Z. Kuang in paper [23], further demonstrated in [157,158]. In [23], a SLM addressed with a series of CGHs was used to generate multiple diffractive spots patterns with varying locations, which corresponded to the applied CGHs on the SLM. The galvo scanner was set to scan a straight line on the sample while the CGHs were sequentially addressed on the SLM, ending up with a pattern contains 2 curved lines and one straight line marked on the sample surface. However, details related to synchronization setup and the real time processing are very limited.

Although the principle of using an SLM for real time control of phase or polarisation for high-throughput ultrafast laser processing has been available, true synchronization of CGH application with a laser micro-machining system has not been reported previously.

2.6 Thin film ablation with ultrafast laser

Thin film patterning is widely deployed in fabrication of displays, radio frequency identification (RFID) antennae, bio-sensors, image sensors, photomasks, semiconductor wafers and so on [180]. The most common thin film patterning technology has been lithography process, which involves several procedures, i.e. coating, UV Exposure, wet etching, stripping and cleaning [181]. Thin film patterning with pulsed laser traces back to 1992. A. Banovec *et al.* [182] reported a comparison of chemical and pulsed laser etching of indium tin oxide (ITO) on glass and pointed out that single step microsecond pulsed laser etching eliminated the pollution of chemicals, however melted edges of the

ITO films and damage to the glass substrate were induced with the long pulse laser. The emergence of ultrashort pulse lasers provides a promising technology for high quality thin film ablation, avoiding the thermal effects typical of micro and nanosecond lasers [183]. This section presents basics of ultrafast laser thin film patterning and state of the art high speed patterning with ultrafast laser systems.

2.6.1 Theory of thin film ablation with ultrafast laser

The advantages of ultrashort laser pulses for thin film patterning still require appropriate optimization of laser parameters such as pulse length, fluence, wavelength and exposure.

- **Pulse duration**

As mentioned in section 2.2.2, the incident pulse length determines the heat penetration depth when ablating a certain material. Also, the electron-phonon coupling time for metals is typically a few ps [184], so that with temporal pulse lengths <10 ps, energy transfer to the atoms in the skin layer (<30 nm) takes place instantaneously with almost no heat diffusion. However, with ns pulses, energy transport is governed by the heat diffusion in the lattice to a depth of microns [185]. For thin films consisting of more than one layer, laser selective ablation of one layer without damaging the bottom layer is important. In this case, the heat penetration depth needs to be considered, which can be mainly affected by the pulse duration. Experimental results from P. P. Pronko *et al.* [186] indicate that the ablation threshold for 600 nm Ag on glass is dependent on the incident pulse length if its duration is longer than $\tau_p = 7$ ps, consistent with calculations that the heat penetration depth at $\tau_p = 7$ ps is equal to the optical penetration depth of 800 nm wavelength. The

ablation threshold for pulse duration from $\tau_p = 0.15 - 7$ ps was shown to be independent of laser pulse length. It is the optical penetration depth determines the volume of material needs to be removed. The above results are in line with papers [187,188], which showed that the ablation threshold for both stainless steel and copper are almost constant for pulse duration shorter than $\tau_p = 10$ ps and increases for longer pulse length. Additional to pulse duration effects on ablation threshold of metals, the ablation depths decrease with increasing pulse duration from $\tau_p > 10$ ps [184]. For example, with 10 ps and 512 pulses, the ablation depth for stainless steel was measured to be 9 nm and down to 1.44 nm with 50 ps, whereas the ablation depth with copper was 31.8 nm for 10 ps, down to 11.6 nm with 50 ps [184]. Other systematic studies of pulse length influence on ablation are presented in [189,190].

- **Wavelength**

For a certain material, the absorption coefficients α varies with the incident laser wavelength, which also determines the optical penetration depth $l_s = 1/\alpha$. With larger absorption coefficient, the skin depth is smaller, which leads to a smaller ablation threshold. G. Raciukaitis [191] reported that the ablation threshold fluence for 120 nm ITO thin film on glass was F_{th} = 0.20 $J{\cdot}cm^{-2}$ for 266 nm radiation, and increased to F_{th}=0.46 $J{\cdot}cm^{-2}$ for 355 nm radiation, which further increased to F_{th} = 2.11 $J{\cdot}cm^{-2}$ for 532 nm radiation. The damage thresholds for the glass substrate were also measured with different wavelength radiations, indicating that 233 nm radiation has the widest processing window.

Wavelength effects on ablation quality of 100 nm ITO thin film on PET were studied by S. Xiao *et al*. with 10 ps radiation source [192]. Results show that 1064 nm radiation gives much smoother and clear rim than both 532 nm and 355 nm pulses at the edge of ablation spots. Spots ablated with 532 nm and 355 nm radiation were found to have a significant amount of delamination on the edge of the ablated spot, where the thin film detached and curled from the central part. A. Risch [193] reported that the ablation threshold fluence of ITO on glass with 10 ps laser is lowest at 355 nm (0.38 $J{\cdot}cm^{-2}$) compared to 532 nm (0.77 $J{\cdot}cm^{-2}$) and 1064 nm (0.40 $J{\cdot}cm^{-2}$), which was believed due to the different transmittance of ITO at different wavelength.

The laser wavelength also has a significant influence on long pulse ablation of thin films. For example, with a 10 ns radiation source, S. Rung *et al.* [194] studied wavelength effects on the ablation threshold of ITO on glass and gallium doped zinc oxide (GZO) on glass with different film thickness. Results show that if the film thickness is smaller than the absorption length, the ablation threshold decreases with increasing film thickness as the entire thin film absorbs more of the laser energy in this regime. In contrast, the ablation threshold increases with increasing of film thickness when the film thickness is larger than the optical penetration depth, which can be explained by the thermal diffusion into surrounding areas with nanoseconds exposure. However, when the film thickness is on order of optical penetration length, the ablation threshold reaches a minimum, which is an optimized situation for processing. Other studies of wavelength influence on nanosecond laser thin film ablation can be found in [195-197].

- **Pulse overlap**

Even with ns-pulse, the ablation threshold was found to be depend on the pulse overlap applied at one position [184], due to incubation. According to an incubation model developed by J. Bonse *et al.* [198], the relation between the ablation threshold for N number of pulse $F_{th}(N)$ and the ablation threshold for single pulse $F_{th}(1)$ is given by:

$$F_{th}(N) = F_{th}(1) \cdot N^{S-1} \tag{2-15}$$

where the exponent S characterizes the degree of incubation, which is typically between 0 and 1 for metals [184]. This model indicates the ablation threshold for most metals decreases linearly with increase of pulse overlap and well proved by experimental results, including stainless steel, copper, tungsten and gold [184].

- **Other factors**

J. Gudde *et al*. [185] studied femtosecond laser ablation of Au and Ni films with varying thickness demonstrated the importance of electron diffusion length, determined by electron-phonon coupling time. The ablation threshold fluence rose linearly with film thickness, saturating at thickness d ~ 50 nm in Ni, whereas the threshold fluence saturated at d ~ 500 nm in Au due to much lower electron-phonon coupling time.

A linear increase of threshold fluence with increasing of film thickness was reported by G. Heise *et al*. [199] as well although they used rear side ablation by applying 10 ps laser pulses through the glass substrate to induce ablation on the interface of thin film and the substrate, known as laser lift-off technique. Comparison of front side and rear side ablation of thin films with femtosecond and picosecond laser were presented in [200] and [192,193] respectively. It was found that front side ablation of 100 nm ITO on 175 um PET with 400 fs and 1030 nm laser give smaller ablation threshold fluence than rear side [200].

However, A. Risch *et al.* reported the results of 10 ps laser front-side and back-side ablation of ITO on glass with different wavelength [193]. The results shown that with 355 nm and 1064 nm irradiation, front-side ablation gives a lower ablation threshold. However, with 532 nm irradiation, the rear-side ablation threshold is lower than front-side ablation. With 10 ps 1064 nm radiation source, S. Xiao [201] reported that rear side ablation of ITO on glass gives much better processing quality showing cleaner and sharper spots with little delamination strips at the rim.

Polarization effect on thin film ablation has been seldom investigated. The only available literature on this area represented by K. Venkatakrishnan *et al.* [202] showing that the hole ablation through a 150 nm gold-chromium thin film on a quartz plate using a linearly polarized beam has an elliptical geometry with its long axis parallel to the polarization direction, and circularly polarized beam produces much rounder holes. Note that the focal lens used in the experiment is a high Numerical Aperture lens (NA=0.65), focusing the UV femtosecond laser beam to a sub-micron sized spot, which can be considered as laser cutting of thin sheet.

2.6.2 High speed patterning of thin film with laser and competing methods

High throughput of ultrafast laser for thin film ablation is essential for industrial applications. Two common routes are used for increasing the processing throughput. First is to use fast scanning devices combined with high repetition rate (low pulse energy) lasers. The second approach is to work with lower rep. rate, high energy systems and use multi-beam processing when the laser output pulse energy is at hundreds-microjoule or

millijoule level. Presently, many industrial companies use ultrafast picosecond lasers capable of high pulse energies and power at up to 200 kHz repetition rate. Hence, a combination of a modern scanning galvanometer together with multi-beam could effectively increase the throughput to industrial level.

- **Fast scanning**

Recent rapid development of high repetition rate ultrafast laser systems, i.e. several megahertz repetition rate, urgently requires a scanning device to separate pulses on the sample surface to avoid heat acumination caused by multi-pulse overlapping. Increasing interests of using polygon scanner combining with MHz picosecond laser systems for high throughput processing can be seen from recent publications [203-208]. The most recent paper by Loeschner *et al.* [206] demonstrated a remarkable 800 $m \cdot s^{-1}$ processing speed with a polygon scanner. With the laser running at 20 MHz repetition rate and a scanning speed of 800 $m \cdot s^{-1}$, surface ablation of stainless steel was achieved at 7680 $cm^2 \cdot min^{-1}$. The ability to remove silicon nitride thin film without damage of the underlying silicon was also demonstrated with a processing rate of 245 $cm^2 \cdot min^{-1}$ with 10 MHz repetition rate and 200 $m \cdot s^{-1}$ scanning speed.

Another merit of recently developed polygon scanner is the capability of full synchronization with the laser system, which enables precise patterning of small features on sample surface at extremely high running speed. Most scanning galvanometers cannot be fully synchronized with the laser, which makes them struggle to produce small feature patterns at high speed, i.e. 200 μm^2 square arrays. With a fully synchronized galvo scanner and an MHz picosecond laser system, B. Jaeggi *et al*. [203,208] managed to produce

various complex patterns, i.e. Linux tux icon and flowers pattern with micron level features, on copper surface at 3 $m \cdot s^{-1}$. Studies of synchronized polygon scanner with laser pulse trains for high speed surface patterning can be found in [203-205,207,208].

- **Multi-beam processing**

Many modern commercial ultrafast laser systems enable hundreds of micro joules or even millijoule level pulse energy output. However, to achieve thermal free ultrafast processing, only a few microjoule pulse energy is needed when focused to a few times ablation threshold at a surface [22]. To avoid throwing away pulse energy, diffracting a single high pulse energy laser beam into multiple beams with microjoule pulse energy for high-throughput ultrafast processing has been adopted [23]. Fixed DOEs can only be used to produce identical patterns, whereas an SLM provides more flexibility when addressed with sequential CGH's and synchronized to scanner motion. Another merit of using SLM for generating multi-beams is the ability of control the pulse energy of individual diffractive beam for certain applications [95]. M. Silvennoinen *et al*. [97] recently demonstrated using SLM to diffract a 1 watt femtosecond laser beam to 576 individual spots all above ablation threshold of silicon for surface patterning. Although SLMs are not designed for handling extremely high average power lasers, they can still handle most state of the art commercial ultrafast lasers with tens of Watts [146]. K. L. Wlodarczyk *et al* [259] reported a novel SLM-based high speed laser micro-patterning approach in which an array of diffracted beamlets is used for sequential-parallel micro-patterning a metal surface. The approach has been demonstrated to overcome the speckle interference problem which is a typical drawback of current SLM-based laser marking processing.

Surface patterning of solar cell with multi-beams were demonstrated in [209-211]. With single spot ablation, 18.4 $mm^2 \cdot s^{-1}$ ablation rate was achieved but increased to 4400 $mm^2 \cdot s^{-1}$ with 81 diffractive spots, which can be further improved with a faster scanning device [210]. The uniformity of multiple diffractive spots is essential as unwanted diffraction peaks would damage the substrate when ablating thin films. Z. Kuang *et al.* [22,96] demonstrated a simple method to optimize the uniformity of multi-beams generated with SLM, by slightly moving the location of multi-beams to avoid high symmetric diffractive patterns. By adopting a SLM in the beam path of a picosecond laser system, ITO thin film on glass was removed with 25 diffractive spots with no damage to the glass substrate [212].

2.7 Summary

This chapter started with a brief introduction of ultrafast laser systems, ultrashort pulse amplification and ultrafast laser material interactions, then pointed out the merits of ultrafast laser processing over long pulse ablation and the low throughput bottleneck of ultrafast machining. The background of phase and polarization generation was then discussed and methods to generate interesting radial and azimuthal polarizations with planar/vortex wavefront and their deployment for ultrafast laser processing in surface processing were presented. LIPSS formation was discussed, a very interesting phenomenon observed during laser-materials interactions are highly polarization sensitive as well as exposure related. Both low frequency and high frequency LIPSS have been well documented. By reviewing the phase and polarization control methodology for high throughput ultrafast processing and surface nano/micro patterning, dynamic control of

polarization and phase with an SLM for advanced surface patterning was proposed. In the last section, thin film patterning with ultrafast laser was reviewed, leading to the idea that by synchronizing a kHz repetition rate ultrafast laser system with a SLM and an advanced galvanometer, this could potentially increase the throughput to a significant level without investing a new MHz laser and an expensive polygon scanner.

Chapter 3 - Experimental Equipment and Techniques

3.1 Introduction

This chapter reviews the main equipment used for current research, including two picosecond laser systems, Spatial Light Modulators, scanning galvanometers and multi-axis control systems. Synchronization of SLM with laser systems and motion systems will be presented in this chapter, followed by experimental setups for each experiment.

3.2 Ultrafast lasers

3.2.1 Coherent Talisker picosecond laser

The picosecond Coherent Talisker laser (Talisker Ultra 1064-16) used in current research features 10 picosecond pulse length, three-wavelength options, and operating up to 200 kHz repetition rate. With a maximum 16 Watt 1064 nm wavelength output, it can be converted to 8 Watt 532 nm or 4 Watt 355 nm output. The Talisker laser consists of laser head, closed cycle water chiller, harmonics controller and a power supply integrated control unit. The laser head comprises three compartments, shown in figure 3.1, which are amplifier compartment, harmonics compartment and service compartment.

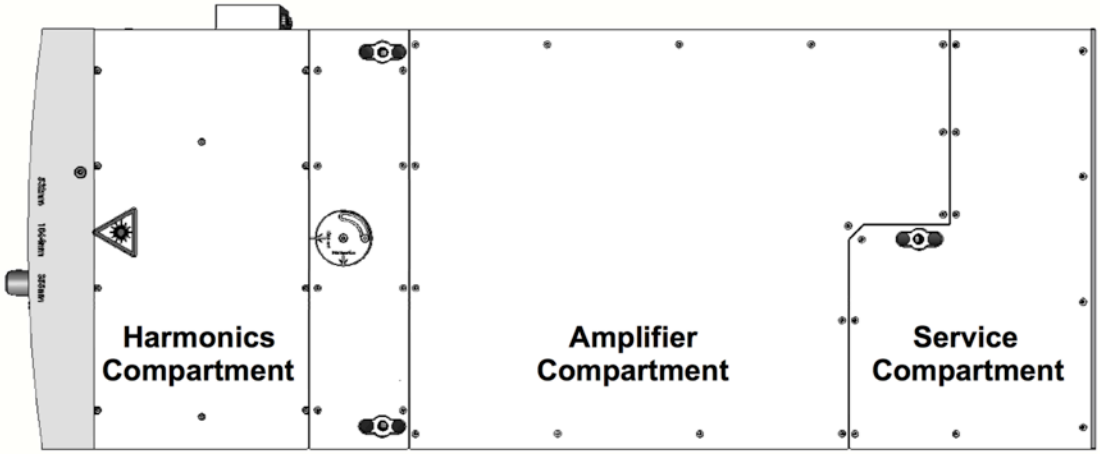

Figure 3.1 *Talisker laser head compartments*

The amplifier compartment contains a seed laser, pockels cell, amplifier gain material, diode pump lasers and a pulse picker. The seed laser is a low power modelocked fiber laser that produces approximately 5 picosecond laser pulses at a repetition rate of 40 MHz and 1064 nm wavelength. The oscillator pulses are selectively injected into a regenerative amplifier cavity by a pockels cell, which is controlled by a High-Speed Driver (HSD) that enables precise and clean selection of individual pulses. The injected pulses are amplified in Nd:YVO_4 pumped by a high power laser diode. An Acousto-Optic Modulator (AOM) pulse picker is used to control repetition rate by diffracting the amplified pulse out of the amplifier compartment. The AOM features several modes of operation for precise control over the output pulses, which are continuous mode, divided mode and burst mode. The harmonics compartment contains two Lithium triborate (LBO) crystals for 2^{nd} and 3^{rd} harmonic generation, which enables selectable wavelength output of Talisker for different tasks.

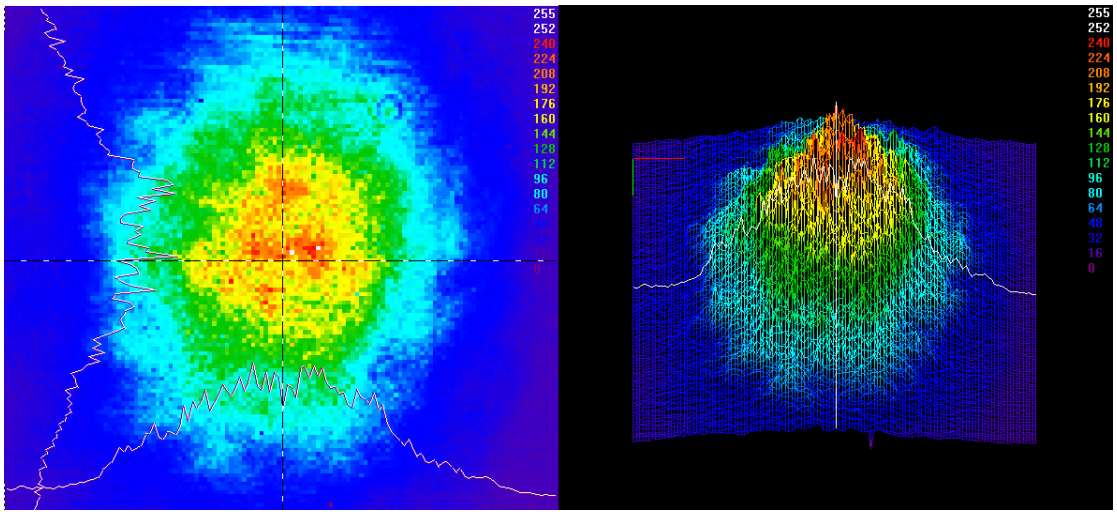

Figure 3.2 *Beam intensity profile of the Talisker picosecond laser system, left: two-dimensional beam profile, right: 3-D beam profile.*

For current research, the output laser wavelength was set at 532 nm with maximum power of 8 watts. The pulse picker was set at divided mode, which enables selection of pulse repetition rate output from 1 kHz to maximum of 200 kHz. The output beam quality is a near Gaussian beam (M^2<1.3). Figure. 3.2 shows the observed intensity profile on a Spiricon camera (model: SP620U).

3.2.2 High-Q picosecond laser

The High-Q picosecond laser (Model: IC-355-800 ps Nd:VAN REG AMP) features 10 picosecond pulse duration and three wavelengths output: 1064 nm, 532 nm, and 355 nm. The system is able to operate at four different repetition rates 5, 10, 20 and 50 KHz with a maximum output power of 2 watts at the fundamental wavelength (1064 nm). The HighQ picosecond laser is mainly composed of three parts: laser head, laser controller with power unit and closed circuit water-air cooling system.

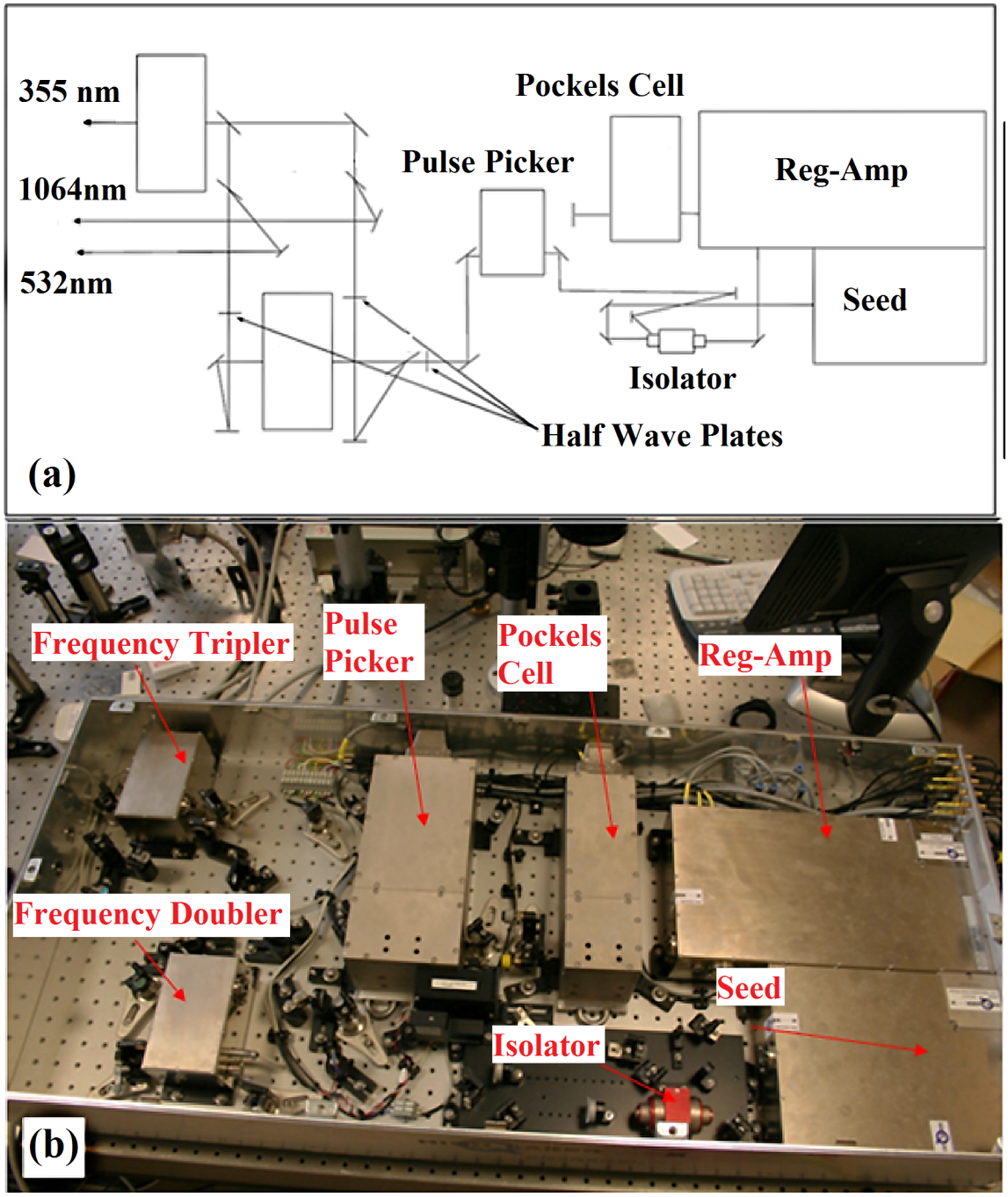

Figure 3.3 *(a) Schematic of optical setup inside HighQ laser head and (b) the corresponding image of laser head internals*

Figure 3.3 shows the schematic of the laser head of HighQ picosecond laser. A mode-locked picosecond Nd:YVO_4 seed oscillator (with SESAM) generates low power picosecond seed beam with 30 MHz repetition rate. The Faraday rotator isolates oscillator

from amplifier. All pulses enter the regenerating amplifier but only certain pulses are trapped and amplified with HV pulses applied to Pockel's cell. The gain medium in the regenerative amplifier is Nd:YVO_4. The output amplified laser pulses are lead to a pulse picker, (second Pockel's cell with polarizer) which enable users to precisely control the pulse numbers for micromachining. A frequency doubler and a frequency tripler enables converting the fundamental wavelength 1064 nm, to 532 nm, or to 355 nm.

Laser beam emitted from HighQ picosecond laser system has a high beam quality factor $M^2 \approx 1.2$. The observed beam profile is shown in Figure 3.4 (Measured by a Spiricon camera model number SP620U). In the current research, the HighQ laser was configured to 1064 nm wavelength output.

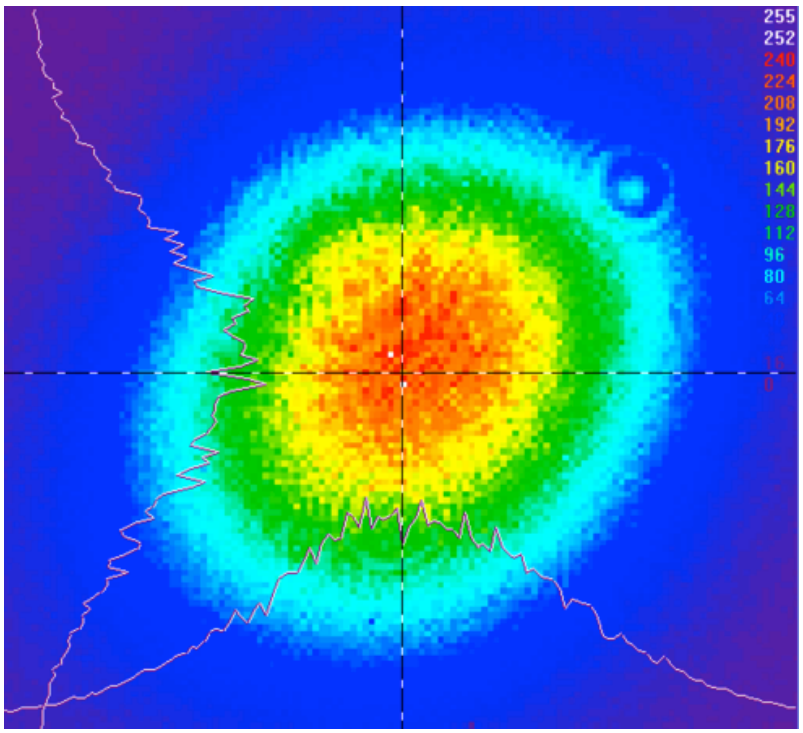

Figure 3.4 *Intensity profile of the beam emitted from HighQ picosecond laser system at 1064nm. Image was taken with a Spiricon Camera.*

3.3 Spatial Light Modulators

3.3.1 Hamamatsu Spatial Light Modulators

Two Hamamatsu SLMs have been employed in current research, models X-10468-03 (1064 nm) and X-10468-04(532 nm). Both SLMs are electrically addressed reflective type PAL-SLMs with appropriate high reflective dielectric coatings. The light utilization efficiency is very high for these PAL-SLMs, >90% [146]. The power handling capability of Hamamatsu SLMs makes them outstanding since they have a ceramic cooling plate connected to the chip. Power handling tests of Hamamatsu SLMs were previously conducted in-house for both devices and found to easily handle the average powers involved with no additional cooling [22,213]. The controller of the SLM enables conversion of CGH to corresponding voltage on each pixel on the SLM, driving them to the desired phase angles. By connecting the digital visual interface (DVI) port on the SLM controller and a DVI port on computer, one can statically address the SLM with one CGH or dynamically address the SLM with multiple CGHs.

Table 3.1 *The specifications of the SLMs used in the current research*

Model	Hamamatsu X10468-03	Hamamatsu X10468-04
LC Type	Parallel aligned nematic	
Number of input level	256 for 8-bit	
Resolution (Pixels)	SVGA (800 × 600)	
Pixel pitch (μm)	20	
Effective area (mm^2)	16 × 12	
Mirror coating	Dielectric	
Frame rate (Hz)	60	
Light utilization efficiency*	>90%	
Readout wavelength (nm)	1000 - 1100	450 - 580
Response Time (rise/fall ms)**	18/76 (1064 nm source)	10/23 (532 nm source)

*** The actual light utilization efficiency depends on the readout light wavelength.**

**** This data is provided by Hamamatsu and the time listed is to change from 10% to 90% for 2π modulation. Tested response time of these two types of SLMs will be presented in the following section.**

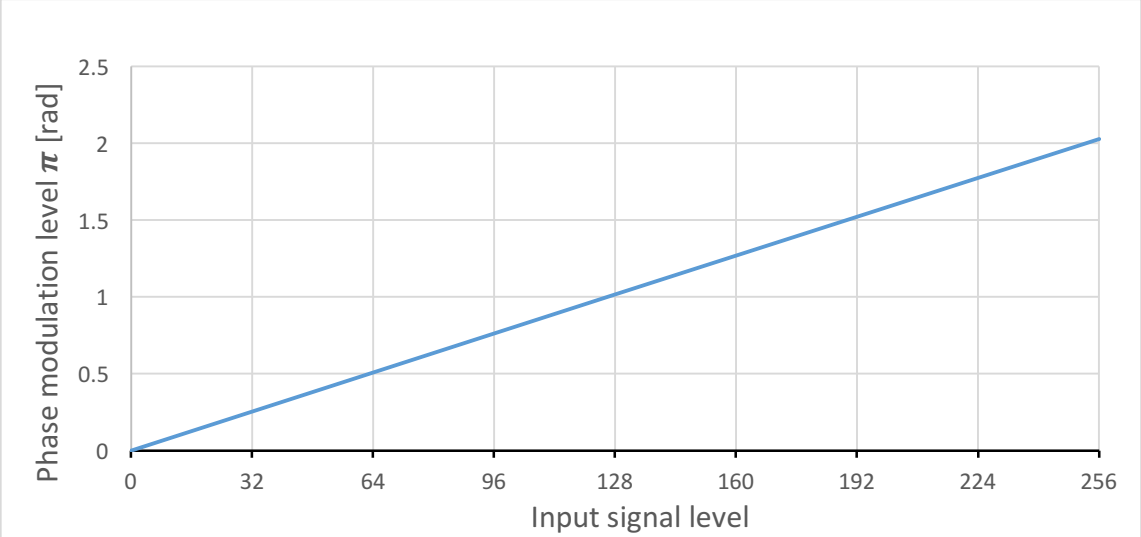

Figure 3.5 *Correlation between the grey level applied on the SLM and the corresponding phase modulation induced by the SLM.*

The Hamamatsu SLM enables users to control the SLM through a graphical user interface on a normal PC. A bitmap CGH (800×600 resolution) can be sent to the SLM controller and the controller converts the grey level (8-bit value) on each pixel to corresponding voltage, which precisely drives the corresponding liquid crystal (pixel) to a desired phase angle, inducing a phase delay to the light passed through it. Figure 3.5 shows the correlation between the grey level applied on the SLM and the corresponding phase modulation induced by the SLM.

3.3.2 Calculation of computer generated holograms

To drive SLM for light modulations, appropriate CGHs need to be generated. A software package based on LabView environment provided by University of Glasgow that was initially designed for optical tweezers was configured to generate the CGHs for addressing SLM statically, shown in Figure 3.6. The algorithms used for generating multiple diffractive spots are iterative Gerchberg-Saxton algorithm (GS algorithm) [214] and non-iterative lens and grating algorithm [215]. The GS algorithm generally provides higher diffraction efficiency and intensity uniformity of multi-diffractive spots than lens and grating algorithm. However, lens and grating algorithm enables superposition of multiple different functional CGHs. For example, by superposition of a multi-beam diffraction CGH with annular beam CGH, both generated with lens and grating algorithm, a Gaussian input beam can be diffracted into multiple annular beams [90].

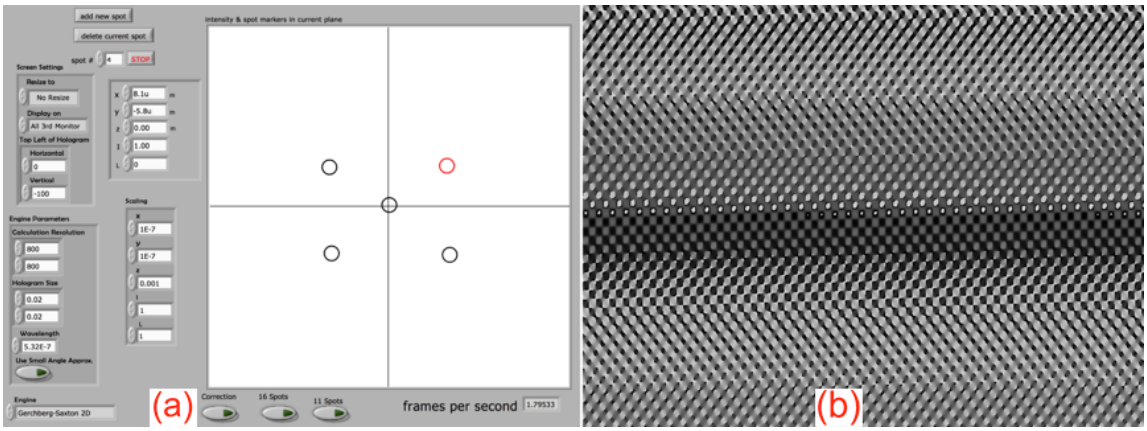

Figure 3.6 *(a) The LabView interface with multiple diffractive beams pattern. (b) The CGH generated with GS algorithm that addresses the SLM.*

To dynamically address the SLM in real time with the motion control system and laser system, software based on LabView background was designed to synchronize the SLM with the laser system and the motion system (scanning galvanometer and multi-axis

motion control system). Details of the software and synchronization will be presented in section 3.5.

The CGHs used in the current research for polarization modulation are homogeneous grey level CGHs and 0 - 4π vortex grey level CGHs, both of which can be generated with Zernike functions in the software provided by University of Glasgow.

3.3.3 Bandwidth test with Hamamatsu Spatial Light Modulators

The technical data sheet of the device (table 3.1) provided the official rise and fall time of the two SLMs adopted in the current research. For the X10468-03 (1064 nm), the rise and fall time required to change from 10% to 90% of 2π phase modulation are specified as 18 ms and 76 ms respectively (table 3.1) while for the X10468-04 (532 nm), are 10 ms and 23 ms respectively [146]. To carry out experiments of driving SLMs in real time with synchronized motion systems and laser systems accurately, the effective bandwidth of these SLMs needs to be confirmed unambiguously. The bandwidth of the SLM refers to how many CGHs can be swopped per second without inducing any beam distortion after the swop.

The experimental setup for testing the bandwidth of SLMs is shown in figure 3.7. A half-wave plate rotated the incident horizontal linear polarization to $+45°$, a test SLM addressed with different homogeneous grey level CGHs and a quarter-wave plate with its fast axis at $-45°$ form a polarization rotator. The angle of the output linear polarization is dependent on the grey level applied on the SLM. The polarization rotator plus a polarizer placed afterwards with its transmission axis set at $+45°$ (Marked green in Figure 3.10) form an amplitude modulator. The modulated beam hit on a white screen with a fast

photodiode (Thorlabs DET210) [216]. The fast photodiode converted the detected scattered signal to voltage and displayed on a fast oscilloscope (Tektronix TDS 2022B).

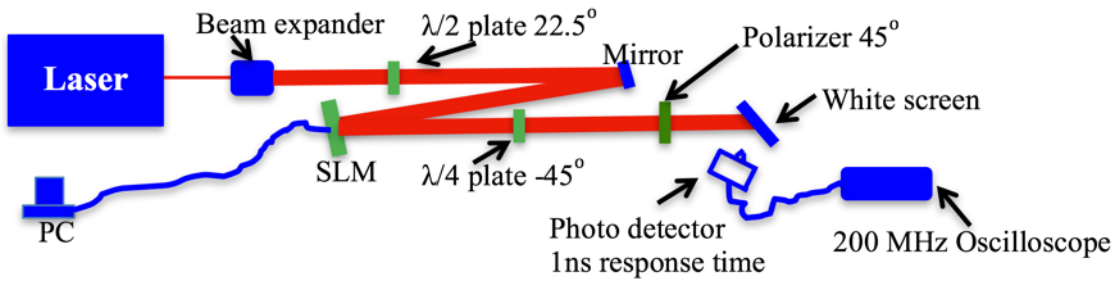

Figure 3.7 *Experimental setup for testing the bandwidth of SLMs.*

By swopping between a grey level zero CGH (phase delay $\phi = 0$) and a non-zero grey level CGH (phase delay ϕ=β) on the SLM, the amplitude of the transmitted laser beam was modified and captured in real time by the photo detector and displayed on the oscilloscope. The time difference between two stabilized amplitude levels gives the effective rise and fall time for the SLM with β phase modulation. By increasing the grey level stepwise, the rise and fall time with different level phase modulation ware measured. Figure 3.8 shows the laser intensity modification with grey level applied on the SLM.

Figure 3.8 shows the measured rise and fall times taken for laser intensity change when swopping CGH1 with a uniform grey level 122 to a new CGH that has a uniform grey level 0 on Hamamatsu SLM X10468-03(1064 nm). The change of grey level from 122 to 0 induced a phase change of π on the incident laser. The highest laser intensity was set at grey level 0, increasing grey level would result in an intensity decrease. Hence, the drop of voltage show in Figure 3.8 actually represents the rise of a new CGH. To measure the rise and fall times from the oscilloscope traces, the times to reach 90% of the stable

maximum and minimum respectively were taken. The time was measured using the cursors (vertical lines in solid yellow) on the oscilloscope.

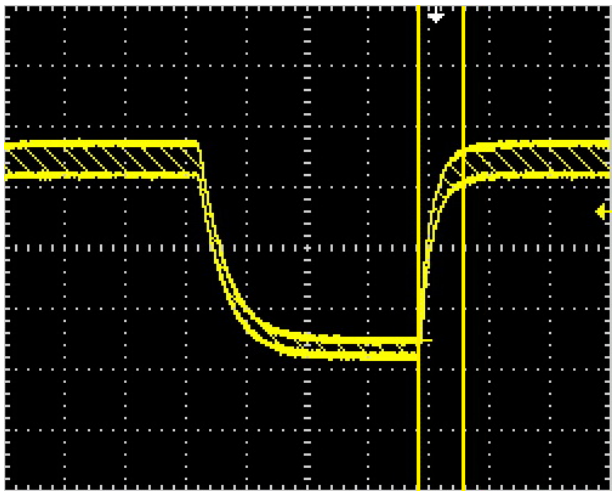

Figure 3.8 *measured fall time of Hamamatsu SLM X10468-03 with π phase modulation (grey level 122 - 0)*

The test was repeated to obtain the rise and fall time for different level of phase modulation for each SLM. Note the time measured was to change from 0% to 90% for different level of phase modulation. Each test was performed 10 times for generating the final figures. The Hamamatsu SLM X10468-03 (1064 nm) and Hamamatsu X10468-04 (532 nm) were tested with HighQ and Talisker system respectively. The results are summarized in Figure 3.9 and Figure 3.10. respectively. The error bar was the standard deviation based on 10 set of measurements. The formula used to calculate the standard deviation was: $\sqrt{\frac{\sum(x-\bar{x})^2}{(n-1)}}$, where $\bar{x}$ is the sample mean average and n is the sample size.

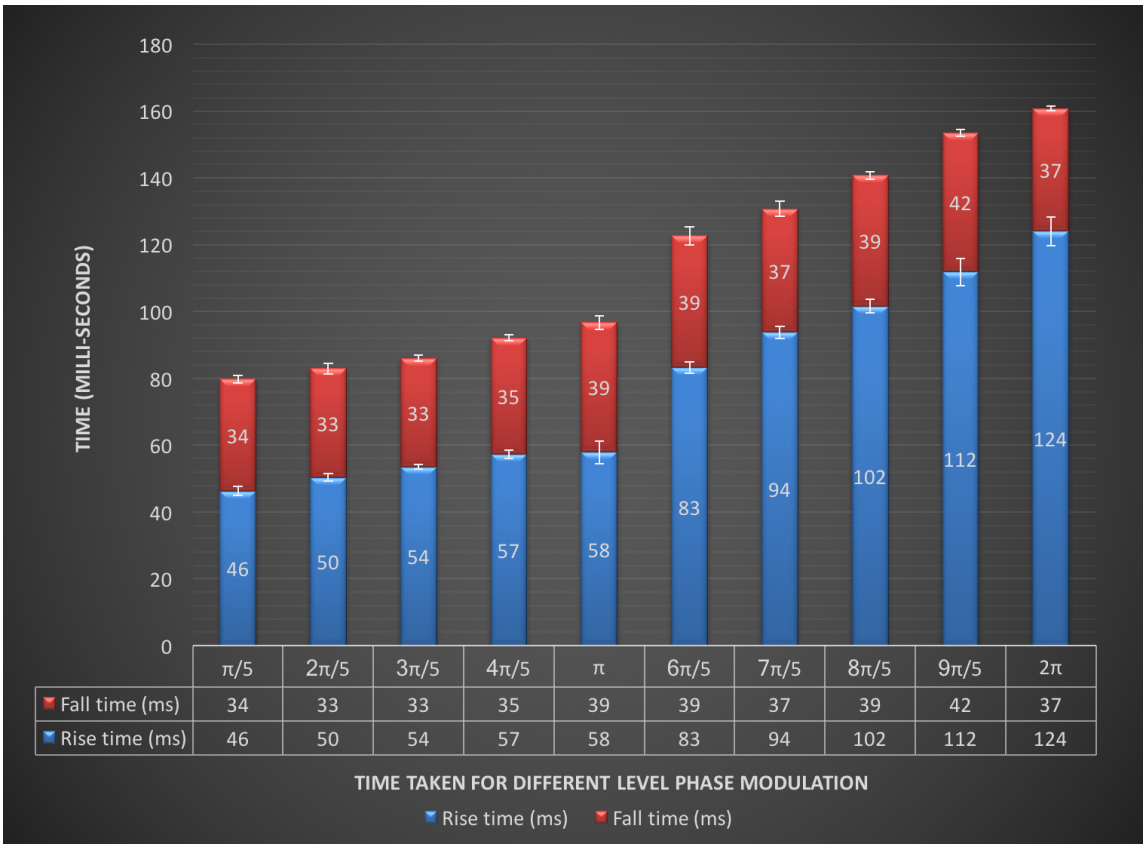

Figure 3.9 *Rise and fall time of Hamamatsu SLM X10468-03 (1064 nm) as a function of phase modulations.*

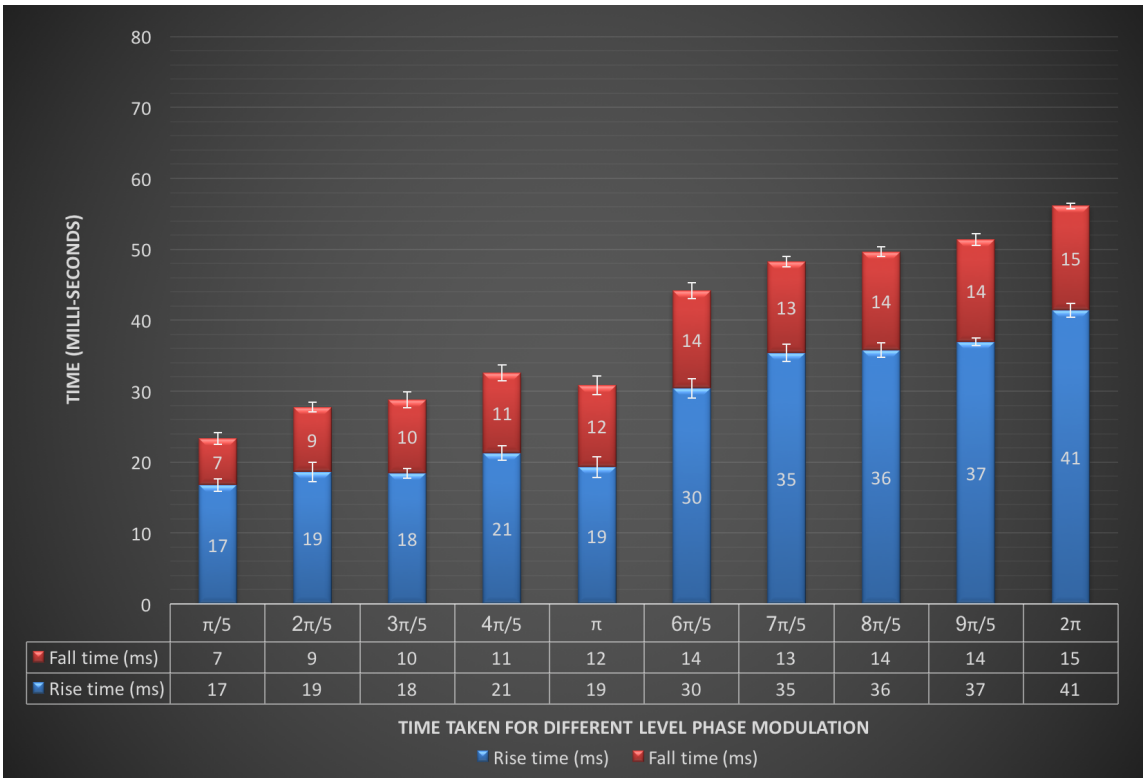

Figure 3.10 *Tested rise and fall time of Hamamatsu SLM X10468-04 (532 nm) with increasing phase modulations.*

The results show that a 2π phase modulation takes the longest time for both SLMs, which are 161 ms and 56 ms for Hamamatsu SLM X10468-03 (1064 nm) and -04 (532 nm) respectively, leading to a bandwidth ~6 Hz and ~18 Hz respectively. However, it is hard to identify the level of phase modulation with complex CGHs, which have varying grey levels on different pixels (see Figure 3.6 (b)). When switching two complex CGHs, it is impossible to identify an exact level of phase modulation. Hence, in determining the effective bandwidth of the SLM, the most secure way to ensure two CGHs are switched completely is to use the time for 2π phase modulation.

Noted that the phase modulation angle is corresponding to the tilted angle of the liquid crystal molecules inside the SLM according to Hamamatsu SLM ebook [146], a bigger

phase modulation angle requires the liquid crystal to tilt to a bigger angle, which takes longer than it take to tilt a small angle.

3.4 Motion systems

3.4.1 Scanning galvanometer systems

Three scanning galvanometer systems were employed in the current research. A Nutfield-XLR8-10 [217] with a F-theta lens (100 mm focal length) was employed on the HighQ picosecond laser system. Two scanning galvanometers were employed on the Talisker picosecond laser system: a Nutfield-XLR8-14 and an Aerotech Nmark AGV-14 HP [218] both installed with a 250 mm focal lens F-theta lens. The drivers for Nutfield-XLR8-14 and Aerotech Nmark AVG-14 HP are provided by the Aerotech Nmark SSam [219] and Nmark GCL [220] controllers respectively. All three scanning galvanometer systems are two-dimensional scanning systems.

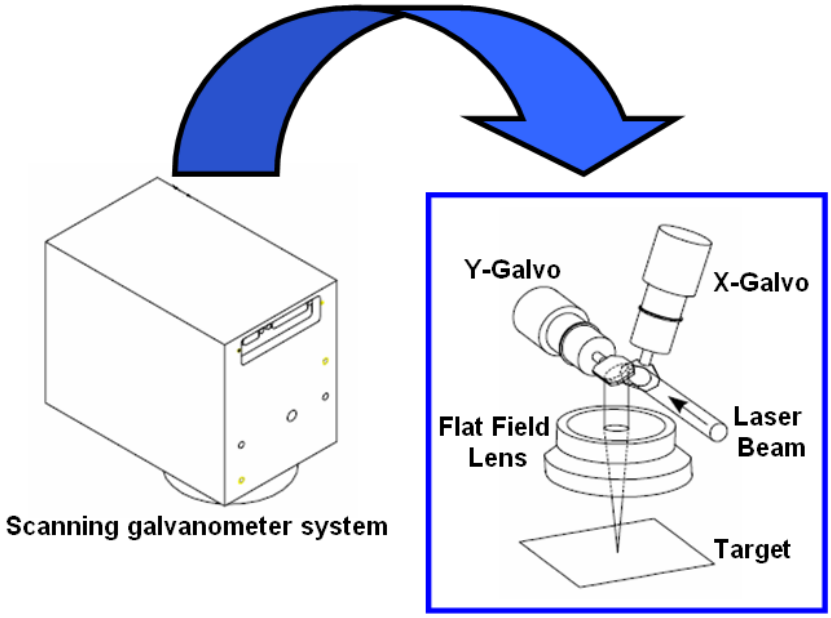

Figure 3.11 *Schematic diagram of a scanning galvanometer system.*

A scanning galvanometer system mainly consists of electronic drivers and two turning mirrors, one mirror to drive the incident laser beam in the X direction and the other one to drive the beam in the Y direction at high speed. Schematic configuration of a scanning galvanometer is shown in Figure 3.11. Scanning galvanometer systems enable high speed (up to 10 $m \cdot s^{-1}$) and high precision (μm level) control of ultrafast laser beam position on a large sample surface.

The Nutfield-XLR8-10 and Nutfield-XLR8-14 scanning galvanometers can be controlled by a Real Time Control (RTC) card [221,222] combined with a graphical interface software, SCAPS-SAMlight [223], as shown in Figure 3.12. Also, the Nutfield-XLR8-14 galvos could be controlled from within the Aerotech system using the SSam controller. However, the open loop nature of the non-digital galvo suffers from the pulse accumulation problem on the scanning edges due to the acceleration and deceleration.

A state-of-the-art digital galvanometer was adopted in this research - Aerotech Nmark AGV-14 HP scanning galvanometer, which has high resolution optical encoders providing precise position feedback to the Aerotech controller [218]. The location of the AGV-HP mirrors can be captured and analysed in real time of scanning, which avoids the complex program delay parameters to compensate for lag of other non-digital scanning galvanometers. Another critical function in the Aerotech Nmark AGV-14 HP scanning galvanometer system is Position Synchronized Output (PSO), which enables the user to trigger laser pulses based on the position of the turning mirrors. In other words, users can program the galvanometer to trigger the laser on and laser off precisely at given positions on the sample surface prior to processing the part. The software used to control the AVG-14 HP was integrated with the software used to control the motion control stages, provided by Aerotech Inc., which make the synchronization of the galvanometer and the motion control stages precise and compact.

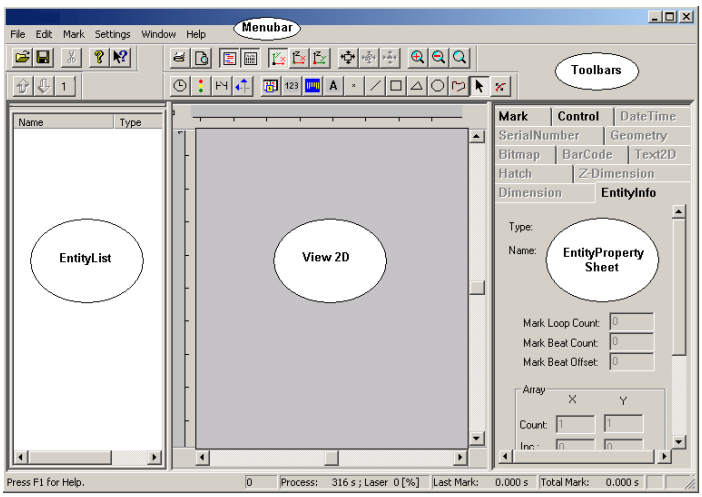

Figure 3.12 *Graphic interface (SCAPS-SAMlight) in PC used for control the Nutfield XLR8-10 and -14 galvanometer systems* [223].

3.4.2 Multi-axis motion control systems

Two Aerotech multi-axis motion control systems, as shown in figure 3.13 (a) and (b), were used in the current research. A three-axis motion control system (x, y, z) was deployed in the Talisker picosecond laser system. The X-axis is an Aerotech ABL 1500WB Air-bearing Direct-Drive Linear Stage (Model: ABL 15040WB-ES16925), which enables sub-micron accuracy ($\pm 0.4\ \mu m$) and 400 mm working distance [224]. The Y-axis is an Aerotech ABL 1500 Air-bearing Direct-drive linear stage (Model: ABL 15030-ES16925), which features 300 mm travel distance and sub-micro accuracy ($\pm 0.4\ \mu m$) [225]. The Z-axis is an AVS/AVSI100 mechanical-Bearing ball-screw lift stage (Model: AVSI125) with 25 mm travel distance, $\pm 5.0 \mu m$ accuracy, and 25 kg maximum loading weight [226].

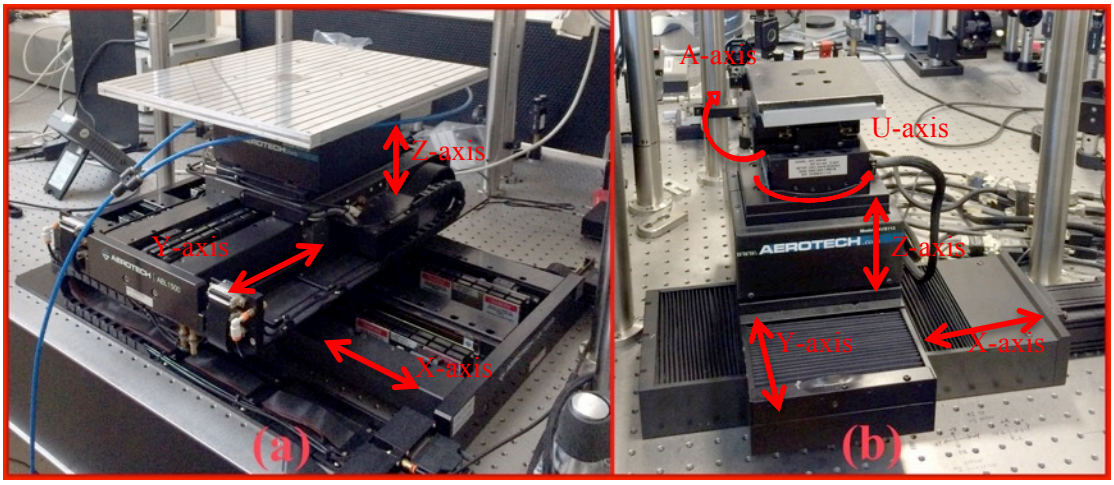

Figure 3.13 *(a) 3-axis motion system in Talisker picosecond laser system, (b) 5-axis motion system in HighQ picosecond laser system.*

A five-axis motion control system (x, y, z, u, a) was used with the HighQ picosecond laser system. The X-axis and the Y-axis are Aerotech ATS150 Mechanical-Bearing Ball-screw linear stage (Model: ATS150-100-M-20P-NM-9DU-NC), which enables 100 mm

traveling distance and $\pm 1\ \mu m$ accuracy [227]. The Z-axis is an Aerotech AVS/AVSI100 Mechanical-bearing ball-screw left stage (Model: AVS113), which is capable of 13 mm travel distance, $\pm 0.3\ \mu m$ accuracy and 25 kg maximum load weight [226]. The two tilting stage axes are Aerotech ANT-20G Goniometers (Model: ANT-20G-50 for the A axis and ANT-20G-90 for the U axis), both feature a 20 degrees rotation angle [228].

All the stages used in the Talisker and the High-Q system are controlled with Aerotech controllers and Aerotech software. The software used for controlling the multi-axis stage and the Aerotech Nmark AGV-14 HP galvo in the Talisker system is the same user interface, which enables the user to control the multi-axis stage and the Nmark AGV-14 HP galvo automatically and simultaneously with G-code programs.

3.5 Synchronization of ultrafast laser systems

Experiments of dynamic control of phase and polarization for ultrafast laser surface processing play a major role in the current research. To achieve dynamic control of phase and polarization for ultrafast laser processing, synchronization of ultrafast laser systems, SLMs, scanning galvanometer systems and motion control systems are necessary. This section presents the methods and details of two synchronized ultrafast laser systems.

3.5.1 Synchronization of Talisker picosecond laser system

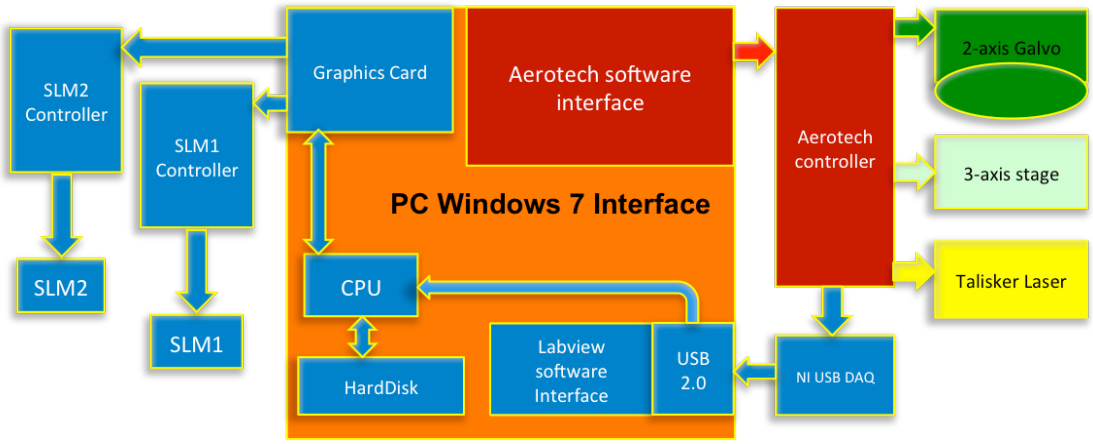

Figure 3.15 *Schematic of the synchronized Talisker picosecond laser system with Aerotech motion system and up to two SLM's.*

Figure 3.15 shows the schematic of the synchronized Talisker picosecond laser system. The first part is the synchronization of the laser, galvanometer and motion stage system. The synchronization of Talisker laser with Aerotech controller was achieved by sending a 5-volt TTL signal from the Aerotech controller to the Talisker controller for fast laser gating. Hence, the Aerotech controller is capable of integrating the galvanometer, motion stages and the Talisker laser within one interface. However, the SLM is controlled through a graphic interface (Standard DVI), which is not available on the Aerotech controller. Hence, the second part is to synchronize the SLM with Aerotech controller.

CGHs (8-bit) generated, for example, using the iterative GS algorithm with high-end PC take a few seconds to create. Hence, for real time applications, only pre-saved CGHs were applied, which is the best approach currently for minimizing time delays. The pre-saved CGHs were saved in the hard disk in the PC. A National Instruments (NI) USB data acquisition device (NI USB-6501) [229] was used to receive TTL signals from the

Aerotech controller. Software based on Labview as shown in figure 3.16, was designed to receive the TTL signal from the NI data acquisition device through a USB port on the PC. After receiving the TTL signal from the Aerotech controller, the software immediately obtains a pre-saved CGH and displays the CGH on the SLM. Hence, the Aerotech controller has made a communication with the SLM control software. After the SLM control software is configured, it can be set to run in the background and wait for the trigger signals from Aerotech controller. The Aerotech control software is the user interface to set parameters to multi-axis stage, Nmark AVG-14 HP galvo, Talisker laser gating, and trigger signal to SLM control software. Note, all the pre-saved CGHs were numbered in sequence and displayed on the desired SLM sequentially after receiving trigger signals.

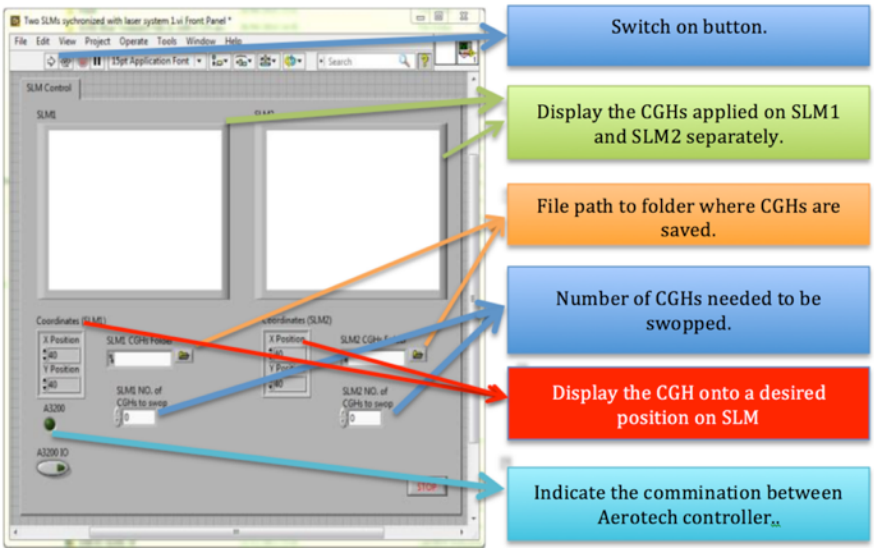

Figure 3.16 *SLM control software used for the synchronization of SLM with laser and motion control systems.*

3.5.2 Synchronization of HighQ picosecond laser system

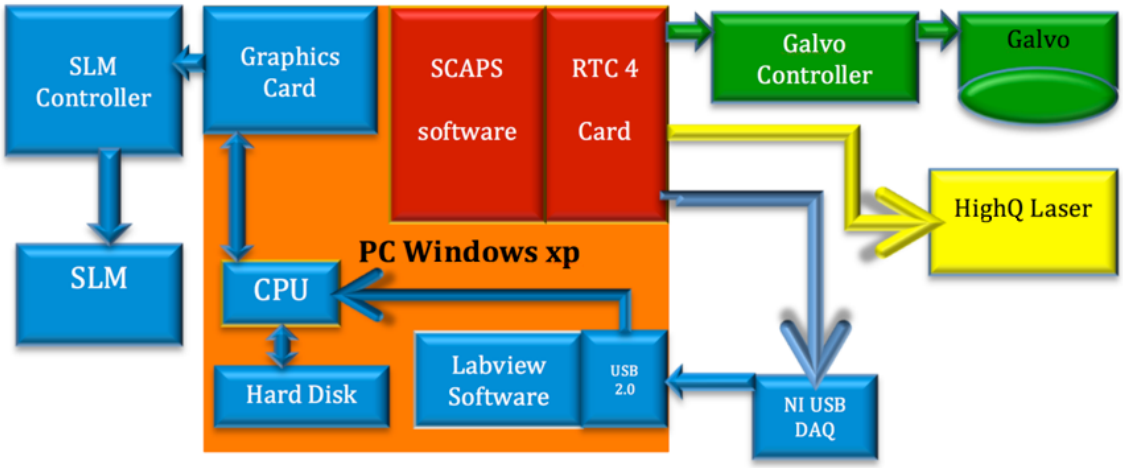

Figure 3.17 *Schematic of synchronized HighQ laser system.*

Figure 3.17 shows the schematic of the synchronized HighQ laser system. The Nutfield-XLR8-10 galvanometer and the shutter of the HighQ picosecond laser are controlled by a RTC 4 card [221] with user-friendly software, SCAPS SAMlight [223]. A 5-volt TTL from the RTC 4 card triggers software based on Labview environment to send CGHs to the SLM. The SLM control software is the same as the one used in Talisker system. Both SCAPS software and the SLM control software are running under Windows XP environment. Note that the 5-axis stage was not synchronized with the other parts of the system, which is possible, but not necessary for the current research.

3.6 Measurement equipment

3.6.1 Beam profiler

Two Spiricon CCD cameras (model: SP620U and model: LBA-300), as shown in Figure 3.18 (a) and (b), were used to capture the beam profile of the ultrafast laser beams [230].

To avoid high power laser beam damaging the CCD camera, a wedged fused silica plate placed before the CCD chip near the Brewsters angle allows a small portion of laser beam reflect onto the sensitive CCD detector. As the fused silica plate is placed at 45° to the incident beam, which is near the Brewsters angle, only a small s-polarized beam will be reflected to the CCD chip, and the rest of the beam transmitted (see Figure 3.18 c). When using the Spiricon camera to capture polarized beams, one should be aware that the fused silica plate acts as a polarizing beam splitter, reflecting the vertically polarized component.

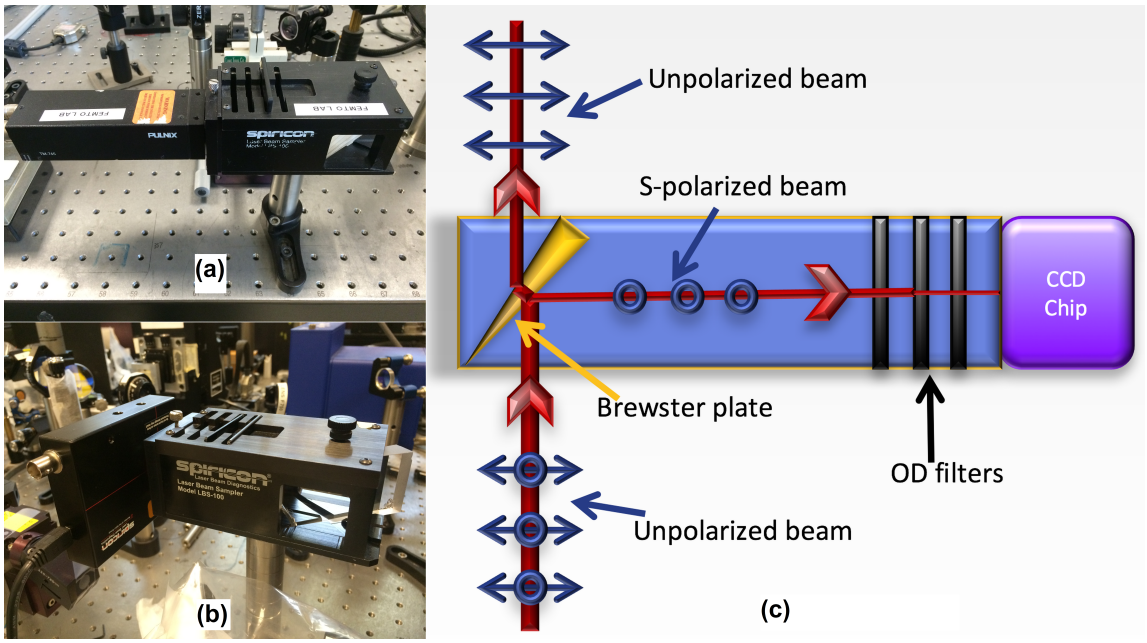

Figure 3.18 *(a) and (b) The Spiricon cameras used in the current research, (c) schematic of the fused silica placed near Brewsters angle with OD filters before the CCD chip to reduce intensity on the sensitive CCD detector.*

3.6.2 Nikon digital microscope

A Nikon digital microscope was the main equipment used to obtain 2D images of surface processed with laser processing. The microscope enables several magnifications of the sample surface, which are ×5, ×10, ×20, ×50, and ×100. The Nikon digital microscope

consists of an optical microscope, a digital camera, and software running in Windows environment for operating the digital camera. A 3-axis stage was integrated with the optical microscope for placing the sample and finding the focal plane of the microscope. The microscope was calibrated regularly by measuring standard samples provided by Nikon.

3.6.3 WYKO NT1100 white light microscope

A WYKO NT1100 white light microscope, was employed to obtain 3D profile of sample surface processed with ultrafast laser. Powerful WYKO 2D/3D software Vision allows users to collect the images and other surface data. A white light illumination source split into two beams, with one beam impinged on the sample surface and reflected back to interfere with the reference beam generating fringe patterns, giving the 3D profile of the sample surface. Vision software was used to measure the surface roughness, ablation depth and period of the surface structures. The WYKO microscope also has several available magnifications, $\times 2.5$, $\times 5$, $\times 10$, $\times 20$, $\times 50$, $\times 100$, which allows users to view overall surface profile or local detailed surface profile.

3.6.4 SEM

In the current research, some surface structures with sub-micron features were observed with a scanning electron microscope (SEM). Model JEOL JSM-7001F SEM was used to obtain sub-micron and nano structures on metal surfaces produced with ultrafast laser. The SEM enables magnification from $\times 10$ to $\times 1{,}000{,}000$, allowing imaging of 1.2 nm structures [231]. The SEM is also integrated with an Energy-dispersive X-ray (EDX)

detector (Oxford Instruments X-Max SDD X-ray detector) [232], which is capable of elemental analysis on a surface.

3.7 Summary

This chapter reviews equipment used in the current research, including picosecond lasers, motion systems including scanning galvanometer systems, SLMs and measurement equipment. The effective bandwidths of SLMs used in the current research were measured and presented in this chapter. The synchronizing methods of two picosecond laser systems with SLMs and motion control systems were also discussed in this chapter.

Chapter 4 - Advanced polarization and wavefront control for ultrafast laser microprocessing

4.1 Introduction

Wavefront and polarization modulation is an effective method to increase the throughput and quality of ultrafast laser processing [11,23,24,32,33,92,95-98,107,109]. For example, theoretical study indicates that a radially polarized beam could potentially increase the cutting speed up of stainless steel to 1.5 - 2 times faster than commonly used circularly polarized beam [107]. Wavefront modulation of a single input laser beam with multiple diffractive beams enables faster processing rates orders of magnitude higher than unmodified beam [11,23,24,95-98]. Also laser ablation with a vortex wavefront produces less recast formation than with Gaussian beams [92,233]. Wavefront and polarization modulation has also been applied in optical tweezers, high-resolution metrology and lithograph [79].

This chapter reports a new technique for ultrafast laser microprocessing with advanced control of the beam wavefront and polarization, using two SLMs in combination. The experimental setup will be presented first, followed by the details for generating a number of structured beams, including parallel linearly polarized vortex beams and parallel radially or azimuthally polarized beams with planar or vortex wavefront. All the structured beams were used to process polished stainless steel samples. LIPSS structures were produced on the sample surface and used to visualize the electric field vectors (polarization) structures at the focal plane unambiguously, helping to characterize the optical properties of the setup.

4.2 Experiment setup

A "SLM converter" setup was formed and used to fully control both the wavefront and polarization of laser beam. The SLM convertor, as shown in Figure 4.1, consists of two phase only Hamamatsu SLMs and a pair of waveplates. SLM 1 is used for structuring the wavefront of the incident horizontal linearly polarized beam only. A half-wave plate placed after SLM1 rotates the incident horizontal linear polarization to +45° linear polarization. With +45° linearly polarized beam incident, SLM 2 combined with a quarter-wave plate with its fast axis rotated to +45° form a polarization converter, which is used for tailoring both the polarization and the phase of the laser beam. The theory and Jones Matrix analysis of the polarization converter is presented in the section 2.5.5 in Chapter 2.

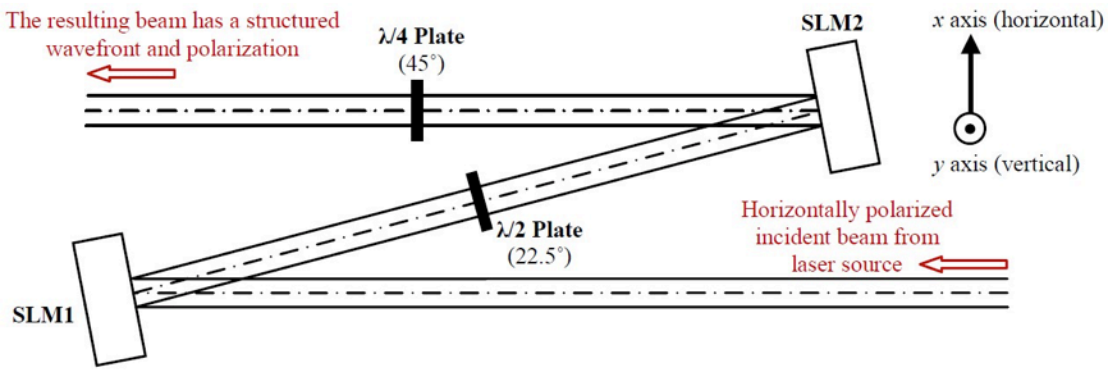

Figure 4.1 *Schematic of the SLM converter.*

A schematic of the experiment setup is shown in Figure 4.2 (a). The laser source is a Coherent Talisker (Talisker Ultra 1064-16) operating at 532 nm. A diffraction limited beam-expanding telescope (Jenoptic) with ×3 magnification was used to reduce the average laser intensity impinged on the SLM. The SLM converter consists of two

Hamamatsu X10468-04 PAL-SLMs and a pair of zero-order waveplates. After the SLM converter, a 4f optical system consisting of two plano-convex lenses (f=400 mm) was used to re-image the surface of SLM2 to the aperture of a scanning galvanometer (Nutfield-XLR8-14). The layout of the 4f re-image system is shown in figure 4.2 (b). The beam was scanned by the scanning Galvo and focused with a flat field f-theta lens (f=250 mm, Linos). Samples were mounted on a precision 3-axis (x, y, z) Aerotech motion control system.

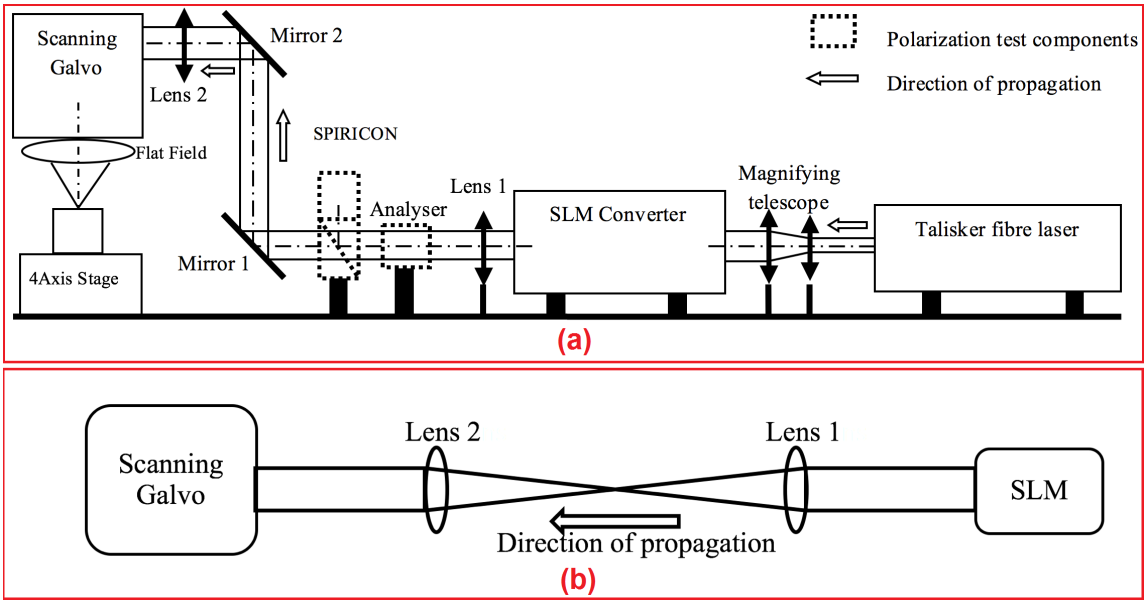

Figure 4.2 *(a) Schematic showing how the SLM converter was used to control the wavefront and polarization of a picosecond laser microprocessing setup. The "Polarization test components" were removed when the microprocessing tests were carried out. (b) the layout of the 4f re-image system*

A number of optical field configurations were produced to demonstrate the capability of the setup. In each case, the structured beams were analysed at two places: immediately after the SLM converter (near field or far field) and at the focal plane of the microprocessing setup (far field). The structured collimated beams or focused beams (focused with Lens 1 shown in Figure 4.2 (a)) were analysed by a polarizer and beam

profiler (model: SP620U) (dotted component in Fig 4.2(a)) placed after the SLM converter. Lens1 was temporally removed to provide a collimated beam on the Spiricon camera. To further analyse the structured beam at the focal plane, LIPSS were produced on a polished stainless steel (SS) sample surface. The LIPSS produced on SS samples with the structured beams are LSFL, which have a periodicity similar to the irradiation wavelength and have a local structure direction perpendicular to the incident linear polarization field direction. By analysis of the LIPSS produced on the SS sample, the polarization states on the focal plane of the microprocessing setup can be visualized and confirmed.

The sample used in the experiment was stainless steel – AISI 316L (Fe/Cr18/Ni10/Mo 3) 2 mm thick foil, purchased from Goodfellow Cambridge Limited. Both sides of the sample have been mirror polished. The average surface roughness has been measured with the WYKO, Ra = 18±3 nm. The original sample was 100×100 mm, which was cut into 50×50 mm samples. A rubber glove has been used when handling the sample to avoid the contamination of the sample. The sample was ultrasonic bathed with acetone (99.99%) before and after laser processing.

For all the single beam microprocessing tests, the laser output was attenuated to produce a pulse energy E_p of 3 μJ (approximately 0.3 J·cm^{-2} fluence at focal plane). For microprocessing test with 3 diffractive spots, the laser output was attenuated to a pulse energy of 11 μJ. The samples were placed at the focal plane of the microprocessing setup and exposed statically for a duration of ~5 ms (~100 pulses at 20 kHz pulse repetition

rate). After laser exposure, the LIPSS structures produced were imaged with an optical microscope.

4.3 Linearly polarized vortex beam

As a first case study, the SLM converter was configured to produce a linearly polarized vortex beam, carrying an OAM with topological charge *m=1*. By adjusting the phase delay $\phi_1(x,y) = e^{i\theta}$ at SLM1 varying from 0 to 2π shown in Figure 4.3 (a), a gradual phase difference from 0 to 2π was added to the incident planar wavefront after the laser beam reflected from SLM1. The output beam from SLM1 then carries a helical wavefront with an associated OAM with topological charge *m=1* and a ring shaped, Laguerre-Gaussian beam intensity with phase singularity at centre [213]. The SLM2 was configured to have a fixed phase (with no effects on the incident wavefront and polarization), hence all pixels on SLM2 were set at: $\phi_2(x,y)=0$, which acts simply as a mirror. As a result, the incident linearly polarized Gaussian beam was structured into a ring shaped beam with vortex wavefront, whilst its polarization remains linear with its direction at $+45°$ due to the half-wave plate, parallel to the fast axis of the quarter-wave plate. The resulting collimated beam was analysed after the SLM converter. As expected, the structured beam profile, as shown in Fig 4.3 (c), has a ring shaped intensity associated with vortex beams, created from the incident Gaussian, Fig 4.3 (b).

Note that the talisker laser has a very high quality coherent beam with high spatial and temporal coherence. A 10 ps pulse will have a coherence length of 3mm. The Spyricon camera has a thin window on the Silicon detector which may allow etaloning and hence multiple beam reflection to reach the detector. This may be a source of the speckle, which

is due to interference with high a spatially coherent laser source. Additionally, scatter from dust particles on the optical surfaces may add to this effect. The M^2 of the Talisker laser was tested to be M^2=1.03.

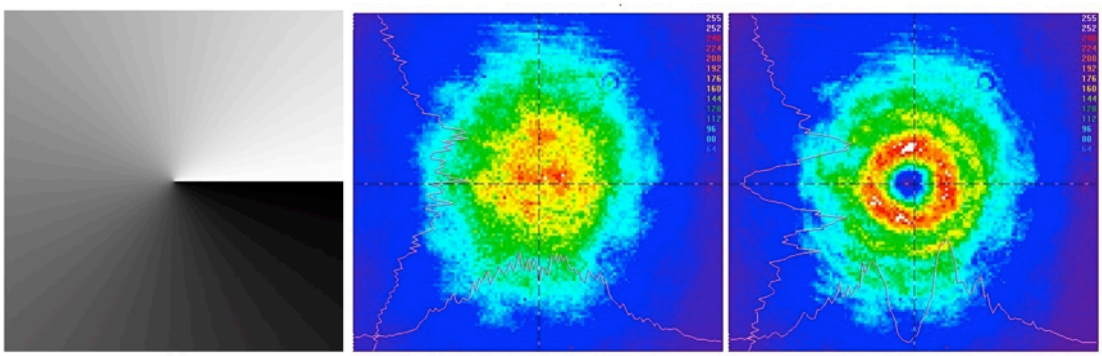

Figure 4.3 *(a) Spiral vortex phase delay, 2π vortex phase delay CGH applied on SLM1, (b) incident Gaussian beam intensity profile, (c)near field structured vortex wavefront beam intensity profile. The colour coded scale represents intensity, in arbitrary units. Images produced using Spiricon beam profiling system with CCD camera (Model: SP620U).*

The setup was then used to imprint focal spots on the surface of a polished stainless steel sample with laser parameter detailed in section 4.2. Figure 4.4 (a) shows the spot produced with no phase modulation on both SLMs, which was produced with the focused Gaussian beam. The roundness here is an indication of the excellent beam quality from the Talisker laser. The structured beam produced a ring shaped spot on the sample, as shown in Figure 4.4 (b), which is consistent with the expected beam intensity after focusing a vortex beam with a low NA lens [39,92]. The spots produced are covered with LIPSS, developing in a direction perpendicular to the incident linear polarization and has a similar periodicity, $\Lambda \approx 0.5$ μm, of the incident wavelength (532 nm). The blue arrows in Fig 4.4 indicate the linear polarization direction of the incident laser beams.

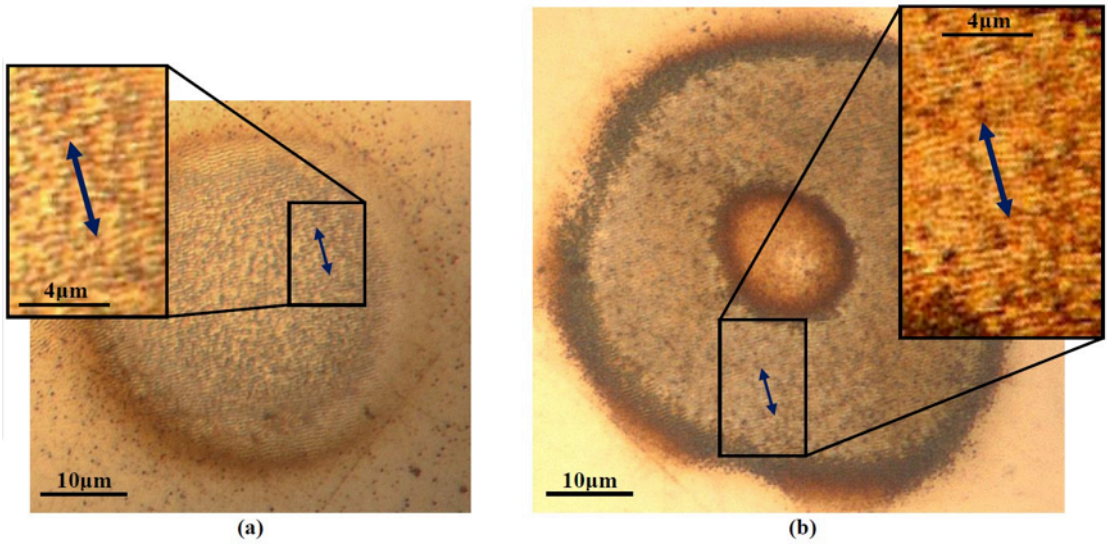

Figure 4.4 *Optical micrographs showing the focal spot produced with 100 pulses at 3 μJ/pulse, with the SLM converter producing a high quality Gaussian beam (a) and a spiral vortex beam (m=1) (b). The direction of the LIPSS developed in the spots is perpendicular to the incident linear polarization, which is indicated with blue arrows.*

4.4 Radially and azimuthally polarized beam with vortex or planar wavefront

4.4.1 Radially and azimuthally polarized beam with vortex wavefront

To further illustrate the capabilities of the SLM converter, this section shows that both the polarization and the wavefront structures of the beam can be structured simultaneously. Firstly, the SLM converter was configured to produce radial or azimuthal polarized vortex beams. In this case, SLM1 in the SLM converter works as a mirror ($\phi_1(x,y)=0$) with no phase modulation to the incident beam. Then, a vortex phase delay of 0 to 4π, shown in Figure 4.5 (a) top left corner, was applied on the SLM2. As $\phi_2(x,y)$ varies from 0 to 4π dependent on the spatial coordinates, it produces a radial polarization overall as described in Eq. (2-14). In this configuration, the structured beam contains a 2π pitch residual

vortex phase, which is described by the phase term $e^{i\frac{\phi_2}{2}}$. Hence the structured beam is radially polarized, with a vortex wavefront carrying an OAM with topological charge of *m=1*. Furthermore, by adding a constant phase term π to the overall vortex phase delay on SLM2, the output polarization can be converted from a radial to its orthogonal azimuthal polarization, as shown in Figure 4.5 (b) top left corner. Since the SLM is only sensitive to horizontal linearly polarized electric vector components, and the laser beam is 45 degrees linearly polarized, only the horizontal component of the electric vectors was modulated by the SLM. In this case, although SLM2 has applied a vortex phase delay of 0 to 4π, which can generate a topological charge of *m=2*, only the horizontal electric vectors were modulated while the vertical unaffected, ending up with a topological charge of *m=1*.

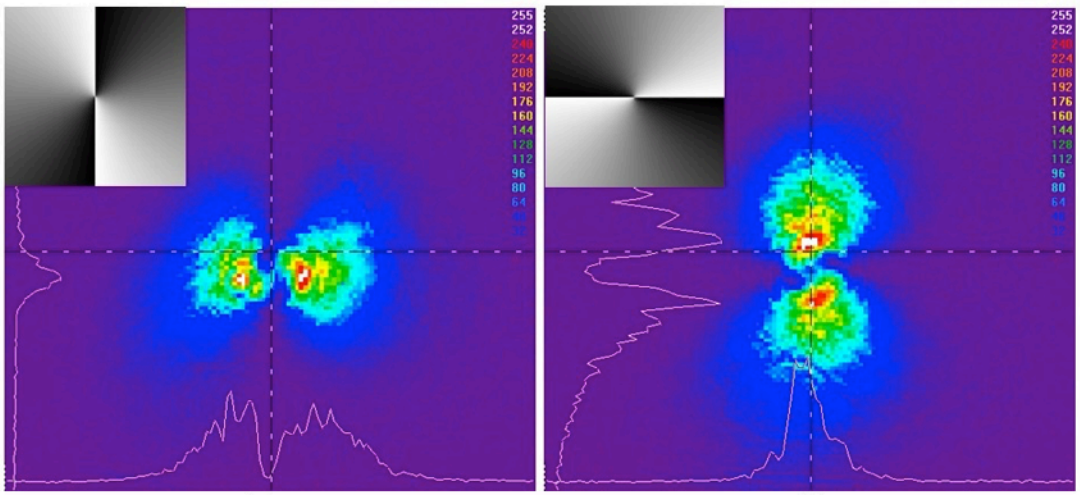

Figure 4.5 *Far field beam profile produced by a (a) radially and (b) azimuthally polarized vortex beams after transmission through a polarizing filter with its transmission axis oriented horizontally. The top left corner CGHs are vortex phase delays applied on SLM2 to produce radial (a) and azimuthal (b) polarization.*

The resulting collimated beam was focused onto the beam profiler with a used low NA lens (focal length 400mm) and analysed with the beam profiler. Figure 4.5 shows the far field beam profile of radially (Fig. 4.5 a) and azimuthally (Fig. 4.5 b) polarized beams after transmission through a polarizer, which are in line with [32,37]. Note that the profiles have a curved S-shaped geometry near the centre, which is due to the vortex wavefront structures of these beams.

To further analyse the intensity profiles and polarization states at the focal plane, focal spots were marked on the surface of stainless steel sample. Optical micrographs and magnified SEM images in Figure 4.6 show the resulting focal spots. The geometry of the laser spots, with deeper ablation in the centre than around the edges, was found to be consistent with a near Gaussian type of intensity profile (albeit with some distortions due to steps in the vortex phase-maps). Due to the near Gaussian beam intensity profile, LIPSS are clearer on the edges of the spots due to the lower fluence, whereas the LIPSS on the centre of the spots are less clear due to over exposure at higher fluence. The depth of the centre was measured to be ~2 μm using optical focus of a Nikon digital microscope. The arrows in Figure 4.6 indicate the incident local polarization directions, which is perpendicular to the direction of the local LIPSS. By analysing the collimated and focused beam, it is clear that the structured beams are radially or azimuthally polarized with a vortex wavefront which converts the ring mode to near Gaussian beam distribution in the far field [173,213,234].

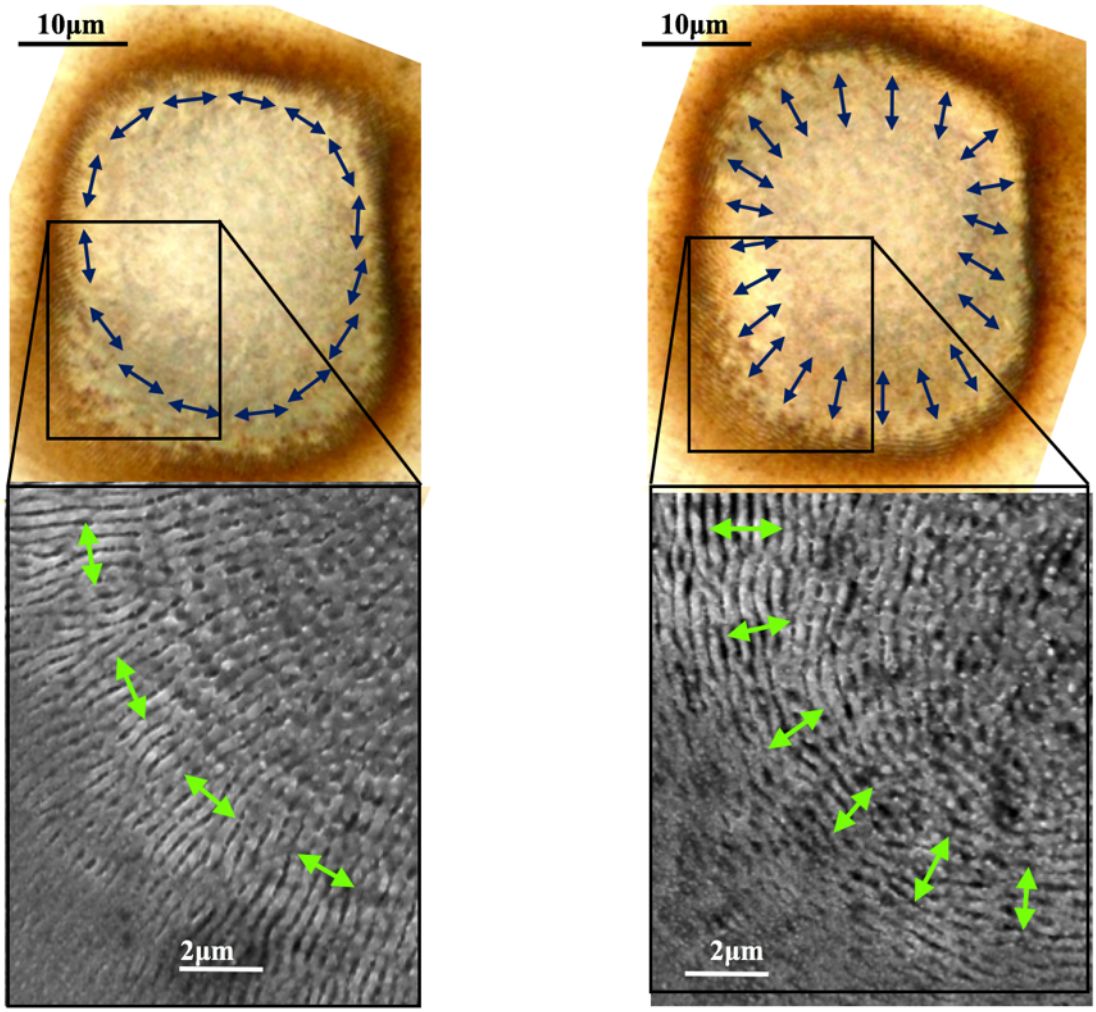

Figure 4.6 *Optical micrographs (top) and SEM images (magnified regions at the bottom) showing the focal spots produced on the surface of a polished steel sample with ~100 pulses at 3 µJ/pulse, with the SLMs producing a vortex beam (orbital angular momentum l=1) polarized radially (a) and azimuthally (b). The arrows indicate the polarization fields, which are orthogonal to the LIPSS direction.*

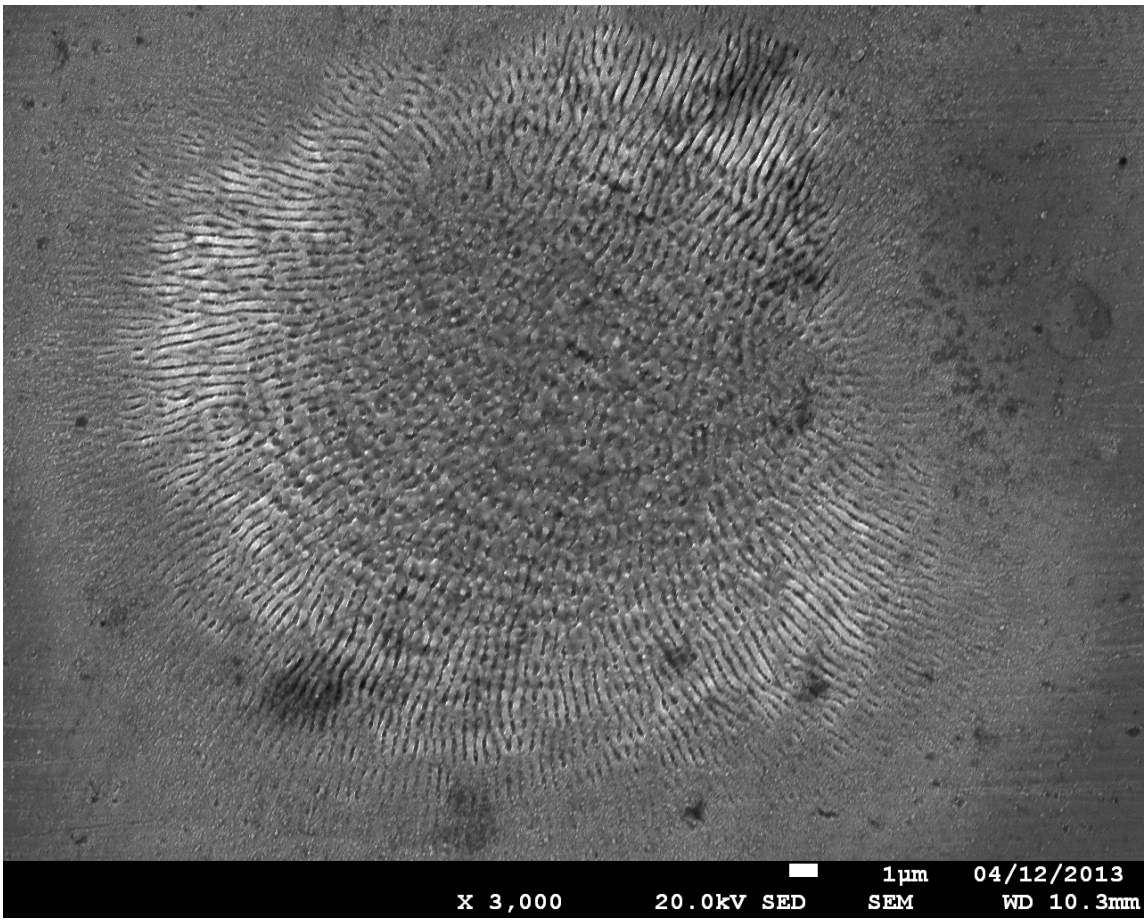

Figure 4.7 SEM images of the spots produced on the surface of a polished steel sample with ~60 pulses at 3 μJ/pulse, with the SLMs producing a vortex beam (orbital angular momentum l=1) polarized azimuthally.

It can be seen from figure 4.7 that the LIPSS along the edge of the spot is well defined. The overall LIPSS direction on the edge of the spot is radially oriented. However, the LIPSS in the center of the spot is hard to define, especially the very center of the spot. According to a model by Allegre [213], the polarization in the center of the spot that produced on the focal plane is circularly polarized and the polarization away from the center is azimuthally oriented. The model also pointed out that the electric vectors within the laser beam with a radial or azimuthal polarization and vortex wavefront do not have a same amplitude at the same time. Figure 4.8 shows the amplitude changes over the time

with an azimuthally polarized vortex beam (the length of the arrow refers to the amplitude of the electric vectors). Since the amplitude of the localized electric vectors of the radial/azimuthal polarized beam with vortex wavefront varies overtime, the overall orientation of the LIPSS between the center and edge of the produced spot can be difficult to defined.

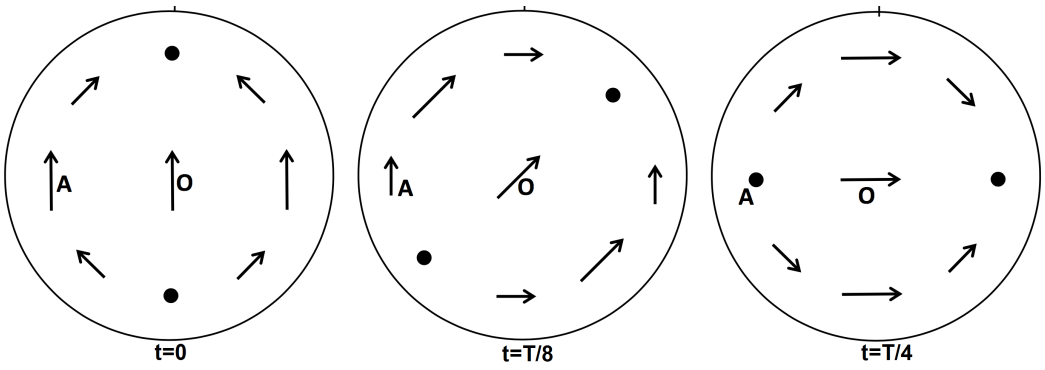

Figure 4.8 *Schematics of the profile of a azimuthally polarized beam with vortex phase pitch of 2π (topological charge of one), showing the amplitude of the electric field vectors varies over time.*

4.4.2 Radially and azimuthally polarized beam with planar wavefront

To produce radially and azimuthal polarized beam with planar wavefront, the only experimental setup change to the above setup is the change of CGH on SLM1. A vortex phase delay of 2π to 0 was applied on the SLM1, which generates a state with negative orbital angular momentum with topological charge of $m_1=-1$. Since SLM2 has a positive helical phase added, inducing a positive orbital angular momentum with topological charge of $m_2=1$, the two opposite orbital angular momenta cancelled each other, hence the overall orbital angular momentum after the SLM2 is $m=m_1+m_2=0$, in which case the laser beam now has a planar wavefront.

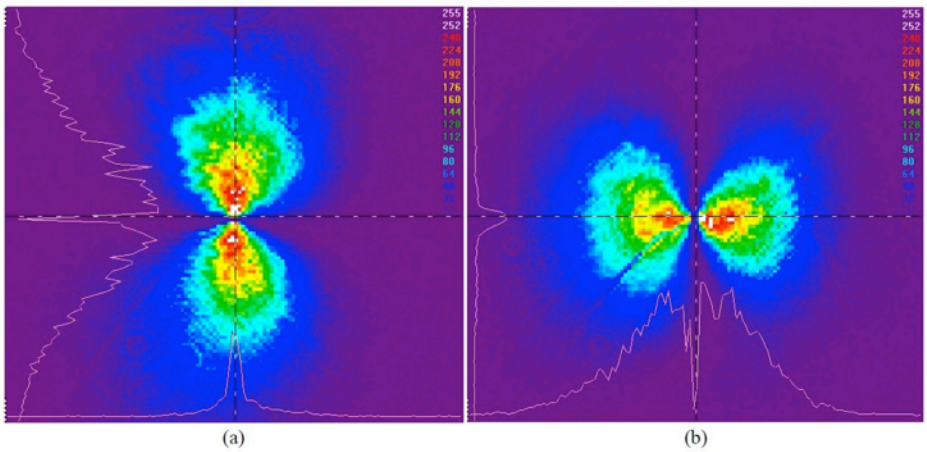

Figure 4.9 *Intensity profiles of a focused (a) radially or (b) azimuthally polarized beam with planar wavefront, after transmission through a polarizing filter with its transmission axis oriented vertically.*

The structured beams were focused and analysed after the SLM converter by transmission through lens1 and a polarizer with its transmission axis placed at horizontal direction. The beam profiles, shown in Figure 4.9, have the typical geometry associated with radially and azimuthally polarized beams [165-168,170,173,234]. Note that, compared to the beam profile of radially and azimuthally polarized vortex beam, there is no S-shaped structure near the centre of the beam, which has only been observed with radially and azimuthally polarized vortex beam [234].

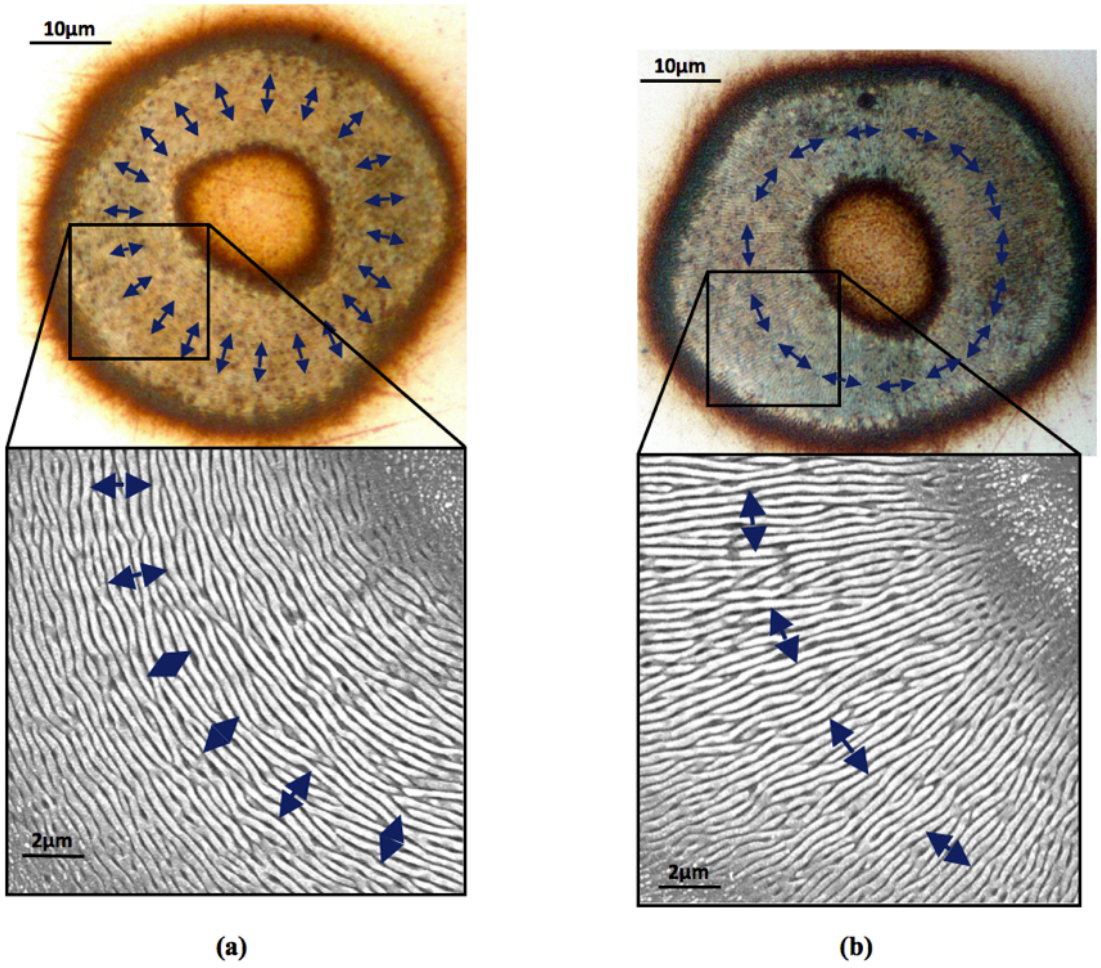

Figure 4.10 *Optical micrographs (top) and SEM images (magnified regions at the bottom) showing the focal ablation spots produced on the surface of a polished steel sample with ~100 pulses at 3 µJ/pulse, with the SLMs producing planar wavefront beams polarized radial (a) and azimuthally (b). The blue arrows indicate the polarization fields and are orthogonal to the LIPSS. Since all the electric field vectors cancel each other out on the optical axis, there is no ablation in the centre.*

The structured beams were then used to produce spots on the stainless steel sample surface. Figure 4.10 shows the optical microscope images of observed surface micro-structures after laser exposure. The produced focal spots had a ring-shaped structure which is consistent with that expected when focusing a radially and azimuthally polarized planar wavefront beams with a low NA lens [32,173,234]. In addition, LIPSS have formed within the laser spots, developing in a direction perpendicular to that of the incident local

polarization vector (see SEM micrographs showing magnified areas in Figure 4.10). The high uniformity of LIPSS within the laser spots confirms that the state of polarization was maintained with a high fidelity at the focal plane.

Although the depth of the LIPSS produce was not measure in this experiment, the literature indicates that the depth of a well-defined LIPSS is normally ~100 μm for metals [235], semi-conductors [236] and polymers [237]. Moreover, the depth of the LIPSS was found to be dependent on the laser fluence [238] and pulse overlaps [236]. It was observed that too low and too high fluence would produce less deep LIPSSs compared to the LIPSSs produced with a properly chosen laser fluence [238]. With the increase of pulse overlap, the depth of the LIPSS was found to be deeper. However, too many pulse overlap would reduce the depth of the LIPSS [236]. As stated in the literature (section 2.4.3), the uniformity of the LIPSS that produced with a static laser beam is dependent on the laser fluence, pulse overlaps, and the surface roughness. The LIPSS produced in this experiment is not as uniform as wanted, which is most likely due to the nonuniform energy distribution of the ring beam. Different pulse overlaps were tried when carrying out this experiment, one of the best results obtained is showing in figure 4.10. It can be seen that there were minor scratches across the laser ablated spot, hence the surface roughness has also affected the uniformity of the LIPSS.

4.5 Diffractive parallel processing with structured beams

To further illustrate the simultaneous control of wavefront and polarization, the SLM converter was configured to produce multiple diffractive first-order beams with arbitrary polarization states and controllable wavefront.

4.5.1 Parallel diffractive beams with vortex wavefront

As a first case study, a CGH designed to produce three first order focal spots (Figure 4.11(a)) was combined with a vortex phase CGH (Figure 4.11 (b)) and addressed on SLM1, which will diffract the incident near Gaussian beam into three diffractive first order beams all with vortex wavefront. The SLM2 in the SLM converter induces no phase modulation, which simply acts a mirror. The structured laser beams were used for parallel marking spots on stainless steel sample, as shown in Figure 4.11 (c). All three diffractive first order spots have ring shaped beam profile, which is expected to produce with a vortex laser beam. The polarization in this case is unmodified, which remains linear for all three diffractive beams.

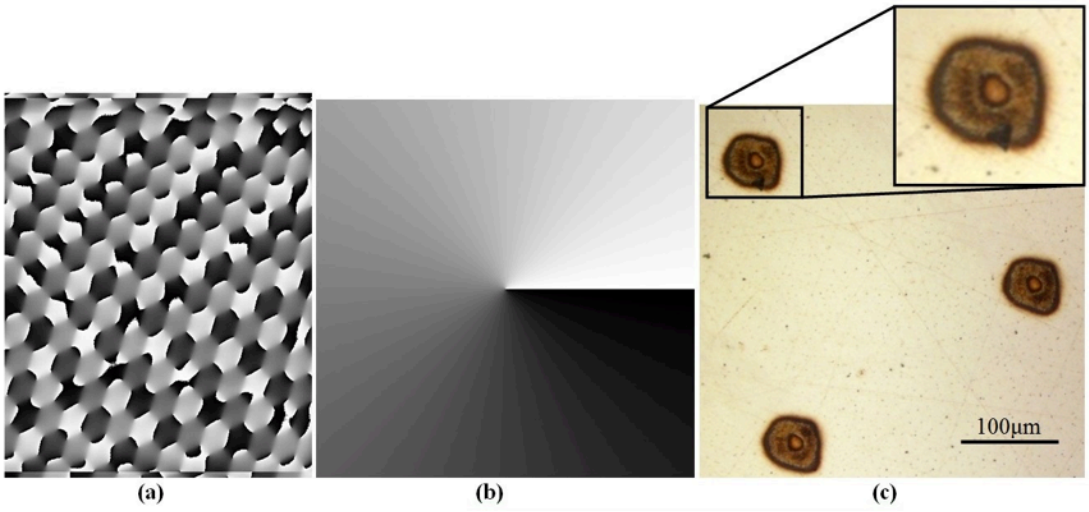

Figure 4.11 *(a) CGH induced on SLM1 to produce three first order diffractive spots, (b) vortex phase CGH address on SLM1, in addition to the diffractive CGH, to produce vortex wavefront, (c) optical micrograph showing the three spots produced simultaneously with a vortex wavefront.*

4.5.2 Parallel diffractive beams with radial or azimuthal polarization and vortex wavefront

The SLM converter was configured to generate parallel diffractive beams with radial or azimuthal polarization with vortex wavefront. The SLM2 in this case was addressed by a 0 to 4π vortex CGH as demonstrated on top-left corners in Figure 4.12 (a) or (b) for the generation of radial or azimuthal polarization. SLM1 was addressed with a CGH used for generating three diffractive beams (as shown in Figure 4.11 (a)). Thus, SLM1 is only used for generating three diffractive spots all with Gaussian beam profile while SLM2 tailors the incident linear polarization to radial or azimuthal polarization, which also induces a residual vortex wavefront. The structured collimated beam was analysed after the SLM converter with a polarizer with its transmission axis oriented horizontally. The beam profile obtained is demonstrated in Figure 4.12. As expected, diffractive fringes produced by the three first order beams superimpose on the beam profiles produced by the radial or azimuthal polarization fields.

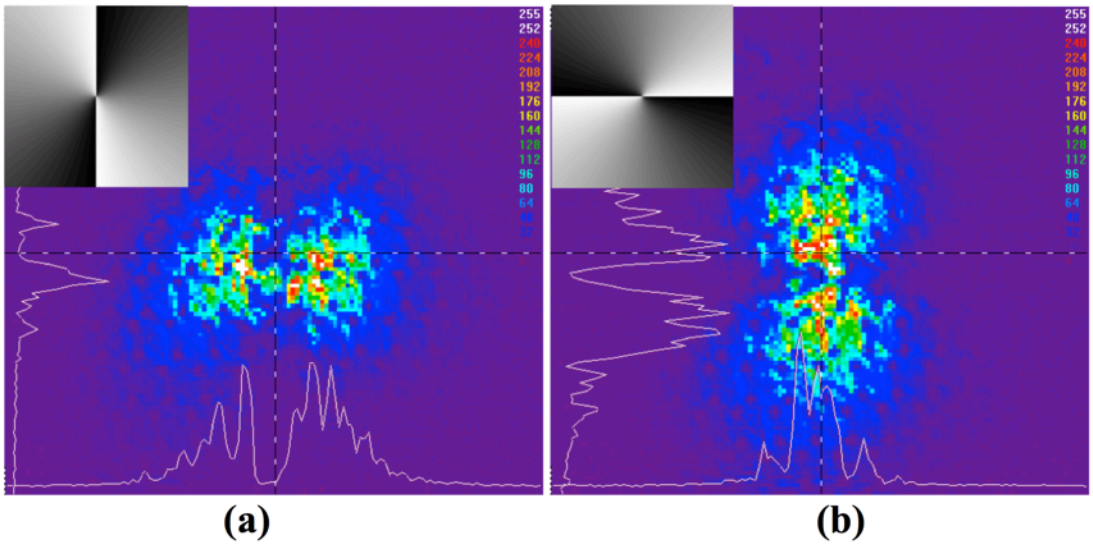

Figure 4.12 *Near field beam profiles produced by (a) three first order diffractive radially polarized beams and (b) three first order diffractive azimuthally polarized beams, after transmission through a polarizer with its transmission axis oriented horizontally. The vortex phase CGHs, which are addressed on SLM2, are shown in the top-left inlays.*

The structured beam was then focused to produce parallel spots on stainless steel surface, as shown in Figure 4.13 (a). LIPSS can be observed on the edge of the spots but not in the center of each spot, shown in Figure 4.13 (b) and (c), which is in the same way as with the single beam in section 4.4.1 above. The LIPSS produced with parallel diffractive radially and azimuthally polarized beams are similar to those produced with single radial or azimuthal polarized beam. However, the discrete phase modulation and pixel structure of SLMs has induced some residual distortion, which affected the polarization purity at the focal plane. This can be seen from the slight irregularity of LIPSS orientations on the edge of produced spots.

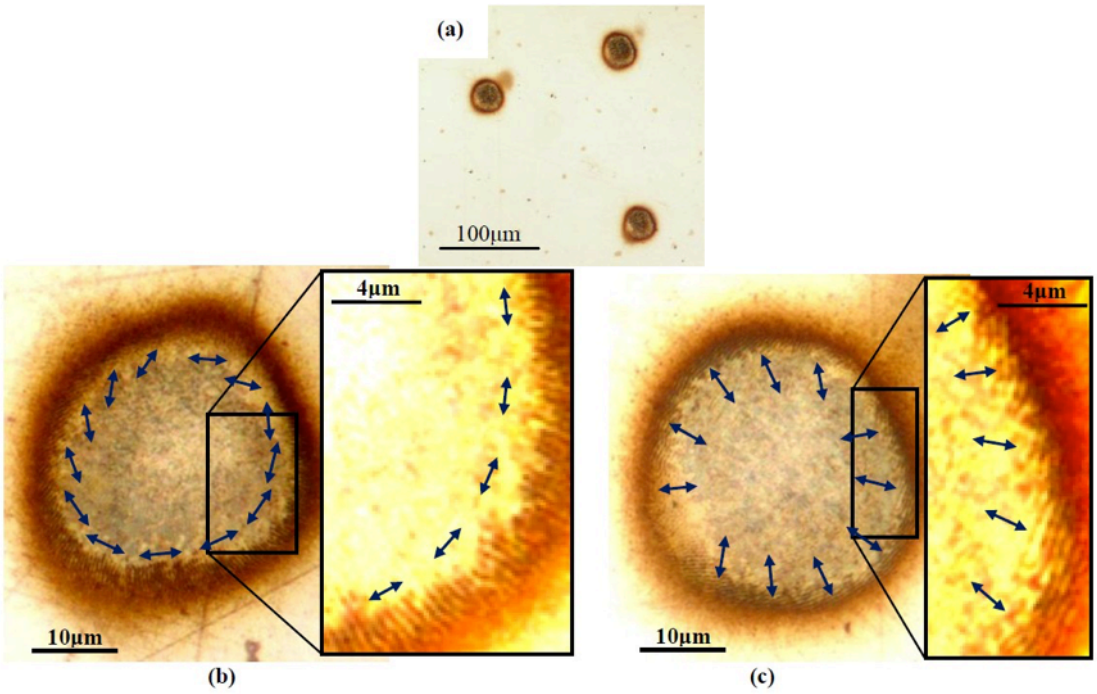

Figure 4.13 *(a) Optical micrograph showing three first order diffractive laser spots with radial or azimuthal polarization marked at the focal plane, (b) A magnification of one of three focal spots produced with a radially polarized beam, (c) One of three focal spots produced with an azimuthally polarized beam. The blue arrows indicate the direction of polarization, which is perpendicular to the LIPSS.*

4.5.3 Parallel diffractive beams with radial or azimuthal polarization and planar wavefront

As in the case with single beam radial or azimuthal polarization and planar wavefront, a compensation vortex wavefront with opposite direction to the residual vortex induced by SLM2 was produced on SLM1. In this case, SLM1 was addressed with a CGH for generating three diffractive vortex wavefront beams, as above, whilst SLM2 was addressed with 0 to 4π vortex phase CGHs demonstrated in Figure 4.12 (a) and (b) to generate radial and azimuthal polarization respectively. The structured beam was then focused to mark spots on a stainless steel sample. Optical micrographs in Figure 4.14 left column show sets of three spots imprinted simultaneously on the surface of the sample.

The three spots produced have an excellent ring shape and within each spot, LIPSS were produced with a radial or azimuthal orientation in the same way as with the single beams in Section 4.4.2 above (Figure 4.10). This confirms that multiple first-order laser spots with either a radial or azimuthal polarization are produced with a high fidelity at the focal plane.

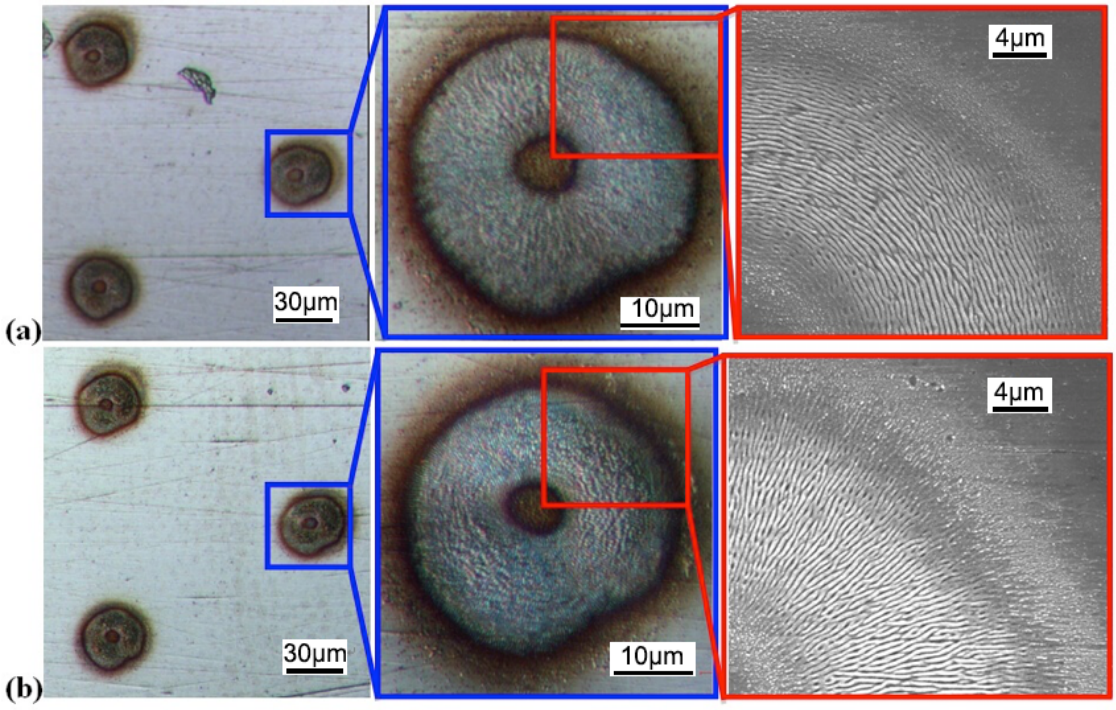

Figure 4.14 *Optical micrographs (left) and SEM images (magnified regions on the right) showing the three first-order focal spots produced simultaneously on the surface of the steel sample, with incident radially (a) or azimuthally (b) polarized, diffractive parallel beams. In each case, the orientation of LIPSS confirms the state of polarization unambiguously.*

Finally, the SLM converter was configured to produce 10 diffractive beams all with azimuthal polarization and planar wavefront. The structured beam was focused to mark spots on stainless steel sample and the results can be seen in Figure 4.15. All the spots ablated on the sample have a uniform ring shape. LIPSS in the magnified optical micrographs confirm the azimuthal polarization states. Notice the debris between the

spots, which is an interesting phenomenon only observed on spots produced with diffractive beams.

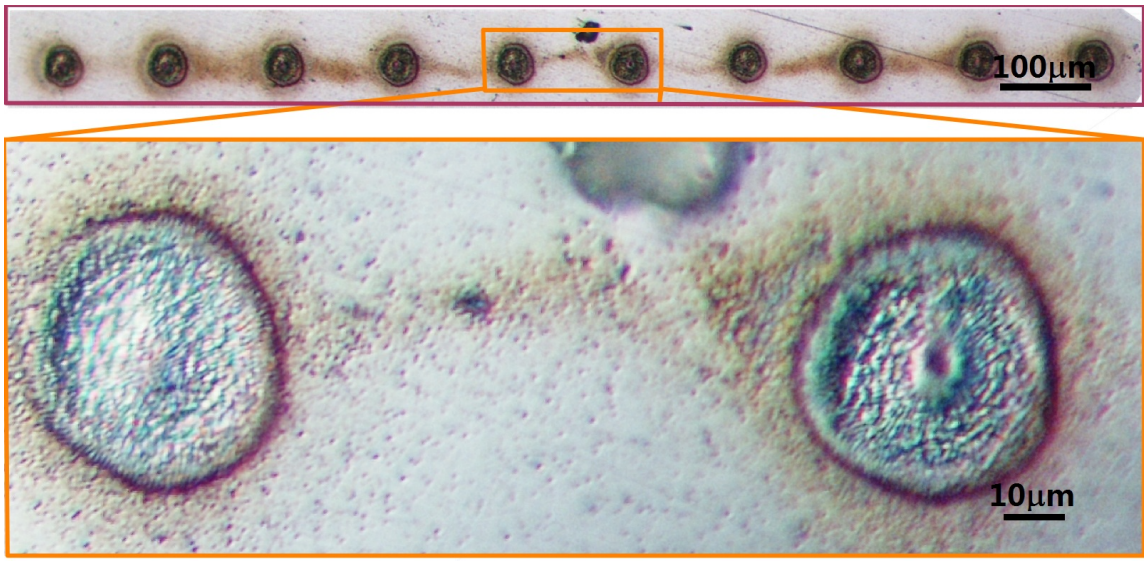

Figure 4.15 *Optical micrograph image of 10 diffractive spots produced on stainless steel sample surface. All 10 diffractive spots are azimuthally polarized with planar wavefront, which can be confirmed by the ring shape and the LIPSS in the spot (Lower magnified optical micrograph image).*

4.5.4 Interesting debris pattern observed only on diffractive multi-beam processing

The debris generated by short pulse laser ablation on metal or semiconductor substrate are nanoparticles [239 - 241]. The unique debris pattern that is generated by multiple diffractive beam ablation has never been reported to the best of author's acknowledge. To confirm the pattern was not a coincident and to try to understand the mechanism of the pattern formation, a number of experiments have been carried out. The first experiment was to observe the effects of the diffractive multi-beams' relative location on the debris pattern formation. 7 diffractive spots focused on the sample to form a circle, or line or rectangular shapes and then used to ablated a highly polished SS sample. It has been found

that all the the debris patterns generated in this cases are trying to connect with the neighbouring ablation spot, see figure 4.16 (a). The experiments were then repeated, using a single beam to ablate 7 holes on SS with a similar spot location, a circular, a line and a rectangular. The results shown that the neighboured debris pattern are independent to each other in all three cases. Figure 4.16 (a) shows the 7 spots produced with diffractive multiple laser beams, the debris outside the holes are trying to connect to the neighbouring spots, especially towards the spot in the centre. As a comparison, a similar spots arrangement was reproduced one by one with single beam, the debris outside each hole are independent of the other debris, as shown in figure 4.16 (b).

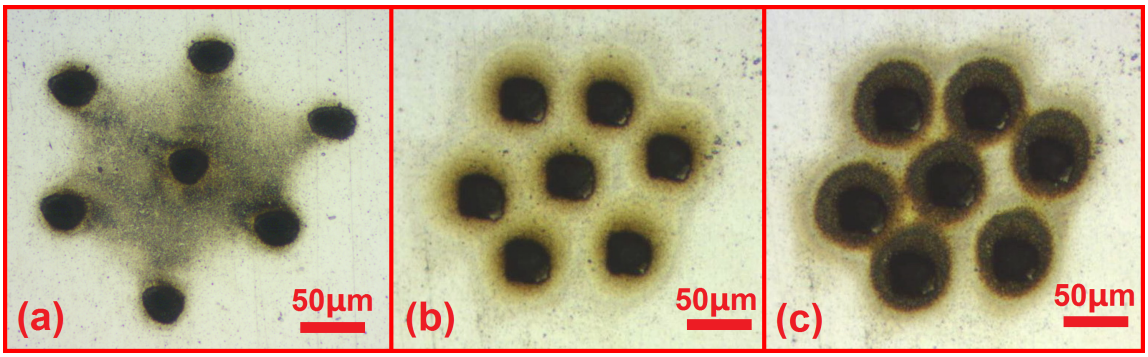

Figure 4.16 *(a) optical micrograph image of spots produced with diffractive multi-beams, the neighboured debris are trying to connect to each other. (b) optical image of spots produced by single beam ablation. The 7 spots were ablated one by one. It is obvious that the debris outside each spot are independent. When apply some water vapour on the ablated spots, the debris becomes bigger, shown on (c).*

From the comparison experiments, the unique debris patterns have been secured to have some relationship with the diffractive laser beams. A distinctive difference between the diffractive multi-spots ablation and the single spot ablation one by one is the time difference, one is simultaneously generating all the debris and the other one has a time difference when producing the debris. One possibility is that the plasma could be the source that affected the debris location on the sample. To test this, another experiment was

carried out a using strong magnet to affect the plasma. A strong NdFeB magnet with a magnetic flux density B ~ 1.2 T was placed on the sample at different places near the laser ablation area during the processing. However, there was no difference compared to the results produced without the magnet. Another interesting phenomena was observed during the processing. One laser processed sample was accidently exposed to a tiny amount of water vapour, the debris near the laser ablated spots becomes significantly bigger, as shown on figure 4.16 (c). Repeat experiments were carried out and confirmed that water vapour takes the debris inside the laser ablated hole to the outside of the spot. This might be caused by the conductivity of water vapour if we assuming the debris is electrostatic. Since this experiment is not the major research direction for the thesis, there was no further experiments carried out. However, this interesting phenomena is worth further exploration for the benefit of understanding more about diffractive multi-beam ablation, debris and potentially plasmas.

4.6 Summary

This chapter demonstrated the SLM converter enables simultaneous control over the phase and polarization of the incident ultrafast laser beam. Single beam with desirable polarization, including linear, radial and azimuthal polarization, and desirable wavefront, i.e. vortex wavefront and planar wavefront, were generated with the SLM converter and analysed in the near and far field. Multiple diffractive beams with radial or azimuthal polarization and vortex or planar wavefront were then produced and applied for surface marking. LIPSS produced on the stainless steel sample surface were used to visualize the

laser polarization state on or near the focal plane, confirming the desired polarization states unambiguously.

Chapter 5 - Dynamic modulation of polarization for real-time control of ultrafast laser-material interaction

5.1 Introduction

Recent years have witnessed a growing interest in polarization modulation as a means to control linear or nonlinear laser-material interactions. For instance, high intensity non-linear phenomena, ultrafast laser surface patterning, laser cutting and drilling are all polarization sensitive. Several polarization control methods have been developed over the years which can be categorized as dynamic or static. Static methods for polarization modification include waveplates, segmented spatially variant retardation plates [161,163], birefringent plate [35-37], and dielectric subwavelength gratings [171]. Dynamic methods typically involve modifying the direction of the incident linear polarization with time. For example, continuous rotating waveplate with a motor or adopting a liquid-crystal polarization rotator in the beam path, the dynamic rotation of linear polarization greatly improved the quality of laser drilling [32,48-50].

This chapter introduces dynamic control of spatially structured polarization field in a picosecond pulse laser microprocessing system, using two phase-only SLMs in series. As a proof of concept, the polarization was modulated at a speed of 12.5 Hz, switching between four distinct states: linear horizontal and vertical, radial and azimuthal, whilst synchronized beam scanning on the surface of a highly polished steel sample. The dynamic polarization modulation was analyzed through surface plasmon nanostructuring of LIPSS within the exposed regions of the sample. Symmetric surface patterns on a steel sample were produced, confirming the polarization switching and the synchronization.

5.2 Experiment setup and procedure

The schematic of the experimental setup is shown in Figure 5.1. The laser source is a Coherent Talisker (Talisker Ultra 1064-16) with a pulse width of 10 ps, operating at 532 nm output, M^2 <1.3, maximum output power of 8 W, 200 KHz maximum repetition rate and horizontal linear polarization output. A telescope (Jenoptic) with $\times 3$ magnification was used to expand the laser output beam. A pair of Hamamatsu phase only SLMs (Hamamatsu X10468-04 PAL-SLM) and a pair of zero-order waveplates were used. SLM1 marked in Figure 5.1 was used to shape the incident Gaussian beam intensity to ring shaped beam intensity. SLM2 combined with two waveplates were used for dynamic modulation of incident horizontal linear polarization. A 4f imaging system was placed after SLM2 to re-image the surface of SLM2 to the input aperture of a galvo scanner (Nutfield-XLR8-14). At the galvo output, the laser beam was focused with a flat field f-theta lens (f=250 mm, Linos). For processing experiments, samples were mounted on a precise 3-axis (x, y, z) motion control system (A3200 Ndrive system, Aerotech) for precise location of the focal plane. The motion control system, including the Galvo and the stage, SLM2 and the laser were all synchronized. Details of the synchronization can be found in section 3.5.1 in Chapter 3.

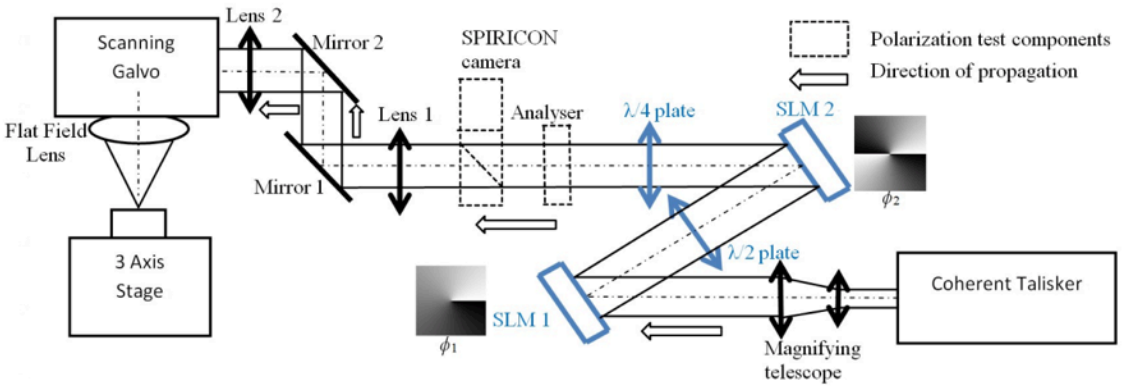

Figure 5.1 *Schematic of the experimental setup. Spiricon camera and the polarizer draw with dotted line were removed when the microprocessing tests were carried out.*

Four distinct optical field configurations were used for the experiment: horizontal and vertical linear polarization, radial and azimuthal polarization, as summarized in Figure 5.2, all with a ring shaped intensity distribution. SLM1 addressed with a static CGH with phase modulation $\phi_1(x,y)$, was used to convert the incident Gaussian beam intensity to ring shaped beam intensity, in which case the ring spots and LIPSS structures inside the spots are easier to visualize. On the other hand, SLM 2 was addressed sequentially with four different CGHs (phase modulation $\phi_2(x,y)$). Combined with a pair of waveplates and synchronized with the motion system and the laser, SLM2 enables modulating the incident horizontal linear polarization to a desired polarization state on the surface. Noted that $\phi_1(x,y)$ applied on SLM1 induces a vortex wavefront. When the output polarization is linear (either horizontal or vertical), the structured beam has a vortex wavefront with linear polarization. However, when the output polarization is radial or azimuthal, a negative vortex wavefront is created by $\phi_2(x,y)$ applied on SLM2, which compensates the vortex wavefront induced by SLM1, resulting in a planar wavefront with radial or azimuthal polarization. The structured collimated beam was analysed by passing

through a polarizer with its transmission axis placed horizontal and an intensity profiler (Spiricon camera, model SP620U), as show in Figure 5.2. Hence the vertical linearly polarized beam was completely filtered by the polarizer, as shown in Figure 5.2.

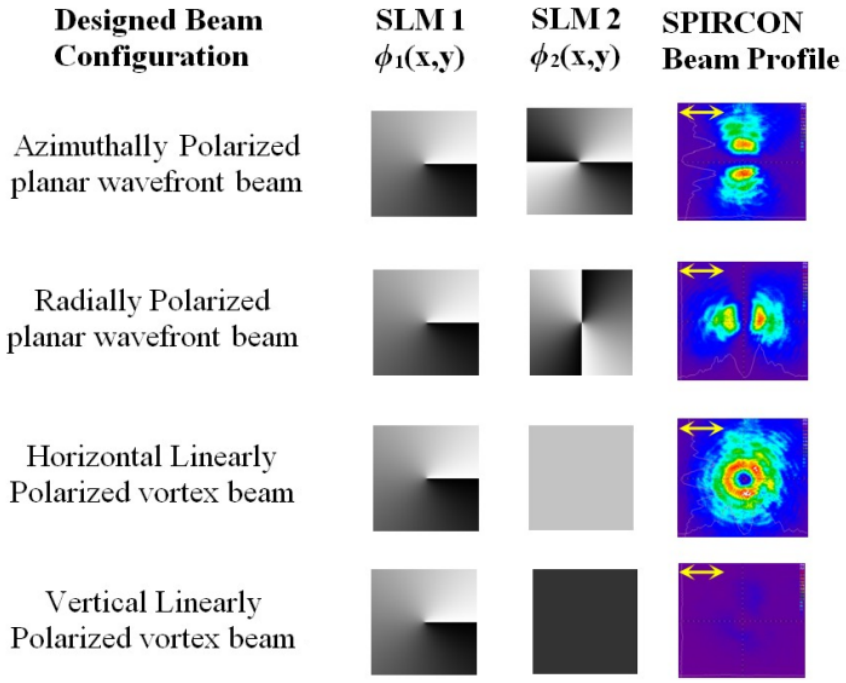

Figure 5.2 *Summary of four distinct optical field configurations. $\phi_1(x, y)$ was statically applied on SLM1 while four different $\phi_2(x, y)$ were dynamically addressed on SLM2. The arrows indicate the transmission axis of the polarizer (horizontal) and all the analysed beams are near field collimated beams. Noted that the vertical linear polarized beam was completely blocked by the polarizer.*

The structured beams were used to microprocess polished stainless steel samples with a fluence near the ablation threshold of steel, which leads to the formation of wavelength-sized LIPSS inside the spots produced on sample. The LIPSS direction inside the spots develops orthogonal to the local polarization directions [4], was used here for visualizing the polarization state focused near the focal plane. Hence, by tailoring the incident polarization state statically or dynamically, one can precisely control the LIPSS development, leading to high speed large area micron/submicron feature processing.

For all the micro-machining tests, the laser output was attenuated to produce a pulse energy of 3 μJ/pulse (fluence F~0.3 J/cm^2 at focal plane) and focused on the sample near normal incidence. An exposure with 100 laser pulses was used to produce discrete spots on the sample surface with 5 kHz laser output repetition rate. For continuous scanned lines, the beam was scanned at 2.5 mm/s, leading to a pulse overlap of ~100 so that exposure was the same. After laser ablation, the specimens are imaged with an optical microscope and SEM.

The sample used in the experiment was stainless steel – AISI 316L (Fe/Cr18/Ni10/Mo 3) 2 mm thick foil, purchased from Goodfellow Cambridge Limited. Both sides of the sample have been mirror polished. The average surface roughness has been measured with the WYKO, Ra = 18±3 nm. The original sample was 100×100 mm, which was cut into 50×50 mm samples. A rubber glove has been used when handling the sample to avoid the contamination of the sample. The sample was ultrasonic bathed with acetone (99.99%) before and after laser processing.

5.3 Discrete patterns of laser spots with polarization control

As a first case study, the experimental setup was configured to produce a discrete pattern of laser spots, where the overall geometry is designed to represent four letters “LLEC”, initials for Lairdside Laser Engineering Centre. Each letter was produced sequentially with a distinct state of polarization from horizontal linear, vertical linear, radial to azimuthal polarization. Since each spot was produced with 100 pulses at 5 kHz laser repetition rate and the whole pattern contained 52 spots, the time taken was 4 seconds and the polarization states were changed 4 times, corresponding to a polarization switch

frequency of ~1 Hz, ~1 second per letter. The time taken for galvo motion to desired spot positions was neglectable.

After laser processing, the specimen was analyzed with an optical microscope and SEM. As showing in Figure 5.3, the overall pattern (center image) shows the "LLEC" consisting of discrete spots. The magnified microscope images of four spots displayed on the sides of the center image shows that all the spots produced on the sample have the expected ring shape. To visualize the LIPSS inside the spots, SEM images were taken and results shown in Figure 5.3 top and bottom. The geometry of LIPSS developed within the 4 different sets of spots is consistent with that expected when processing with horizontal linear, vertical linear, radial and azimuthal polarization, in line with [4,56,124,242]. The LIPSS produced has a periodicity of Λ~0.5 μm, which is similar to the incident irradiation wavelength, 532 nm, indicating the LIPSS type is LSFL. Orientations of LSFL formed on strong absorbing materials such as metals or semiconductors are observed perpendicular to the incident linear polarization direction [4]. The red arrows in Figure 5.3 top and bottom SEM images therefore represent the localized electric field vectors, which is perpendicular to the direction of localized LIPSS.

Note that the micro-machined spots do show some residual distortion in their shape due to the resolution limit of the SLMs, where the pixel pitch (20 μm) and discrete phase modulation induced some discontinuity in the produced wavefronts which affected the focal intensity distributions. More recent SLMs, for example, produced by Holoeye Photonics AG [243] have reduced the pixel size pitch to 8 μm, which could greatly reduce the distortion caused by the current resolution limitation.

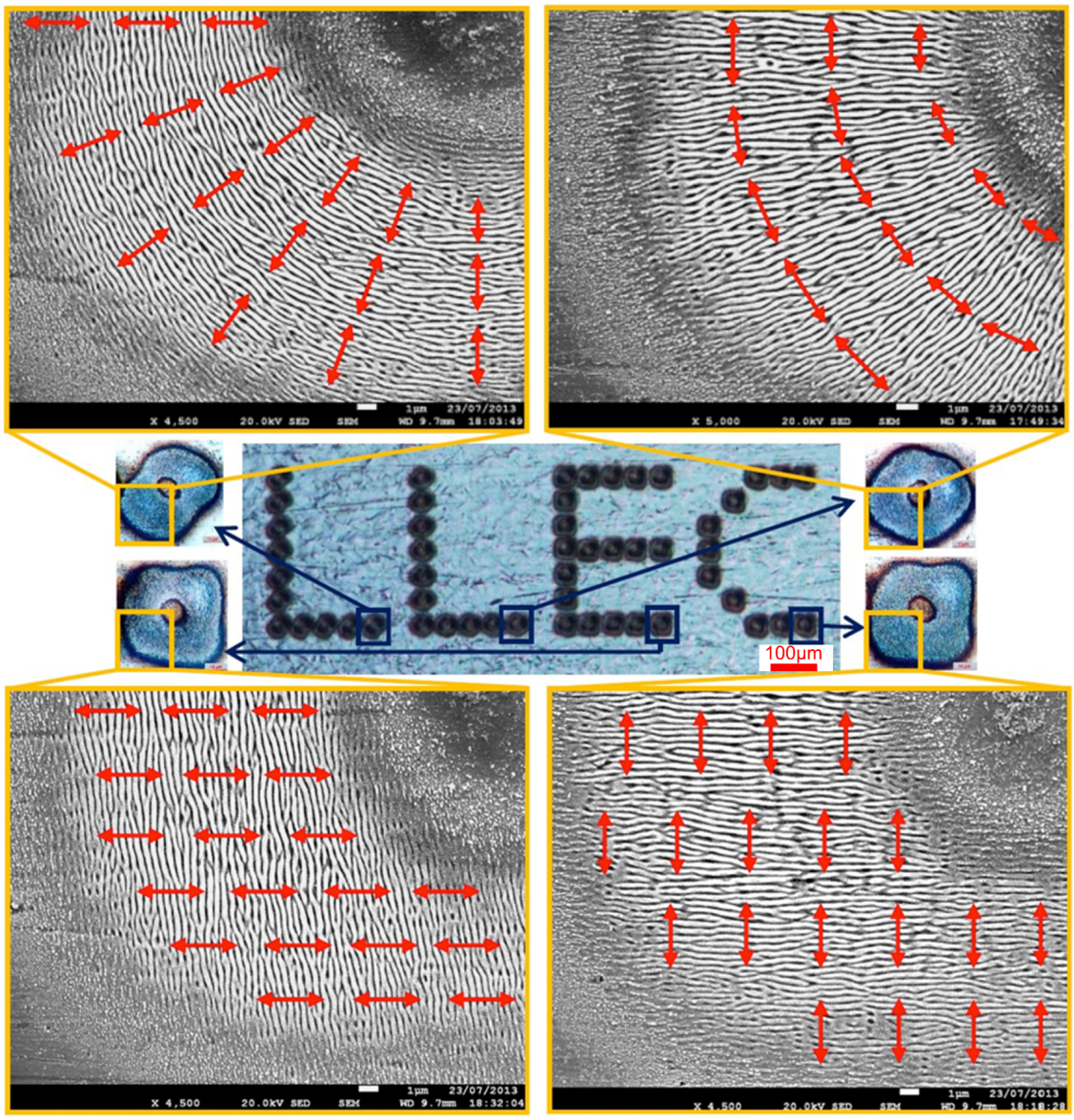

Figure 5.3 *Optical image (centre) showing the overall pattern produced on the sample, consisting of four distinct sets of spots with each set using a different type of polarization state; The images on the sides of the centre image are magnified microscope images, showing all the spots produced on the sample have a ring shape, confirming that the incident beam intensity profile is ring shape; Top and bottom images are SEM, showing the LIPSS developed inside the spots have a pitch of Λ~0.5 μm. The red arrows indicate the localized electric field vectors.*

LIPSS produced on the sample enabled the visualization of polarization state near the focal plane. For large area processing, the 4 polarization states could be observed by low angle white light diffraction from the LIPSS. As shown in Figure 5.4, a white light

luminescent source was used to illuminate the specimen at grazing incident. As the LIPSS has a periodicity Λ~0.5 μm, they act as a surface grating, high resolution SEM image is shown in Figure 5.5. For LIPSS with direction perpendicular to the incident white light, blue light is diffracted to the observer. As the periodicity of the LIPSS is around 0.5 μm, it is easier to diffract light with wavelength λ<500 nm and blue light is the easiest to obtain by this method. However, for LIPSS with direction parallel or at an angle to the incident white light, the intensity reduced considerably, allowing one to differentiate the polarization states.

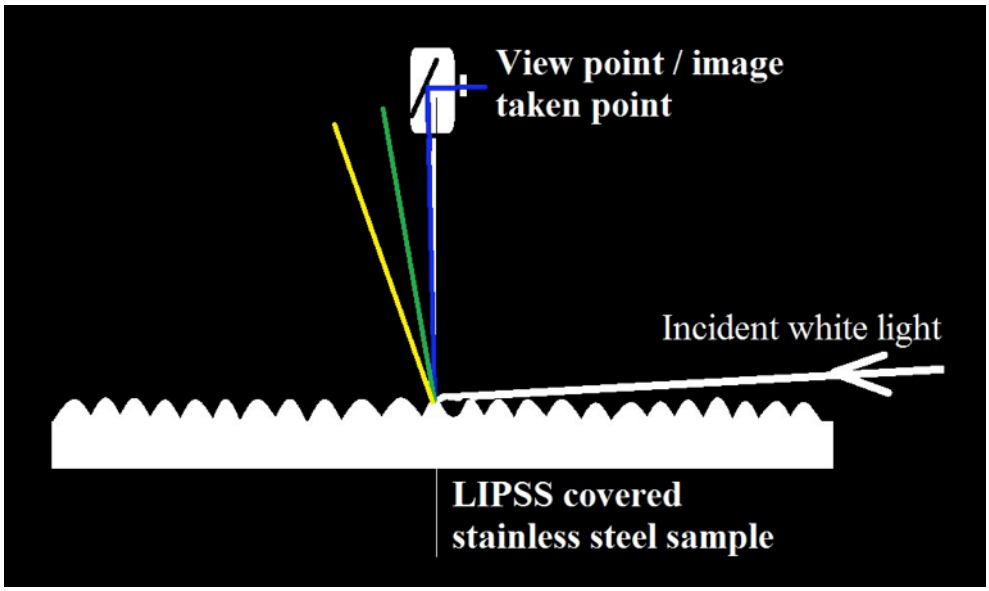

Figure 5.4 *Schematic of the simplified method for visualizing the LIPSS directions on the sample. For LIPSS direction perpendicular to the incident white light, observer can see blue light on the view point.*

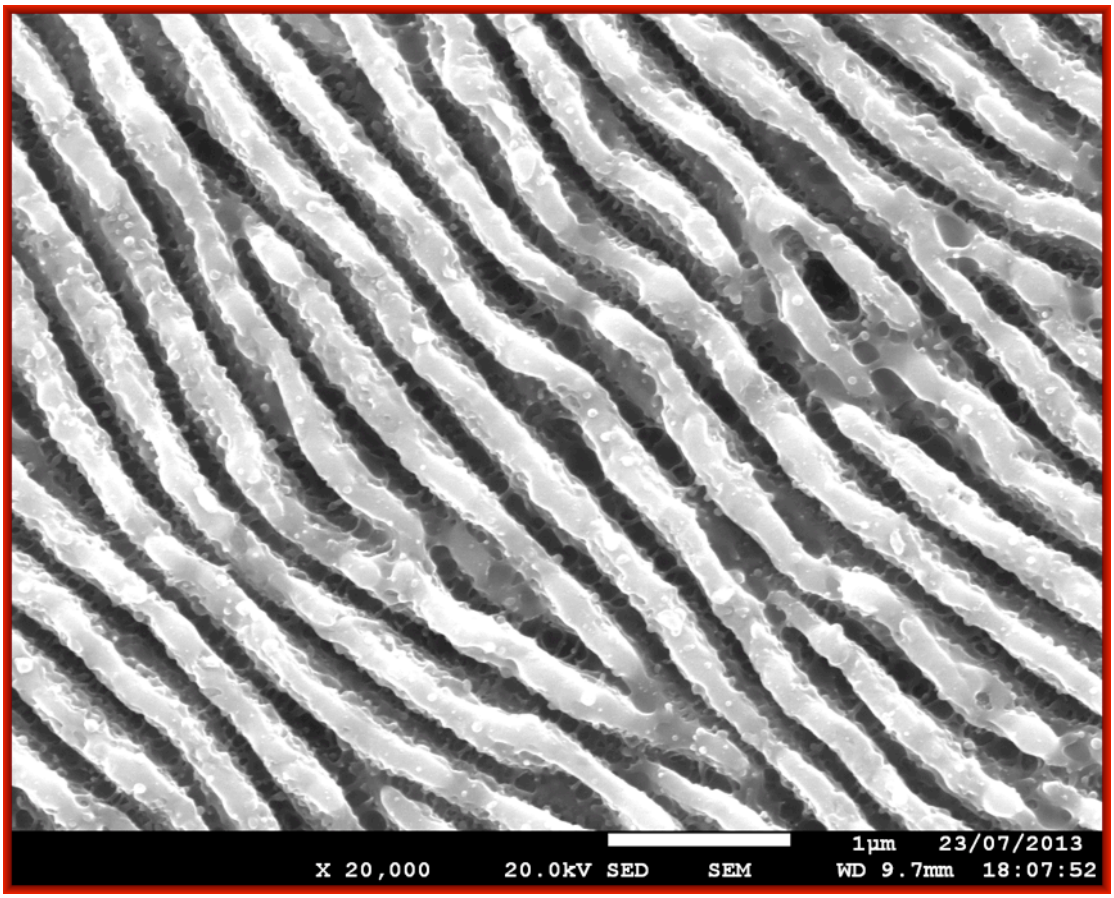

Figure 5.5 *High resolution SEM image of LIPSS produced on a stainless steel sample exposed at 532 nm with 10 ps pulses. Due to the periodicity and the geometry of LIPSS, these act as a surface grating.*

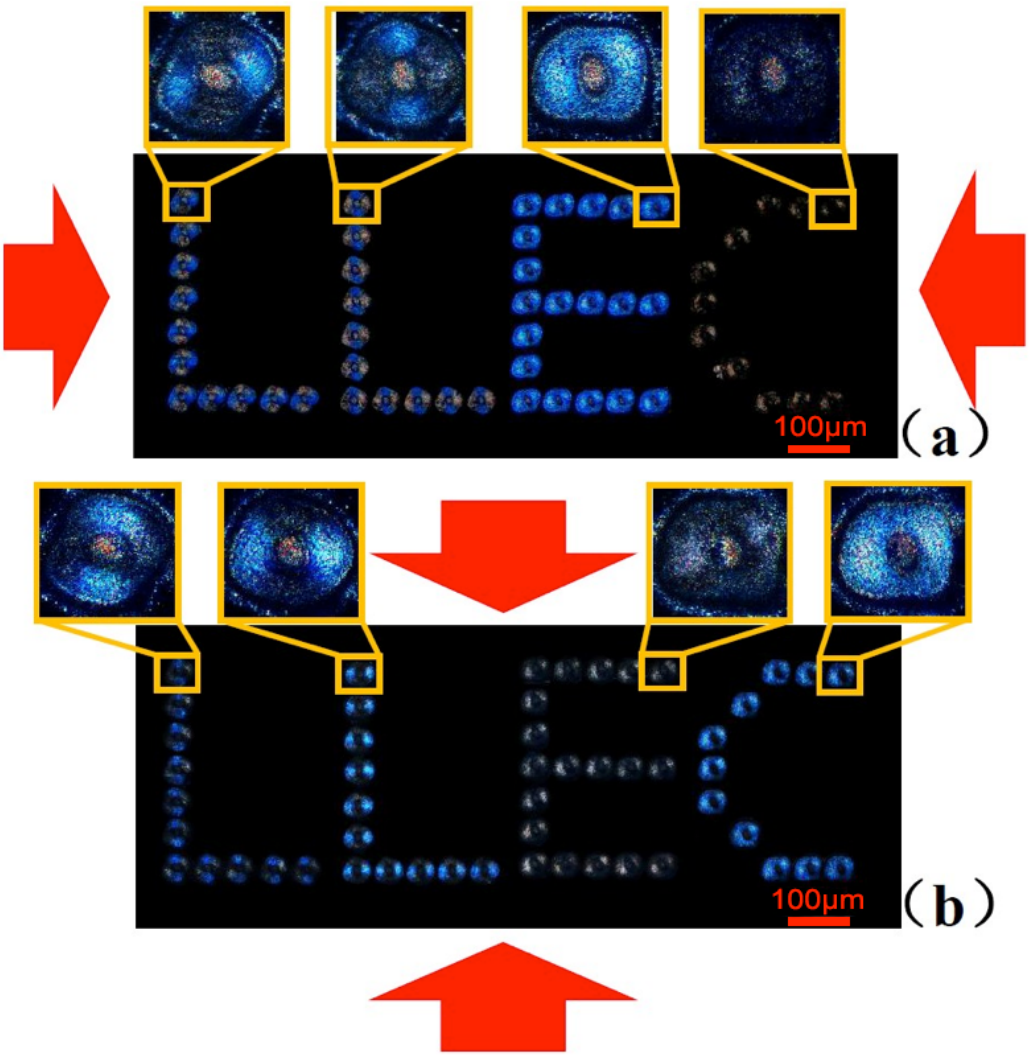

Figure 5.6 *Optical image of "LLEC" pattern produced on stainless steel sample with white light side-illumination at grazing incidence. The red arrows indicate the direction of illumination incident direction, (a) the white light illumination on the left and right hand side, (b) the white light illuminates on the top and bottom side. Due to diffractive property of LIPSS, areas with LIPSS direction perpendicular to the direction of incident light diffract blue light through the microscope, whereas the other areas remain dark.*

This method was then used to exame the sample with "LLEC" pattern. Figure 5.6 (a) and (b) show the optical observed with low angle illumination direction (red arrows) at around 10 degrees to the sample surface. One can see that the blue area inside the spots in Figure 5.6 (a) and Figure 5.6 (b) are complementary for each set of orthogonal polarization. For

the case of spots produced with radial polarization, which forms the first letter "L", left and right side areas in the spots diffract light when the light source is on left and right hand side, as one expect from from their near perpendicular orientation. Detailed LIPSS direction produced with radial polarization is shown in Figure 5.3 top left corner. The test confirms the method is effective for visualizing the direction of LIPSS produced on sample, and that clearly discernible the "LLEC" pattern is produced with four distinct polarization states.

5.4 Arrays of laser spots with dynamic polarization control

The state of polarization can be easily modulated in real time during processing. The experimental setup was configured to produce discrete patterns of laser spots arranged in a square array, each with the desired LIPSS orientation.

Figure 5.7 shows an array spots produced with two orthogonal linear polarization states: horizontal linear and vertical linear polarization. The polarization state was set to horizontal linear polarization to produce a set of four spots at chosen location, forming a small square shape. After the first set of four spots are produced on the sample, the polarization state was switched synchronously to vertical linear polarization to produce a second set of four spots next to the first set of four spots. This process was repeated several times to produce the overall array, which in total consist of 36 sets of four spots. The result pattern illuminated by two white light sources at grazing incident, as shown in Figure 5.7, is beautifully symmetric with alternating arrays of spots with orthogonal LIPSS orientations. The continuous lines on the top and bottom of the discrete spots were

produced with radial polarization, while the left and right hand side lines were produced with azimuthal polarization.

As the hardware and software time delays were not optimized at this stage, the time taken to produce the whole pattern was 22 seconds. The average time to micromachining each set of four spots was 22/36 = 0.61 s, giving the effective polarization switching bandwidth of 1.6 Hz.

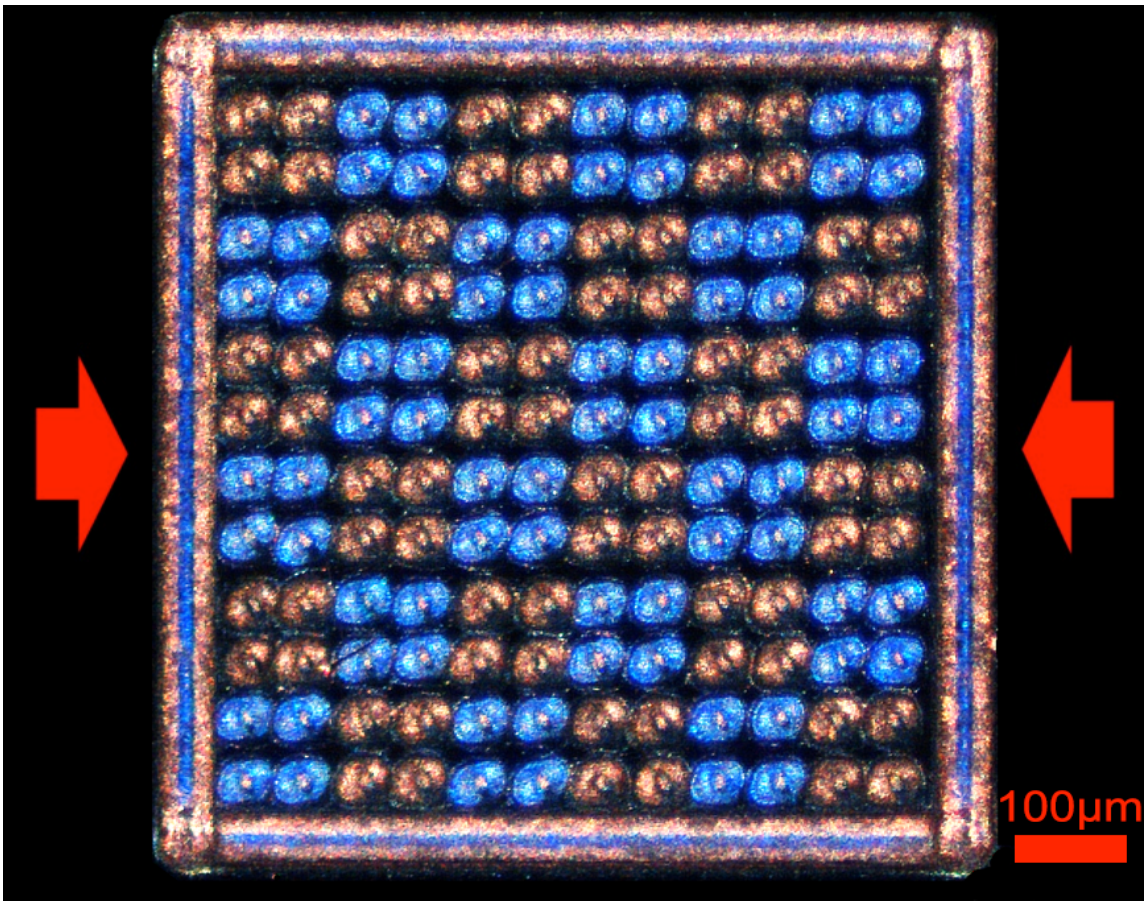

Figure 5.7 *Optical image of spots array produced by dynamic changing of two distinct polarization states during laser processing. The sample was illuminated by two white light sources at grazing incidence and the illumination directions are demonstrated by the red arrows in the figure. Due to the diffractive property of LIPSS, only spots covered with LIPSS with its direction perpendicular to the red arrows diffract blue wavelength through the microscope.*

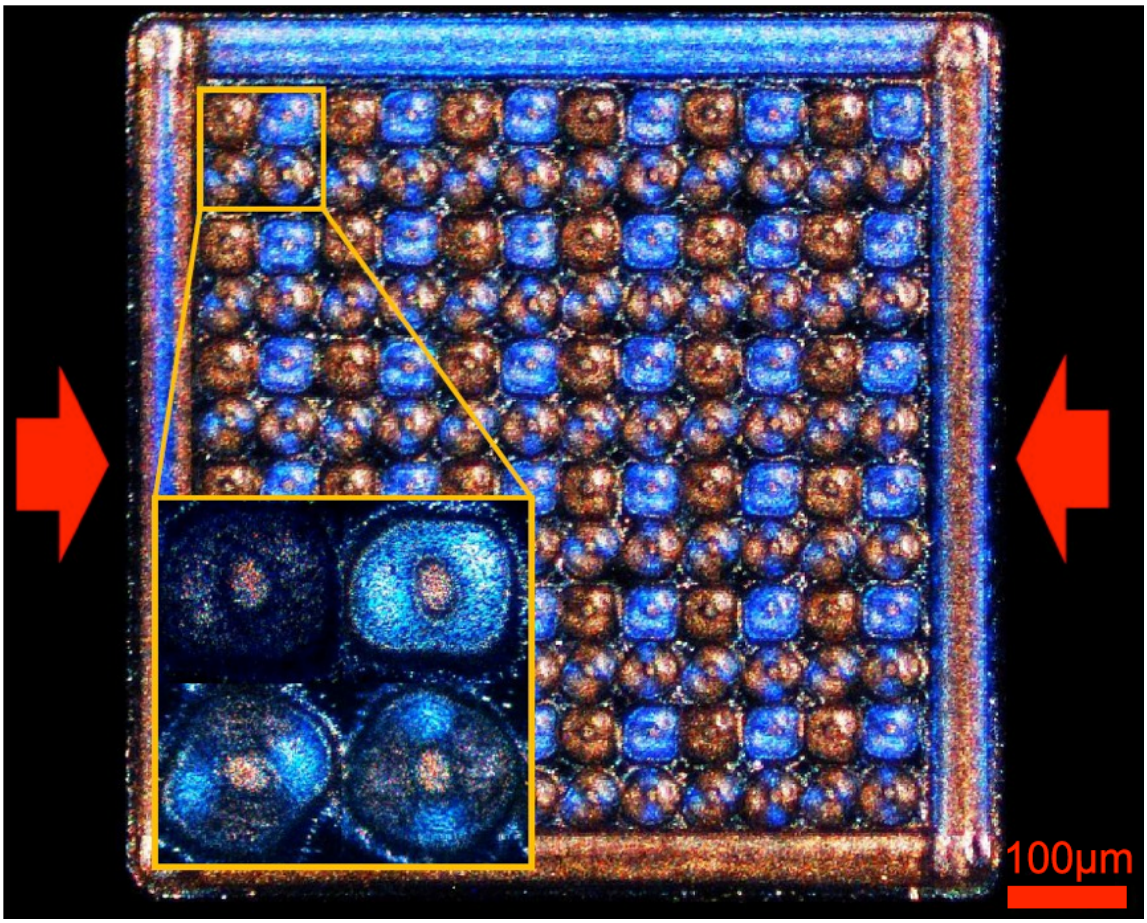

Figure 5.8 *Optical image showing a laser spots array with white light illuminated from left and right side of the sample at grazing incidence, as indicated by the red arrows. Due to the diffractive property of LIPSS, only areas covered with LIPSS with its direction perpendicular to the direction of incident white light reflect blue light. The bottom-left inlay shows a magnified image of a set of four spots produced with four distinct polarization states.*

The experimental setup was then configured to produce a new spot array, as shown in Figure 5.8. By sequentially switching the four distinct polarization states in real time with the laser processing, a new pattern of 2 x 2 arrays with 4 polarization states was produced, Figure 5.8 bottom-left inlay. Each spot inside the new set has a distinct LIPSS micro/nano structure, as shown by the SEM images in Figure 5.9. After the first set of four spots was produced, the laser beam was offset to the next position in x and y to create a 12 x 12 spots array as shown in Figure 5.8. Both the low angle side illumination (Figure 5.8) and the

SEM images (Figure 5.9) confirm the dynamic modulation of polarization in real time with the laser microprocessing.

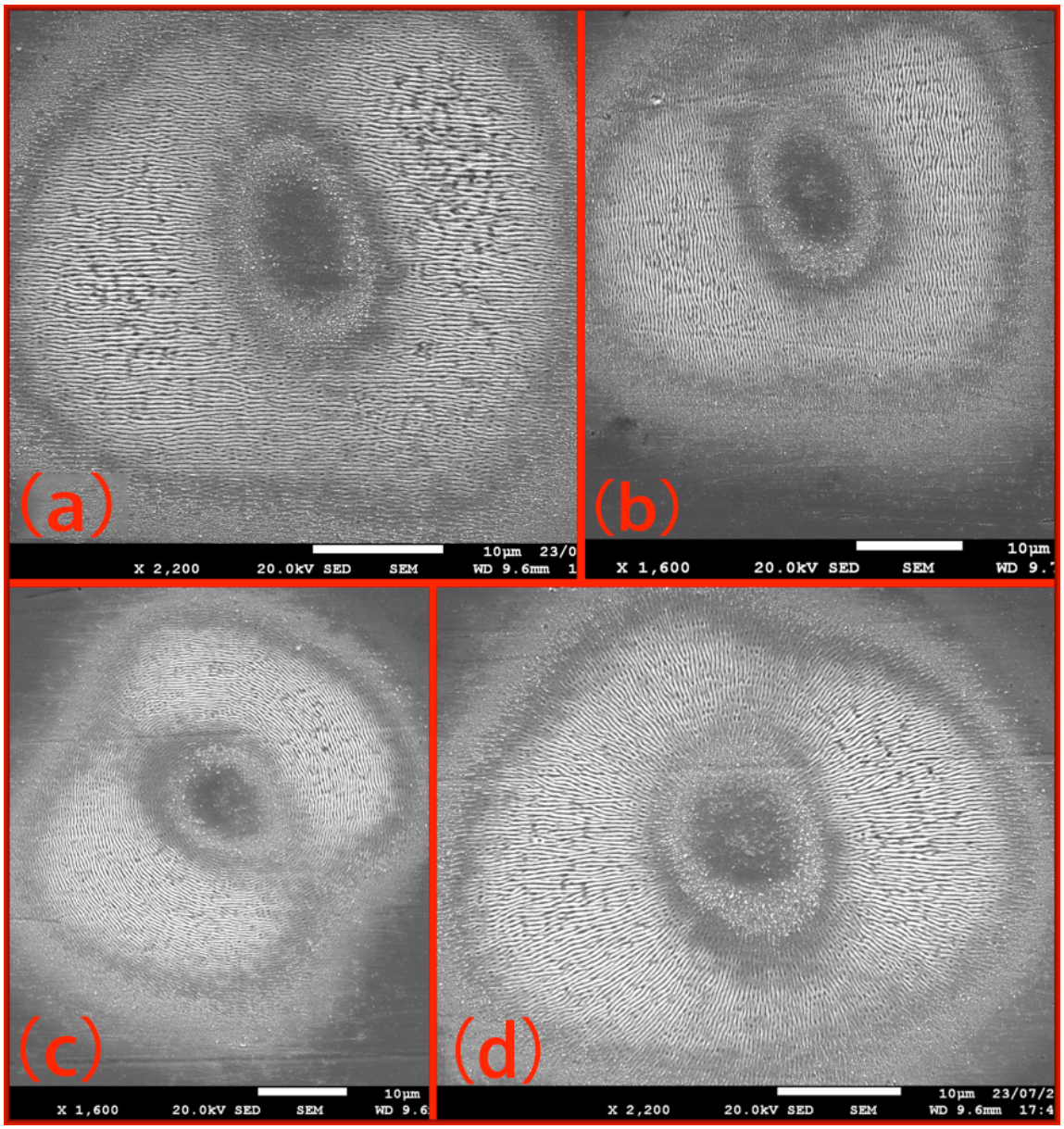

Figure 5.9 *SEM images of laser produced spots on stainless steel sample with four distinct polarization states; (a) spot produced with vertical linearly polarized light, (b) horizontal linearly polarized beam, (c) radially polarized beam, and (d) azimuthal polarized beam.*

The new spot array was produced with optimized software and hardware time delays and the polarization states were modulated from one spot to the next spot in real time. The time taken to micro-machining the whole spot array (144 spots) was 11.5 seconds, hence the average time period between each spot was 11.5/144 = 0.08 s, giving a polarization switching bandwidth of 12.5 Hz.

To achieve dynamic control of polarization in real time of laser microprocessing, a full synchronization of SLM, laser trigger, and the motion system is needed. The SLM is the main device used to modify the polarization, whereas motion control system is used to move the laser beam or the stage to allow desired area to be processed. In the current synchronization system, the laser trigger, which is actually the pockels cell inside the laser system, is controlled by the galvo driver. The galvo triggers the laser on and off at a desired position. The SLM (SLM2 in the current setup) driver, which is a PC, has a communication to the galvo driver. A time delay is usually given in the software used for control the SLM, allowing the CGH to be fully displayed on the SLM, otherwise the tearing CGHs (tearing measns that part of the SLM displays the new uploaded CGH and part of the SLM shows the previous CGH) displayed on the SLM causes distortion, as show in Figure 5.10.

The synchronized system works as follows: the galvo moves the laser beam to desired position, and fires a signal from the galvo driver to SLM driver, triggers the SLM driver displaying the desired CGH on the SLM. A time delay is given in the SLM control software to allow the fall and rise of the previous and current CGH. After the time delay, a signal is sent back to the galvo driver, which enables the galvo driver to trigger the laser

on and off to micromachine the sample. At the end of the processing, a new signal is sent to the SLM driver to request a new CGH to be displayed.

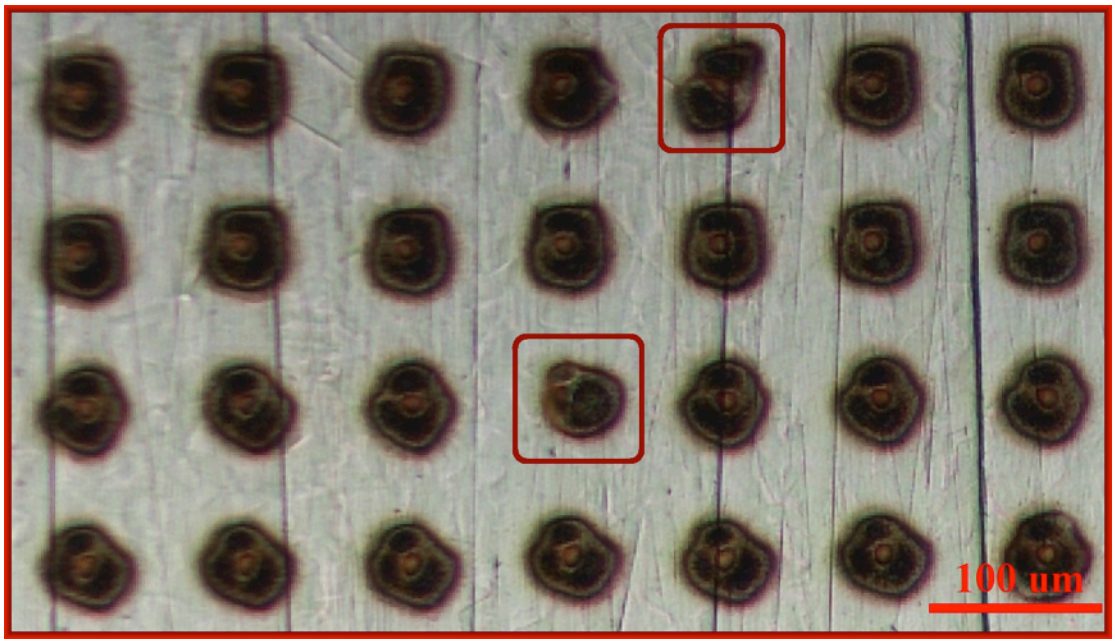

Figure 5.10 *Optical image of spot array produced by switching four distinct polarization states at 13 Hz. Spots marked by the red squares indicate the beam distortion caused by the tearing CGH displayed on the SLM.*

The maximum frequency used to change the CGHs, that generate the above four polarization states without beam distortion, was tested to be 12.5 Hz. Higher bandwidths, from 13 Hz to 20 Hz, were attempted but failed. As an example shown in Figure 5.10, the four CGHs were swopping at 13 Hz in real time with the laser microprocessing. The spots marked by the red squares in Figure 5.10 show beam distortion caused by the tearing of CGH. The SLM bandwidth test results in section 3.3.3 in Chapter 3 shows that the SLM used for this experiment (Hamamatsu SLM X10468-04) has a bandwidth of 18 Hz for 90% of a 2π phase modulation. However, the swopping of CGHs for generating the radial and azimuthal polarization may well be need 100% of 2π phase modulation.

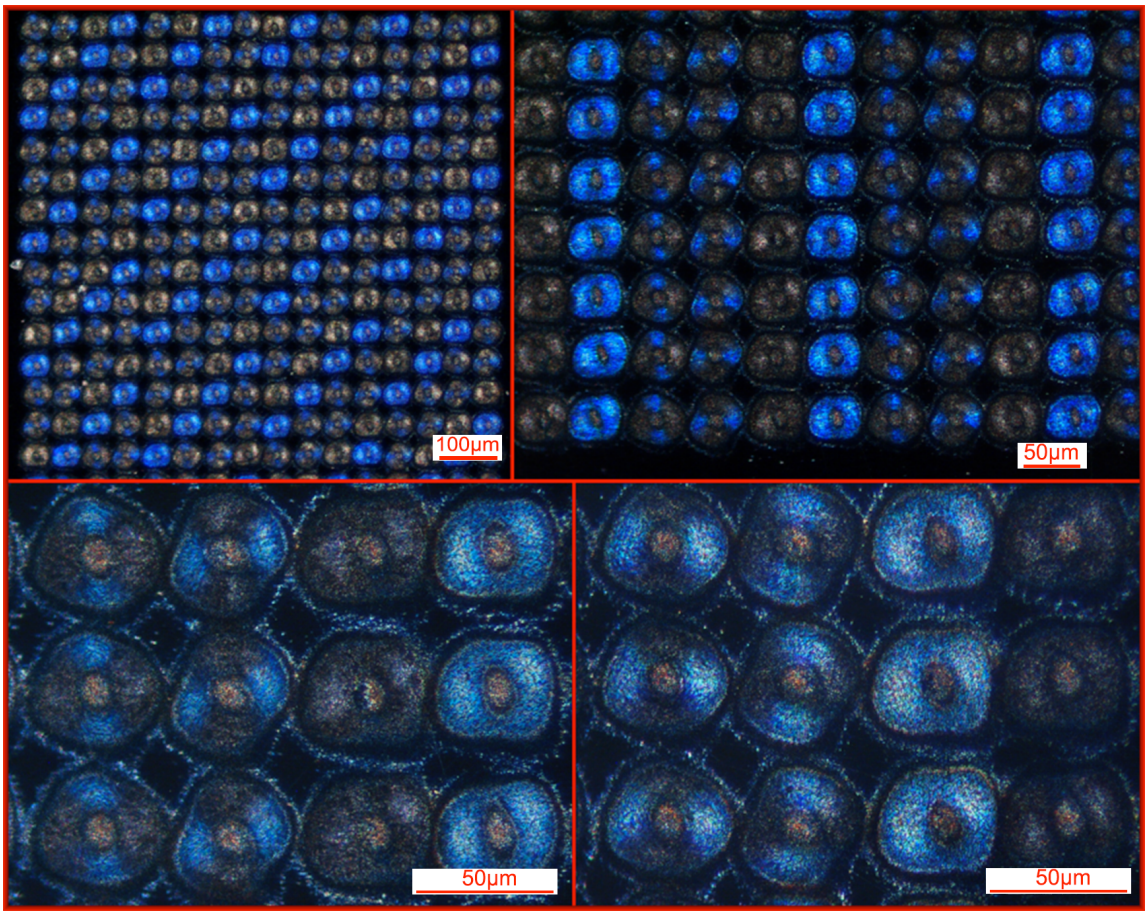

Figure 5.11 *Optical images of other spots arrays produced with dynamic change of polarization in real time with laser microprocessing. Samples were illuminated by two white light sources at grazing incidence with left-and-right or top-and-bottom incidence direction.*

By re-designing the spots array with desired positions for spots with different LIPSS direction, this system could be used to produce large area complex two-dimensional discrete spots arrays, which could be potentially used for security metal surface encoding and encryption. Figure 5.11 shows some other discrete spots arrays produced with dynamic control of polarization in real time with microprocessing. Spots with different LIPSS structures can be easily recognised by low angle white light illumination at different microscope magnifications.

5.5 Continuous linear scanning with dynamic polarization control

Finally, the system was configured to produce scanned lines with complex LIPSS structures inside the lines. The galvo was configured to do raster scan at 2.5 mm/s with laser repetition rate of 5 kHz and pulse energy of 3 μJ/pulse, whilst the polarization states were changing at 12.5 Hz during the scan line at desired points (corners and middle points). After the processing, the sample was analysed by obtaining optical images with low angle white light illumination and SEM images. Figure 5.12 shows the resulting scanned pattern (centre image) and the SEM images at the top and bottom showing the detailed LIPSS structures produced by four distinct polarization states and also the transition region produced during the change of linear vertical polarization to radial polarization (bottom SEM image). Results confirm the ability of modulating polarization in real time with laser microprocessing and show the ability of producing complex two-dimensional scanned lines.

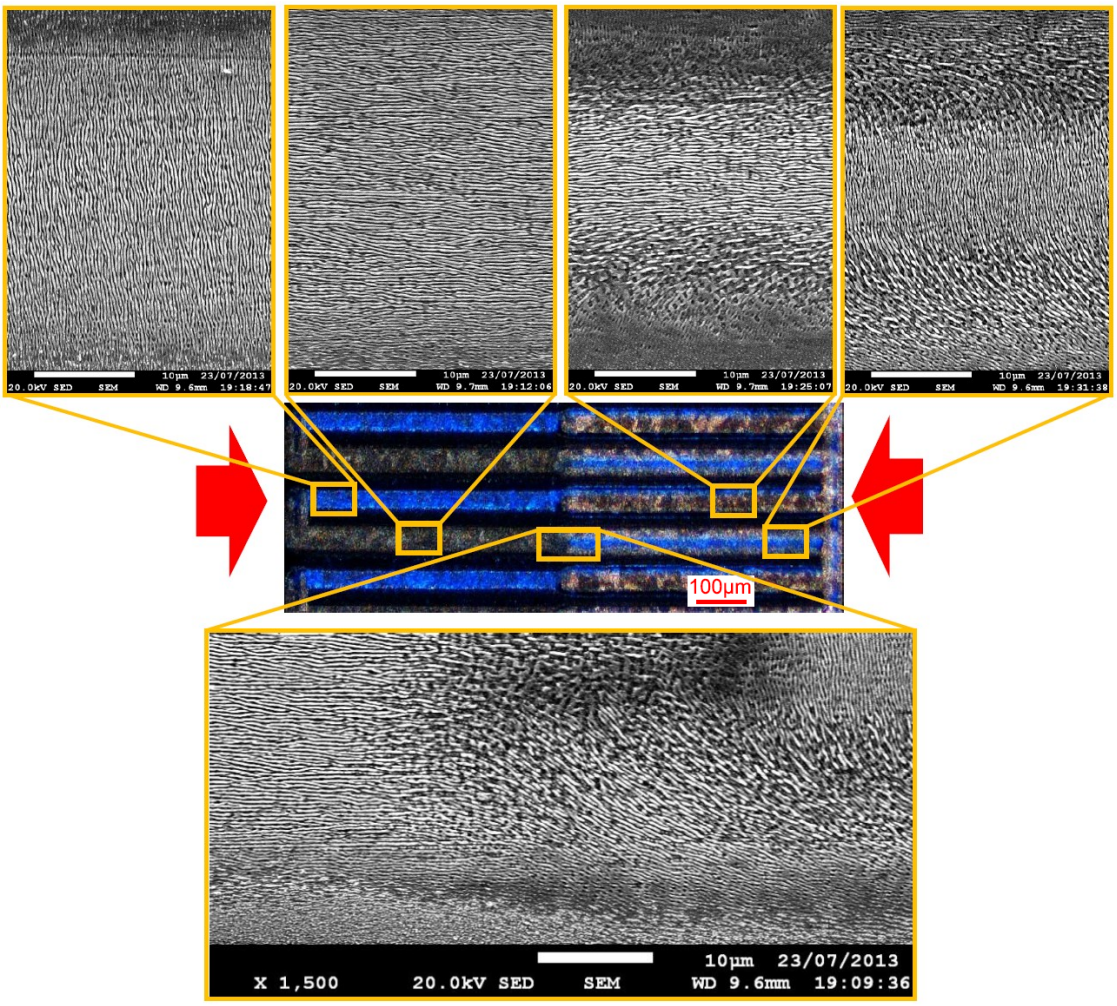

Figure 5.12 *Centre white light illumination optical image shows the laser produced raster scan pattern on stainless steel sample with dynamic change of polarization during scanning. The magnified inlays (SEM images) on the top show the detailed LIPSS structures produced with the 4 different polarization states. The bottom SEM image shows the transition region when changing from linear to radial polarization.*

5.6 Summary

Real time modulation of polarization with laser microprocessing has been successful demonstrated, using two phase-only SLMs combined with two waveplates and addressed dynamically to produce four distinct polarization states, sequentially swapped at a frequency of up to 12.5 Hz. Radial and azimuthal as well as two orthogonal linear

polarization states were generated with high accuracy, all with a ring intensity distribution. Discrete spots array, chessboard spots array and scanned lines with complex LIPSS structures inside spots and lines are produced with dynamic control of polarization. Arrays of desired polarization states and associated vector fields were confirmed unambiguously by observing LIPSS, which are generated orthogonal to the local electric field vector components and further elucidated by the directional light diffraction from the LIPSS.

Chapter 6 - Dynamic modulation of polarization for colourizing metal surfaces

6.1 Introduction

Colouring in nature mostly comes from the inherent colours of the material, but it sometimes comes from other physical origins such as diffraction or interference of light. For example, polychrome colour on the iridescent beetle is due to the interference of light on the multilayer structure and the brilliant blue colour from the wing of the Morpho butterfly primarily comes from a combined action of interference and diffraction of light [244]. The ability of controllably modifying the optical property of metal surfaces to achieve iridescent colours is highly desirable [6]. Artificial metal surface colouring by manufacturing periodic micro/nano structures on the metal surface have been investigated in the last few years [6-8,58]. As well as colourizing metal surfaces, surface micro/nano structuring is important in several other applications, including optics, optoelectronics, mechanics and microfluidics [8]. Different methods have been used to produce large area micro/nano structures on metal surfaces, for example, lithography, chemical etching and ultrafast laser irradiation [245].

This chapter presents a novel method to colourize a metal surface with controllable complex surface micro/nano structures by dynamically modulating the polarization state of the incident irradiation. LIPSS structures with different orientations and geometries were produced at desired positions on a highly polished brass sample. For laser produced large area colourized patterns, a scanner for home or office was used to obtain uniform colour appearance on the micro-structured metal surface.

As an example of a potential application, a colourized metal surface which could be used for a high value item security pattern is demonstrated.

6.2 Experimental setup

A schematic of the experimental setup is shown in Figure 6.1. The laser source is a High-Q picosecond laser (Model: IC-355-800 ps Nd:VAN REG AMP) with a pulse duration of 10 ps, M^2<1.3, average power of 2 W, 50 kHz maximum repetition rate, operating at 1064 nm wavelength and horizontal linear polarization output. The emitted laser beam was expanded with a $\times 3$ telescope to a diameter of 8 mm, passed through an attenuator, which consists of a half-wave plate and a Glan-laser polarizer (Newport). The transmission axis of the polarizer was fixed at 45° to the horizontal. The output 45° linearly polarized beam then impinged on a reflective type phase-only SLM (Hamamatsu X10468-03) while a zero order quarter-wave plate with its fast axis rotated to 45° was placed after the SLM. With 45° linear polarization beam incident on the SLM and the quarter-wave plate placed after the SLM, CGH's with uniform grey levels applied on the SLM thus created elliptical states of polarization, which on transmission through the λ/4 plate, converted these to linear polarization states whose angle of rotation depends on the grey level applied to the SLM. The polarization angles used in this chapter were experimentally checked with a powermeter and a polarizer before laser marking. The polarization angle values have an accuracy of $\pm$2.5%. A 4f image system after the quarter-wave plate was used to reimage the SLM to the aperture of a galvanometer (Nutfield-XLR8-10). The laser beam was focused with a flat field f-theta lens (f =100 mm, Linos). Highly polished brass samples, placed on a 5-axis (x, y, z, A, U) motion control system (Aerotech A3200 system) were carefully positioned on the focal plane of the lens.

It has been shown that LIPSS can be produced on most of the materials [26, 27, 58, 115-118, 119] and the surface colouring is based on the diffraction of the LIPSS, which is a type of surface grating [5-7]. Hence two metal sample substrate could well prove this technique can be used on most of the polished metal substrates. Highly polished basic brass sheets (grade CZ108/CW508L) were mainly used in this experiment. The sample was purchased from eBay and the average surface roughness was measured with the WYKO, Ra = 6±2 nm. The thickness of the sample is 2 mm and the size is 200×200 mm. As a comparison, stainless steel samples were used with the same experimental configuration and laser parameters. The sample is AISI 316L (Fe/Cr18/Ni10/Mo 3) 2 mm thick foil, purchased from Goodfellow Cambridge Limited. Both sides of the sample have been mirror polished. The average surface roughness has been measured with the WYKO, Ra = 18±3 nm. A rubber glove has been used when handling the sample to avoid the contamination of the sample. The sample was cleaned with acetone (99.99%) before and after laser processing.

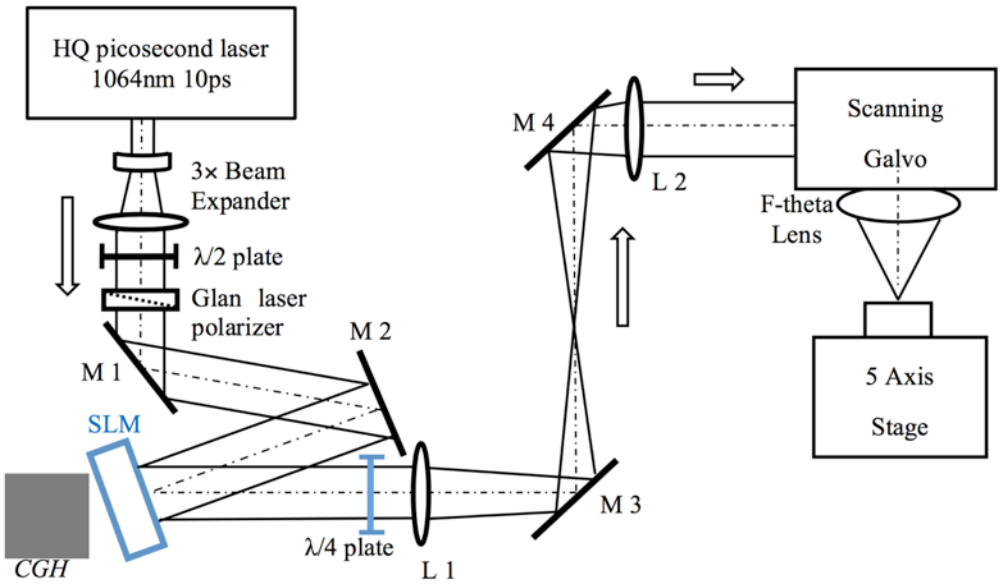

Figure 6.1 *Schematic of the experimental setup.*

The addressing of CGHs to the SLM was fully synchronized with the laser system and the scanning galvanometer. The schematic of the synchronization is shown in section 3.5.2, in Chapter 3. The galvanometer and the laser shutter were controlled by a RTC4 card from Scanlab. The SLM was controlled with a normal PC through a computer graphics interface. A communication of the RTC4 card and the PC that used to control the SLM was built for the synchronization of the SLM, laser, and the scanning galvo. CGHs with different uniform grey levels were used to change the direction of the incident polarization. In order to avoid tearing of the CGH (part of the SLM shows the changed CGH and part of the SLM shows the previous CGH) when changing the CGHs, the frequency CGHs application on the SLM was tested and presented in section 3.3.3 in Chapter 3. These results shown that the maximum time taken for fall and rise CGHs for a

2π phase change was 161 milliseconds, which is ~ 6Hz. The bandwidth of the SLM used in these experiments was 5 Hz to avoid any potential tearing of CGHs.

6.3 Dynamic control of polarization for metal surface colorizing

The experiment was configured to produce a circular pie chart with 36 segments on the highly polished brass sample. The aim was to produce a pie chart fully covered with LIPSS but with different orientations on each segment. In this case, the directions of the linear polarization directions used for producing each segment of the pie chart was altered, rotating from 0° (Horizontal linear polarization) to 175° clockwise with an incremental change of 5°, as shown in Figure 6.2. For highest processing speed, the laser repetition rate was set at 50 kHz with 7 μJ/pulse (P = 0.35 W) while the laser beam was scanned horizontally at 500 mm/s on the sample. The spacing between scanned lines (hatch distance) was set at 10 μm. These parameters produced clear LIPSS on the brass plate. The processing starts from the top-centre segment and each segment was produced one by one in a clockwise sequence while the linear polarization orientation was synchronously automatically changing from segment to segment. The time taken to process each segment was ~2 seconds including a 200 ms delay for CGH change, the whole disc was patterned in ~70 seconds. The produced pie shaped pattern was then illuminated with incident white light while taking an image with a camera. As shown in Figure 6.2, the colour appearance on the laser processed pie pattern is brilliant and iridescent.

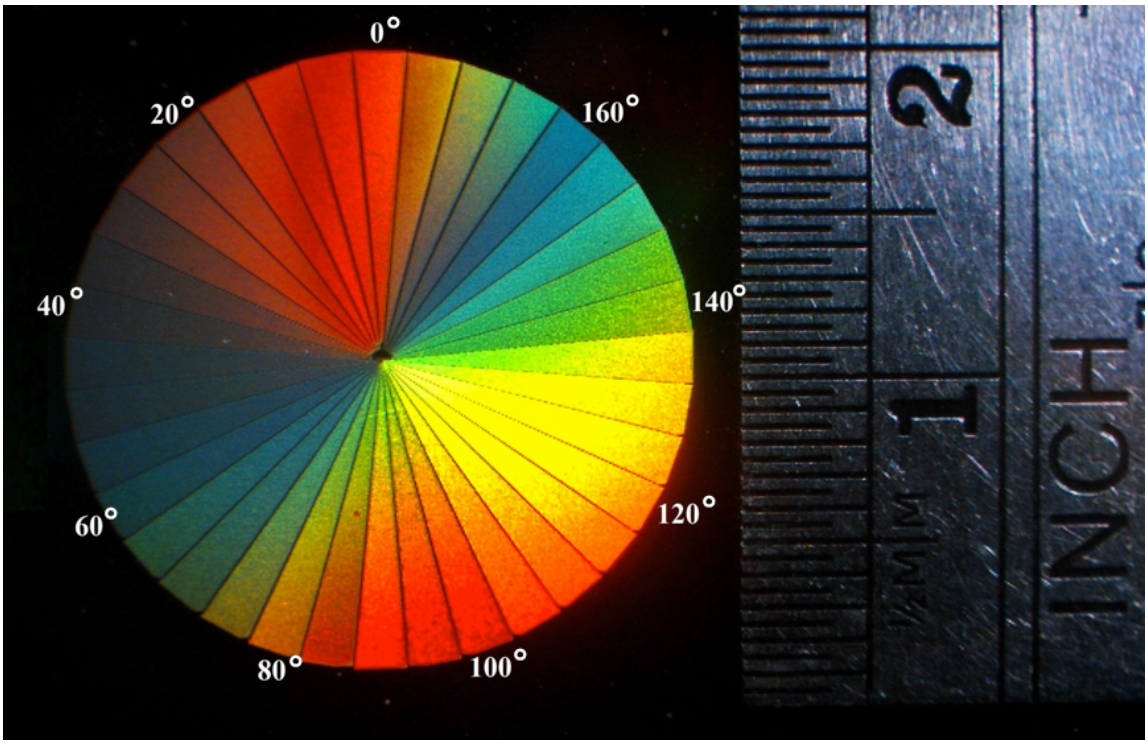

Figure 6.2 *Pie pattern with 36 segments produced on polished brass sample; the pie pattern is covered with LIPSS structures, which gives a brilliant colour with white light illumination. Each segment of the pie was produced with a different linear polarization orientation (indicated by the number around the pie). 0° stands for horizontal linear polarization and the polarization rotates clockwise with an incremental change of 5°, which gives a different LIPSS orientation in each segment of the pie.*

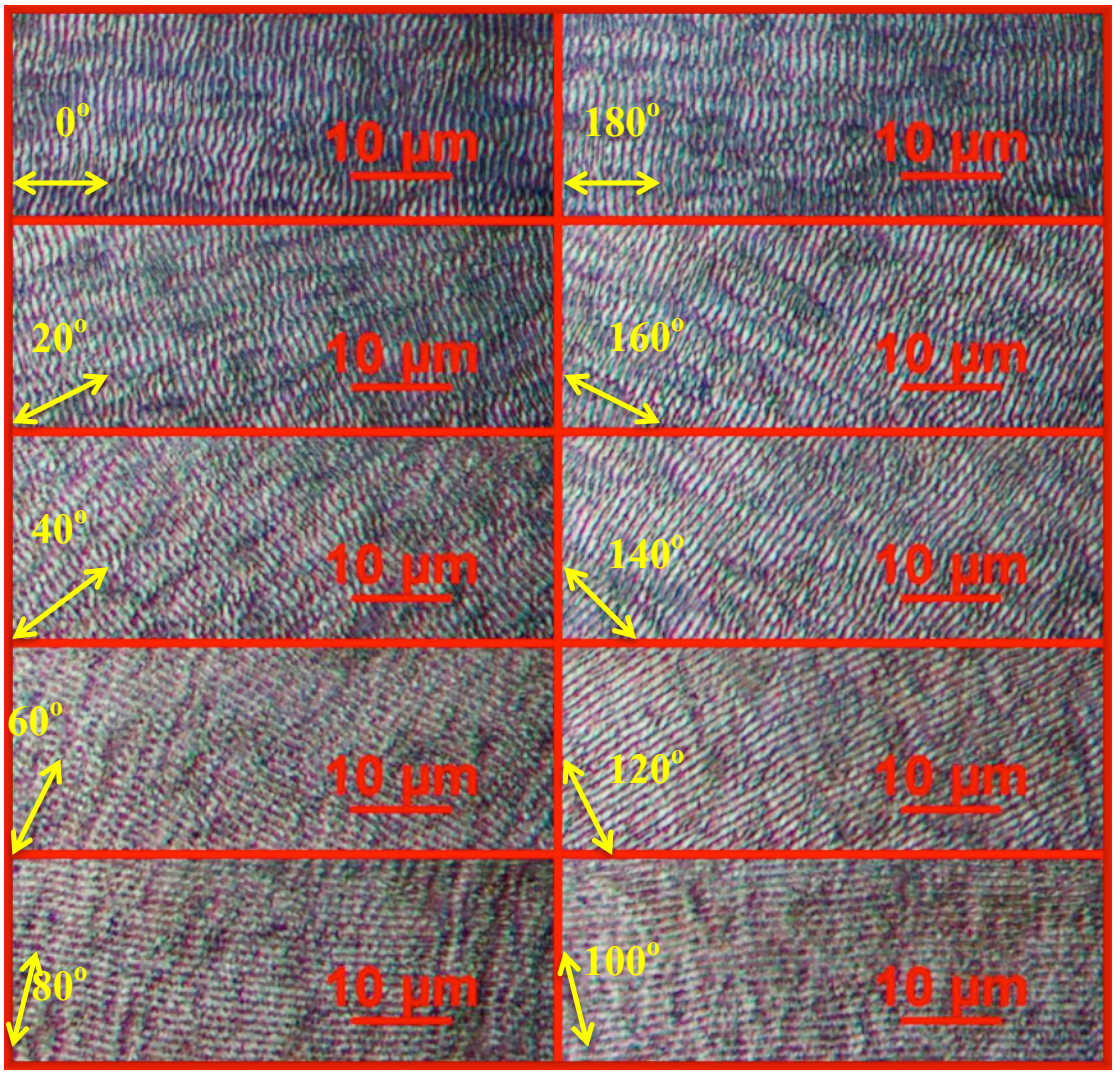

Figure 6.3 *Microscope image of the microstructures and LIPSS orientations produced dynamically in different segments of the pie pattern. The yellow arrows indicate the direction of the incident linear polarization.*

Optical microscope images in Figure 6.3 show the microstructures observed and the LIPSS direction on different segments of the pie shaped pattern created in real time. These results show that the synchronization technique developed here works well. The yellow arrows in the Figure 6.3 indicate the direction of the linear polarization used, which produces LIPSS with its orientation perpendicular to the incident polarization direction and have a near wavelength-sized periodicity. As stated in the literature, the angle between

the LIPSSs direction and the laser beam scan direction has an impact on the uniformity of the LIPSS. Since the laser beam scan direction was horizontal, when the LIPSS orientation is towards horizontal, the uniformity and continuality of the LIPSSs are better than when the LIPSS direction is towards vertical. The effects can be seen in figure 6.3, the LIPSSs produced with 100° linear polarization direction (LIPSS direction towards horizontal) has a better uniformity and continuality than LIPSS produced with 0° linear polarization direction (LIPSS direction towards vertical).

When changing the angle of the incidence of the white light illumination, the colour appearance on the sample changes accordingly, as shown in Figure 6.4 (a), (b) and (c). The angle between the incident light and the camera that were used for taken figure 6.4 (a), (b), and (c) were measured to be ~20° (a), ~28° and ~32°, respectively. This is due to angular dispersion, diffracting different wavelengths to the observer as the light source is moved. The schematic diagram in Figure 6.5 shows this effect when changing observing position and vice versa, with a fixed viewing position while changing the angle of the incident light source, this will also change the colour appearance on the sample.

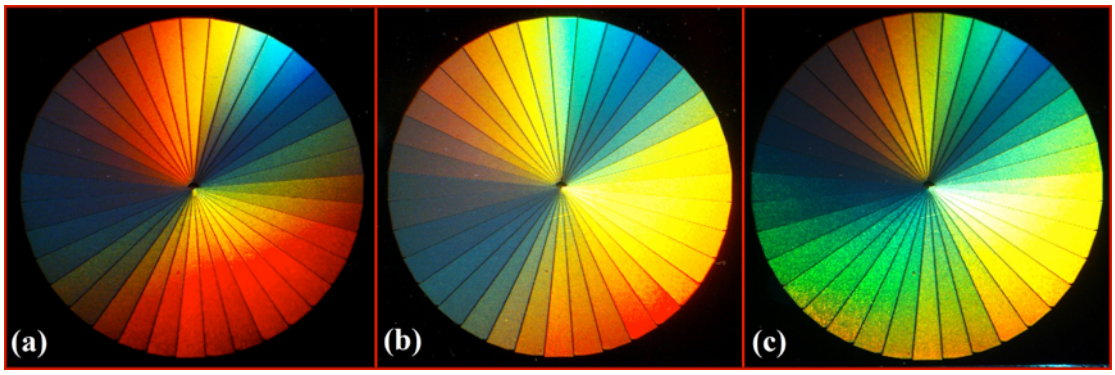

Figure 6.4 *Varying the angle of the incident white light source changes the colour appearance on the sample with a fixed viewing point; (a), (b) and (c) are images taken with the same sample but different white light incident angles.*

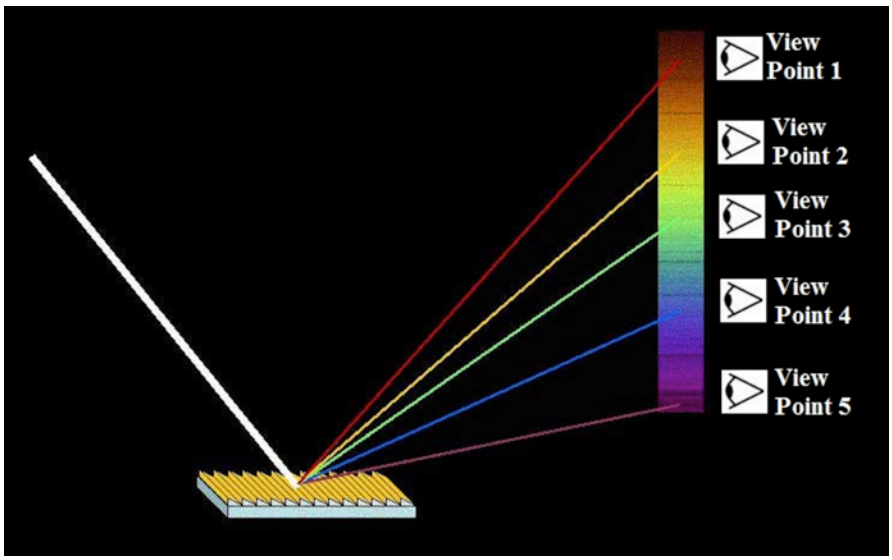

Figure 6.5 *Illustration of the colour difference observed at different viewing angles with fixed white light source.*

6.4 Defining the colour diffracted from certain micro/nano surface structures

With a normal white light source or sun light illumination, the colour appearance on the sample covered with structured micro/nano LIPSS cannot be precisely defined due to

variations in the source spectrum combined with the orientation and pitch of the micro/nano structure.

B. Dusser *et al.* [8] introduced an innovative method to help define the colour distribution diffracted from a metal surface covered with certain micro/nano structures: by using a scanner for home or office to scan the micro/nano-structured sample. The schematic of a scanner is shown in Figure 6.6, with the white light incident at an angle to the local area of the micro-structured sample which diffracts and disperses the white light spectrum, by introducing an aperture, most of the spectrum is blocked and a particular colour transmitted and captured by the CCD. When the micro/nano-structures on the sample changed, e.g. a smaller periodicity, angular dispersion changes the spectrum and so another colour is detected. Note the lamp (white light source) in a scanner is in a bar shape located very close to a transparent glass screen that supports the sample. In this case, the lamp only illuminate localized areas on the sample along the lamp direction when it is static. While the lamp is moving in an axis perpendicular to the lamp direction, different localized areas on the sample are illuminated stepwise and the lights are collected by the CCD. The CCD is also in a bar shape to receive all the lights that diffracted or reflected from the sample. Assuming the incident angle of the white light is α, the diffracted light angle is θ, the period of the LIPSS is d, m is the diffraction order, the wavelength λ captured by the CCD can be found with the diffraction Equation [8]:

$$\boldsymbol{m\lambda = d(sin\alpha + sin\theta)} \tag{2-4}$$

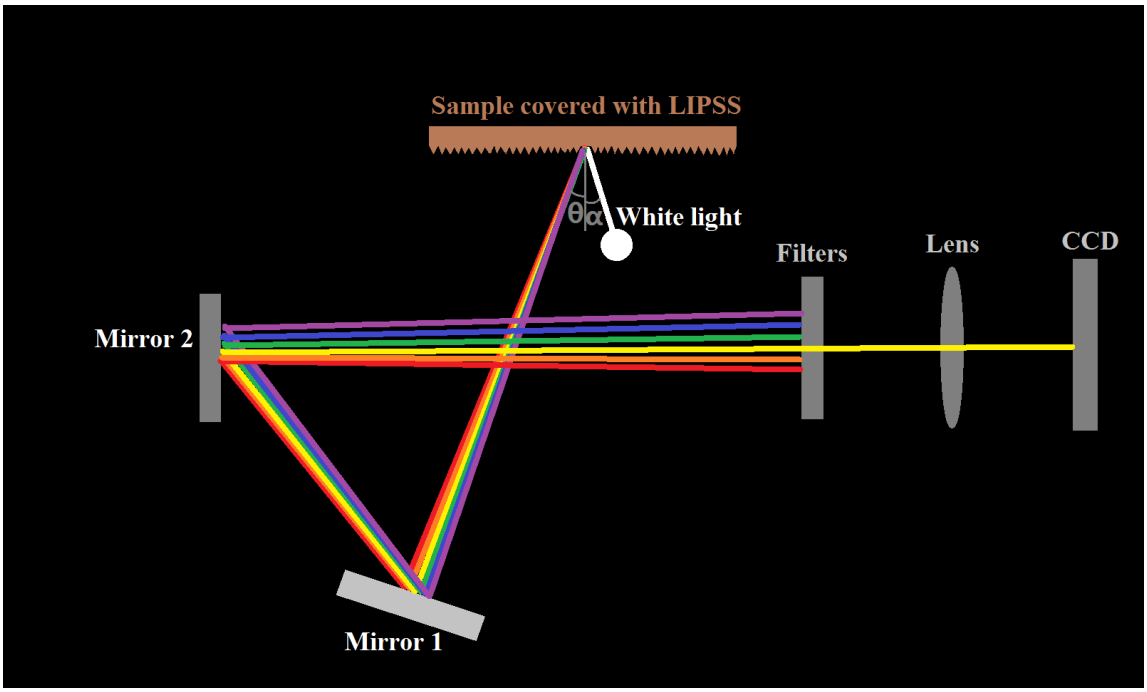

Figure 6.6 *Schematic of a scanner. The sample covered with micro/nano structures diffracts the white light and only a particular wavelength transmitted through an aperture to the CCD detector with other wavelengths being blocked. When the micro/nano structure changes, the wavelength detected on the CCD will change.*

With this method, the sample produced earlier was scanned with a scanner for home or office (HP LaserJet Pro 200 MFP) and the result is shown in Figure 6.7 (a). The colour on each segment is uniform while the colour hue varies gradually from one segment to another. To check that this method is reliable, another pie pattern was produced on the polished brass sample but in this case, the polarization was fixed at 0° (horizontal linear polarization) for all the segments, which will produce LIPSS with only one direction on the whole pie. As shown in Figure 6.7 (b), the scanned image of a uniform LIPSS direction also has a uniform colour appearance regardless of the LIPSS position on the sample. These results indicate that a colour calibration may be achieved.

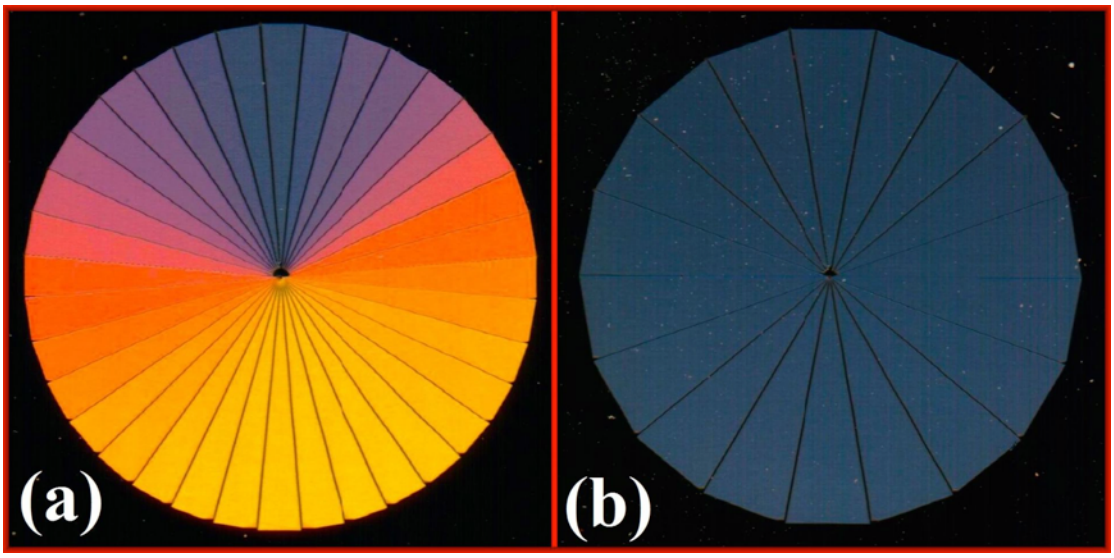

Figure 6.7 *Scanned image of laser produced pie shape pattern with a normal scanner; (a) pie shape with 36 segments and each segments was processed with a different linear polarization orientation, (b) pie with 18 segments and all the segments are produced with horizontal linear polarization.*

Although figure 6.4 and figure 6.7 (a) were taken from the same sample, the colour shown in the two figures are totally different. Because the observed colour is from surface diffraction, the angle between the incident light and the CCD determines the colour. In the case of using a phone camera to take images, the CCD receives all the diffracted lights from the whole sample simultaneously. The pie pattern on the sample is 19 mm in diameter, the lights diffracted from different areas on the sample to the phone camera has different angles, which caused the polychrome effect, even in one segment of the pie. Whereas, the CCD in a scanner only receives the lights diffracted from a small illuminated area on the sample at any one time. While the light source moves along the scanned sample, lights diffracted from localised sample are collected step by step and build the image. In this case, the lights diffracted from the localized area to the CCD of the scanner can be regarded as having no angle difference, leading to a constant localized colour.

Those localized colour build up, forming a colourized pie shape image. Within the pie, different segments have different colour, but the colour inside each segment is the same.

In figure 6.4, the pie shows a wider range of colour than in figure 6.7, especially the red and green colour shown in figure 6.4. This is due to the limitation of a scanner for home or office, the angle between the illumination source and the CCD is not adjustable. With a phone camera, the angle between the light source and the CCD is flexible, a wider range of spectrum can be diffracted from the sample with a wider range of adjustable angles

Note that the colour map in Figure 6.7 (a) has an axial symmetry, in this case, aligned 5° from the vertical. Reflection through this axis yields the same hue. One would expect 36 different colours on the pie pattern, as there are 36 different LIPSS orientations in the 36 segments from 0° (vertical LIPSS) to 175° with an incremental change of 5°. However, there are 18 colours. Assume that the LIPSS in Figure 6.8 (a) have an angle of θ to the horizontal and $-\theta$ to the horizontal for LIPSS in Figure 6.8 (b). Let the periodicity of the LIPSS be Λ and the white light source is scanning vertically across the sample. The effective pitch for LIPSSs in both cases is $\Lambda cos\theta$, which will present the same colour after scanning with a normal scanner. Hence, although the pie pattern contains 36 different directional LIPSS structures, the number of colours actually observed is halved due to symmetry.

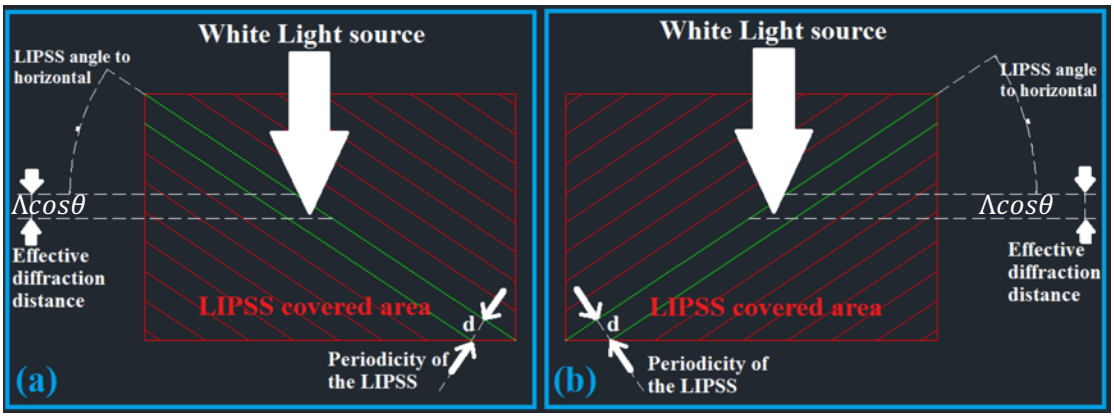

Figure 6.8 *Schematic of the effective diffraction distance for LIPSS with an angle θ and -θ to the horizontal direction. As the incident white light was scanned vertically, the effective periodicity of the LIPSS for (a) and (b) should be the same, Λcosθ, both areas diffract the same colour after scanning with a normal scanner.*

With the ability to generate a calibrated, uniform colour map corresponding to the LIPSS direction on the brass sample, the experimental setup was then configured to produce a University of Liverpool logo pattern, in which each letter of the logo was encoded with a different linear polarization direction. The laser beam was attenuated to 7 μJ/pulse with 50 kHz laser repetition rate, 500 mm/s horizontal scan speed, and hatch distance = 10 μm . The result of this unique colour encoding on each letter can be seen to be satisfactory, see Figure 6.9. Thus, dynamic control of polarization for ultrafast laser processing combined with a white light scanner is able to generate uniform, reproducible iridescent colours on metal surface. Note that the ghost line on the left-hand side of letter "O" is due to the relatively slow response of the mechanical shutter in the laser system, which controls the laser gating.

Figure 6.9 *Image of the University of Liverpool logo obtained with a normal scanner; the pattern was produced by dynamic rotation of the angle of the linear polarization, which produced different LIPSS orientations in each letter, ending up with different colour appearance after scanning.*

6.5 Enhanced colour appearance with the change of laser scan speed

The chromatogram obtained by rotating only the angle of the incident linear polarization is limited. Modulating both the polarization and scan speed as well in real time, this produced a richer chromatogram with a wider range of colour hue. As incident linear polarization was rotated from 0° (horizontal linear polarization) to 90° (vertical linear polarization) with an incremental change of 5° clockwise, a row contains 19 squares was produced. This procedure was repeated 10 times with different laser scanning speeds, starting from 100 mm/s to 1000 mm/s with an incremental change of 50 mm/s. The result was a 19 by 19 square array, produced with 7 μJ/pulse, 50 kHz repetition rate, and 10 μm hatch space with horizontal scan direction, which is the same as before. The resulting chromatogram is shown in Figure 6.10. With the modulation of the incident linear polarization orientation and the change of the laser scanning speed on the sample, the LIPSS structures produced in the squares are distinct, which diffracts different

wavelengths when scanned with a normal scanner, resulting in different colour appearance on the CCD of the scanner.

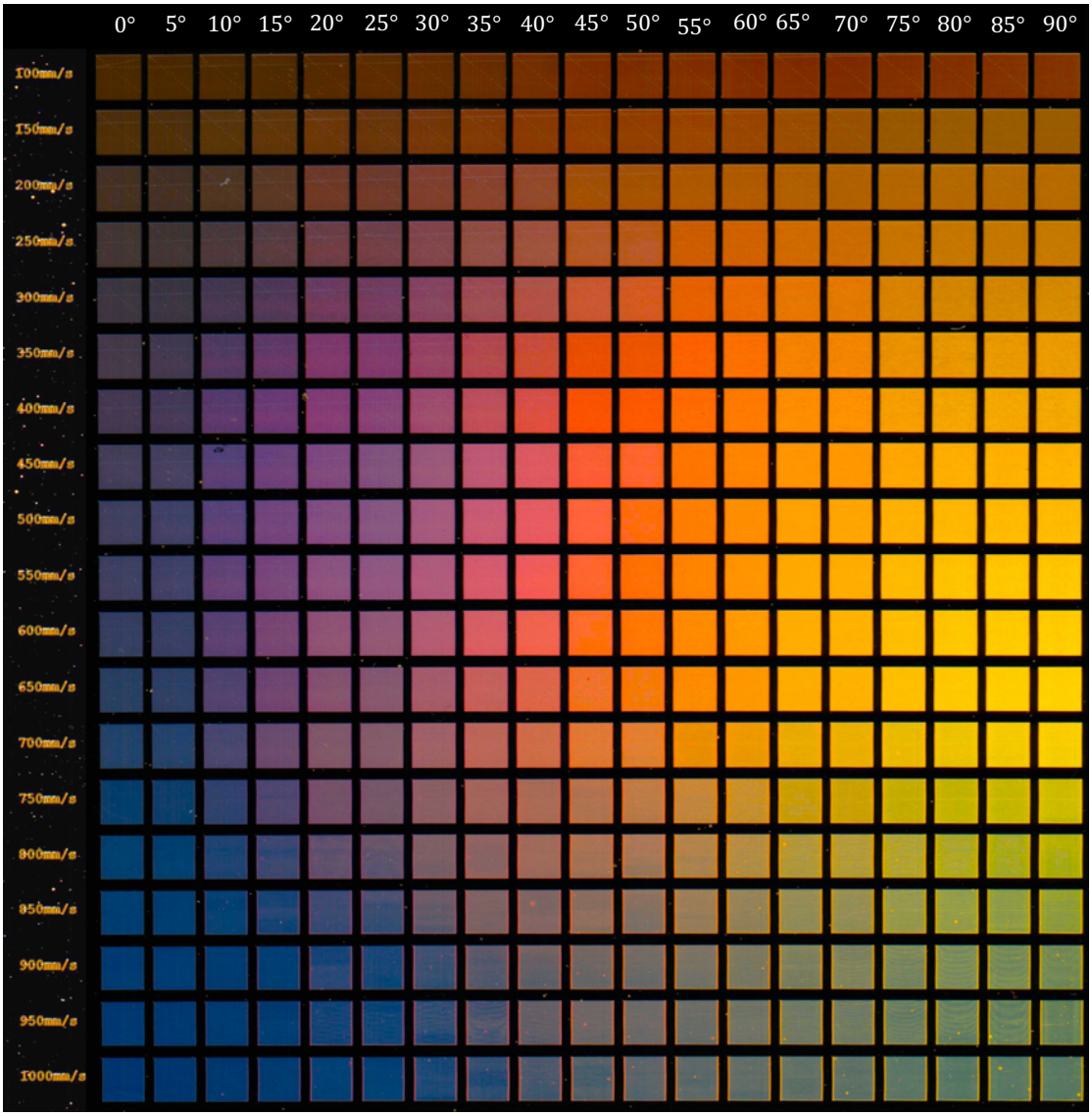

Figure 6.10 *Scanned image of laser processed brass plate when both polarization and scan speed were altered. The colour appearance is due to the diffraction of LIPSS produced in the squares. Horizontal variation is due to the change of the incident linear polarization orientation, starting from 0° (horizontal linear polarization) to 90° (vertical linear polarization) with an incremental change of 5° clockwise. The vertical variation is caused by the modulation of the laser scan speed on the sample, starting from 100mm/s to 1000mm/s with an incremental change of 50mm/s.*

The morphology of the LIPSS structures produced with different laser scanning speed is shown in Figure 6.11. With 100 mm/s and 200 mm/s laser scanning speed, the higher pulse overlap caused some ablation of the sample as well as the LIPSS structures which are not very clear, due to overexposure on the sample surface. As the laser scanning speed increases, and pulse overlap decreases, the appearance of the LIPSS structures gradually becomes clearer up to 800 mm/s laser scan speed. Above this speed, exposure is insufficient and LIPSS finesse reduces again. Although the LIPSS morphologies produced with 500 mm/s to 700 mm/s look similar, the depth and the periodicity of the LIPSS structures alter with laser scanning speed, clearly demonstrated by the colour differences observed in Fig.6.10.

The number of pulses per unit area Np for speed increasing from 100 mm/s to 1000 mm/s are 45 (100 mm/s), 30 (150 mm/s), 22.5 (200 mm/s), 18 (250 mm/s), 15 (300 mm/s), 12.9 (350 mm/s), 11.3 (400 mm/s), 10 (450 mm/s), 9 (500 mm/s), 8.2 (550 mm/s), 7.5 (600 mm/s), 6.9 (650 mm/s), 6.4 (700 mm/s), 6 (750 mm/s), 5.6 (800 mm/s), 5.3 (850 mm/s), 5 (900 mm/s), 4.7 (950 mm/s), and 4.5 (1000 mm/s). From Np = 4.7 to 5.6, only small patches of periodical structures are observed in various isolated locations within the scanned area. With increasing Np ≥ 6.4, the LIPSS grow and become clearly recognisable under optical microscope. For Np > 22.5, LIPSS starts to disappear and becomes unclear in various locations. The same effect has also been reported by A. Y. Vorobyev [131]. The period of the LIPSS was also altered by the pulse overlap. It can be seen, in figure 6.11, that the period of the LIPSS produced with Np = 9 (500 mm/s) has a slightly bigger period than LIPSS produced with Np =22.5 (200 mm/s), which is in line with the work carrid out by A. Y. Vorobyev [131], and Lingling Ran [132].

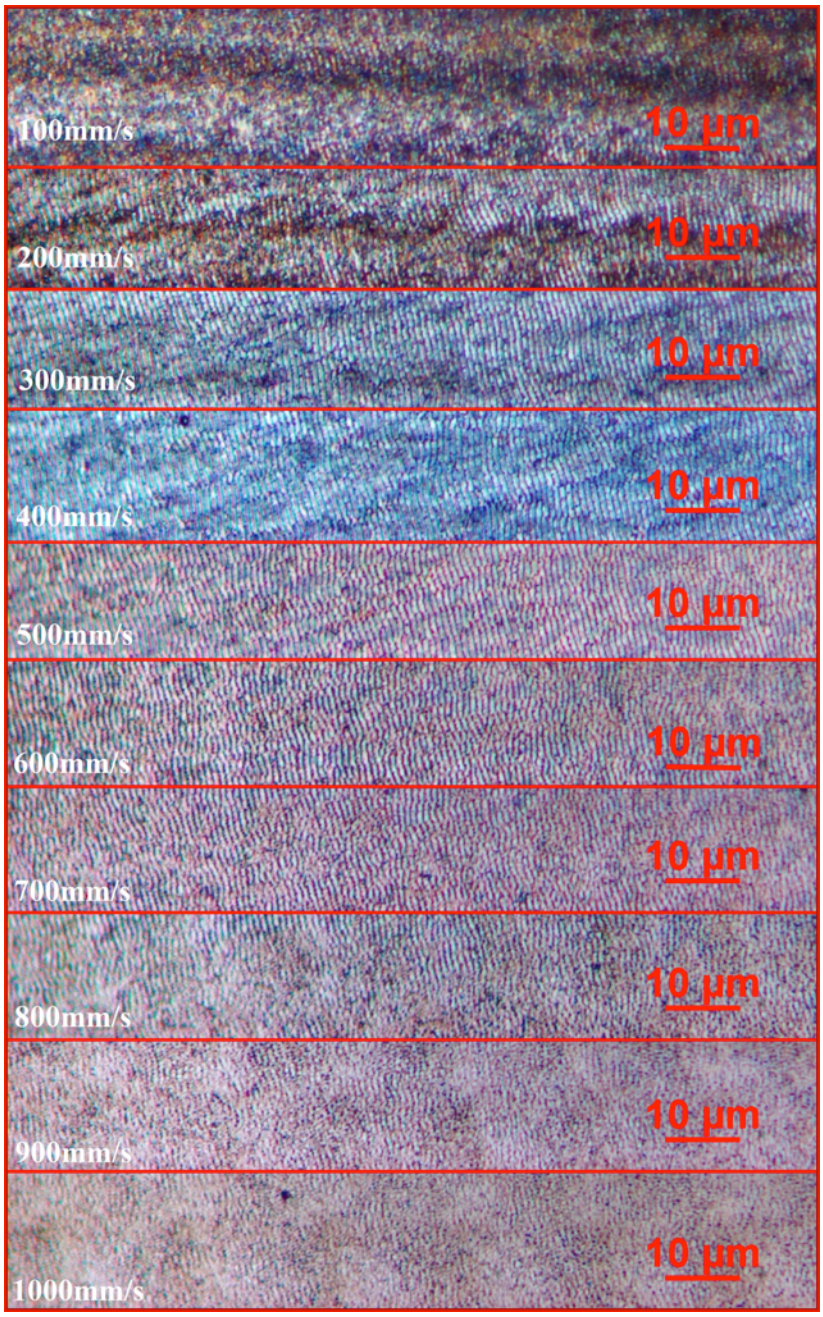

Figure 6.11 *Microscope image of LIPSS structures produced with linear polarized polarization incident with different laser scanning speeds, varying from 100 mm/s to 1000 mm/s with an incremental change of 100 mm/s. The colour difference of the microscope images produced at 300 mm/s and 400 mm/s is due to the auto white balance function of the microscope image capture software.*

6.6 Colorizing metal surface for advanced security patterning

For volume-produced items, surface security using holographic patterning is useful due to the high throughput of the process. However, holographic surface security patterning is inflexible, as each different pattern requires a redesign of the hologram. On the other hand, laser induced surface patterning on metal surfaces are both permanent and highly flexible. For high value products, for instance, precious metal and cash notes, each item could have a unique polarization encoded surface security pattern or barcode with the company logos, which makes the security level even higher than imprinting single product design surface security pattern on every item. As a demonstration of the principle, this section presents an example of high-speed production of a metal surface security pattern on a highly polished brass sample. The aimed logo and the barcode are shown in Figure 6.12, which comes from a Chinese cigarette brand: Yellow Crane Tower.

Figure 6.12 *The logo and barcode that will be reproduced with the advanced security patterning method to enhance the security level of the product. The item is a Chinese cigarette, called Yellow Crane Tower.*

The experimental setup was configured to reproduce the logo and a barcode shown in Figure 6.12. Ten different colours (polarization/scan speed) were chosen from the chromatogram shown in Figure 6.10 then numbered for easier reference as shown in Figure 6.13. As before, the laser energy was attenuated to 7 μJ/pulse with 50 kHz laser repetition rate, 500 mm/s horizontal scan speed and line-to-line spacing of 10 μm. Laser scanning speed and the direction of the incident linear polarization were controlled in real time with the processing speed to reinforce different colours on selective areas of the reproduced logo and the barcode. A scanned image of the sample was obtained by using a normal scanner while a picture of the sample was taken with a camera at an angle where there was no diffraction, see Figure 6.14 (a) and (b), respectively.

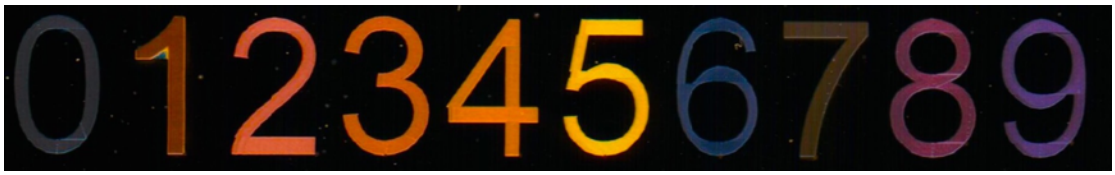

Figure 6.13 *Ten different colours were chosen from the chromatogram shown in Figure 6.10. The colours are numbered from 0 to 9 for easier reference. These numbers were produced by laser microprocessing of a brass plate with dynamic control of laser scanning speed and change of the incident linear polarization orientation, which was then imaged with a normal scanner.*

These results show that each part in the cigarette logo has a different colour appearance corresponding to the colour codes selected. The barcode contains 10 numbers and lines above. Every number and corresponding coloured lines of the bar code are clearly discernible. Note the 10 little rectangular areas underneath the main tower in the logo pattern, which all have a different colour. The colours of the little rectangles from left side to right side are actually in the same order used to produce the barcode, but starting from number 1.

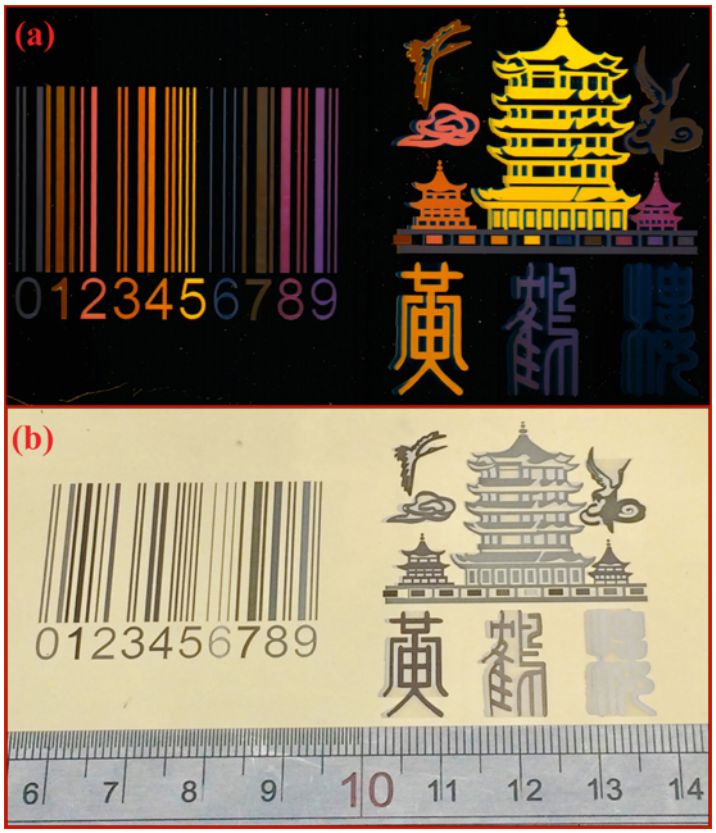

Figure 6.14 *Laser reproduced cigarette logo and barcode pattern. (a) is the image obtain by scanning the sample with a normal scanner, (b) is taken with a camera at an angle with no surface diffraction.*

With this method, high value product companies could generate different barcodes for each of their high value products and make the little rectangles have the same colour order as the numbers underneath the barcode. The customer could check their product by simply scanning the item with a normal scanner, which is a simple, inexpensive procedure. Besides, as the metal surface contains periodic surface micro/nano structures, which are highly diffractive under sunlight and normal lamplight, the customer could see iridescent colours when they rotate the item. Figure 6.15 shows the strong diffraction of the laser processed pattern under normal lamplight (Figure 6.15 (b)) and sunlight (Figure 6.15 (c), (d), and (e)) with different incident light angles. Also, with certain angle of placing the

sample under the light source, the pattern could be non-diffractive, as shown in Figure 6.15 (a).

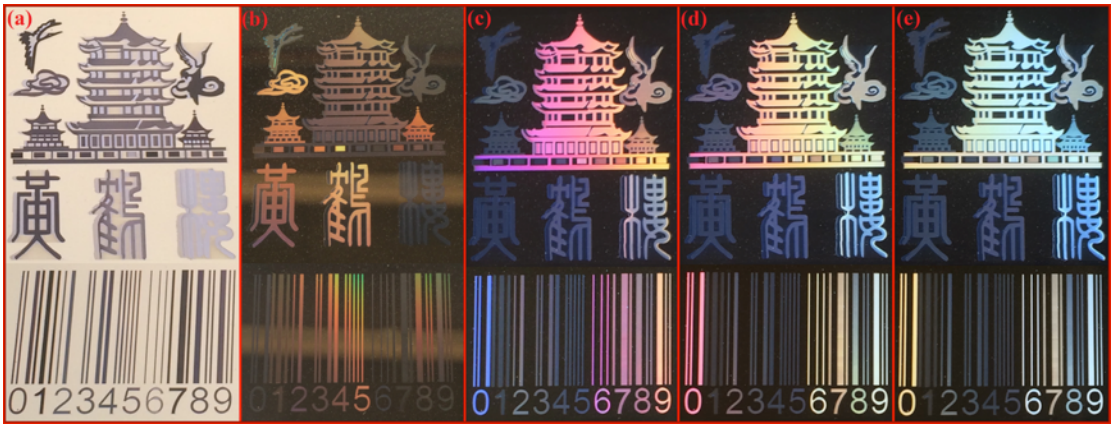

Figure 6.15 *Images taken with a camera with the the sample placed under normal lamplight (a, b) and sunlight (c-e). Image (a) is taken with a particular angle with no diffraction while colour appearance on the sample shown in images (b), (c), (d) and (e) is due to white light diffraction from the periodic surface structures on the sample. The colour difference between the images is due to the changing angle of incidence.*

6.7 Discussion

The technique was then applied to produce the same pattern on a highly polished stainless steel for comparison and prove that the technique can be used widely on different metal surfaces. The pie shape that contains 36 segments was re-produced on the SS sample with the same parameter and optical setup as the one used for brass sample. After laser processed, a scanned image was obtained, as shown in figure 6.16 (a). A comparison image was taken by a smart phone camera under sun light, the angle between the sun light and the camera was ~30°. The image is shown in figure 6.16 (b). In the scanned image, every segment has shown a different colour, which is in line with the results produced on the brass sample. However, the colour spectrums shown on SS sample is slightly different to the one produced on brass sample, which was most likely due to the surface roughness.

The SS sample (R_a = 6±2 nm) has a bigger surface roughness compared to the brass sample (R_a = 18±3 nm). As stated in the literature chapter (section 2.4.3), the LIPSS direction could be easily affected by the surface roughness, leading to a slightly scanned colour difference to brass sample. Although there is a slight colour difference between the different substrates, this experiment has shown that the colorizing technique could be applied on different metal substrates, which in principle is applicable to most substrates that can be covered by LIPSS. The limit of the current method is the uniformity of the LIPSSs. Better LIPSS uniformity could potentially lead to a more uniform colour regime and eliminate the colour difference on different substrates.

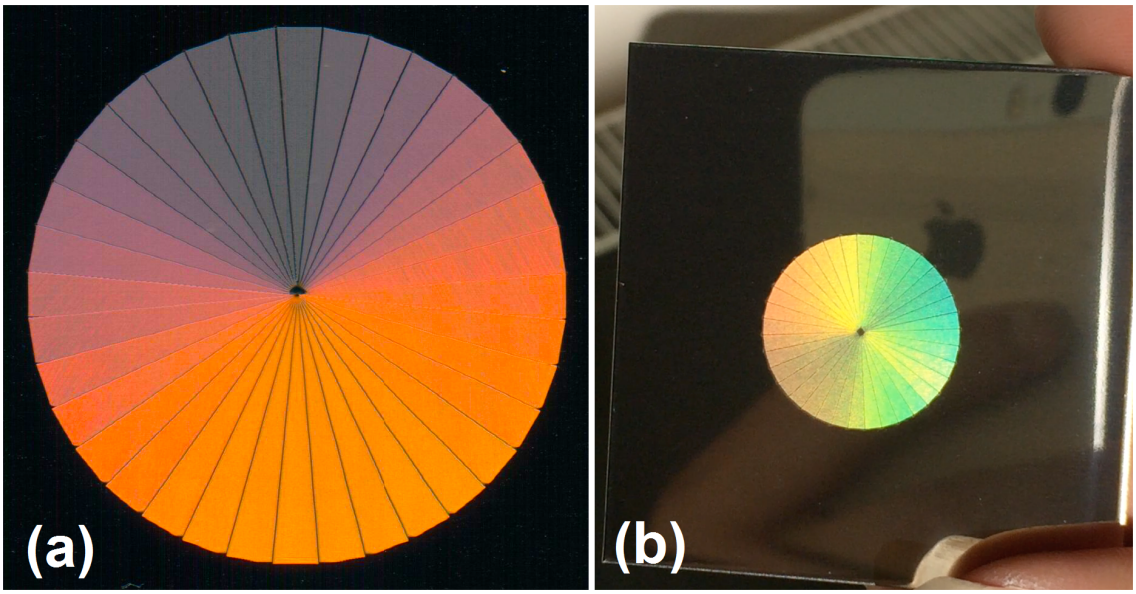

Figure 6.16 *(a) scanned image of a pie shape produced on SS sample. The pie contains 36 segments, which were produced with 36 different linear polarization orientations. (b) shows the same sample but the image was taken by a smart phone. The angle between the sunlight (window) and the camera was measured to be ~30°.*

In addition to use LIPSS as a method of generating a surface grating for metal surface colorizing, another laser colour marking method utilizes lasers as a heat source to oxidise the metal surface. This normally use nanosecond lasers, to generate a transparent or semi-

transparent oxide layer on the metal surface [246]. When illuminate the sample surface with white light, the reflected light from the surface of metal and oxide interfere with each other, resulting in a colour effect. The colour spectrum is determined by the thickness of the oxide layer, the order of interference and the refractive index of the oxide layer [246]. The colour produced with this method on the metal surface is constant when changing the illumination angle. The method has been widely applied on SS and titanium substrates, but rarely on other metals [246, 247]. Whereas, metal surface colorizing with LIPSS is relies on diffraction. It can be applied on almost all the metal surfaces and semiconductor surfaces as long as LIPSS can be produced[248]. A unique property of this type of surface colouring is that the colour on the sample varies with different illumination angles. The laser sources used for generate LIPSSs are femtosecond lasers and picosecond lasers, which is regarded as thermal free laser processing [22]. Figure 6.15 (a) shows the pattern illuminated at a special angle when there was no diffraction. It can be see that the colour of the pattern is greyish without diffraction, which is due to diffuse reflection compared to the smooth surface where mirror reflection happens. When the sample was illuminated in other angles that diffraction occurs, the colours shown on the sample surface varies with the illumination angle. As a conclusion, the surface colorizing using oxidation method is not considered has contribution to the surface colorizing in this experiment. However, a combination of the two could make the security patterning to a higher level.

6.8 Summary

Dynamic control of polarization has been demonstrated and used to manufacture complex surface micro/nano structures in real time with 1064 nm, picosecond laser processing.

This method allows the large area micro/nano surface structuring towards industrial application level. The resulting metal surface colouring with controllable LIPSS structure could potentially be applied in security metal surface patterning of valuable components and possibly for artworks. A highly flexible security patterning method is demonstrated with a calibrated colour scheme when the metal substrate was scanned with a normal scanner. This approach could provide a convenient method for customers who are eager to check the authenticity of a high value item colour encoded with this method.

Chapter 7 - Multi-beam high-speed thin film patterning of Aluminium on polyethylene terephthalate

7.1 Introduction

Thin film metal patterning of Cu, Au, Ag and Pt using picosecond and nanosecond solid state and UV Excimer lasers on polymers such as PET, polyimide, polyethylene naphthalate (PEN) and PMMA is employed in the fabrication of displays, RFID antennae, bio-sensors, photomasks and micro-fluidic devices [180]. With the synchronized picosecond laser and advanced micro-positioning control system described in section 3.4 in Chapter 3, high speed patterning of 30 nm thick Aluminium (Al) thin film on a flexible PET substrate is demonstrated with the aid of a phase only SLM addressed with optimised CGHs. Low fluence picosecond laser pulses minimize thermal damage to the sensitive substrate, leading to a clean, parallel beam, front and rear side thin film removal and good edge quality. With laser repetition rate of 200 kHz and 8 multiple diffractive beams, a film removal rate of $R_r > 0.5$ $cm^2 \cdot s^{-1}$ is demonstrated during selective patterning with a fixed CGH and 5 W average laser power. The application of 30 stored CGH's switching up to 10 Hz was also synchronized with motion control, allowing dynamic large area multi-beam patterning.

7.2 Experimental setup

A schematic of the experimental system is shown in Fig.1. The horizontally polarized output beam from the Coherent Talisker (Model: Talisker Ultra 1064-16) was expanded x3 (Jenoptic) then directed to a phase only SLM (Hamamatsu X-10468-04) addressed with appropriate CGHs. The laser was operating at 532 nm output for this experiment. A 4f optical system (f=400 mm) re-images diffracted multi-beams to the input aperture of the scanning galvo (Aerotech Nmark AGV-14HP) with 250 mm f-theta lens. Samples

(20 μm thick) were mounted carefully on a horizontally positioned mirror mount, allowing any transmitted radiation to expand freely below the PET substrate. This assembly was supported on a precision 3-axis (x,y,z) motion control system (Aerotech, A3200 Ndrive). The Aerotech Nmark AGV galvo scanner was combined with an Nmark CLS controller. This galvo has high resolution optical encoders allowing PSO triggering such that laser gating is synchronised to galvo mirror positions, allowing precise pointing of laser spots on target, even when using meters per second scan speeds.

The sample used in the experiment was 30 nm thick pure aluminium that screen printed on a 20 μm thick PET substrate. The PET substrate is optical transparent in visible light. The sample was provided by Centre for Phosphors and Display Materials, Brunel University. A soft plastic tweezer was being used for handling the sample and there was no cleaning before or after laser processing.

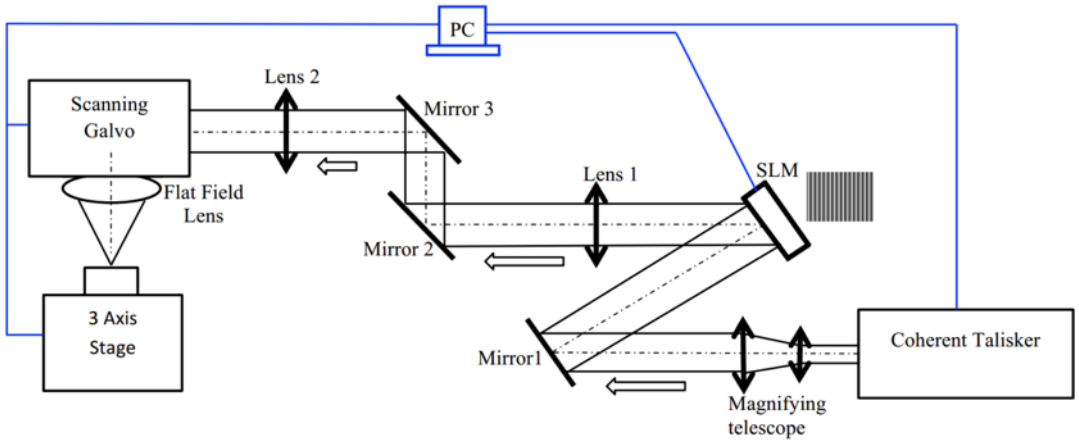

Figure 7.1 *Schematic of experimental setup, showing synchronous control of scanner, CGH application to SLM and laser gating.*

7.3 Single pulse ablation threshold

The experimental started with single pulse ablation. Two processing methods were adopted, front side and rear side ablation so that the incident light was absorbed in the aluminium film (front side) or transmitted through the PET and absorbed at the PET-Aluminium interface (rear side). Figure 7.2 shows the optical images of front side and rear side single pulse ablation of Al film with a fluence range of $0.3 < F < 1.5$ J·cm^{-2}. Ablated spot diameters are larger when using rear side ablation compared with the front side ablation with the same ablation fluence. This is an advantage, however, a disadvantage of rear side is observed in that delamination of the film occurs and so curls over at the edges much more in this case as can be seen in Figure 7.2 (e-h).

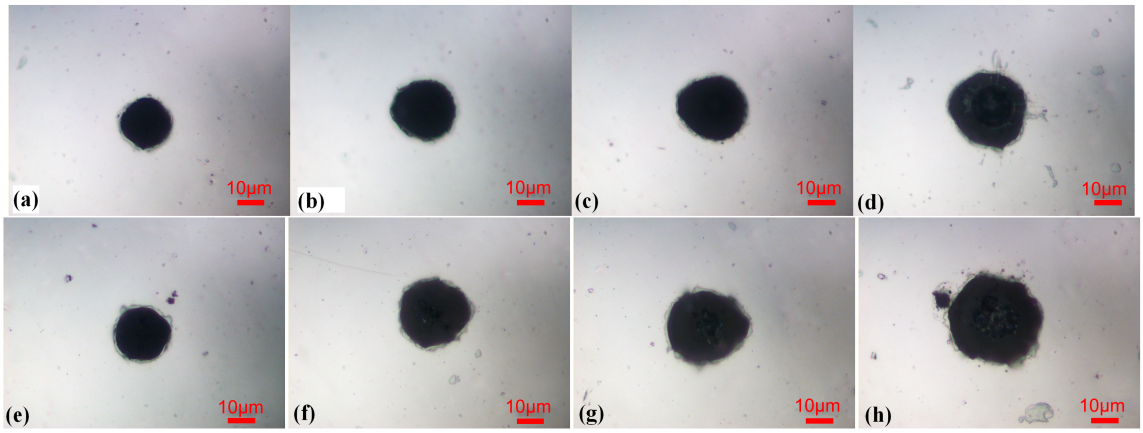

Figure 7.2 *(a-d) Optical image of single pulse front side ablation of Al/PET at fluence F = (a) 0.30, (b) 0.57, (c) 0.74 and (d) 1.48 J·cm^{-2}. There is clear PET damage at F = 1.48 J·cm^{-2}. (e-h) Optical image of single pulse rear side ablation of Al/PET at fluence F = (e) 0.30, (f) 0.57,(g) 0.74 and (h) 1.48 J·cm^{-2}. Scale bar represents 10μm. There is increased level of delamination with rear side ablation at the film edges and PET damage above F = 0.6 J·cm^{-2}.*

SEM images of the front and rear side single pulse ablation shown in Figure 7.3 (a) and (c) confirmed the delamination occurring at the film edge with rear side ablation is more

severe. Elemental analysis of the laser ablated area and the unprocessed area with Energy-dispersive X-ray spectroscopy (EDX) shows the complete removal of the Al from the PET substrate, which is shown in Figure 7.3 (b) and (d).

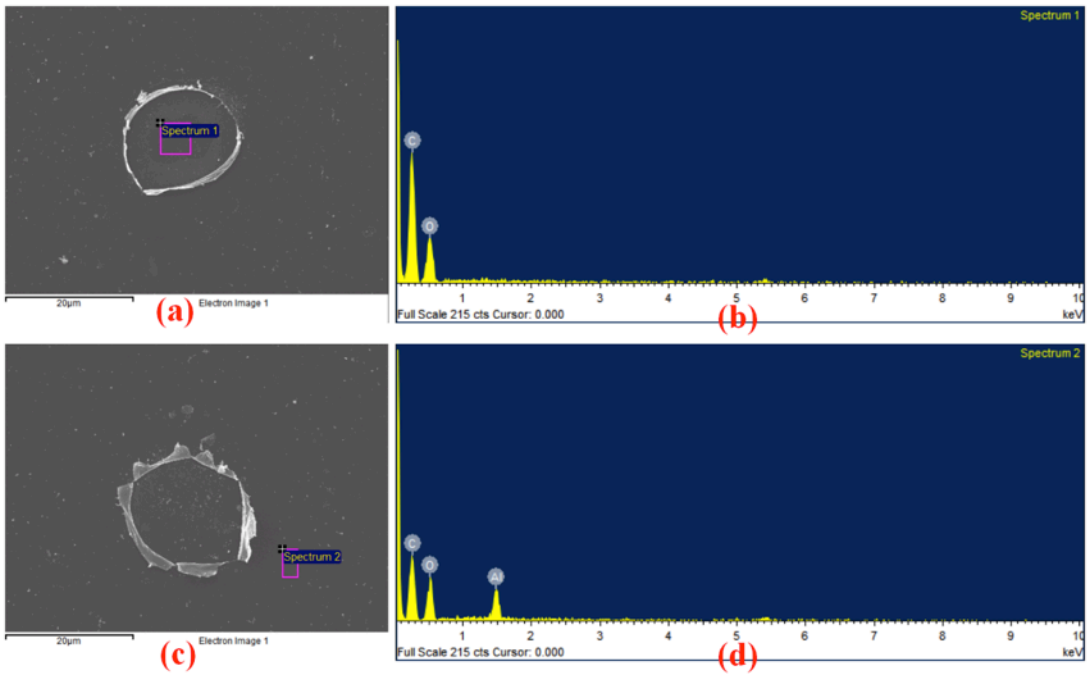

Figure 7.3 *(a) SEM image of single spot front side ablation with fluence F= 0.57 J·cm^{-2}, (b) elemental analysis in ablated spot using EDX, (c) SEM image of rear side single spot ablation at fluence F = 0.57 J·cm^{-2}, (d) EDX spectrum of Al film with Al peak near 1.5keV. In (b) there is no evidence of an Al peak indicating complete film removal. Delamination is more severe with rear side ablation than with front side ablation.*

The ablation threshold of the 20 nm Al thin film with front and rear side processing and also the damage threshold of the PET substrate with front side ablation were determined. Figure 7.4 shows a graph of the measured ablation spot diameter squared versus lnE_p where E_p is the incident pulse energy. By extrapolating to the x-axis, the front and rear side single pulse ablation threshold energy were measured to be $E_{p\ th}$ =0.69 µJ and 0.50 µJ respectively. The gradient ($2\omega_0^2$) yields the $1/e^2$ focal spot diameter to be $2\omega_0 \sim 29.7\mu m$ and hence ablation thresholds F_{th} = 0.20 ± 0.01 J·cm^{-2} (front) and

F_{th} = 0.15 ± 0.01 J·cm^{-2} (rear) respectively. The quoted errors are estimated by allowing variation of the gradient fits to the data. The lower threshold for rear side ablation is not unexpected, since direct heating of the interface between Al and PET (transparent) occurs with this geometry. The damage threshold of PET with front side ablation is measured to be $E_{p,th\ PET}$ = 4.06 μJ and fluence threshold $F_{th,PET}$ = 1.2 J·cm^{-2}, indicating a clear energy window for removing the Al thin film without damage to the PET substrate exists.

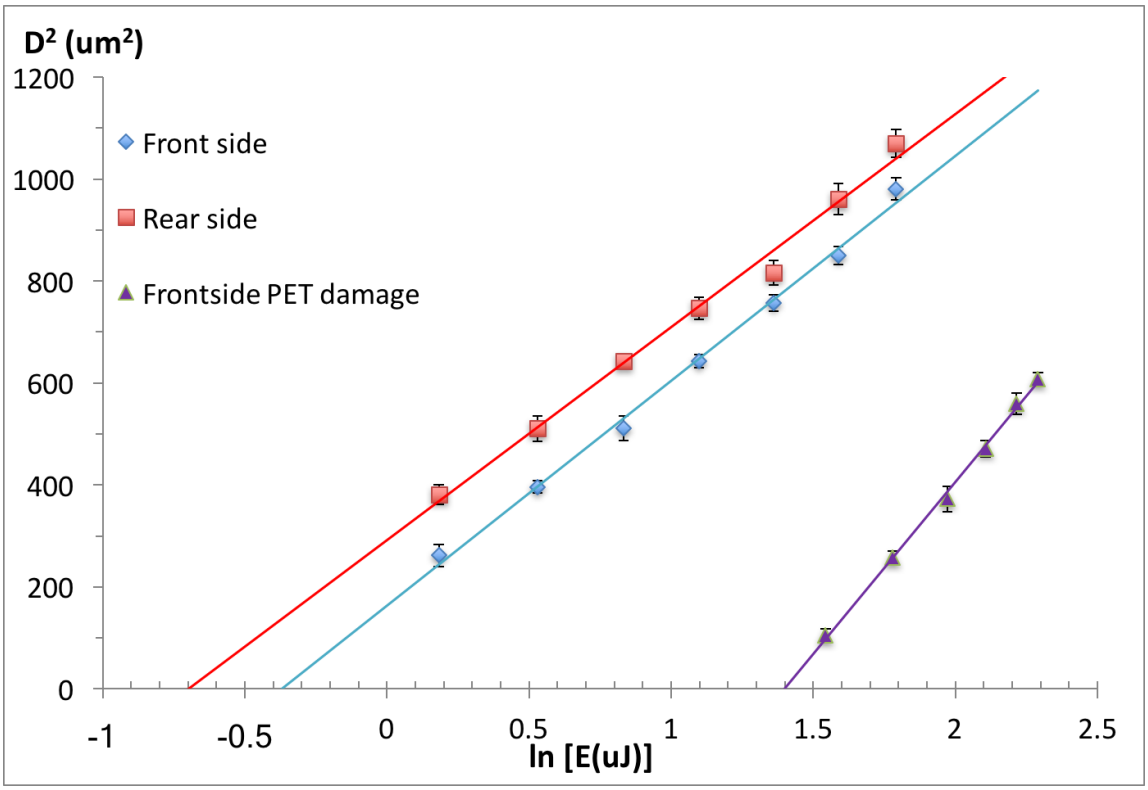

Figure 7.4 *Graph of ablation diameter squared versus lnE_p for both front and rear side ablation. Each point represents average of 10 measurements. The ablation thresholds are F_{th} = 0.20 ± 0.01 J·cm^{-2} (front) and F_{th} = 0.15 ± 0.01 J·cm^{-2} (rear) respectively. Front side ablation of the PET has a threshold $F_{th,PET}$ = 1.2 J·cm^{-2}.*

7.4 Single beam scribing

Since the rear side laser ablation of the Al on PET induces significant delamination on the edges of the ablated area, which reduced the processing quality, Al thin film on PET processing carried out in the following experiments are all with front side laser ablation. To achieve continuous scribing, a reasonable pulse overlap is required. Figure 7.5(a-f) shows the effect of varying pulse overlap at laser frequencies f = 1 kHz, 10 kHz and 100 kHz repetition rate with pulse energy E_P = 3 μJ (F=0.74 J·cm^{-2}). A straight edge was obtained when pulse overlap $N \geq 5$ but too high an overlap appeared to create edge tears in the Al film. These small tears were more apparent as laser repetition rate was increased. These were almost absent at 1 kHz, appear for pulse overlap N >20 at 10 kHz while at 100 kHz, they appear even for N > 6. This is likely related to thermal accumulation, increasing as repetition rate increases and period between pulses decreases. Too high a pulse overlap also leads to substrate damage through this thermal accumulation.

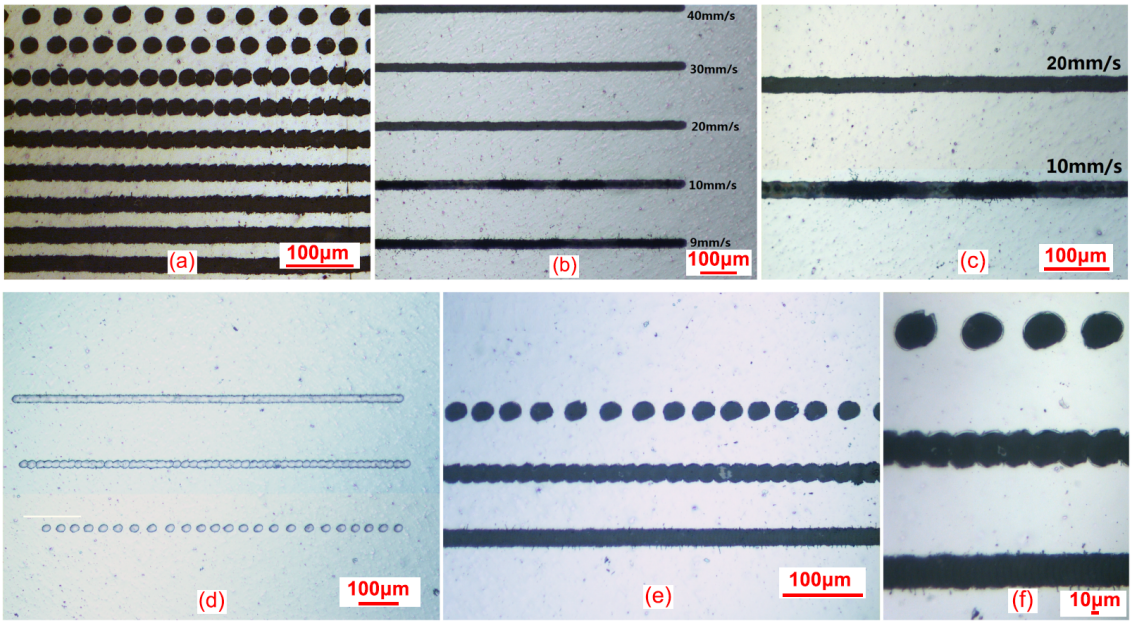

Figure 7.5 *(a) Effect of scribing at 1kHz rep. rate while varying pulse overlap with scan speed (top to bottom) 50, 40, 30, 20, 10, 5, 4, 3 and 2 mms^{-1}, (b) scribing at 10 kHz and scan speeds of 9 – 40 mms^{-1}, (c) detail of scribing at 10 kHz with 10 and 20 mms^{-1}, (d) scribing at 100 kHz with scan speeds 0.5, 2 and 4 ms^{-1}, (e) higher magnification image of scribing in (d), (f) detail of scribing in (e). At 1kHz, edge quality becomes acceptable around 4mms^{-1} or pulse overlap N ~ 8. Small tears are apparent in (c) at 10 kHz where pulse overlap N = 32 while in (f) at 100 kHz, small edge tears are clear in the lower scribe at 0.5 ms^{-1} where overlap N = 6.*

7.5 Single beam patterning

The experimental setup was configured to produce patterns on Al on PET thin films since the front side scribing with the picosecond laser system provides clean film removal and minimal damage to the PET substrate. Figure7.6 (a) shows a large zone plate type mask (~20 mm diameter) machined with E_P = 3 µJ pulse energy (F = 0.74 J·cm^{-2}) at f = 40kHz repetition rate, 200mm·s^{-1} scan speed and 10µm hatch (pulse overlap N ~ 6/spot diameter). Figure 7.6 (b, c) shows optical images of a section of the mask in more detail showing good edge quality. The surface roughness of the PET before Al coating was applied was R_a *(PET)* = 43 ± 4 nm. The Surface roughness of the Al on PET and the exposed PET after

Al ablation was measured using the Wyko NT1100 white light interferometer and found to be, R_a *(Al/PET)* = 62 ± 4 nm, R_a *(PET)* = 55 ± 2 nm respectively, shown in Figure 7.6 (e) and (f) respectively. A view through the exposed PET with visible light illumination confirmed optical transparency is slightly affected. However, the minimal damage to the PET is still acceptable in lots of the applications. The edge between Al/PET and exposed PET is shown in Figure 7.6 (g), showing a melt burr, approximately 1 µm in height.

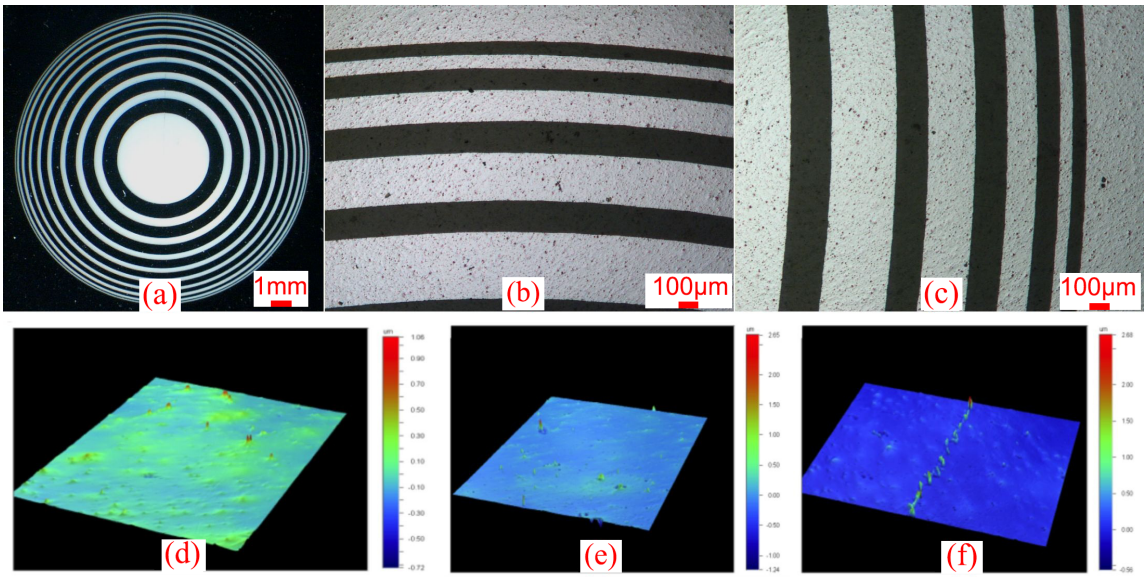

Figure 7.6 *(a) Optical image with front side illumination of single beam scribing with large zone plate type pattern, (b) detail of edge definition of outer ablated rings at top of (a), (c) detail of outer ablated rings at right side of (a), (e) White light interferometry image of the surface roughness on Al/PET, (f) exposed PET surface after Al ablation, and (g) edge between Al/PET and exposed PET showing a melted burr ~ 1µm in height.*

The system was then configured to ablation a square area of 1.1 x 1.2 cm^2 at 1 ms^{-1} with no laser gating (except at the start and end of scan lines) and 10 µm scan offsets, the processing time took τ = 13 s, slightly higher than expected (~10 s) due to deceleration times at scan start and end delays in implementing G code (motion control) programming

in the Aerotech system. Processing rate was therefore R_r = 10.2 mm^2·s^{-1}. A chessboard pattern (1.1 cm x1.2 cm) with 200 µm squares was micro-machined at 200 kHz, s = 1 m·s^{-1} scan speed, and 10 µm offsets, created by setting appropriate gating windows in the scan program for PSO. The results are shown in Figure 7.7(a-c). The time taken to produce the chessboard pattern was τ ~22 s, giving a processing rate of R_r ~6.0 mm^2·s^{-1} for this pattern, nearly double the fabrication time compared to the complete film removal, showing that the inclusion of the PSO gating for patterning has a cost in terms of film removal speed. This is due to implementing real time feedback signals from the AGV-14 galvo mirrors by the CLS controller in the Aerotech system. On the other hand, the PSO gating is very effective for patterning.

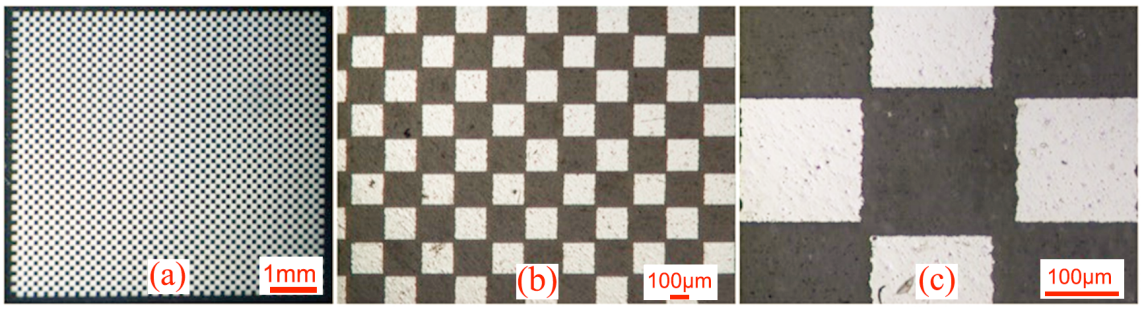

Figure 7.7 *(a) Optical micrograph of chess board pattern created with single beam (f = 200 kHz, E_P = 3 µJ, s = 1 ms^{-1}, P = 0.6 W, (b) higher magnification image of (a), (c) detail of (b). Edge quality looks reasonable. The chessboard pattern resulted from line by line scanning combined with precise laser gating.*

To emphasize the significant advantage of the PSO function in generating high quality patterning, a comparison process without PSO function during laser ablation of the chessboard pattern was carried out.

Figure 7.8 (a) shows the schematic of the laser scanning geometry without applying the PSO function: every single 0.2 mm^2 square was produced one by one, hence the laser

beam needs to accelerate and decelerate within the 0.2 mm distance. The maximum speed achieved by the beam moving within a 0.2 mm square was tested to be 210 $mm \cdot s^{-1}$. Setting scan speed any higher was therefore avoided. Figure 7.8(b), on the other hand, shows the strategy with the PSO function on: the laser beam was scanning a 12 mm × 12 mm square with a constant speed of 2 $m \cdot s^{-1}$ while the laser was gated on and off at desired positions where the PSO provides feedback signals in real time. As an example, the laser beam was gated on only in windows that formed by a green line on the left side and a blue line on the right side that shown in Figure 7.8 (b) and the laser was gated off outside the windows, which produces a batch of squares with one step. The acceleration distance for laser beam to achieve $1 m \cdot s^{-1}$ from static was tested to be 1 mm. The space for galvo acceleration and deceleration were all set at the outside of the processing window. The red arrows in Figure 7.8 indicate the laser beam scanning paths on the sample with a line offset of 10 μm.

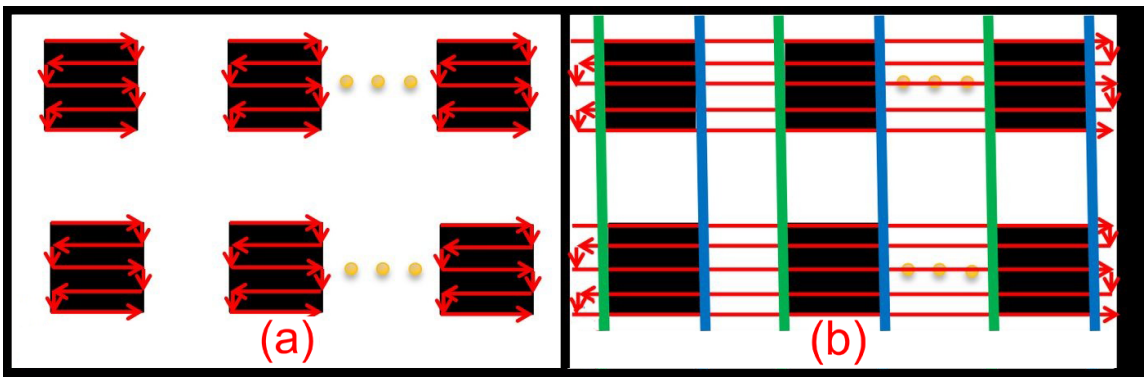

Figure 7.8 *(a) schematic showing the single beam laser processing without PSO function and (b)single beam laser processing with PSO function active. The window between the green and blue lines formed the "laser on" processing windows, while the laser was gated off outside these regions. The red arrows indicate the laser beam paths on the sample.*

The comparison experiments were carried out with three processing parameters but the same processing pattern – a chessboard pattern as shown in Figure 7.7(a). Laser fluence was attenuated to F = 0.74 Jcm^{-2} and the laser beam was scanning horizontally with 10 μm vertical separation (hatch) between lines providing pulse overlap in the vertical. Without PSO function, processing parameters were set at: 10 mm·s^{-1} laser scanning speed at f =1 kHz rep. rate, 20 mm/s at f =2 kHz and 200 mm·s^{-1} at f = 20 kHz. The results are shown in Figure 7.9 (a-c) respectively.

In each case, with f =1 kHz -20 kHz, squares produced without PSO functions have significant damage to the substrate at the edges of the squares, which is caused by the accumulation of laser pulses due to the acceleration and deceleration of the scanning galvo, even with 1 kHz laser repetition rate and 10 mm/s laser scanning speed.

Result shown in Figure 7.9 (d) was produced with PSO function and f = 200 kHz with 1m·s^{-1} laser scanning speed, gated in real time. The squares produced with PSO function exhibit no substrate damage to the edges or any other areas even with scan speed of 1000 mm·s^{-1} at f =200 kHz. One may point out the "laser on" delay and "laser off" delay functions normally available in most non-digital galvo software control systems, which could be adopted to eliminate the substrate edge damage. However, the efficiency of the processing would still be very low compared processing with PSO function as the maximum laser scanning speed for 200 μm lines is 210 mm·s^{-1}.

The processing time to produce the same chessboard pattern with no PSO function was τ = 273 seconds (4.5 mins) with 200 mm·s^{-1} laser scanning and f = 20 kHz, giving a processing rate of R_r = 0.48 mm^2·s^{-1}. This rate would be even lower using lower scanning

speed, which causes slightly less damage to the scan ends. However, with PSO function, scan speed of 1000 mm/s and the laser operating at highest rep. rate, f = 200 kHz, the processing rate R_r = 6 $mm^2 \cdot s^{-1}$, a gain of G = 12.5.

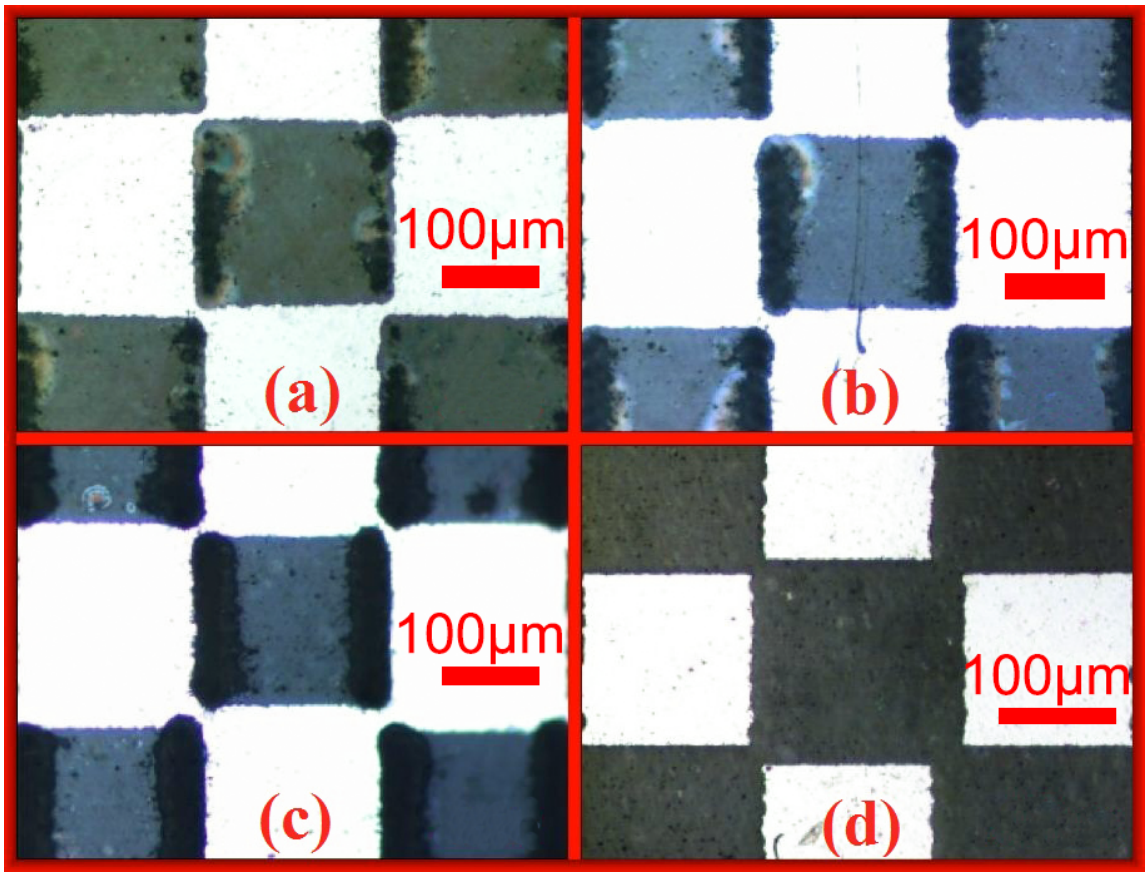

Figure 7.9 *microscope images of processed squares in a chessboard pattern; (a) 1kHz laser repetition rate and 10 $mm \cdot s^{-1}$ scan speed without PSO function, (b) 2 kHz and 20 $mm \cdot s^{-1}$ scan speed without PSO function, (c) 20 kHz and 200 $mm \cdot s^{-1}$ without PSO function, (d) 200 kHz laser repetition rate and 1000 $mm \cdot s^{-1}$ laser scanning speed with PSO function switched on. The squares produced without the PSO function cause damage to the edges of the squares (with a darker colour) by pulse accumulation due to the beam acceleration and deceleration.*

Note that the corner of the squares in figure 7.9 (d) are overlapped and asymmetric, while the squares in figure 7.9 (a-c) are not. This is due to the laser gating position setting error,

which can be easily corrected by recalibrate the gating position according to the focused beam size.

7.6 Multi-beam high speed patterning with fixed hologram on SLM

By applying an optimized CGH on the SLM, produced with GS algorithm [214] shown in Figure 7.10 (a), 8 diffractive spots with uniform energy distribution were produced on the focal plane with their positions located at desired places, shown in Figure 7.10 (b) red spots. These 8 diffractive spots, all with the required energy were used for high speed patterning the same chessboard pattern on Al/PET combined with PSO function. The result is shown in Figure 7.11.

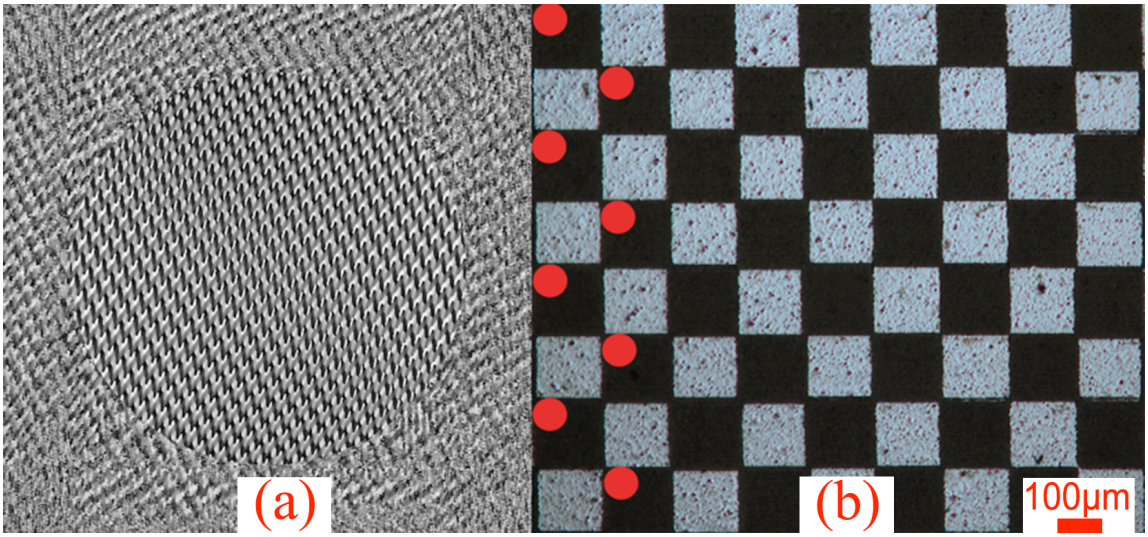

Figure 7.10 *(a) an optimized phase CGH with the GS algorithm which generated a 2×4 spot array for multi-beam processing, (b) a schematic indicating the approximate 2×4 array spot positions on the substrate used to create the chessboard pattern. The array was scanned horizontally to the right at s = 1 m·s^{-1} while the beams were synchronously gated on and off. The chessboard pattern resulted from line by line scanning.*

The resulting chessboard pattern (Figure 7.11 (a)) was completed in $\tau = 3.5$ s with a scan speed of 1 m·s^{-1} at $f = 200$ kHz and pulse energy $E_p \sim 3$ µJ/spot. This corresponds to a processing rate of 37.7 mm^2·s^{-1} with this 200 µm size pattern with no loss of resolution apparent. The gain in micro-structuring rate over single beam with PSO function for this pattern is therefore $G = 6.3$, and gain over single beam without PSO function is $G = 78.5$. The significant gain in throughput with no cost in patterning quality while used the full available laser output (7.5 W) and delivered nearly 5 W in first order diffracted beams at the substrate, with a diffraction efficiency $\eta_{+1} > 80\%$ and overall optical transmission of ~67%. The zero (and higher) order spot energies were well below threshold, thus leaving the Al film untouched.

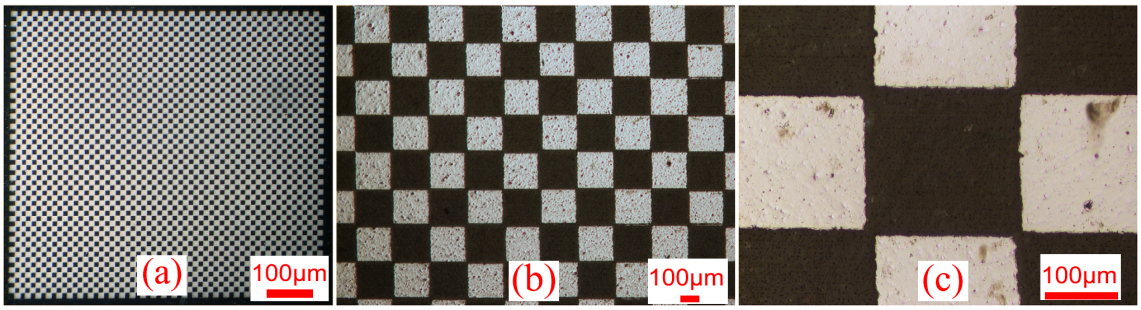

Figure 7.11 *(a) Low magnification optical image of chess board pattern created with high speed multi-beam processing of 200 µm squares at f = 200 kHz, s = 1 ms^{-1} scan speed with 8 near uniform beams, (b) higher magnification image of (a), (c) detail of squares in (b). Edge quality looks just as good as single beam.*

By using higher scan speed of $s = 2$ m·s^{-1}, the 200 µm pitch chessboard pattern was completed in $\tau = 2$s, corresponding to micro-machining rate $R_r \sim 66$ mm^2·s^{-1} with slightly degraded vertical edge quality due to the fact that the laser was free running and laser pulses were not precisely synchronized with motion control system. This can lead to a spot horizontal offset of up to ±5 µm from line to line at 200 kHz repetition rate. It can be

seen that after the laser gating position is re-calibrated, the squares are more symmetrical and less overlapped with each other, see figure 7.11 (c) and figure 7.6 (c).

7.7 Multi-beam patterning with dynamic modulation of beam position

A series of 30CGH's (pre-calculated with GS algorithm and saved in the computer used to control the SLM) producing 5 spots with varying separation were run in real time to create circuit electrode type patterns while synchronized to the scanner motion control (Nmark-CLS), results are shown in Figure 7.12. The scan speed was kept constant at s = 10 mm·s^{-1} at $f = 10$ *kHz* with pulse energy $E_p \sim 3$ μJ/spot, resulting in clean Al film removed with a continuous line pattern. The region where the electrode dimensions widen had 28 CGH's, applied at 10 Hz, close to the present bandwidth limit with CGH synchronization. While this limits throughput even with 5 diffractive spots, nevertheless, patterning was achieved with application of dynamic phase masks applied to the SLM.

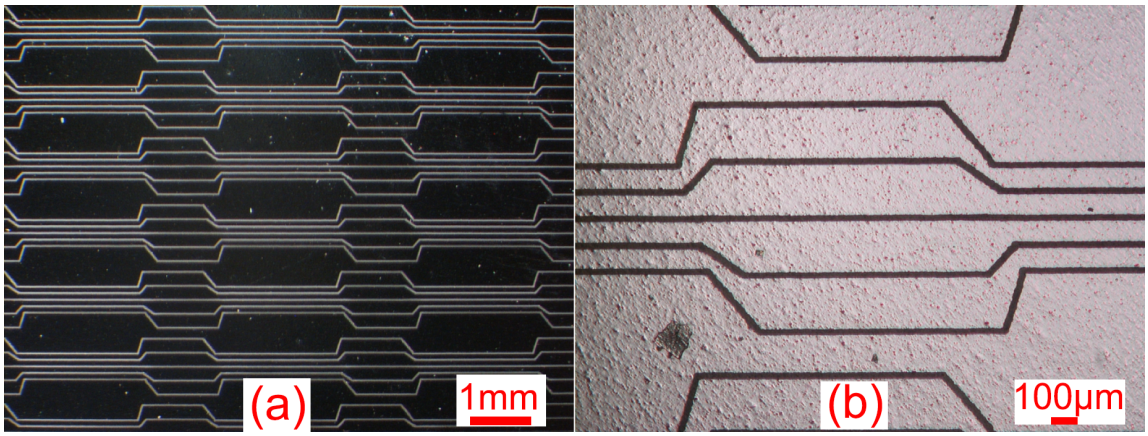

Figure 7.12 *(a) Optical image of large area multi-beam (5 spot) structuring of electrode pattern created with real time application of 30 CGH's synchronized with scanner motion, (b) magnified optical image (detail) of electrode pattern shown in (a). The region where the scribes expand off axis was patterned with 28 CGH's while the parallel scribe regions are due to CGH 1 and 30, which are identical.*

7.8 Applications of high speed ultrafast laser thin film patterning

An application of picosecond laser patterning Al thin film on PET is demonstrated in Figure 7.13, which shows light emission from two Alternating Current Electroluminescent Lamps (ACEL) created at Brunel University from samples produced by our picosecond laser system. Figure 7.13 (a) is the pattern produced on Al on PET sample (dark areas are Al whilst white lines are ablated by laser beam). The patterned Al on PET, which is acting as an electrode, is then coated with a layer of phosphor material and followed by sputtering a transparent conducting oxide (TCO) layer on the top, which is ITO, acting as a top electrode. The schematic of the ACEL formation is shown in Figure 7.14. Applying AC current on the finished device, shown in Figure 7.13 (b), produces uniform light source. Figure 7.13 (b) is another ACEL device produced with a simple rectangular area.

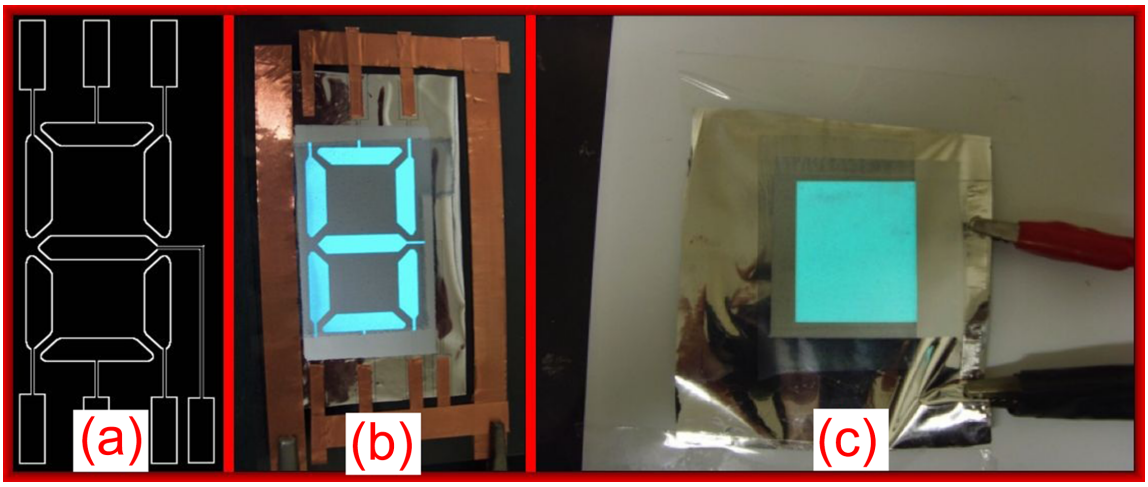

Figure 7.13 *(a) pattern produced on Al on PET thin film with picosecond laser beam, back areas are Al thin film and white lines are produced with laser ablation; (b) lamellar digital number 8 ACEL device produced and emits uniform light with AC current applied (c) rectangular ACEL device emitting uniform blue light. The ACEL devices were coated by Dr.Paul G Harris, Brunel University.*

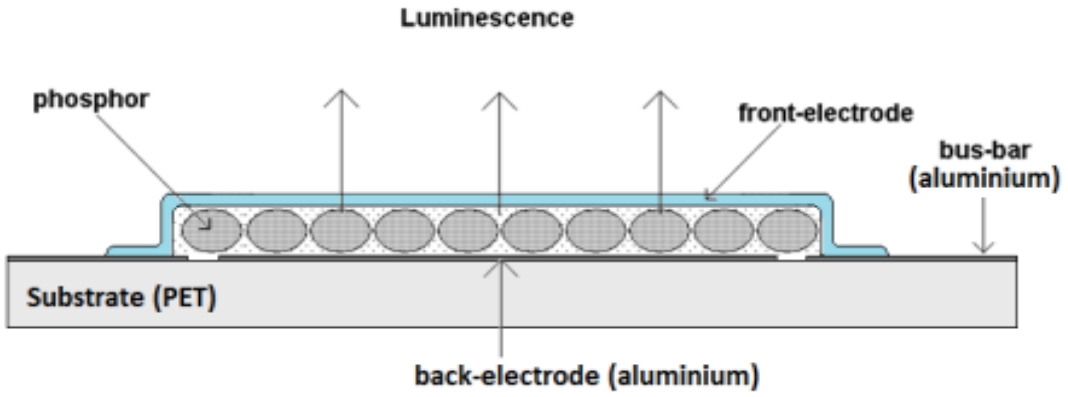

Figure 7.14 *Schematic of the ACEL structure, which is a sandwich structure with the laser scribed Al pattern acting as the back-electrode and TCO layer on the top act as a front-electrode. By applying AC high voltage (>50V) across the two electrodes, the phosphor sandwiched between the electrodes emits uniform luminescence.*

Figure 7.15(a) shows two interdigitated structures produced with 30 μm pitch which is significantly better than the resolution that normal screen-printing can achieve (~100 μm). Details of the interdigitated pattern are shown in Figure 7.15 (b, c), within which the black areas are Al thin film and the white lines result from the laser ablation of Al thin film. The

capacitance of interdigitated structure was measured to be 2 nF, hence these devices could be used as flexible capacitors. The capacity could be further improved by coating with high dielectric constant inks, which are relatively easy to formulate and are readily available commercially.

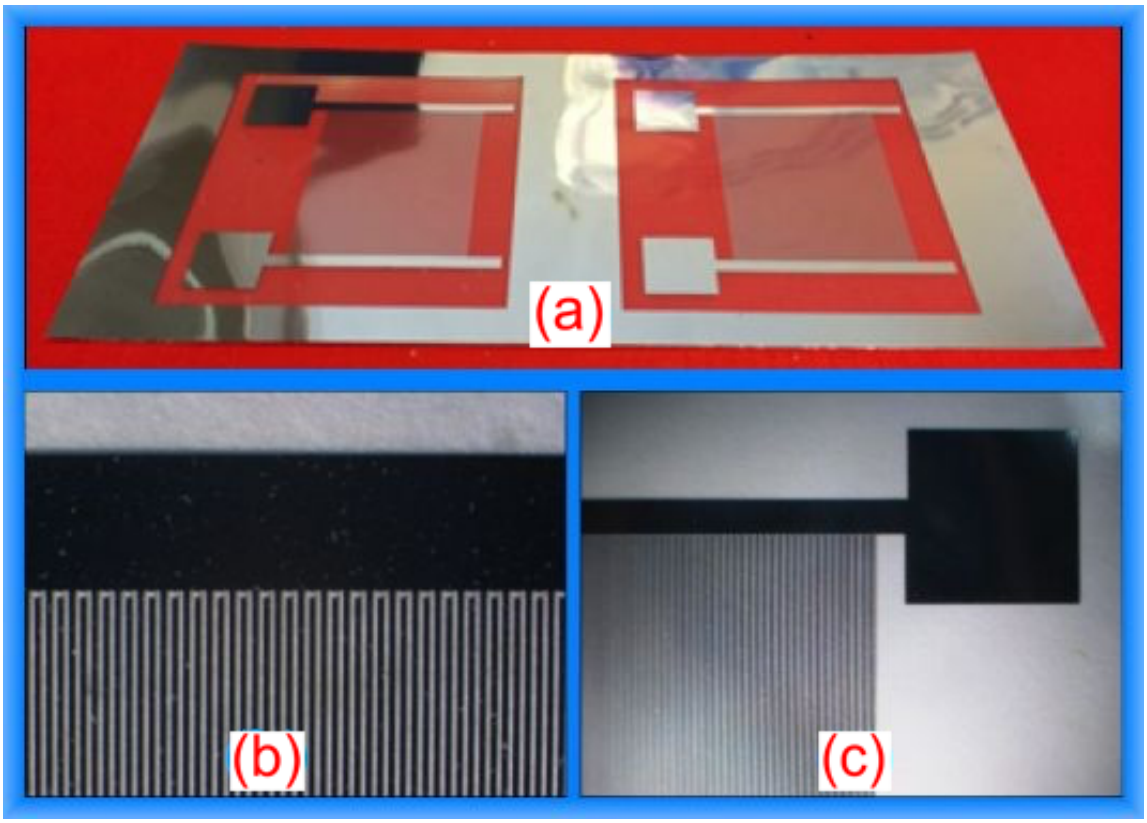

Figure 7.15 *(a) Photograph of 30 μm pitch interdigitated structures produced on Al on PET thin film with picosecond laser system, (b) and (c) magnified images of the interdigitated structure (Dark areas are remained Al and the white lines are laser scribed lines).*

7.9 Discussion

Since the focal spot size on the substrate is ~30 μm while Al film thickness is d ~30 nm, heat diffusion and ablation can be considered to be a 1-dimensional process. The complex refractive index of Aluminium is given by [249], $n_{532} = n_0 + ik = 0.94 + 6.42i$, hence the

reflectivity $R_{532} = [(n_0 -1)^2 + k^2] / [(n_0 +1)^2 + k^2] = 0.92$, while the absorption coefficient $\alpha_{Al} = 4\pi k/\lambda = 1.52 \times 10^6$ c/m. The optical penetration depth l_s is therefore $l_s \sim 1/\alpha = 6.6$ nm while 86% of incident pulse absorbed within $2l_s \sim 13$ nm, significantly less than the film thickness.

A study of the ultrafast dynamics of the solid-to-liquid transition in a 1μm thick Aluminium film using 40fs pulses showed that this transition takes place within 1.5 – 2 ps [250]. As the laser temporal pulse length τ_p (10 ps) is significantly longer than electron-phonon coupling time $\tau_{e\text{-}ph}$, then phonons carry energy to a depth $l_{th} \sim \sqrt{(2D_{Al}\tau_P)} \sim 40$ nm, just larger than the film thickness, where diffusivity of Al is taken as $D_{Al} = 0.9$ cm^{2}s^{-1} [251]. However, the thermal diffusivity of PET is very much lower, $D_{PET} = 0.001$ cm^{2}s^{-1} [252], giving a heat diffusion depth of $\sqrt{(2D_{PET}\tau_P)} \sim 1.4$ nm. In this case, the PET produces an effective stop for heat diffusion at the interface. While the melting point of Al is $T_m = 660$°C, PET melts at a modest 254°C and so, can easily be damaged. However, PET is essentially transparent in the visible and NIR, with an absorption coefficient at 532 nm, $\alpha_{PET,532} \sim 3$ cm^{-1} [201]. This high transparency helps to minimize the likelihood of PET damage from laser exposure once the Al film has been removed.

The measured ablation threshold here, $F_{th} = 0.20 \pm 0.01$ J·cm^{-1} is similar to the damage threshold measured by Kandyla [250], $F_{th} \sim 0.21$ J·cm^{-1} on Al film/glass using 40 fs pulses at 800 nm and close to that of Doerr [251] who measured a damage threshold, $F_{th} = 0.18$ J·cm^{-1} at $\tau_p = 2$ps pulse length and wavelength 400 nm on a 20 nm thick Aluminium film on fused silica. The similarity of these thresholds is interesting in spite

of the differences in temporal pulse lengths and wavelengths. The pulse length used here, τ_P = 10 ps is much shorter than the critical pulse length τ_c ~ 60 ps in Al, below which the ablation threshold is expected to be independent of temporal pulse length and calculated from reference [253].

An estimate of the ablation threshold has been made for a 30 nm film thickness as follows. The ablation threshold can be estimated with a hypothesis that the Al film is brought from room temperature to the melting point then evaporation temperature within the temporal pulse duration. Assuming that surface reflectivity drops from R = 0.92 (solid) to around R = 0.88 (liquid) after approximately 2ps when the surface has melted [254] and that the diffusivity drops to D_{liq} ~ 0.32 $cm^2 \cdot s^{-1}$ [255] at the melting point. The heat diffusion depth is then slightly lower than in the solid, $l_{th} = \sqrt{(2D_{liq}\tau_p)}$ ~25 nm, close to the film thickness. Assuming the film comes to a uniform temperature throughout, the absorbed fluence needed to evaporate the film completely is given by:

$$F_{th,\,inc} = [F_1 + F_2 + F_3 + F_4] \quad (1)$$

where F_1 is the fluence required to achieve the melting point of Al, F_2 is the fluence needed to complete melting, F_3 is the fluence needed to heat the Al to the boiling temperature, and fluence for complete vaporization, F_4. Then,

$$F_1 = d\,(1-R_1)^{-1}\,C_S(T_m - T_0) \quad (2)$$

$$F_2 = d\,(1-R_2)^{-1}\,H_m \quad (3)$$

$$F_3 = d\,(1-R_2)^{-1}\,C_l\,(T_v - T_m) \quad (4)$$

$$F_4 = d\,(1-R_2)^{-1}\,H_v \quad (5)$$

where d is the film thickness (3×10^{-6} cm), R_1 is the reflectivity of the Al when it is solid (0.92) and R_2 is the reflectivity of Al when it is melted (0.88), Tm is the melting point (660°C), T_0 is room temperature (assuming 20°C), T_v is the boiling point (2470°C), C_S is the volume specific heat of the solid Al (2.43 $Jcm^{-3}K^{-1}$), C_l is the volume specific heat of liquid Al (2.38 $Jcm^{-3}K^{-1}$), H_m is the melting enthalpy (1.08×10^3 $J{\cdot}cm^{-3}$) and H_v is the evaporation enthalpy (3.19×10^4 Jcm^{-3}). The four terms of equation (1) when calculated, yield $F_{th,\mathrm{inc}} = F_1 + F_2 + F_3 + F_4 = (0.058 + 0.027 + 0.107 + 0.78) = 0.972$ $J{\cdot}cm^{-2}$.

This simple estimate indicates that complete evaporation of the film would require almost five times the ablation threshold actually observed. However, the sum of the first three terms needed to bring the film to the boiling point is $F = 0.19$ $J{\cdot}cm^{-2}$, close to the measured front side ablation threshold. This fluence can account only for some limited evaporation. According to the above model and the increased surface roughness of the PET substrate, it is likely that heat diffusion to the interface will raise the polymer surface temperature above its melting point, causing decomposition of a very thin, nm thick layer of the PET, resulting in an explosive type removal process due to pressure build up at the Al/PET interface. The observed lower rear side ablation threshold supports this method of film removal. This mechanism was first described by J. E. Andrew *et al.* [256] during excimer studies of 308 nm ablation of Al films on Mylar, where a threshold $F_{th} = 0.14$ $J{\cdot}cm^{-2}$ (120 nm thick) was consistent with theoretical calculation of fluence required to melt the film.

7.10 Summary

Front and rear side ablation of thin film (30 nm) Aluminium on flexible PET has been demonstrated with minimal damage to the sensitive polymer and ablation thresholds determined. Although the rear side ablation provides a lower ablation threshold, the delamination on the edges of the ablated spot was observed to be more severe than with front side, which may result from in-sufficient fluence on the wings of the Gaussian intensity profile. The installation of a new high resolution Galvo, the Aerotech Nmark AGV-14HP galvo with optical encoders, combined with the Aerotech CLS controller has created a high speed precision micro-fabrication system.

By applying optimized CGH's to a phase only SLM to create uniform multi-beams, high speed 8 spot patterning of the Al film with fixed CGH was demonstrated, providing a film removal rate of $R_r > 0.5$ cm^2·s^{-1} with average power of $P \sim 5$ W with minimal damage to the sensitive PET. Dynamic, multi-beam large area patterning of the Al film was also demonstrated with optimized 30 CGHs applied at 10 Hz and synchronized to the scanning galvo. Finally, applications of picosecond laser patterning of Al thin film on PET were demonstrated -ACEL devices and capacitors indicating future potential industrial applications.

Chapter 8 - Conclusions and recommendation for future work

8.1 Conclusions

In this thesis, static and real time dynamic modulation of polarization and wavefront of ultrafast picosecond laser beams using phase only SLMs have been investigated. The modified polarization states, including novel radial and azimuthal polarization states were confirmed by complex LIPPS patterns ablated on polished metal surfaces.

After static modulation of the incident linear polarization with planar wavefront to radial or azimuthal polarization with vortex or planar wavefront, this was followed by demonstrating the generation of multi-diffractive beams with arbitrary polarization and wavefront structures.

A novel optical setup with two phase-only SLMs was fully synchronized with the 532 nm picosecond laser and advanced digital galvo with 3-axis motion control system. Hence, for the first time, real time, dynamic control of four distinct polarization states, - radial, azimuthal and two orthogonal linear polarization states all with a Laguerre–Gaussian ring intensity distribution were employed in ultrafast laser surface micro-structuring. A maximum bandwidth of 12.5 Hz was demonstrated, limited by the response time of the SLM. This technique enabled metal surface encoding with controllable complex, sub-micron (Λ ~0.5 μm pitch) plasmonic structures.

With a 10 ps, 1064 nm source and single phase only SLM, dynamic, large area colourizing of metal surfaces with direction controlled laser induced periodic surface structures, (LIPSS~1μm pitch) was achieved by dynamically tailoring the linear polarization orientations (0 - 360°) using grey level CGH'S synchronized with a galvo scanner. This

is an interesting method for synchronous linear polarization rotation, avoiding a mechanically driven rotating half wave plate. Examples of utilizing this method for security metal surface patterning were then demonstrated.

The front and rear side single pulse ablation thresholds of a 30 nm thick Al film on flexible PET were determined at 10 ps, 532 nm and found to be F_{th}= 0.20±0.01 J·cm^{-2} and 0.15±0.01 J·cm^{-2} respectively, much lower than the PET ablation threshold, F_{th}=1.2 J·cm^{-2}. A simple calculation of the expected Al film ablation threshold, however, gave F_{th} ~1 J·cm^{-2}, a factor of 5 higher. The observed experimental ablation threshold can be explained due to heat diffusion to the interface which leads to melting and decomposition of the polymer, blowing off the film above. A clear fluence window was determined which allows film ablation while avoiding PET damage. With this knowledge, high speed parallel beam patterning of aluminium thin film on flexible PET substrate was carried out at λ = 532 nm using an optimized CGH generating a uniform, 8 spot array combined with precise, fast gating of the laser ps laser source on target. Laser power of 5 W of the 8 W laser output was thus delivered to the substrate at the highest laser repetition rate, f = 200 kHz while scanning at a constant speed *s* = 1m·s^{-1} and patterning rate = 0.5 cm^2·s^{-1}. By avoiding accelerations and decelerations during galvo motion, this advanced optical setup improved the efficiency of thin film processing by a gain factor of ~ 6 over single beam processing with the advanced AGV scanner and by a gain factor G > 78 compared to single beam thin film patterning with a normal scanning galvo. Synchronised, real time application of 30 CGH's was also used to pattern the Al/PET but at significant cost to processing speed.

8.2 Recommendation for future work

The Hamamatsu SLMs (X-10468 series) used in this thesis can clearly handle 8 W average power with stable diffraction efficiency over many hours without damage. The 532 nm model was previously tested with ns pulses with >10W average power [213] with no additional cooling required due to a ceramic cooling plate integrated into the SLM structure. In fact, a 14.7 W average power laser beam has been successfully applied on a water-cooled SLM (Holoeye LC-R 2500) without inducing any detrimental thermal effects [257]. As the Hamamatsu devices have dielectric coatings with high damage thresholds, the addition of liquid cooling to this type of SLM may well allow handling of average laser power over 100 W so that industrial applications of laser-materials micro-structuring with SLM technology is likely to increase in importance in the next few years. Higher average powers increase likely hood of industrial take-up. Hence, processing with current high average power ps laser systems (>50 W) combined with synchronized, liquid cooled SLM and motion control is recommended for higher speed, precision surface processing.

Moreover, surface encoding with complex submicron periodic structures is worth further investigation for applications of security data encoding on metal surfaces in anti-counterfeiting. Since optical field of a picosecond laser beam can be manipulated arbitrarily, the nano- or micro-structures produced on a metal surface can be highly controllable, encoding metal surface or metal thin film with the complex micro-structures. After encoding, the next stage would be to read the data back reliably.

Metal surface colourising could be further improved by using a flattop beam with better prepared surface finish, which would produce more uniform LIPSS structures [129] and a purer colour diffraction. Since LIPSS structures (LSFL) are on the same order of the wavelength of the incident beam, incident wavelength modulation could also be exploited. Optical Parametric Amplifiers such as a Topas-C or Topas-prime, made by Light Conversion [258], is a widely tunable ultrafast laser source which could be fully synchronized with a motion system for dynamic control of wavelength for metal surface encoding. This would add an additional degree of complexity for security marking by altering LIPPS period, provided the SLM also had a wide wavelength capability.

Surface colouring by modifying the oxide layer thickness on SS and titanium has been well researched. However, the combination of using LIPSS and oxidation has never been researched. The combination of the two could improve the security patterning to a higher level. Hence, the combination of using LIPSS and oxidation for security patterning is worth to be carried out. The effect the depth of the LIPSS on colorizing metal surface was not carried out due to equipment and time limit. However, this area is an interesting area to industrialize the colouring metal surface with LIPSS.

In the area of thin film processing, stacking multiple layers of Al on PET thin films together and processing the stacked thin films simultaneously with parallel beams could increase throughput even further but this would require higher available pulse energy and average power. If one had higher available pulse energy, shaping beam geometry for thin film patterning is also worth investigating. For example, square-shaped or cross-shaped geometries with uniform intensity can be used for high speed patterning Al on PET for possible terahertz filters, capacitors and strain sensors.

Finally, the dynamic techniques developed here could be useful in femtosecond micro-structuring inside transparent dielectrics which are sensitive to incident polarization [11,30,101-103], and intensity distribution. Hence, multi-diffractive beams with dynamic, controllable polarization and mode could be exploited for more complex internal structuring of materials. For example, dynamic modulation of polarisation from linear to circular or using multi-spot cylindrical vector beams might be useful in modifying filamentary structures for inscribing photonic components such as waveguides, splitters and Volume Bragg Grating.

As stated in section 4.5.4, an interesting phenomer has been observed during this research. Due to the time limited, further research was not carried to exploit the reason causing the debris outside the holes that were produced by multi-diffractive spots are trying to connect with each other. This research could lead to a better understanding the diffractive beam processing and the debris generated by laser ablation in air.

References

[1] Sugioka K and Cheng Y 2014 Ultrafast lasers—reliable tools for advanced materials processing *Light Sci Appl* **3** e149–12

[2] Liu X, Du D and Mourou G 1997 Laser Ablation and Micromachining with Ultrashort Laser Pulses *IEEE Journal of Quantum Electronics* **33** 1706–16

[3] Bizi-bandoki P, Valette S, Audouard E and Benayoun S 2013 Time dependency of the hydrophilicity and hydrophobicity of metallic alloys subjected to femtosecond laser irradiations *Applied Surface Science* **273** 399–407

[4] Bonse J, Krüger J, Höhm S and Rosenfeld A 2012 Femtosecond laser-induced periodic surface structures *J. Laser Appl.* **24** 042006–8

[5] Yao J, Zhang C, Liu H, Dai Q, Wu L, Lan S, Gopal A V, Trofimov V A and Lysak T M 2012 Selective appearance of several laser-induced periodic surface structure patterns on a metal surface using structural colors produced by femtosecond laser pulses *Applied Surface Science* **258** 7625–32

[6] Vorobyev A Y and Guo C 2008 Colorizing metals with femtosecond laser pulses *Appl. Phys. Lett.* **92** 041914–4

[7] Ou Z, Huang M and Zhao F 2014 Colorizing pure copper surface by ultrafast laser-induced near-subwavelength ripples *Opt. Express* **22** 17254–65

[8] Dusser B, Sagan Z, Soder H, Faure N, Colombier J P, Jourlin M and Audouard E 2010 Controlled nanostructrures formation by ultra fast laser pulses for color marking *Opt. Express* **18** 2913–24

[9] Carter R M, Chen J, Shephard J D, Thomson R R and Hand D P 2014 Picosecond laser welding of similar and dissimilar materials *Applied Optics* **53** 4233–8

[10] Boyd R W 2008 Nonlinear Optics (Academic press, Burlington MA, Elsevier)

[11] Ye L, Perrie W, Allegre O J, Jin Y, Kuang Z, Scully P J, Fearon E, Eckford D, Edwardson S P and Dearden G 2013 NUV femtosecond laser inscription of volume Bragg gratings in poly(methyl)methacrylate with linear and circular polarizations *Laser Phys.* **23** 084002(10pp)

[12] Braun A, Korn G, Liu X, Du D, Squier J and Mourou G 1995 Self-channeling of high-peak-power femtosecond laser pulses in air *Opt. Lett.* **20** 73–5

[13] Panov N A, Makarov V A, Fedorov V Y and Kosareva O G 2013 Filamentation of arbitrary polarized femtosecond laser pulses in case of high-order Kerr effect *Opt. Lett.* **38** 537–9

[14] Fox R A, Kogan R M and Robinson E J 1971 Laser Triple-Quantum Photoionization of ^{Cesium} *Phys. Rev. Lett.* **26** 1416–7

[15] Theodosiou C E and Armstrong L 1979 Two-photon ionisation of caesium *J. Phys. B: At. Mol. Phys.* **12** L87–L91

[16] Carman H S and Compton R N 1989 High-order multiphoton ionization photoelectron spectroscopy of nitric oxide *J. Chem. Phys.* **90** 1307–12

[17] Venable D D and Kay R B 1975 Polarization effects in four-photon conductivity in quartz *Appl. Phys. Lett.* **27** 48–9

[18] Temnov V V, Sokolowski-Tinten K, Zhou P, El-Khamhawy A and Linde von der D 2006 Multiphoton Ionization in Dielectrics: Comparison of Circular and Linear Polarization *Phys. Rev. Lett.* **97** 237403–4

[19] Osellame R, Cerullo G and Ramponi R 2012 *Femtosecond Laser Micromachining: Photonic and Microfluidic Devices in Transparent Materials* vol 123 (Springer Science & Business Media)

[20] Coherent Libra Series Data Sheet (COHERENT 2016), file was available at: https://www.coherent.com/products/?903/Libra-Series , retrieved Oct 2016. *www.coherent.comproductsLibra-Series*

[21] TRUMPF Scientific Lasers: Dira 200-1 (TRUMPF Scientific Lasers 2016), file was available at:http://www.trumpf-scientific-lasers.com/fileadmin/DAM/trumpf-scientific-lasers.com/PDFs/TRUMPF_Scientific_Lasers_Dira_200_1.pdf , retrieved Oct 2016.

[22] Kuang Z 2010 *PhD Thesis: Parallel diffractive multi-beam ultrafast laser micro-processing* (University of Liverpool)

[23] Kuang Z, Perrie W, Leach J, Sharp M, Edwardson S P, Padgett M, Dearden G and Watkins K G 2008 High throughput diffractive multi-beam femtosecond laser processing using a spatial light modulator *Applied Surface Science* **255** 2284–9

[24] Hayasaki Y, Sugimoto T, Takita A and Nishida N 2005 Variable holographic femtosecond laser processing by use of a spatial light

modulator *Appl. Phys. Lett.* **87** 031101–4

[25] Hnatovsky C, Shvedov V G and Krolikowski W 2013 The role of light-induced nanostructures in femtosecond laser micromachining with vector and scalar pulses *Opt. Express* **21** 12651–6

[26] Borowiec A and Haugen H K 2003 Subwavelength ripple formation on the surfaces of compound semiconductors irradiated with femtosecond laser pulses *Appl. Phys. Lett.* **82** 4462–4

[27] Bonse J, Munz M and Sturm H 2005 Structure formation on the surface of indium phosphide irradiated by femtosecond laser pulses *J. Appl. Phys.* **97** 013538–10

[28] Miyaji G and Miyazaki K 2008 Origin of periodicity in nanostructuring on thin film surfaces ablated with femtosecond laser pulses *Opt. Express* **16** 16265–71

[29] Vorobyev A Y and Guo C 2013 Direct femtosecond laser surface nano/microstructuring and its applications *Laser & Photonics Reviews* **7** 385–407

[30] Zhang J, Gecevičius M, Beresna M and Kazansky P G 2014 Seemingly Unlimited Lifetime Data Storage in Nanostructured Glass *Phys. Rev. Lett.* **112** 033901–5

[31] Öktem B, Pavlov I, Ilday S, Kalaycıoğlu H, Rybak A, Yavaş S, Erdoğan M and Omer Ilday F 2013 Nonlinear laser lithography for indefinitely large-area nanostructuring with femtosecond pulses *Nature Photonics* **7** 897–901

[32] Allegre O J, Perrie W, Edwardson S P, Dearden G and Watkins K G 2012 Laser microprocessing of steel with radially and azimuthally polarized femtosecond vortex pulses *J. Opt.* **14** 085601(9pp)

[33] Weber R, Michalowski A, Abdou-Ahmed M, Onuseit V, Rominger V, Kraus M and Graf T 2011 Effects of Radial and Tangential Polarization in Laser Material Processing *Physics Procedia* **12** 21–30

[34] Guay J-M, Villafranca A, Baset F, Popov K, Ramunno L and Bhardwaj V R 2014 **Polarization-dependent femtosecond laser ablation of poly-methyl methacrylate** *New J. Phys.* **14** 085010(17pp)

[35] Beresna M, Gecevičius M and Kazansky P G 2011 Polarization sensitive elements fabricated by femtosecond laser nanostructuring of glass [Invited] *Optical Materials Express* **1** 783–95

[36] Beresna M and Kazansky P G 2010 Polarization diffraction grating produced by femtosecond laser nanostructuring in glass *Opt. Lett.* **35** 1662–

4

[37] Beresna M, Gecevičius M, Kazansky P G and Gertus T 2011 Radially polarized optical vortex converter created by femtosecond laser nanostructuring of glass *Appl. Phys. Lett.* **98** 201101–4

[38] Beversluis M R, Novotny L and Stranick S J 2006 Programmable vector point-spread function engineering *Opt. Express* **14** 2650–6

[39] Qi J, Sun W, Liao J, Nie Y, Wang X, Zhang J, Liu X, Jia H, Lu M, Chen S, Liu J, Yang J, Tan J and Li X 2013 Generation and analysis of both in-phase and out-phase radially polarized femtosecond-pulse beam *Opt. Eng* **52** 024201–11

[40] Han W, Yang Y, Cheng W and Zhan Q 2013 Vectorial optical field generator for the creation of arbitrarily complex fields *Opt. Express* **21** 20692–15

[41] Wang X-L, Li Y, Chen J, Guo C-S, Ding J and Wang H-T 2010 A new type of vector fields with hybrid states of polarization *Opt. Express* **18** 10786–95

[42] Hashimoto M, Yamada K and Araki T 2005 Proposition of Single Molecular Orientation Determination Using Polarization Controlled Beam by Liquid Crystal Spatial Light Modulators *Optical Review* **12** 37–41

[43] Bashkansky M, Park D and Fatemi F K 2010 Azimuthally and radially polarized light with a nematic SLM *Opt. Express* **18** 212–7

[44] Maurer C, Jesacher A, Furhapter S, Bernet S and Ritsch-Marte M 2007 **Tailoring of arbitrary optical vector beams** *New J. Phys.* **9** 1–20

[45] Rong Z-Y, Han Y-J, Wang S-Z and Guo C-S 2014 Generation of arbitrary vector beams with cascaded liquid crystal spatial light modulators *Opt. Express* **22** 1636–44

[46] Neil M A A, Massoumian F, Juskaitis R and Wilson T 2002 Method for the generation of arbitrary complex vector wave fronts *Opt. Lett.* **27** 1929–31

[47] Dong X, Weng X, Guo H and Zhuang S 2012 Generation of radially polarized beams using spatial light modulator *Optik - International Journal for Light and Electron Optics* **123** 391–4

[48] Nolte S, Momma C, Kamlage G, Ostendorf A, Fallnich C, Alvensleben von F and Welling H 1999 Polarization effects in ultrashort-pulse laser drilling *Appl. Phys. A* **68** 563–7

[49] Hahne S, Johnston B F and Withford M J 2007 Pulse-to-pulse polarization-switching method for high-repetition-rate lasers *Applied Optics* **46** 954–8

[50] Fohl C, Breitling D and Dausinger F 2003 Precise drilling of steel with ultrashort pulsed solid-state lasers *Proceedings of SPIE* **5121** 271–9

[51] Allegre O J, Perrie W, Bauchert K, Liu D, Edwardson S P, Dearden G and Watkins K G 2012 Real-time control of polarisation in ultra-short-pulse laser micro-machining *Appl. Phys. A* **107** 445–54

[52] Clegg J H and Neil M A A 2013 Double pass, common path method for arbitrary polarization control using a ferroelectric liquid crystal spatial light modulator *Opt. Lett.* **38** 1043–5

[53] Liu S, Li P, Peng T and Zhao J 2012 Generation of arbitrary spatially variant polarization beams with a trapezoid Sagnac interferometer *Opt. Express* **20** 21725–21721

[54] Chen H, Hao J, Zhang B-F, Xu J, Ding J and Wang H-T 2011 Generation of vector beam with space-variant distribution of both polarization and phase *Opt. Lett.* **36** 3179–81

[55] Maluenda D, Juvells I, Martinez-Herrero R and Carnicer A 2013 Reconfigurable beams with arbitrary polarization and shape distributions at a given plane *Opt. Express* **21** 5424–31

[56] Lou K, Qian S, Wang X, Li Y, Gu B, Tu C and Wang H 2011 Two-dimensional microstructures induced by femtosecond vector light fields on silicon *Opt. Express* **20** 120–7

[57] Tripathi S and Toussaint K C 2012 Versatile generation of optical vector fields and vector beams using a non-interferometric approach *Opt. Express* **20** 10788–95

[58] Yao J, Zhang C, Liu H, Dai Q, Wu L, Lan S, Gopal A V, Trofimov V A and Lysak T M 2012 Selective appearance of several laser-induced periodic surface structure patterns on a metal surface using structural colors produced by femtosecond laser pulses *Applied Surface Science* **258** 7625–32

[59] Maiman T H 1960 Stimulated Optical Radiation in Ruby *Nature* **187** 493–4

[60] DeMaria A J, Stetser D A and Heynau H 1966 Self Mode-Locking of Lasers with Saturable Absorbers *Appl. Phys. Lett.* **8** 174–6

[61] Rulliere C 2005 *Femtosecond Laser Pulses - Principles and Experiments* (Springer-Verlag New York)

[62] Uesaka M 2005 *Femtosecond Beam Science* (Imperial College Press, London)

[63] Krueger A and Feru P 2004 Getting Practical *httpspie.orgnewsroomgetting-practical* 23–5

[64] Keller U 2003 Recent developments in compact ultrafast lasers *Nature* **424** 831–8

[65] Keller U, Miller D A B, Boyd G D, Chiu T H, Ferguson J F and Asom M T 1992 Solid-state low-loss intracavity saturable absorber for Nd:YLF lasers: an antiresonant semiconductor Fabry-Perot saturable absorber *Opt. Lett.* **17** 505–7

[66] Spence D E, Kean P N and Sibbett W 1991 60-fsec pulse generation from a self-mode-locked Ti:sapphire laser *Opt. Lett.* **16** 42–4

[67] Sutter D H, Steinmeyer G, Gallmann L, Matuschek N, Morier-Genoud F and Keller U 1999 Semiconductor saturable-absorber mirror–assisted Kerr-lens mode-locked Ti:sapphire laser producing pulses in the two-cycle regime *Opt. Lett.* **24** 631–3

[68] Ell R, Morgner U, Kartner F X, Fujimoto J G, Ippen E P, Scheuer V, Angelow G, Tschudi T, Lederer M J, Boiko A and Luther-Davies B 2001 Generation of 5-fs pulses and octave-spanning spectra directly from a Ti:sapphire laser *Opt. Lett.* **26** 373–5

[69] Perry M, Shore B, Boyd R and Britten J 1995 Multilayer dielectric gratings: Increasing the power of light *Science and Technology Review* **9** 25–33

[70] Strickland D and Mourou G 1985 Compression of amplified chirped optical pulses *Optics Communications* **56** 219–21

[71] Treacy E B 1969 Optical Pulse Compression With Diffraction Gratings *IEEE Journal of Quantum Electronics* **QE-5** 454–8

[72] Steen W M 2003 *Laser material processing* (Springer London)

[73] Pronko P P, Dutta S K, Squier J, Rudd J V and Mourou G 1995 Machining of sub-micron holes using a femtosecond laser at 800 nm *Optics Communications* **114** 106–10

[74] Breitling D, Ruf A and Dausinger F 2004 Fundamental aspects in machining of metals with short and ultrashort laser pulses Proceedings of SPIE vol 5339, ed P R Herman, J Fieret, A Pique, T Okada, F G Bachmann, W Hoving, K Washio, X Xu, J J Dubowski, D B Geohegan and F Traeger (SPIE) pp 49–63

[75] Stoian R, Ashkenasi D, Rosenfeld A and Campbell E E B 2000 **Coulomb explosion in ultrashort pulsed laser ablation of Al_2O_3** *Phys. Rev. B* **62**

13167–73

[76] Stoian R, Rosenfeld A, Ashkenasi D, Hertel I V, Bulgakova N M and Campbell E E B 2002 Surface Charging and Impulsive Ion Ejection during Ultrashort Pulsed Laser Ablation *Phys. Rev. Lett.* **88** 097603–4

[77] Leitz K-H, Redlingshöfer B, Reg Y, Otto A and Schmidt M 2011 Metal Ablation with Short and Ultrashort Laser Pulses *Physics Procedia* **12** 230–8

[78] O'Shea D C 1985 *Elements of Modern Optical Design* (New York: Wiley)

[79] Zhan Q 2009 Cylindrical vector beams: from mathematical concepts to applications *Adv. Opt. Photon.* **1** 1–57

[80] Phelan C F, Donegan J F and Lunney J G 2011 Generation of a radially polarized light beam using internal conical diffraction *Opt. Express* **19** 21793–802

[81] Beijersbergen M W, Coerwinkel R P C, Kristensen M and Woerdman J P 1994 Helical-wavefront laser beams produced with a spiral phaseplate *Optics Communications* **112** 321–7

[82] Schulz S, Machula T, Upham J, Karimi E and Boyd R W 2013 On Chip Generation and Sorting of Orbital Angular Momentum Beams *Advanced Photonics 2013 (2013), paper IT5A.2* IT5A.2

[83] Alexeev I, Leitz K H, Otto A and Schmidt M 2010 Application of Bessel beams for ultrafast laser volume structuring of non transparent media Physics Procedia vol 5 (Elsevier) pp 533–40

[84] Courvoisier F, Zhang J, Bhuyan M K, Jacquot M and Dudley J M 2013 Applications of femtosecond Bessel beams to laser ablation *Appl. Phys. A* **112** 29–34

[85] Yalizay B, Ersoy T, Soylu B and Akturk S 2012 Fabrication of nanometer-size structures in metal thin films using femtosecond laser Bessel beams *Appl. Phys. Lett.* **100** 031104–031103

[86] Bhuyan M K, Courvoisier F, Lacourt P A, Jacquot M, Furfaro L, Withford M J and Dudley J M 2010 High aspect ratio taper-free microchannel fabrication using femtosecond Bessel beams *Opt. Express* **18** 556–74

[87] Courvoisier F, Lacourt P A, Jacquot M, Bhuyan M K, Furfaro L and Dudley J M 2009 Surface nanoprocessing with nondiffracting femtosecond Bessel beams *Opt. Lett.* **34** 3163–5

[88] Bhuyan M K, Velpula P K, Colombier J P, Olivier T, Faure N and Stoian R 2014 Single-shot high aspect ratio bulk nanostructuring of fused silica using

chirp-controlled ultrafast laser Bessel beams *Appl. Phys. Lett.* **104** 021107–6

[89] Zeng D, Latham W P and Kar A 2006 Optical trepanning with a refractive axicon lens system Proceedings of SPIE vol 6290, ed F M Dickey and D L Shealy (SPIE) pp 62900J–10

[90] Kuang Z, Perrie W, Edwardson S P, Fearon E and Dearden G 2014 Ultrafast laser parallel microdrilling using multiple annular beams generated by a spatial light modulator *J. Phys. D: Appl. Phys.* **47** 115501(7pp)

[91] Omatsu T, Chujo K, Miyamoto K, Okida M, Nakamura K, Aoki N and Morita R 2010 Metal microneedle fabrication using twisted light with spin *Opt. Express* **18** 17967–73

[92] Hamazaki J, Morita R, Chujo K, Kobayashi Y, Tanda S and Omatsu T 2010 Optical-vortex laser ablation *Opt. Express* **18** 2144–51

[93] Hnatovsky C, Shvedov V G, Krolikowski W and Rode A V 2010 Materials processing with tightly focused femtosecond vortex laser beams *Opt. Lett.* **35** 3417–9

[94] Polynkin P 2014 Intense femtosecond shaped laser beams for writing extended structures inside transparent dielectrics *Appl. Phys. A* **114** 143–9

[95] Silvennoinen M, Kaakkunen J, Paivasaari K and Vahimaa P 2014 Parallel femtosecond laser ablation with individually controlled intensity *Opt. Express* **22** 2603–8

[96] Kuang Z, Perrie W, Liu D, Edwardson S, Cheng J, Dearden G and Watkins K 2009 Diffractive multi-beam surface micro-processing using 10ps laser pulses *Applied Surface Science* **255** 9040–4

[97] Silvennoinen M, Kaakkunen J, Paivasaari K and Vahimaa P 2013 Parallel Microstructuring using Femtosecond Laser and Spatial Light Modulator Physics Procedia vol 41 (Elsevier Srl) pp 686–90

[98] Liu D, Kuang Z, Perrie W, Scully P J, Baum A, Edwardson S P, Fearon E, Dearden G and Watkins K G 2010 High-speed uniform parallel 3D refractive index micro-structuring of poly(methyl methacrylate) for volume phase gratings *Appl. Phys. B* **101** 817–23

[99] Grant R F 1989 *Introduction to modern optics* (Dover Publications)

[100] Gawelda W, Puerto D, Siegel J, Ferrer A, Ruiz de la Cruz A, Fernández H and Solis J 2008 Ultrafast imaging of transient electronic plasmas produced in conditions of femtosecond waveguide writing in dielectrics *Appl. Phys. Lett.* **93** 121109–4

[101] Yamada K, Watanabe W, Asano T, Nishii J and Itoh K 2003 Polarization dependence of refractive-index change in silica glass induced by self-trapped filament of femtosecond laser pulses Proceedings of SPIE vol 4830 pp 581–4

[102] Yamada K, Watanabe W, Itoh K and Nishii J 2001 Dependence of refractive index change in silica glass on polarization of incident ultrashort laser pulses Proceedings of SPIE vol 4416 pp 334–47

[103] Yamada K, Watanabe W, Nishii J and Itoh K 2003 Anisotropic refractive-index change in silica glass induced by self-trapped filament of linearly polarized femtosecond laser pulses *J. Appl. Phys.* **93** 1889–5

[104] Reiss H R 1972 Polarization Effects in High-Order Multiphoton Ionization *Phys. Rev. Lett.* **29** 1129–31

[105] Olsen F O 1980 *Cutting with polarized laser beams* vol 63 (DVS Berichte)

[106] Olsen F O 1982 Studies of Sheet Metal Cutting with Plane-Polarized CO2-Laser *Optoelectronics in Engineering* (Berlin, Heidelberg: Springer Berlin Heidelberg) pp 227–31

[107] Niziev V G and Nesterov A V 1999 Influence of Beam Polarization on Laser Cutting Efficiency *J. Phys. D: Appl. Phys.* **32** 1455–61

[108] Kraus M, Ahmed M A, Michalowski A, Voss A, Weber R and Graf T 2010 Microdrilling in steel using ultrashort pulsed laser beams with radial and azimuthal polarization *Opt. Express* **18** 22305–13

[109] Meier M, Romano V and Feurer T 2007 Material processing with pulsed radially and azimuthally polarized laser radiation *Appl. Phys. A* **86** 329–34

[110] Venkatakrishnan K and Tan B 2006 Interconnection microvia drilling with a radially polarized laser beam *J. Micromech. Microeng.* **16** 2603–7

[111] Stratakis E, Ranella A and Fotakis C 2011 Biomimetic micro/nanostructured functional surfaces for microfluidic and tissue engineering applications *Biomicrofluidics* **5** 013411–31

[112] Yong Hwang T and Guo C 2012 Polarization and angular effects of femtosecond laser-induced conical microstructures on Ni *J. Appl. Phys.* **111** 083518–5

[113] Zhu J-T, Shen Y-F, Li W, Chen X, Yin G, Chen D-Y and Zhao L 2006 Effect of polarization on femtosecond laser pulses structuring silicon surface *Applied Surface Science* **252** 2752–6

[114] Birnbaum M 1966 Semiconductor Surface Damage Produced by Ruby

Lasers *J. Appl. Phys.* **36**

[115] Wu Q, Ma Y, Fang R, Liao Y, Yu Q, Chen X and Wang K 2003 Femtosecond laser-induced periodic surface structure on diamond film *Appl. Phys. Lett.* **82** 1703–5

[116] Reif J, Costache F, Henyk M and Pandelov S V 2002 Ripples revisited: non-classical morphology at the bottom of femtosecond laser ablation craters in transparent dielectrics *Applied Surface Science* **197-198** 891–5

[117] Costache F, Henyk M and Reif J 2003 Surface patterning on insulators upon femtosecond laser ablation *Applied Surface Science* **208-209** 486–91

[118] Huang M, Zhao F, Cheng Y, Xu N and Xu Z 2009 Mechanisms of ultrafast laser-induced deep-subwavelength gratings on graphite and diamond *Phys. Rev. B* **79** 125436–9

[119] Costache F, Kouteva-Arguirova S and Reif J 2004 Sub–damage–threshold femtosecond laser ablation from crystalline Si: surface nanostructures and phase transformation *Appl. Phys. A* **79** 1429–32

[120] Dong Y and Molian P 2004 Coulomb explosion-induced formation of highly oriented nanoparticles on thin films of 3C–SiC by the femtosecond pulsed laser *Appl. Phys. Lett.* **84** 10–2

[121] Skolski J Z P, Römer G R B E, Obona J V, Ocelik V, Huis in 't Veld A J and De Hosson J T M 2012 Laser-induced periodic surface structures: Fingerprints of light localization *Phys. Rev. B* **85** 075320–9

[122] Emmony D C, Howson R P and Willis L J 1973 Laser mirror damage in germanium at 10.6 μm *Appl. Phys. Lett.* **23** 598–600

[123] Sipe J E, Young J F, Preston J S and van Driel H M 1983 Laser-induced periodic surface structure. I. Theory

Phys. Rev. B **27** 1141–54

[124] Guosheng Z, Fauchet P M and Siegman A E 1982 Growth of spontaneous periodic surface structures on solids during laser illumination *Phys. Rev. B* **26** 5366–81

[125] Ruiz de la Cruz A, Lahoz R, Siegel J, la Fuente de G F and Solis J 2014 High speed inscription of uniform, large-area laser-induced periodic surface structures in Cr films using a high repetition rate fs laser *Opt. Lett.* **39** 2491–4

[126] Liu P, Jiang L, Hu J, Zhang S and Lu Y 2014 Self-organizing microstructures orientation control in femtosecond laser patterning on

silicon surface *Opt. Express* **22** 16669–75

[127] Dostovalov A V, Korolkov V P, Golubtsov S K and Kondrat'ev V I 2014 Specific features of formation of self-induced gratings on metal foils during scanning by a tightly focused femtosecond laser beam *Jpn. J. Appl. Phys* **44** 330–4

[128] Fauchet P M and Siegman A E 1982 Surface ripples on silicon and gallium arsenide under picosecond laser illumination *Appl. Phys. Lett.* **40** 824–6

[129] Mellor L F *PhD Thesis: Periodic structuring of metallic surfaces using picosecond laser systems* (UK: University of Liverpool)

[130] Ruiz de la Cruz A, Lahoz R, Siegel J, la Fuente de G F and Solis J 2014 Large area, high speed inscription of laser-induced periodic surface structures (LIPSS) in Cr using a high repetition rate fs-laser *IEEE Lases and Electro-Optics Europe* 1–1

[131] Vorobyev A Y, Makin V S and Guo C 2007 Periodic ordering of random surface nanostructures induced by femtosecond laser pulses on metals *J. Appl. Phys.* **101** 034903–5

[132] Ran L and Qu S 2010 Structure formation on the surface of alloys irradiated by femtosecond laser pulses *Applied Surface Science* **256** 2315–8

[133] Gurevich E L and Gurevich S V 2014 Laser Induced Periodic Surface Structures induced by surface plasmons coupled via roughness *Applied Surface Science* **302** 118–23

[134] Ardron M, Weston N and Hand D 2014 A practical technique for the generation of highly uniform LIPSS *Applied Surface Science* **313** 123–31

[135] Yu X, Liao Y, He F, Zeng B, Cheng Y, Xu Z, Sugioka K and Midorikawa K 2011 Tuning etch selectivity of fused silica irradiated by femtosecond laser pulses by controlling polarization of the writing pulses *J. Appl. Phys.* **109** 053114–6

[136] Bonse J, Koter R, Hartelt M, Spaltmann D, Pentzien S, Höhm S, Rosenfeld A and Krüger J 2014 Femtosecond laser-induced periodic surface structures on steel and titanium alloy for tribological applications *Appl. Phys. A* **117** 103–10

[137] Buividas R, Fahim N, Juodkazytė J and Juodkazis S 2014 Novel method to determine the actual surface area of a laser-nanotextured sensor *Appl. Phys. A* **114** 169–75

[138] Chou A, Jaatinen E, Buividas R, Seniutinas G, Juodkazis S, Izake E L and Fredericks P M 2012 SERS substrate for detection of explosives *Nanoscale*

4 7419–24

[139] Lazarev G, Hermerschmidt A, Kruger S and Osten S 2012 LCOS Spatial Light Modulators: Trends and Applications *Optical Imaging and Metrology: Advanced Technologies* 1–30

[140] Zupancic P P J 2013 *Dynamic Holography and Beamshaping using Digital Micromirror Devices* (Ludwig-Maximilians-Universitat Munchen)

[141] Mills B, Feinaeugle M, Sones C L, Rizvi N and Eason R W 2013 Sub-micron-scale femtosecond laser ablation using a digital micromirror device *J. Micromech. Microeng.* **23** 035005–9

[142] Hossack W J, Theofanidou E and Crain J 2003 High-speed holographic optical tweezers using a ferroelectric liquid crystal microdisplay *Opt. Express* **11** 2053–9

[143] Das A and Boruah B R 2014 Note: Laser beam scanning using a ferroelectric liquid crystal spatial light modulator *Review of Scientific Instruments* **85** 046103–4

[144] B N S 2013 BNS Spatial Light Modulators – XY Series *httpbnonlinear.compdfXYSeriesDS.pdf* 1–12

[145] Mukohzaka N, Yoshida N, Toyoda H, Kobayashi Y and Hara T 1994 Diffraction efficiency analysis of a parallel-aligned nematic-liquid-crystal spatial light modulator *Applied Optics* **33** 2804–11

[146] 2014 Phase spatial light modulator LCOS-SLM *httpswww.hamamatsu.comresourcespdfssdehandbooklcosslm.pdf* 1–14

[147] Arlt J and Dholakia K 2000 Generation of high-order Bessel beams by use of an axicon *Optics Communications* **177** 297–301

[148] Watanabe T, Fujii M, Watanabe Y, Toyama N and Iketaki Y 2004 Generation of a doughnut-shaped beam using a spiral phase plate *Review of Scientific Instruments* **75** 5131–5

[149] Matsuo S, Kondo T, Juodkazis S, Mizeikis V and Misawa H 2002 Fabrication of Three-Dimensional Photonic Crystals by Femtosecond Laser Interference *Proceedings of SPIE* **4655** 327–34

[150] Matsuo S, Miyamoto T, Tomita T and Hashimoto S 2007 Applications of a microlens array and a photomask to the laser microfabrication of a periodic photopolymer rod array *Applied Optics* **46** 8264–7

[151] Matsuo S, Juodkazis S and Misawa H 2005 Femtosecond laser microfabrication of periodic structures using a microlens array *Appl. Phys.*

A **80** 683–5

[152] Courvoisier F, Lacourt P A, Jacquot M, Bhuyan M K, Furfaro L and Dudley J M 2009 Surface nanoprocessing with nondiffracting femtosecond Bessel beams *Opt. Lett.* **34** 3163–5

[153] Ma H, Zhou P, Wang X, Ma Y, Xi F, Xu X and Liu Z 2010 Near-diffraction-limited annular flattop beam shaping with dual phase only liquid crystal spatial light modulators *Opt. Express* **18** 8251–60

[154] Liu D, Kuang Z, Shang S, Perrie W, Karnakis D, Kerasley A, Knowles M, Edwardson S, Dearden G and Watkins K 2009 *Ultrafast parallel laser processing of materials for high throughput manufacturing*

[155] Chen M, Mazilu M, Arita Y, Wright E M and Dholakia K 2013 Dynamics of microparticles trapped in a perfect vortex beam *Opt. Lett.* **38** 4919–22

[156] Ambrosio A, Marrucci L, Borbone F, Roviello A and Maddalena P 1996 Light-induced spiral mass transport in azo-polymer films under vortex-beam illumination *Nature Communications* **3** 1–9

[157] Kuang Z, Liu D, Perrie W, Edwardson S, Sharp M, Fearon E, Dearden G and Watkins K 2009 Fast parallel diffractive multi-beam femtosecond laser surface micro-structuring *Applied Surface Science* **255** 6582–8

[158] Kuang Z, Perrie W, Edwardson S P, Fearon E and Dearden G 2014 Ultrafast laser parallel microdrilling using multiple annular beams generated by a spatial light modulator *J. Phys. D: Appl. Phys.* **47** 115501(7PP)

[159] Ye C 1995 Construction of an optical rotator using quarter-wave plates and an optical retarder *Opt. Eng* **34** 3031–5

[160] Zhan Q and Leger J R 2002 Focus shaping using cylindrical vector beams *Opt. Express* **10** 324–31

[161] Machavariani G, Lumer Y, Moshe I, Meir A and Jackel S 2007 Efficient extracavity generation of radially and azimuthally polarized beams *Opt. Lett.* **32** 1468–70

[162] Wang X, Ding J, Ni W, Guo C and Wang H 2007 Generation of arbitrary vector beams with a spatial light modulator and a common path interferometric arrangement *Opt. Lett.* **32** 3549–51

[163] Lai W J, Lim B C, Phua P B, Tiaw K S, Teo H H and Hong M H 2008 Generation of radially polarized beam with a segmented spiral varying retarder *Opt. Express* **16** 15694–9

[164] Yonezawa K, Kozawa Y and Sato S 2006 Generation of a radially polarized

laser beam by use of the birefringence of a c-cut Nd:YVO *Opt. Lett.* **31** 2151–3

[165] Machavariani G, Lumer Y, Moshe I, Meir A, Jachel S and Davidson N 2007 Birefringence-induced bifocusing for selection of radially or azimuthally polarized laser modes *Applied Optics* **46** 3304–10

[166] Yonezawa K, Kozawa Y and Sato S 2007 Compact Laser with Radial Polarization Using Birefringent Laser Medium *Jpn. J. Appl. Phys* **46** 5160–3

[167] Kozawa Y and Sato S 2005 Generation of a radially polarized laser beam by use of a conical Brewster prism *Opt. Lett.* **30** 3063–5

[168] Ahmed M A, Voss A, Vogel M M and Graf T 2007 Multilayer polarizing grating mirror used for the generation of radial polarization in Yb:YAG thin-disk lasers *Opt. Lett.* **32** 3272–4

[169] Tidwell S C, Ford D H and Kimura W D 1990 Generating radially polarized beams interferometrically *Applied Optics* **29** 2234–9

[170] Grosjean T, Courjon D and Spajer M 2002 An all-fiber device for generating radially and other polarized light beams *Optics Communications* **203** 1–5

[171] Bomzon Z, Biener G, Kleiner V and Hasman E 2002 Radially and azimuthally polarized beams generated by space-variant dielectric subwavelength gratings *Opt. Lett.* **27** 285–7

[172] Stalder M and Schadt M 1996 Linearly polarized light with axial symmetry generated by liquid-crystal polarization converters *Opt. Lett.* **21** 1948–50

[173] Machavariani G, Lumer Y, Moshe I and Jackel S 2007 Effect of the spiral phase element on the radial-polarization $(0,1)^*$ LG beam *Optics Communications* **271** 190–6

[174] Hasegawa S and Hayasaki Y 2013 Polarization distribution control of parallel femtosecond pulses with spatial light modulators *Opt. Express* **21** 12987–95

[175] Davis J A, McNamara D E, Cottrell D M and Sonehara T 2000 Two-dimensional polarization encoding with a phase-only liquid-crystal spatial light modulator *Applied Optics* **39** 1549–54

[176] ARCoptix Switzerland *www.arcoptix.com*

[177] Davis J A, McNamara D E, Cottrell D M and Sonehara T 2000 Two-dimensional polarization encoding with a phase-only liquid-crystal spatial

light modulator *Applied Optics* **39** 1549–54

[178] Padgett M and Bowman R 2011 Tweezers with a twist *Nature Photonics* **5** 343–8

[179] Zhan Q 2004 Trapping metallic Rayleigh particles with radial polarization *Opt. Express* **12** 3377–82

[180] Paetzel B and Spiecker G 2007 Excimer Lasers Support Industrial Micromachining Diversity *Laser Technik Journal* **4** 36–9

[181] Sillanpaa J, Jarkko K Y and Asonen H 2007 Precise Patterning of Thin Films with Picosecond Fiber Laser *Proceedings of the ICALEO Conference* **ICAL07** 1–7

[182] Banovec A and Kern M 2002 Comparison between chemical and pulsed laser etching of indium tin oxide thin films *Vacuum* **43** 737–9

[183] Lemke A, Ashkenasi D and Eichler H J 2013 Picosecond Laser Induced Selective Removal of Functional Layers on CIGS Thin Film Solar Cells *Physics Procedia* **41** 769–75

[184] Neuenschwander B, Jaeggi B, Schmid M and Hennig G 2014 Surface Structuring with Ultra-short Laser Pulses: Basics, Limitations and Needs for High Throughput *Physics Procedia* **56** 1047–58

[185] Gudde J, Hohlfeld J, Muller J G and Matthias E 1998 Damage threshold dependence on electron–phonon coupling in Au and Ni films *Applied Surface Science* **127** 40–5

[186] Pronko P P, Dutta S K, Squier J, Rudd J V, Du D and Mourou G 1995 Machining of sub-micron holes using a femtosecond laser at 800 nm *Optics Communications* **114** 106–10

[187] Jaeggi B, Neuenschwander B, Schmid M, Muralt M, Zuercher J and Hunziker U 2011 Influence of the Pulse Duration in the ps-Regime on the Ablation Efficiency of Metals *Physics Procedia* **12** 164–71

[188] Schmid M, Neuenschwander B, Romano V, Jaeggi B and Hunziker U W 2011 Processing of metals with ps-laser pulses in the range between 10ps and 100ps SPIE LASE vol 7920, ed B Gu, G Hennig, X Xu and H Niino (SPIE) p 792009(7pp)

[189] Neuenschwander B, Jaeggi B, Schmid M, Rouffiange V and Martin P-E 2012 Optimization of the volume ablation rate for metals at different laser pulse-durations from ps to fs SPIE LASE vol 8243, ed G Hennig, X Xu, B Gu and Y Nakata (SPIE) p 824307(13pp)

[190] Neuenschwander B, Jaeggi B and Schmid M 2013 From fs to sub-ns: Dependence of the Material Removal Rate on the Pulse Duration for Metals *Physics Procedia* **41** 794–801

[191] Račiukaitis G, Brikas M, Gedvilas M and Rakickas T 2007 Patterning of indium–tin oxide on glass with picosecond lasers *Applied Surface Science* **253** 6570–4

[192] Xiao S, Fernandes S A and Ostendorf A 2011 Selective Patterning of ITO on flexible PET Substrate by 1064nm picosecond Laser *Physics Procedia* **12** 125–32

[193] Risch A and Hellmann R 2011 Picosecond Laser Patterning of ITO Thin Films *Physics Procedia* **12** 133–40

[194] Rung S, Christiansen A and Hellmann R 2014 Influence of film thickness on laser ablation threshold of transparent conducting oxide thin-films *Applied Surface Science* **305** 347–51

[195] Takai M, Bollmann D and Haberger K 1994 Maskless patterning of indium tin oxide layer for flat panel displays by diode-pumped Nd:YLF laser irradiation *Appl. Phys. Lett.* **64** 2560–2

[196] Yavas O and Takai M 1998 High-speed maskless laser patterning of indium tin oxide thin films *Appl. Phys. Lett.* **73** 2558–60

[197] Yavas O and Takai M 1999 Effect of substrate absorption on the efficiency of laser patterning of indium tin oxide thin films *J. Appl. Phys.* **85** 4207–12

[198] Bonse J, Rudolph P, Krüger J, Baudach S and Kautek W 2000 Femtosecond pulse laser processing of TiN on silicon *Applied Surface Science* **154-155** 659–63

[199] Heise G, Domke M, Konrad J, Sarrach S, Sotrop J and Huber H P 2012 Laser lift-off initiated by direct induced ablation of different metal thin films with ultra-short laser pulses *J. Phys. D: Appl. Phys.* **45** 315303(8pp)

[200] Fernandes S A, Schoeps B, Kowalick K, Nett R, Esen C, Pickshaus M and Ostendorf A 2013 Femtosecond Laser Ablation of ITO/ZnO for Thin Film Solar Cells *Physics Procedia* **41** 802–9

[201] Xiao S, Gröger B, Fernandes S A and Ostendorf A 2011 Laser selective patterning of ITO on flexible PET for organic photovoltaics SPIE LASE vol 7921 (SPIE) p 79210I(8pp)

[202] Venkatakrishnan K, Tan B, Stanley P and Sivakumar N R 2002 The effect of polarization on ultrashort pulsed laser ablation of thin metal films *J. Appl. Phys.* **92** 1604–4

[203] Jaeggi B, Neuenschwander B, Meier T, Zimmermann M and Hennig G 2013 High Precision Surface Structuring with Ultra-Short Laser Pulses and Synchronized Mechanical Axes *Physics Procedia* **41** 319–26

[204] De Loor R 2013 Polygon Scanner System for Ultra Short Pulsed Laser Micro-Machining Applications *Physics Procedia* **41** 544–51

[205] Jaeggi B, Neuenschwander B, Zimmermann M, De Loor R and Penning L 2014 High throughput ps-laser micro machining with a synchronized polygon line scanner *Physics Procedia* 1–8

[206] Loeschner U, Schille J, Streek A, Knebel T, Hartwig L, Hillmann R and Endisch C 2015 High-rate laser microprocessing using a polygon scanner system *J. Laser Appl.* **27** S293031–8

[207] Zimmermann M, Jaeggi B and Neuenschwander B 2015 Improvements in ultra-high precision surface structuring using synchronized galvo or polygon scanner with a laser system in MOPA arrangement SPIE LASE vol 9350, ed S Roth, Y Nakata, B Neuenschwander and X Xu (SPIE) pp 9350161–8

[208] Jaeggi B, Neuenschwander B, Hunziker U, Zuercher J, Meier T, Zimmermann M, Selbmann K H and Hennig G 2012 Ultra-high-precision surface structuring by synchronizing a galvo scanner with an ultra-short-pulsed laser system in MOPA arrangement SPIE LASE vol 8243, ed G Hennig, X Xu, B Gu and Y Nakata (SPIE) pp 82430K1–11

[209] Schoonderbeek A, Schütz V, Haupt O and Stute U 2015 *Laser Processing of Thin Films for Photovoltaic Applications* vol 5

[210] Haupt O, Schütz V and Stute U 2011 Multi-spot laser processing of crystalline solar cells SPIE LASE vol 7921 (SPIE) p 79210V(9pp)

[211] Schütz V, Horn A and Stute U 2012 High-throughput process parallelization for laser surface modification on Si-solar cells: determination of the process window SPIE LASE vol 8244, ed F G Bachmann, W Pfleging, K Washio, J Amako, W Hoving and Y Lu (SPIE) p 82440X(7pp)

[212] Kuang Z, Perrie W, Liu D, Fitzsimons P, Edwardson S P, Fearon E, Dearden G and Watkins K G 2012 Ultrashort pulse laser patterning of indium tin oxide thin films on glass by uniform diffractive beam patterns *Applied Surface Science* **258** 7601–6

[213] Allegre O J 2013 *PhD Thesis: Advanced polarization control for optimizing ultrafast laser micro-processing* (UK: University of Liverpool)

[214] Gerchberg R W 1972 A practical algorithm for the determination of phase

from image and diffraction plane pictures *Optik* **35** 237

[215] Leach J, Wulff K, Sinclair G, Jordan P, Courtial J, Thomson L, Gibson G, Karunwi K, Cooper J, Laczik Z J and Padgett M 2006 Interactive approach to optical tweezers control *Applied Optics* **45** 897–903

[216] THORLABS detectors, Official webpage of THORLABS [cited ct. 2016; Available at: https://www.thorlabs.com/thorproduct.cfm?partnumber=DET210]

[217] NUTFIELD scanning galvanometer systems, Official webpage of NUTFIELD TECHCHNOLOGY [cited Oct. 2016; Available at: [https://nutfieldtech.com/xlr8-10-packaged-2-axis-scan-head/] *nutfieldtech.comxlr--packaged--axis-scan-head*

[218] AEROTECH galvanometer, Official webpage of AEROTECH [cited ct. 2016; Available at: https://www.aerotech.com/product-catalog/galvanometers/nmark-agv-hp.aspx?p=%2fproduct-catalog%2fgalvanometers.aspx]

[219] AEROTECH drives and drive racks, Official webpage of AEROTECH [cited ct. 2016; Available at: https://www.aerotech.com/product-catalog/drives-and-drive-racks/nmark-ssam.aspx]

[220] AEROTECH drives and drive racks, Official webpage of AEROTECH [cited ct. 2016; Available at: https://www.aerotech.com/product-catalog/drives-and-drive-racks/nmark-gcl.aspx]

[221] SCANLAB control electronics, Official webpage of SCANLAB [cited ct. 2016; Available at: http://www.scanlab.de/en/products/control-electronics/rtc4]

[222] SCANLAB control electronics, Official webpage of SCANLAB [cited ct. 2016; Available at: http://www.scanlab.de/en/products/control-electronics/rtc5]

[223] SCAPS scanner application software, Official webpage of SCAPS [cited Oct. 2016; Available at: http://www.scaps.com/index.php?id=10]

[224] AEROTECH linear stage, Official webpage of AEROTECH [cited ct. 2016; Available at: https://www.aerotech.com/product-catalog/stages/linear-stage/abl1500wb.aspx]

[225] AEROTECH linear stage, Official webpage of AEROTECH [cited ct. 2016; Available at: https://www.aerotech.co.uk/product-catalog/stages/linear-stage/abl1500-air-bearing.aspx]

[226] AEROTECH lift and z-axis stages, Official webpage of AEROTECH [cited

ct. 2016; Available at: https://www.aerotech.com/product-catalog/stages/lift-and-z-axis-stages/avsavsi100.aspx]

[227] AEROTECH linear stage, Official webpage of AEROTECH [cited ct. 2016; Available at: https://www.aerotech.co.uk/product-catalog/stages/linear-stage/ats150.aspx]

[228] AEROTECH goniometers, Official webpage of AEROTECH [cited ct. 2016; Available at: https://www.aerotech.com/product-catalog/goniometer/ant-20g.aspx]

[229] NATIONAL INSTRUMENTS data acquisition, Official webpage of NATIONAL INSTRUMENTS [cited ct. 2016; Available at: http://sine.ni.com/nips/cds/view/p/lang/en/nid/201630]

[230] OPHIR PHOTONICS beam profilers, Official webpage of SCANLAB [cited ct. 2016; Available at: http://www.ophiropt.com/de/laser-measurement-instruments/beam-profilers/products/camera-based-profilers/the-camera/SP620U]

[231] JEOL scanning electron microscope (SEM), Official webpage of JEOL [cited ct. 2016; Available at: http://www.jeol.co.jp/en/products/detail/JSM-7001F.html]

[232] OXFORD INSTRUMENTS microanalysis systems, Official webpage of OXFORD INSTRUMENTS [cited ct. 2016; Available at: https://www.oxford-instruments.com/products/microanalysis/energy-dispersive-x-ray-systems-eds-edx/eds-for-sem/sdd]

[233] Duocastella M and Arnold C B 2012 Bessel and annular beams for materials processing *Laser & Photonics Reviews* **6** 607–21

[234] Ouyang J, Perrie W, Allegre O J, Heil T, Jin Y, Fearon E, Eckford D, Edwardson S P and Dearden G 2015 Tailored optical vector fields for ultrashort-pulse laser induced complex surface plasmon structuring *Opt. Express* **23** 12562–72

[235] Nayak B K and Gupta M C 2017 Self-organized micro/nano structures in metal surfaces by ultrafast laser irradiation *Optics and Lasers in Engineering* **48** 940–9

[236] Wang X C, Lim G C, Ng F L, Liu W and Chua S J 2005 Femtosecond pulsed laser-induced periodic surface structures on GaN/sapphire *Applied Surface Science* **252** 1492–7

[237] Rebollar E, Castillejo M and Ezquerra T A 2015 Laser induced periodic surface structures on polymer films: From fundamentals to applications

European Polymer Journal **73** 162–74

[238] Qi L, Nishii K and Namba Y 2009 Regular subwavelength surface structures induced by femtosecond laser pulses on stainless steel *Opt. Lett.* **34** 1846–8

[239] Semaltianos N G, Logothetidis S, Perrie W, Romani S, Potter R J, Edwardson S P, French P, Sharp M, Dearden G and Watkins K G 2009 Silicon nanoparticles generated by femtosecond laser ablation in a liquid environment *J Nanopart Res* **12** 573–80

[240] Tsuji T, Iryo K, Watanabe N and Tsuji M 2002 Preparation of silver nanoparticles by laser ablation in solution: influence of laser wavelength on particle size *Applied Surface Science* **202** 80–5

[241] Dolgaev S I, Simakin A V, Voronov V V, Shafeev G A and Bozon-Verduraz F 2002 Nanoparticles produced by laser ablation of solids in liquid environment ed S I Dolgaev *Applied Surface Science* 546–51

[242] Klug U, Düsing J F, Sato T, Washio K and Kling R 2010 Polarization converted laser beams for micromachining applications MOEMS-MEMS vol 7590, ed M A Maher, J-C Chiao and P J Resnick (SPIE) pp 7590061–8

[243] HOLOEYE PHOTONICS AG spatial light modulator, Official webpage of HOLOEYE PHOTONICS AG [cited ct. 2016; Available at: http://holoeye.com/spatial-light-modulators/slm-pluto-phase-only/]

[244] Kinoshita S and Yoshioka S 2005 Structural Colors in Nature: The Role of Regularity and Irregularity in the Structure *ChemPhysChem* **6** 1442–59

[245] Buividas R, Mikutis M and Juodkazis S 2014 Surface and bulk structuring of materials by ripples with long and short laser pulses: Recent advances *Progress in Quantum Electronics* **38** 119–56

[246] Antończak A J, Kocoń D, Nowak M, Kozioł P and Abramski K M 2013 Laser-induced colour marking—Sensitivity scaling for a stainless steel *Applied Surface Science* **264** 229–36

[247] Antończak A J, Stepak B, Kozioł P E and Abramski K M 2014 The influence of process parameters on the laser-induced coloring of titanium *Appl. Phys. A* **115** 1003–13

[248] Ionin A A, Kudryashov S I, Makarov S V, Seleznev L V, Sinitsyn D V, Golosov E V, Golosova O A, Kolobov Y R and Ligachev A E 2012 Femtosecond laser color marking of metal and semiconductor surfaces *Appl. Phys. A* **107** 301–5

[249] Palik E D 1985 *Handbook of optical constants* (London: Academic Press

Inc)

[250] Kandyla M 2006 *PhD Thesis: Ultrafast dynamics of the laser-induced solid-to-liquid phases transition in aluminium* (Cambridge, Massachusetts: Harvard University)

[251] Doerr D W *Ph.D thesis, femtosecond laser microprocessing of aluminum films and quartz* (United States: University of Nebraska-Lincoln)

[252] Tokunaga Y, Kobayashi H, Ishimaru Y, Aizawa K and Hirama J 2010 Thermal diffusivities of commercial transparent polymer films measured using laser induced thermal wave *Acoust. Sci. & Tech.* **31** 288–92

[253] Sherman N K, Brunel F, Corkum P B and Hegmann F A 1989 Transient response of metals to ultrashort pulse excitation *Opt. Eng* **28** 1114–20

[254] Akashev L A and Kononenko V I 2001 Optical Properties of Liquid Aluminum and Al–Ce Alloy *High Temperature* **39** 384–7

[255] 1980 Brookhaven national laboratory selected cryogenic data notebook: section 15. Thermal diffusivity, Jan. 1980; Brookhaven National Laboratory. vol 2 (Brookhaven National Laboratory)

[256] Andrew J E, Dyer P E, Greenough R D and Key P H 1983 Metal film removal and patterning using a XeCl laser *Appl. Phys. Lett.* **43** 1076–8

[257] Beck R J, Parry J P, MacPherson W N, Waddie A, Weston N J, Shephard J D and Hand D P 2016 Application of cooled spatial light modulator for high power nanosecond laser micromachining *Opt. Express* **18** 17059–65

[258] LIGHT CONVERSION opa topas, Official webpage of LIGHT CONVERSION [cited ct. 2016; Available at: http://lightcon.com/Product/TOPAS-Prime.html]

[259] Krystian L. Wlodarczyk • Jarno J. J. Kaakkunen • Pasi Vahimaa • Duncan P. Hand 2014 Efficient speckle-free laser marking using a spatial light modulator *Appl*. *Phys*. *A* **116** 111-118 *J*